STELLINGEN

behorende bij het proefschrift

'Bends in Optical Ridge Waveguides'

van

E.C.M. Pennings

Delft, 12 juni 1990

I

De formules, die Heiblum and Harris geven voor de verzwakking van het licht door middel van afstraling in bochten of in prisma-koppelaars, zijn een factor twee te groot.

M. Heiblum en J.H. Harris: *IEEE J. Quantum Electron.*, **QE-11**, 1975, pp. 75-83.

M. Heiblum: *IEEE J. Quantum Electron.*, **QE-12**, 1976, pp. 463-469.

Dit proefschrift, p. 70 en p. 101.

II

De dichtheid van poreus technisch keramiek kan nauwkeurig bepaald worden door de waterverplaatsingsmethode uit te breiden tot drie wegingen en daarbij glycerol te gebruiken in plaats van water.

E.C.M. Pennings en W. Grellner: *J. Am. Ceram. Soc.*, **72**, 1989, pp. 1268-1270.

III

De in dit proefschrift gepresenteerde berekeningen rechtvaardigen twijfel aan de juistheid van de door Singh *et al.* gepubliceerde resultaten.

J. Singh *et al.*: *Electron. Lett.*, **25**, 1989, pp. 899-900.

Dit proefschrift, pp. 186-188.

IVa

Deze stelling wordt niet afgedrukt in het NRC Handelsblad.

IVb

Het NRC Handelsblad is een dagblad, dat ofwel niet alle ware stellingen ofwel tegenstrijdige stellingen afdrukt.

K. Gödel: Monatshefte für Mathematik und Physik, **38**, 1931.

V

De natuur kan effectiever beschermd worden door haar tot rechts-persoon te maken.

VI

Indien de inschrijving voor de Varsity open staat voor een ieder die zichzelf student noemt, zal Nederland haar meest ludieke studenten-evenement verliezen.

VII

De enige winst van een geoptimaliseerd Black Jack spel, waarbij de speler niet alle kaarten onthoudt die al uit het spel zijn, is een onuitputtelijke hoeveelheid borrelpraat.

VIII

De filosofie van Popper dient aangevuld te worden met de stelling, dat de contradictie vanuit wetenschappelijk standpunt de meest interessante uitspraak is.

K.R. Popper: The logic of scientific discovery (Hutchinson, London, 1968) Ch. 6, § 31.

IX

Gebogen optische multimodale richelgolfgeleiders kunnen vervaardigd worden met verliezen kleiner dan $0.5\,dB/90°$ en kromtestralen kleiner dan $200\,\mu m$. Voor monomode gebogen golfgeleiders zijn deze waarden niet haalbaar, maar biedt de 'vanzelf uitgerichte dubbel geëtste' bocht een goed perspectief om dit wel te realiseren.

X

Optimaal ontworpen gebogen golfgeleiders kunnen gebruikt worden om een geïntegreerde externe trilholte voor een laser te vervaardigen, waarbij de trilholte een lengte heeft van drie centimeter of langer en welke desondanks een oppervlak op het substraat beslaat dat kleiner is dan $0.25\ cm^2$.
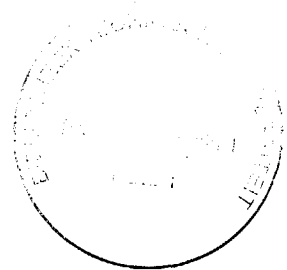
Bends in Optical Ridge Waveguides
Modeling and Experiments

The photograph on the cover shóws a waveguide
which contains four loops with radii of curvature
of 150 µm. The source of light is an He-Ne laser
with a wavelength of 632.8 nm.
(*See also* Fig. 6.5)

Bends in Optical Ridge Waveguides
Modeling and Experiments

Proefschrift

ter verkrijging van de graad van
doctor
aan de Technische Universiteit Delft,
op gezag van de rector magnificus,
prof. drs. P.A. Schenck,
in het openbaar te verdedigen ten overstaan van een commissie
aangewezen door het College van Dekanen
op dinsdag 12 juni 1990 te 16.00 uur.

door

Engelbertus Caspar Maria Pennings

geboren te Sassenheim,
natuurkundig ingenieur

Dit proefschrift is goedgekeurd door de promotoren
Prof. Dr. G.A. Acket en Prof. Dr. Ir. H. Blok

aan Marije
aan Albert en Joost

Contents

Chapter 4   Two-dimensional solutions

Chapter 5   Numerical results

Chapter 6 Al_2O_3/SiO_2 ridge waveguides; experiments

Chapter 7   GaInAsP/InP waveguides; experiments

Appendix A   Implementation of the Bessel functions

Appendix B   The WKB approximation

Appendix C   WKB integrals

Appendix D   Dirac's notation

Appendix E   Recipe

Bibliography

Summary

This thesis deals with the modeling and the fabrication of curved optical wave-guides and the subsequent assessment of their losses.

The properties of curved waveguides—radiation loss and modal field distribu-tions—have been calculated by means of the method of effective dielectric constant in combination with three techniques that can handle the resulting curved slab waveguide; (a) an approach with Bessel functions, (b) a transformation has been applied to the curved slab waveguide and the resulting straight waveguide is analyzed by means of the WKB approximation and (c) the same transformation in conjunction with the staircase approximation and the transfer-matrix method. The numerical results of these three methods have been found to be in good agreement with each other. It has been shown that the method of the effective dielectric constant can be applied to curved waveguides in a similar way as to straight waveguides.

The junction of the straight and the curved waveguide has been studied as well and in order to do so, the orthogonality relations have been derived for the curved waveguide. Exact solutions have been found for the junction of slab waveguides. Numerical results have, however, been obtained by approximating these exact solutions by overlap integrals.

A transformation is proposed in order to analyze two coupled oppositely curved waveguides with identical radii of curvature. This transformation provides insight into the coupling and loss mechanisms of such a geometry and can be used to obtain numerical results, although these have not been pursued in the thesis.

The models and the accompanying computer programs have been used to minimize the losses of curved waveguides. Normalized graphs are given for the radiation loss, the minimum width that a curved waveguide should have and the lateral offset at the junction. Design rules are given.

The computer programs have also been applied to the multi-mode-interference coupler. The results of the modeling show that a multimoded coupler which guides up to eleven modes may show a performance superior to conventional couplers that guide two modes only. The explanation which has been found basically involves the self-focussing effect of multimode slab waveguides.

Experiments have been performed in buried multimode Al_2O_3/SiO_2 waveguides at wavelengths of 0.6328 and 1.3 μm and in multimode GaInAsP/InP waveguides at wavelengths of 1.3 μm and 1.52 μm.

The influence of the lateral offset at the junction of the straight and the curved waveguide has been investigated experimentally for buried Al_2O_3/SiO_2 ridge waveguides. The minimum excess loss has been found for the U-bend with an offset that is very close to the predicted optimum offset.

Two new solutions have been proposed and tested that combine a large lateral refractive-index contrast, which is required for small low-loss bends, and a small lateral refractive-index contrast which is desired in order to reduce the scattering losses and to obtain monomode operation.

The 'double-ridge' waveguide shows scattering and radiation losses that are reduced with respect to those of a corresponding 'single-ridge' waveguide. This has been verified experimentally.

The 'self-aligned doubly etched' bend has a ridge height which is larger for the curved waveguide than for the straight waveguide. S-bends of this type have been fabricated in the form of buried Al_2O_3/SiO_2 ridge waveguides by means of a self-aligned photolithographic technique. A lowest excess loss for the S-bend with a radius of curvature of 200 μm of 0.5 dB/90° has been measured at a wavelength of 632.8 nm. This value of 0.5 dB equals to a large extent the transition loss at one junction of the small-contrast monomode waveguide and the large-contrast waveguide.

The lowest measured excess losses for various S-bends are; 0.23 dB/90° for $R = 75$ μm in Al_2O_3/SiO_2 waveguides at $\lambda_0 = 1.3$ μm, 0.6 dB/90° for $R = 50$ μm in the 'double-ridge' Al_2O_3/SiO_2 waveguide at $\lambda_0 = 632.8$ nm and 0.5 dB/90° for $R = 150$ μm in MOVPE-grown GaInAsP/InP ridge waveguides at $\lambda_0 = 1.52$ μm.

These experimental results demonstrate the effectiveness of the modeling and the loss-minimization strategies.

Chapter 1

General introduction

1.1 Introduction

Communication and telecommunication have always been very important to mankind and much of the communication is optical since a large part of all information eventually reaches us by means of light. Although this form of communication is analogue, it presents a good example of one of the advantages of light, i.e. massive parallelism. A preliminary form of digital optical communication was already used by the ancient Greeks who lit fires on successive mountain tops to herald the fall of Troy[§]. This digital optical communication network possessed the total transmission capacity of one bit and was hampered by one of the difficulties of earlier optical communication systems, i.e. their vulnerability to atmospheric disturbances. Clouds or fog could have caused the Greek communication network to malfunction with the consequence, that this might have saved Agamemnon's life and at the same time would have withheld mankind from one of the most beautiful classic epics.

In modern times, the revolution in optical telecommunication or lightwave communication has been initiated by the development of the semiconductor laser and the glass fiber.

[§] S.L. Radt: *Range: Philips Telecommunication Journal*, **25** (4), 1964, pp. 12-19.

The first laser was the ruby laser built by Maiman[§] in 1960 who followed the proposal by Schawlow and Townes[¶]. The ruby laser was followed by many other types of laser such as the semiconductor laser, gas laser, the dye laser, the X-ray laser, the free-electron laser, et cetera.

The laser exhibits a remarkable combination of properties that have led to a widespread application. Lasers provide a source of coherent light of very high intensity that initiated experiments and the development of a technology, hitherto inaccessible. The combination of a diffraction-limited beam size and a large brightness of the laser light have led to medical applications, to nuclear-fusion experiments while carbon-dioxide lasers are used in machining, welding and cutting. Its high power has even led the military to speculations and investments in order to achieve a sort of 'star-wars' scheme. It seems, however, that the destructive capacity of a laser is larger when it is dropped than when it is fired. The advent of the laser stimulated the research into the area of nonlinear optics, because the laser can provide the large brightness that is required in order for nonlinear effects to become effective. Nonlinear optics is an exciting branch of optics that includes a wide variety of effects and promises such as phase conjugation, four-wave mixing, solitons and in the future possibly an 'optical computer'.

It was soon recognized after the invention of the laser that a frequency of the order of 2×10^{14} Hz in combination with the coherence properties of the laser light yielded an incredible bandwidth that could be exploited for telecommunication purposes. One laser beam could, in principle, transmit information at a rate of, say, 10^{12} bit per second, which is according to present standards adequate to transmit approximately 7000 television programs. It was, on the other hand, clear that a laser beam in free space would be attenuated too much by atmospheric influences to permit the transmission of information over long distances by means of such a freely propagating laser beam.

Soon after the first development of the laser and the realization of its enormous potential bandwidth, attempts were made to confine the light in a lightguide in order to keep the weather and the dirt out of the optical path. A first suggestion as to the use of glass fibers was made by Kao and Hockham[‡] in 1966 and they suggested at that time that an attenuation of 20 dB/km for glass fibers could be achieved, which was a bold suggestion since the bulk attenuation of the best glasses

---

§ T.H. Maiman: "Stimulated optical Radiation in ruby", *Nature*, **187**, 1960, pp. 493-494.
¶ A.L. Schawlow and C.H. Townes: "Infrared and optical masers", *Phys Rev.*, **112**, 1958, pp. 1940-1949
‡ K.C. Kao and G.A. Hockham, *Proc. IEE* (London), **113**, 1966, p. 1151.

was several thousand dB/km in 1966. Since the introduction of glass fiber, their losses have been steadily decreased by means of technological improvements to a present value below 0.2 dB/km at a wavelength of 1.55 μm and we can safely say that the theoretical limit of the attenuation has been reached. Because of the glass fibers, lasers have, indeed, fulfilled part of their potential with respect to telecommunication.

Although the monomode glass fiber is of special importance to lightwave communication, many other types of fiber exist and apart from the application to lightwave communication, many other applications of glass fibers exist; they are applied in "endoscopes" for medical diagnostics, they are applied in optical gyroscopes and the electromagnetic compatibility of fibers has caused many other applications of glass or plastic fibers.

In the same time of the invention of the laser, from 1960 onwards, there was a huge effort to fabricate electronic integrated circuits as a partial spin-off of the Apollo project that put the first men on and off the moon. The integration of many electronic components on one chip results in an increased reliability, a reduced size, a reduced power consumption, and it lends itself to mass-production and consequently reduces the price per chip. The economic driving force and the technology push have led to ever better photolithographic techniques and to a large range of new deposition and etching techniques. These new technologies permit the fabrication of chips which have a size of several square millimeter and contain a million or more transistors.

The combination of the laser and integrated electronics resulted in the semiconductor laser although the invention of the semiconductor junction laser preceded the era of integrated electronics. Semiconductor lasers show many advantages to other types of lasers such as differential quantum efficiencies that approach one hundred per cent, a small size (a typical length of 0.3 mm), high reliability and a reduced price. Many of these features are similar to those encountered in integrated electronics. Widespread application of the semiconductor junction laser has been found in lightwave communication, in the optical storage of digital information, as laser scanners (bar-code readers) and lasers printers (one of the products of which might be enjoyed by the reader right now).

The semiconductor lasers may, in fact, be considered as the first product of *integrated optics*. The phrase 'integrated optics' was coined by Miller[§] in 1969

§   S.E. Miller: "Integrated optics: an introduction", *B.S.T.J.*, **48** (7), 1969, pp. 2059-2069.

and is used to described the integration of optical components on one chip by means of the same photolithographic techniques that are being used to fabricate integrated electronics circuits. A more suitable phrase might be *integrated optoelectronics* since the semiconductor junction laser is both an optical and an electronic device (i.e. a diode). The advantages that apply to integrated electronics apply even better to integrated optics because optical systems are much more vulnerable to their environment than electronic circuits because optical systems are sensitive to alignment and stability, dust and absorption.

From the semiconductor junction laser, it seems a natural step towards more complex lasers such as the distributed feedback laser, the distributed Bragg-reflector laser, the multi-stripe laser, the ring laser et cetera. Not only do semiconductor lasers become more complex, but there is also a tendency to combine the laser with other components in the form of an *optoelectronic integrated circuit* (OEIC). A similar demand for integrated optical circuits comes from the side of lightwave-communication systems which require apart from the laser, optical switches, power splitters, modulators, multiplexers and demultiplexers, polarization controllers, detectors, isolators, et cetera.

A lightwave-communications device which is well suited to an integration in the form of an optoelectronic integrated circuit is the coherent optical transmitter or receiver. The coherent-detection scheme consists of mixing the light that emanates from the glass fiber with the light of a local tunable laser before it is detected (this scheme is similar to the signal detection that is employed in a radio). An impression of such an optoelectronic chip is given in Fig. 1.1. The glass fiber is coupled to a waveguide on the chip. The local-oscillator laser is contained on the chip and is coupled to a similar waveguide. The driving and processing electronics could be placed on the chip as well. A mixing network combines the light from the glass fiber and the local-oscillator laser. In order to preserve the narrow line width of the laser (of the order of one per cent of the bit rate that is to be detected) an optical isolator is required and it is probably this isolator that is the most difficult component to integrate. In order to eliminate fluctuations of the polarization of the light, polarization diversity may be applied which requires polarization splitters, polarization controllers and a double circuitry as shown Fig. 1.1.

The interconnecting waveguides on the chip shown in Fig. 1.1 consist of both straight and curved sections. The curved waveguides are the topic of the thesis and the next section expands on the problems that are encountered for curved waveguides.
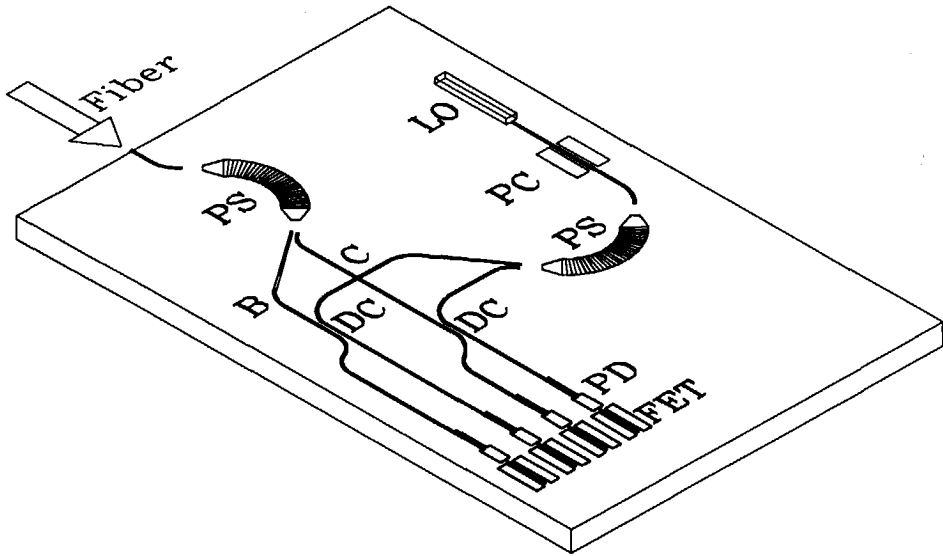
Fig. 1.1 *A schematic impression of an optoelectronic integrated circuit (OEIC) which contains a coherent optical receiver. (LO = local-oscillator laser, PC = polarization controller, PS = polarization splitter, C = waveguide crossing, DC = directional coupler, B = waveguide bend, PD = photodiode and FET = field-effect transistor) (Drawing by Y.S. Oei, Delft University of Technology)*

1.2 The subject of the thesis

Curved open waveguides like the ones shown in Fig. 1.1 exhibit a fundamental loss in the form of radiation. In straight waveguides, the tendency of light to diffract is compensated for by the higher index of refraction of the waveguide core and the guided mode has a plane wave front. In curved waveguides on the other hand, the wave front rotates around a center of rotation. Since the phase velocity of the wave fronts cannot exceed the local speed of light, there is a point beyond which the wave front curves and where radiation occurs [79]. Curved waveguides pose the following dilemma: the radiation losses increase almost exponentially with decreasing radius of curvature. The successful fabrication of integrated optoelectronic circuits, however, requires that waveguides can change direction over a short distance and with small losses. An optoelectronic integrated circuit can have a maximum size of, say, 5 cm and this chip must contain at least a few components. A large radius of curvature is thus of the order of 1 cm and a short radius of curvature is approximately one hundred times as small and of the order of 100 μm. What is meant by 'low-loss' depends on the system specification or its 'power

budget'. Generally speaking, we might say that a loss of 0.1 dB for a component is very good, a loss of 1 dB is reasonable but on the high side and a loss of 10 dB is unacceptable.

The scope of the thesis consist of the following aspects:
- The development of the theoretical and numerical tools that enable the calculation of the losses and other properties of a 'waveguide track' that consists of both curved and straight waveguide sections. The calculations take radiation into account as well as the effect of the junction of the straight and the curved waveguide.
- The use of these numerical tools to analyze the influence of the waveguide parameters, such as the width of the waveguide, its radius of curvature and the influence of the indices of refraction on the transmission properties.
- The development of strategies to minimize the losses of waveguides that include curved sections.
- The fabrication of waveguides with curved sections and the assessment of their losses. These measurements must be related to the predicted losses and can be used to verify the loss-minimization schemes.
- New fabrication techniques have been proposed and tested in order to reduce both the losses and or the radii of curvature.
- Some applications have been considered, studied or fabricated that specifically use very small bends.

1.3 Review of the literature

This section reviews the status quo with respect to curved optical waveguides. Excluded from the review are some papers that discuss curved waveguides but which have nevertheless been considered as being outside the scope of the thesis:
- Open curved waveguides that are operated at microwave wavelengths are not considered. These waveguides often include metal strips.
- Bends and microbending effects in glass fibers fall outside the scope of the thesis.
- Limited attention is given to $LiNbO_3$ bends.
- The review pertains to published measurements of the losses of curved waveguides and not to publications on fabricated waveguide structures such as switches, couplers, ring lasers or ring filters that contain curved waveguide sections but do not report on their losses.
- Only gradual bends are considered. Abrupt bends, 'Shiina' bends and 'coherent' bends fall outside the scope of the thesis, although 'Shiina' bends

are of importance to integrated optics[§]. Totally-reflecting corner mirrors are excluded from the review for the same reason.

• The review does not include the work that is discussed in the thesis.

The publications to which the reader is referred in this section and not in the rest of the thesis, are listed in footnotes rather than in the bibliography at the end of the thesis. An attempt has been made to make this review as complete as possible. The literature concerning the theory and modeling of curved waveguide will be reviewed separately from the reports on experimental work since the existing literature naturally divides itself into these two categories (the reader is also referred to section § 3.1 for an overview).

Theory and modeling

The theoretical treatment of the curved optical waveguide can be traced back in history to the issue of the Bell system technical journal that appeared in September of 1969 and in which Miller introduced the phrase 'integrated optics'. That issue contains a paper by Marcatili on the curved waveguide with a two-dimensional cross-section. Marcatili treats the curved waveguide in a way, similar to the straight waveguide [66][67] and uses Bessel functions and their first-term approximations.

Perturbation techniques are a common approach to solve the problem of the curved optical waveguide. Perturbation techniques come in two versions. One version approximates the field in the curved waveguide by the field of the corresponding straight waveguide. The curved waveguide is then viewed upon as a contrast source and its radiated power is calculated by means of a Kirchhoff-type integral (the Kirchhoff-perturbation technique). A second version of the perturbation techniques expands the equations that govern the problem of the curved waveguide and its solutions in powers of the inverse of the radius of curvature (the $1/R$-perturbation technique). The first term in this approximation corresponds to the solution of the straight waveguide.

---

§ H.F. Taylor: *Applied optics*, 13 (3), 1974, pp. 642-647. H.F. Taylor: *Applied optics*, 16 (3), 1977, pp. 711-716. D. Yap and L.M. Johnson: *Applied optics*, 23 (17), 1984, pp. 2991-2999. S. Kawakami and K. Baba: *Applied optics*, 24 (21), 1985, pp. 3643-3647. T. Shiina, K. Shiraishi and S. Kawakami: *Optics letters*, 11 (1), 1986, pp. 736-738.

Marcuse [70][71] has used a perturbation technique to solve the problem of the curved *slab* waveguide. The field in the curved waveguide is approximated by that of the corresponding straight waveguide. The radiation loss is found by evaluating Poynting's vector at infinity, where the electromagnetic field at infinity in the form of the Hankel function of the second kind has been approximated by the first term of Debye's asymptotic expansion. The resulting formula for the radiation loss has later been used by Chen and Unger [18] and by Geshiro and Sawa[§].

The important book on curved waveguides by Lewin, Chang and Kuester [65] contains much material that is also found in their previous publications[¶]. The work by Lewin, Chang and Kuester includes the transformation of the curved *slab* waveguide plus a subsequent WKB approximation and their work states the eigenvalue equation of the curved *slab* waveguide in terms of Bessel functions. Subsequent solutions and their evaluation, however, are always pursued in the form of the Kirchhoff-perturbation technique or the $1/R$-perturbation technique. The work of Maley[‡] discusses the curved and the straight *slab* waveguide and their junction.

The Kirchhoff-type perturbation technique has also been used by Snyder and Love [106] and in an adapted version by White[†] who refers to it as the volume-current method (VCM). The VCM has subsequently been applied to a number of integrated-optics structures by Kuznetsov and Haus [62]. The VCM is applicable in the weak-guidance approximation only and Kendall *et al.* [8][51][52][53][55] [107] have adapted the VCM to waveguide structures with a strong dielectric discontinuity such as the one that occurs at the semiconductor-air interface.

The problem of the curved multilayer *slab* waveguide has been studied by Kawakami, Miyagi, Nishida and Takuma[§§]. They used a transformation (different

§ M. Geshiro and S. Sawa: *IEEE Transactions on microwave theory and techniques*, **MTT-29** (11), 1981, pp. 1182-1187. M. Geshiro and S. Sawa: *Electronics letters*, **19** (9), 1983, pp. 321-322.

¶ L. Lewin: *IEEE Transactions on microwave theory and techniques*, **MTT-22** (7), 1974, pp. 718-727, plus *ibidem*, 1975, p. 779. E.F. Kuester and D.C. Chang: *IEEE Journal of quantum electronics*, **QE-11** (11), 1975, pp. 903-907. D.C. Chang and E.F. Kuester: *Radio science*, **11** (5), 1976, pp. 449-457. E.F. Kuester: *Radio science*, **12** (4), 1977, pp. 573-578.

‡ S.W. Maley: *Radio science*, **12** (4), 1977, pp. 579-585.

† I.A. White: *Microwaves, optics and acoustics*, **3** (5), 1979, pp. 186-188.

§§ S. Kawakami, M. Miyagi and S. Nishida: *Applied optics*, **14** (11), 1975, pp. 2588-2597. Y. Takuma, S. Kawakami and S. Nishida: *Electronics and communications in Japan*, **60-C** (11), 1977, pp. 111-119. Y. Takuma, M. Miyagi and S. Kawakami: *Applied optics*, **20** (13), 1981, pp. 2291-2297. M. Miyagi, S. Matsuo and S. Nishida: *Journal of the optical society of America A*, **4** (4), 1987, pp. 678-682.

from the one by Chang and Barnes [16]) in combination with the perturbation approach. This approximation has also been applied by them to the curved waveguide with a rectangular cross-section[§].

A different approach has been used by Rozzi *et al*. [100]. Their approach to the problem of the curved waveguide consists of the method of the effective dielectric constant in combination with a local coupled-mode formalism. The modal field distribution in the curved waveguide is approximated by that of the corresponding straight waveguide and effect of the curvature is accounted for by the coupling of the guided mode to the continuous modes (of the straight waveguide). An advantage of this approach is that the additional coupling of guided to continuous modes caused by corrugations can be accounted for as well.

The two-dimensional beam-propagation method (BPM) has been used to study curved waveguides as well. The paraxial approximation that underlies the BPM does not permit the study of curved waveguide sections that subtend a large angle. Baets and Lagasse [7] have overcome this problem by first transforming the curved waveguide into an equivalent straight waveguide [16] and then applying the 2-D BPM. This technique has found widespread application. An adapted version of the BPM has been applied to bends by Yevick and Hermansson[¶]. An interesting application of the BPM is found in a paper[‡] by Okamoto and Ito who applied the BPM to the nonlinear curved *slab* waveguide and found that the self-focusing effect of nonlinear waveguides leads to a reduced radiation loss.

The curved *slab* waveguide can be transformed into an equivalent straight waveguide, where the effect of the curvature is accounted for by a transformed refractive-index profile. This transformation is first described by Chang and Barnes [16] and has later been used in the form of a conformal mapping by Heiblum and Harris [40][41]. Both Chang and Barnes and Heiblum and Harris used a WKB approximation to solve the problem of the straight waveguide with the transformed refractive-index profile. Thyagarajan, Shenoy and Ghatak [112] solved the problem of the straight waveguide with the transformed refractive-index profile by means of the transfer-matrix method. Ma and Liu[†] have studied the curved waveguide with a rectangular cross-section by means of a technique that

§ M. Miyagi and S. Nishida: *Journal of the optical society of America*, **68** (3), 1978, pp. 316-319.
¶ D. Yevick and B. Hermansson: *Electronics letters*, **21** (22), 1985, pp. 1029-1030.
‡ N. Okamoto and S. Ito: *IEEE Journal of quantum electronics*, **24** (10), 1988, pp. 1966-1969.
† C. Ma and S. Liu: *Optical and quantum electronics*, **19**, 1987, pp. 83-92.

might be classified as the method of effective-dielectric constant in combination with the transformation and a WKB-like approximation. Sheem and Whinnery [102][103] solved the problem of the straight waveguide with the transformed refractive-index profile in terms of Airy functions which may be compared to the solution provided by the WKB approximation. Sheem and Whinnery also noted the importance of the single-boundary bend.

The paper by Morita and Yamada [75] discusses the problem of the curved *slab* waveguide plus the corresponding junctions. They expressed the field in terms of Bessel functions without calculating the modes, i.e. without requiring the radiation condition. Consequently, the radiation loss is determined by considering Poynting's vector at infinity in much the same way as Marcuse [70] has done.

The problem of the curved waveguide can also be approached by expressing its solution in terms of Bessel functions and by evaluating the Bessel functions numerically. Neumann and Richter [81] reported on the actual evaluation of the Bessel functions in relation to the problem of the curved *slab* waveguide. The work of Neumann is also important since he has studied the problem of the junction of the straight and the curved waveguide, for which he suggested the application of a lateral offset to reduce the transition losses [80][82]. Van der Pauw[§] used the numerical evaluation of the Bessel functions to analyze the multilayer *slab* waveguide with a lossy coating where the losses are caused by the lossy coating instead of radiation. Novel is the method of lines for curved waveguides by Gu [36][37]. It is the only method that combines the Bessel-function approach with a technique that is applicable to waveguides with a two-dimensional cross-section.

Experimental work

LiNbO3

Minford, Korotky and Alferness[¶] reported on waveguide bends in Ti:LiNbO$_3$ at a wavelength of 1.3 µm and found losses as low as 0.2 ± 0.2 dB for an S-bend with a lateral displacement of 0.1 mm and transition length of 3.25 mm (which amounts to an effective radius of curvature of approximately 26 mm). Later, Korotky,

---

§ L.J. van der Pauw: *Philips journal of research*, **41** (5), 1986, pp. 431-444.

¶ W.J. Minford, S.K. Korotky and R.C. Alferness: *IEEE Journal of quantum electronics*, **QE-18** (10), 1982, pp. 1802-1806.

Marcatili, Veselka and Bosworth reported[§] on the CROWNING technique to
reduce the bending losses of Ti:LiNbO$_3$ S-bends and they measured an excess loss
of 0.1 dB for an S-bend with a radius of curvature of 5.5 mm at a wavelength of
1.48 μm.

Döldissen *et al.* [31] have reported on the fabrication and measurement of
S-bends in Ti:LiNbO$_3$ at a wavelength of 1.3 μm, where a lateral offset has been
introduced at junction of the straight and the curved waveguide. They reported a
loss reduction of up to 2 dB for the complete S-bend by using an optimized offset.

Majd, Schüppert and Petermann[¶] have reported a loss of 1 dB for an S-bend with
a radius of curvature of 6 mm in Ti:LiNbO$_3$ at a wavelength of 0.79 μm. This result
was achieved by means of two extra MgO diffusions in order to reduce the index
of refraction at the outside of the bend and by means of an increased width of the
curved waveguide.

AlGaAs

Austin was the first to report on curved waveguides in AlGaAs with submillimeter
radii of curvature[‡]. He reported a 3 dB loss for an MOCVD-grown multi-mode
90° bend with a radius of curvature of 300 μm at a wavelength of 1.15 μm, and a
loss Of 8.5 dB for a single-mode 90° bend with a radius of curvature of 400 μm.
Austin and Flavin [6] fabricated monomode S-bends with a radius of curvature of
300 μm for which they measured a loss of 0.9 dB at a wavelength of 1.15 μm.

Inoue *et al.*[†] have reported on low-loss straight and curved waveguides in
MOCVD-grown AlGaAs. The S-bend losses are assessed to be below 0.5 dB for
a radius of curvature of 10 mm at a wavelength of 1.3 μm.

Rolland *et al.*[§§] published an experimental excess loss below 0.15 dB for an
S-bend with a lateral displacement of 10 μm and a transition length of 100 μm (
which amounts to an effective radius of curvature of approximately 250 μm) at a

§ S.K. Korotky, E.A.J. Marcatili, J.J.Veselka and R.H. Bosworth: Proceedings of ECIO'85, pp.
   207-209. S.K. Korotky, E.A.J. Marcatili, J.J.Veselka and R.H. Bosworth: *Applied physics
   letters*, **48** (2), 1986, pp. 92-94.
¶ M. Majd, B.Schüppert and K. Petermann: Proceedings of the ECOC '89, 1989, paper TuB6.
‡ M.W. Austin: *IEEE Journal of quantum electronics*, **QE-18** (4), 1982, pp. 795-800.
† H. Inoue, K. Hiruma, K. Ishida, T. Asai and H. Matsumura: *Journal of lightwave technology*,
   LT-3 (6), 1985, pp. 1270-1276.
§§ C. Rolland, G. Mak, K.E. Fox, D.M. Adams, A.J. Springthorpe, D. Yevick and B. Hermansson:
   Electronics letters, **25** (18), 1989, pp. 1256-1257.

wavelength of 1.3 μm. They found the measured excess loss to be in good agreement with the predictions of the 3-D beam propagation method.

Takeuchi and Oe[§] have fabricated S-bends in single-mode AlGaAs waveguide with radii of curvature below 1 mm. They assessed the propagation losses to be 0.58 and 0.69 dB/cm at wavelengths of 1.3 and 1.55 μm, respectively, and they measured an excess loss of 0.61 dB and 0.46 dB for the S-bend with a radius of curvature of 2 mm and at wavelengths of 1.3 and 1.55 μm respectively.

An extensive investigation into the scattering and radiation losses of AlGaAs waveguides has been performed by Deri *et al.*[¶] [25] and by Seto *et al.* [101] where an excess loss of 1 dB/90° has been reported for single-mode S-bends with a radius of curvature of 300 μm at a wavelength of 1.5 μm and simultaneously a propagation loss for the straight waveguides of 1 dB/cm.

GaInAsP

Singh, Henning, Harlow and Cole have fabricated single-mode S-bends in GaInAsP on InP, for which they reported a loss of 1.1 dB for a radius of curvature of 200 μm at a wavelength of 1.553 μm [104]. The single-mode operation was achieved by means of a small width of the waveguides of 1 μm.

1.4 Outline of the thesis

The thesis is divided in three parts. A theoretical part and an experimental part are separated by a part that is devoted to numerical results and design rules, i.e. Chapter 5.

Chapter 2

Chapter 2 gives the basic relations concerning optical waveguides (section § 2.1) and it describes the general configuration of the straight waveguide, the curved waveguide and the junction of the two in section § 2.2. The electromagnetic problem is formulated in section § 2.3, where attention is paid to the modal representation of the electromagnetic field in curved open waveguides. The field orthogonality relations for modes in curved open waveguides are derived in section § 2.3.3. These relationships are required for the full treatment of the problem of the junction of the curved and the straight waveguide.

---

§   H. Takeuchi and K. Oe: Proceedings of the IGWO '88, paper MB6. H. Takeuchi and K. Oe: *Applied physics letters*, **54** (2), 1989, pp. 87-89. H. Takeuchi and K. Oe: *Journal of lightwave technology*, **7** (7), 1989, pp. 1044-1054.

¶   R.J. Deri, E. Kapon and L.M. Schiavone: *Electronics letters*, **23** (16), 1987, pp. 845-847.

Chapter 3

The method of the effective dielectric constant is the topic of Chapter 3. This well-known method approximates the three-dimensional waveguiding configurations by equivalent two-dimensional ones. It will be shown in that chapter that the method of the effective dielectric constant is applicable to both straight and curved waveguides.

Chapter 4

The resulting effective two-dimensional configuration is discussed in Chapter 4 That chapter is divided into four parts. Section § 4.1 discusses three methods to solve to the problem of the curved waveguide. Section § 4.2 deals with the junction of the straight and the curved waveguide. Section § 4.3 explains how the properties of a complete waveguide track which consists of multiple interconnected straight and curved waveguides may be calculated in terms of the solutions that have been developed in the previous sections. Section § 4.4 introduces a transformation that is capable of handling the two-dimensional problem of two coupled oppositely curved waveguides.

Chapter 5

Section § 5.1 is devoted to the assessment of the numerical accuracy and the merits of the various techniques that have been developed in the Chapters 2, 3 and 4. Section § 5.2 is devoted to the modeling of curved waveguides. Normalized graphs are given for the radiation loss, the minimal width that a curved waveguide must have, and an estimate of the optimum lateral offset that must be used at the junction of a straight and a curved waveguide. Section § 5.3 is entitled "using bends" and discusses one application, i.e. the multi-mode interference coupler with curved access waveguides. The sections § 5.3 and § 4.4 are, therefore, linked. The modeling of this coupler leads to some interesting results with respect to the self-focussing properties of multimode waveguide which can be used to advantage.

Chapter 6

Chapters 6 and 7 describe the results of experiments. Buried ridge waveguides in the form of S-bends have been optimized and fabricated in the Al_2O_3/SiO_2 material system and the losses of these S-bends have been determined at wavelengths of 632.8 nm and 1.3 μm. These experiments are described in the sections § 6.2 and § 6.6, respectively. The influence of the lateral offset at the junction of a straight and a curved waveguide has been investigated experimentally, the results of which have been condensed into section § 6.3. The minimization of the radiation loss of curved waveguides may be in conflict with requirements that result from

the optimization of other components on the same chip. Two schemes have been proposed and tested that compromise between these conflicting requirements: the 'double-ridge' waveguide and the 'self-aligned doubly etched' bend. The report on these experiments may be enjoyed by the reader in sections § 6.4 and § 6.5, respectively.

Chapter 7

S-bends have been fabricated in the form of ridge or rib waveguides in LPE-grown GaInAsP/InP and their losses have been determined for a wavelength of 1.3 μm. These experiments are the topic of section § 7.1. Similarly, curved waveguides have been fabricated in the form of rib waveguides in MOVPE-grown GaInAsP/InP. These waveguides have been designed in the form of U-bends or 'chicanes' and their optical losses at a wavelength of 1.52 μm are reported in section § 7.2. Chapter 7 is structured around two publications that report on these measurements. The two manuscripts are supplemented by respective introductions and addenda.

Chapter 2

Basic relations

This chapter is devoted to basic relations and definitions. Section § 2.1 deals with Maxwell's equations, boundary conditions, time dependence and basic assumptions about the media under consideration. It also introduces frequently used parameters such as the plane-wave index of refraction and the wave number of light in vacuum. The description of the general structure of the curved waveguide is the topic of the section § 2.2, which also introduces the appropriate coordinate systems. Section § 2.3 formulates the problem of electromagnetic waves in curved waveguiding structures.

2.1 Basic equations

The waveguiding structures of interest operate at one wavelength. Consequently, the electromagnetic fields are time harmonic and it is convenient to introduce the complex representation of the electromagnetic field quantities. The time-dependence of the electric field strength, for example, is defined as

$$E(r,t) = \text{Re}\{E(r,\omega)e^{j\omega t}\}. \tag{2.1.1}$$

The imaginary unit j has been chosen in accordance with precedents in electrical engineering, ω denotes the angular frequency and t is the time coordinate. As Paris

is nearer to the Netherlands than the USA, we adopt the system of S.I. units and they are used throughout the thesis. The names and units of all symbols are listed in the table on page 217.

The electromagnetic field quantities in a source-free domain satisfy the Maxwell equations in complex form

$$\nabla \times E(r,\omega) + j\omega B(r,\omega) = 0 , \tag{2.1.2}$$

$$\nabla \times H(r,\omega) - j\omega D(r,\omega) = 0 . \tag{2.1.3}$$

They can be supplemented with the divergence relations

$$\nabla \cdot D(r,\omega) = 0 , \tag{2.1.4}$$

$$\nabla \cdot B(r,\omega) = 0 . \tag{2.1.5}$$

The media under consideration are assumed to have the following properties:
- locally reacting,
- isotropic,
- linear,
- time-invariant and
- dielectric.

These assumptions lead to constitutive relations between the quantities D and E and the quantities B and H

$$D(r,\omega) = \varepsilon(r,\omega)E(r,\omega) , \tag{2.1.6}$$

$$B(r,\omega) = \mu_0 H(r,\omega) , \tag{2.1.7}$$

where the permeability of vacuum $\mu_0 \overset{\text{def}}{=} 4\pi \times 10^{-7} \, \text{NA}^{-2}$, while $\varepsilon(r,\omega)$ denotes the scalar complex dielectric permittivity

$$\varepsilon(r,\omega) = \varepsilon'(r,\omega) - j\varepsilon''(r,\omega) . \tag{2.1.8}$$

From energy considerations we have

$$\begin{aligned}
\varepsilon''(r,\omega) &\geq 0 , \quad \text{for passive media} , \\
\varepsilon''(r,\omega) &< 0 , \quad \text{for active media} .
\end{aligned} \tag{2.1.9}$$

In view of the causality, the real part $\varepsilon'(\omega)$ and the imaginary part $-\varepsilon''(\omega)$ of $\varepsilon(\omega)$ are interrelated through the Kramers-Kronig relations [50].

It is convenient to introduce the plane-wave index of refraction

$$n(r,\omega) = n'-jn'' \stackrel{\text{def}}{=} \sqrt{\frac{\varepsilon(r,\omega)}{\varepsilon_0}} \, , n' > 0 \, . \tag{2.1.10}$$

The real part of the plane-wave index of refraction relates the velocity of electromagnetic plane waves in vacuum c to the phase velocity in the bulk medium and is therefore positive. The dielectric permittivity of vacuum ε_0 and the permeability of vacuum μ_0 are related to the velocity of light $c \stackrel{\text{def}}{=} 2.99792458 \times 10^8$ m s^{-1} and the vacuum wave number k_0 through

$$k_0^2 = \frac{\omega^2}{c^2} = \omega^2 \varepsilon_0 \mu_0 \, . \tag{2.1.11}$$

The value of the dielectric permittivity of vacuum $\varepsilon_0 = 8.854187817... \times 10^{-12}$ F m^{-1} now follows from the definitions of μ_0 and c because $\varepsilon_0 = 1/(\mu_0 c^2)$.

Across an interface S between two dielectric media, with an outward normal $\hat{n}$, Maxwell's equations have to be supplemented with the boundary conditions
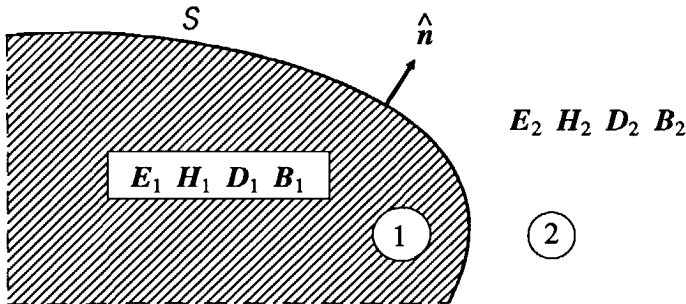
Fig. 2.1 *A schematic diagram of the boundary interface S between two different media.*

$$\hat{n} \times (E_2 - E_1) = 0 \, , \tag{2.1.12}$$

$$\hat{n} \times (H_2 - H_1) = 0 \, , \tag{2.1.13}$$

$$\hat{n} \cdot (D_2 - D_1) = 0 , \qquad\qquad\qquad\qquad (2.1.14)$$

$$\hat{n} \cdot (B_2 - B_1) = 0 . \qquad\qquad\qquad\qquad (2.1.15)$$

For the boundary conditions at the surface of a perfect electrical conductor we have

$$\hat{n} \times E_2 = 0 , \qquad\qquad\qquad\qquad\qquad (2.1.16)$$

$$\hat{n} \cdot B_2 = 0 . \qquad\qquad\qquad\qquad\qquad (2.1.17)$$

The power-flow density of the electromagnetic fields is given by the time average of Poynting's vector

$$<S(r,t)>_T = <E(r,t) \times H(r,t)>_T = \frac{1}{2} \cdot \text{Re}[E(r,\omega) \times H^*(r,\omega)] . \qquad (2.1.18)$$

Poynting's vector has been averaged over a period $T = 2\pi\omega^{-1}$ and the time dependence Eq. (2.1.1) has been used. In the remaining part of the thesis we will omit ω in the complex field quantities.

2.2 General configuration

2.2.1 Introduction

It is of paramount importance that the general configuration be explained before going into mathematical details. The objective is to analyze the waveguide *tracks* along which light is guided on an optoelectronic chip. These tracks may connect more sophisticated devices, such as lasers, photodiodes and switches. They consist of straight and curved sections connected head to tail as shown in the example in Fig. 2.2. These sections can be concatenated in arbitrary order and every section is permitted to have different widths, lengths and radii of curvature. Any gradual changes in waveguide configuration that occur, for example, in Y-junction splitters and tapered transitions between two waveguides of different widths are excluded from the present analysis. The track in Fig. 2.2 is depicted two-dimensionally, but all structures are understood to be three-dimensional. Figures 2.3 and 2.4 thus give a more realistic impression of the straight and the curved sections.

The waveguides in Fig. 2.2 are bounded by two interfaces, denoted by $y = y_1$ and
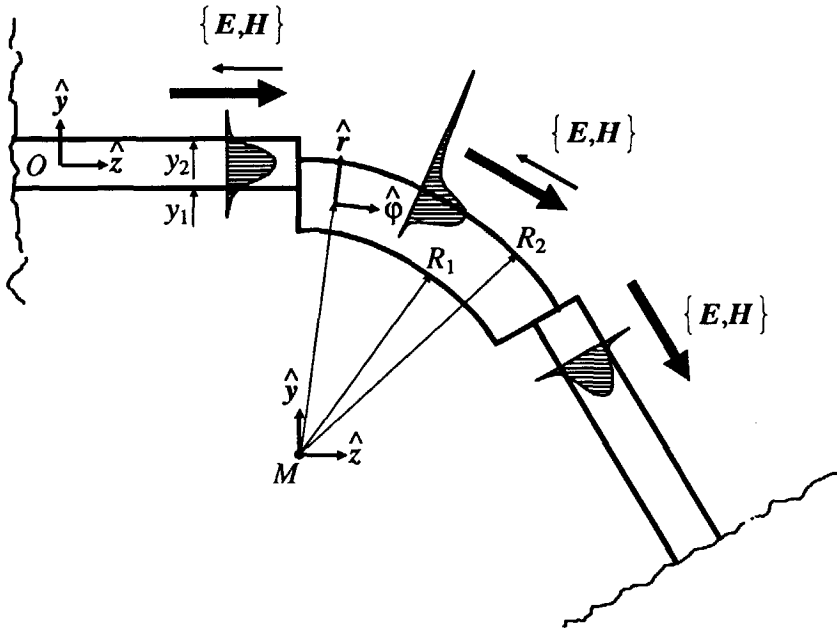
Fig. 2.2 *General 2-D waveguide track, consisting of a circularly curved section joining two straight sections. The order in which the curved and the straight parts are concatenated is arbitrary thereby including bend-bend and straight-straight transitions. Every section is characterized by its own width, length and radius of curvature. The lateral field distributions of the fundamental modes are shown as illustrations.*

$y = y_2$ for the first straight section and by $r = R_1$ and $r = R_2$ for the bend. This is merely an example and our analysis will be more general. The number of these interfaces is not limited to a maximum, thus allowing for the analysis of more complex waveguides and systems of coupled waveguides.

2.2.2 The straight waveguide

Nothing is simpler than being straight. By straight we mean that a waveguide is invariant under the translation along one coordinate, which we take to be the z-coordinate of a right-handed Cartesian coordinate system $Oxyz$. This coordinate defines the direction of propagation or the longitudinal direction. It is customary to distinguish the directions perpendicular to the longitudinal direction between lateral and transversal respectively as shown in Fig. 2.3. The electromagnetic properties in the various domains D_i of the cross-section of the waveguide are
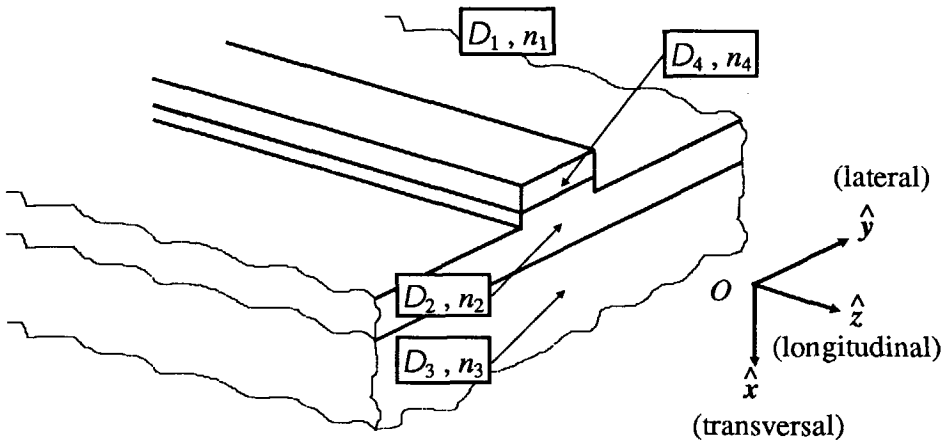
Fig. 2.3 Straight waveguide configuration. This is not the most general structure but serves merely as an example. We fabricated this specific waveguide in InP/GaInAsP (compare with Fig. 7.5).

described in terms of the plane-wave refractive indices n_i. The refractive indices are assumed to be constants in each domain D_i, i.e.

$$n(r) = n_i \text{ for } r \in D_i \text{ with } i = 1, 2, ..., M .$$

(2.2.1)

Although in the specific example shown in Fig. 2.3, $M = 4$, the number M is not limited to a maximum. Every domain is bounded by horizontal planes, $x = $ constant, and by vertical interfaces, $y = $ constant. It is assumed that the outermost regions extend to infinity. The lowest domain is generally called the substrate while the uppermost region is called the superstratum or cover. In order to make waveguiding possible, at least one central domain should have an index of refraction larger than those of both the substrate and the cover. This domain is aptly called the guiding channel. It is obvious that there are a multitude of different waveguiding configurations. I refer the reader to Tamir [110] for a list of the structures and the applied nomenclature. In the waveguide configuration shown in Fig. 2.3, the guiding film D_2 is locally made thicker to form a waveguide and it is then called a ridge waveguide. Most of the waveguides discussed in the thesis are of the ridge-guide type.

2.2.3 The curved waveguide

The discussion will be restricted to sections of curved waveguides that are rotationally invariant around some center of rotation serving as the origin M of a right-handed Cartesian coordinate system $Mxyz$ where the transversal or $\hat{x}$-direction and the axis of symmetry coincide. Because of this symmetry, it is convenient to use a right-handed cylindrical coordinate system $M'r\varphi x$ with $M' = M$. The coordinate system $M'r\varphi x$ is related to $Mxyz$ by
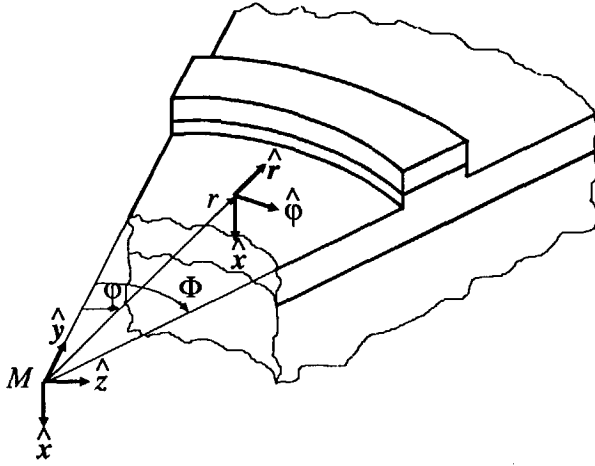
Fig. 2.4 *Example of a curved waveguide. Both the Cartesian and the cylindrical coordinate systems are indicated.*

$$\begin{pmatrix} x \\ y \\ z \end{pmatrix} = \begin{pmatrix} x \\ r\cos\varphi \\ r\sin\varphi \end{pmatrix} \quad \begin{pmatrix} x \\ r \\ \varphi \end{pmatrix} = \begin{pmatrix} x \\ \sqrt{y^2+z^2} \\ \arctan(z/y) \end{pmatrix}. \tag{2.2.2}$$

The lateral direction is now equivalent to the $\hat{r}$-direction. The cylindrical coordinates are bounded by

$$-\infty < x < +\infty, \tag{2.2.3}$$

$$0 \le r < +\infty, \tag{2.2.4}$$

$$0 \le \varphi \le \Phi \le 2\pi. \tag{2.2.5}$$

The remarks made in the preceding section about the domains D_i for straight waveguides apply here as well. Their number M is not limited, the outer ones extend to infinity, they are characterized by a constant complex index of refraction n_i and the lower and upper regions are called the substrate and the cover. There is one difference however; the domains D_i are bounded here by the surfaces $r =$ constant and $x =$ constant.

2.2.4 Junctions

On an actual optoelectronic chip waveguides form tracks where straight and curved waveguides are connected. The junction of a straight waveguide and a bend requires special attention. Light, guided by a straight waveguide, is launched into a bend and we would like to solve the coupling problem of knowing how much power is launched into the bend and how much power is lost. In order to do this, all local coordinate systems have to be expressed in terms of each other. From Fig. 2.5, the interrelation between coordinate systems $O_1x_1y_1z_1$, $M_2x_2y_2z_2$, $M_2'x_2r_2\varphi_2$ and $O_3x_3y_3z_3$ can be easily derived, namely
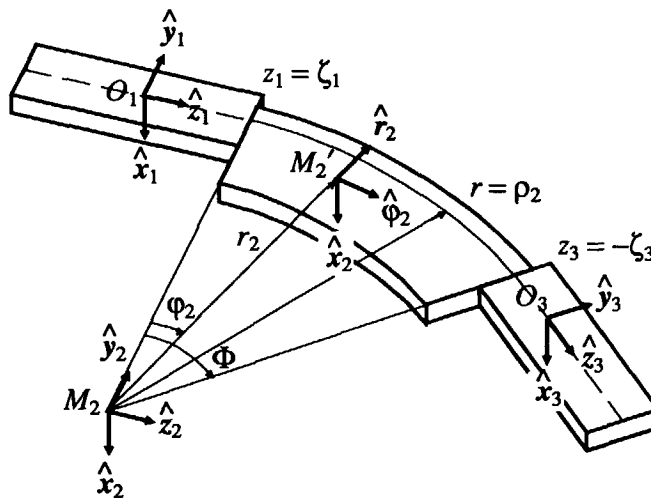
Fig. 2.5 A 3-D view of a waveguide track that includes two junctions of straight and curved waveguides. The waveguide is schematically represented in the form of the guiding layer or the ridge. Every straight section has its own Cartesian coordinate system while every curved section has both a Cartesian and a cylindrical coordinate system.

$$\begin{pmatrix} x_1 \\ y_1 + \rho_2 \\ z_1 - \zeta_1 \end{pmatrix} = \begin{pmatrix} x_2 \\ y_2 \\ z_2 \end{pmatrix} = \begin{pmatrix} x_2 \\ r_2\cos\varphi_2 \\ r_2\sin\varphi_2 \end{pmatrix} = \begin{pmatrix} 1 & 0 & 0 \\ 0 & \cos\Phi & -\sin\Phi \\ 0 & \sin\Phi & \cos\Phi \end{pmatrix} \begin{pmatrix} x_3 \\ y_3 + \rho_2 \\ z_3 + \zeta_3 \end{pmatrix}. \qquad (2.2.6)$$

In the introduction to this section, the possibility of connecting bends to bends and straight waveguides to straight waveguides was mentioned. In these cases the connection between the coordinate systems follows similarly.

2.2.5 Screening the origin

It would be of great advantage to exclude the influence of distant waveguide sections on the coupling problem. Referring to Fig. 2.6, this would be the case if the curved section bent back on itself. To isolate these sections from each other a perfectly conducting screen is put around the origin M at some point $r = R_{sc}$. This screen forces the tangential electric field components to vanish as in Eq. (2.1.16). An identical screen is placed in the straight waveguide configuration at $y = y_{sc}$, in such a way that both screens are aligned at the transition. The exclusion of the origin is not difficult to justify. We look for field distributions that peak near the outer boundary of the curved waveguide structure, with a long tail in the positive r-direction, but with exponentially decreasing behavior towards the origin as sketched in Fig. 2.2. Placing the screen at points where the field is small justifies the assumption of the screen.
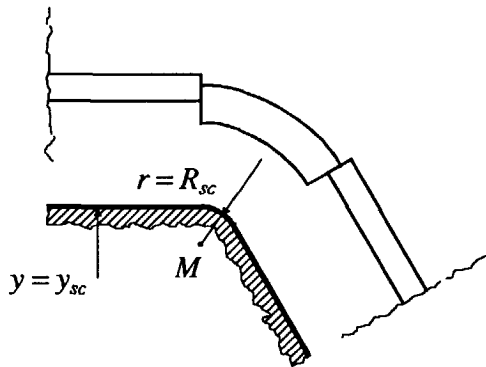
Fig. 2.6 *A perfectly conducting screen is put around the origin to simplify the coupling problem at the junction of the straight and the curved waveguide.*

2.3 Formulation of the bending problem

2.3.1 Introduction

Optical waveguides can be used for the sole purpose of guiding optical power flow from one point to another, or they form a part of more complicated components such as lasers, photodiodes, switches, modulators et cetera. Where they are exclusively used to guide optical power, it seems obvious that no power should be lost. Waveguide tracks include directional changes on optoelectronic chips and, since the manufacture of sophisticated devices with a various components on a small chip is desired, these directional changes have to be achieved in as short a distance as possible. This leads to a conflict because curved open waveguides always radiate light and the smaller the radius of curvature the more the light is radiated. *This is the main problem dealt with in this thesis.*

The bending problem, i.e. a finite bend plus junctions that is both low loss and has a short radius of curvature, is not an isolated problem. First of all there are many other loss mechanisms. Radiation losses are relevant only when they become large compared to those other losses. These mechanisms will be discussed in due time, but are at the moment not crucial to the curved waveguide. Other criteria play a role in the optimization problem of waveguide tracks too. It is often desirable to have single-mode waveguides and any solution to achieve low-loss curved waveguides has to be simple and compatible with the existing technology. Improvements usually require an extra effort and the result should justify this extra effort.

The electromagnetic problem can be formulated as follows. If, in one way or another, a guided mode or some linear combination of guided modes has been excited in the incoming straight waveguide referred to in Fig. 2.2, how much power is still guided in the last waveguide section relative to the input waveguide in the form of guided modes and to what causes can the losses be attributed? If these losses can be calculated, loss optimization follows by calculating the losses while varying the geometry of the configuration.

In order to calculate the losses, we look for solutions of Maxwell's equations that represent guided modes that propagate in straight as well as in curved waveguides. At the junctions, one solution has to be represented in solutions of the other section, i.e. the coupling problem must be solved. Finally these solutions have to be represented in terms of power-flux density, because power is the measured physical quantity.

2.3.2 Straight waveguides

The invariance of the straight waveguide structure with respect to translation along the $\hat{z}$-direction immediately suggests the application of a spatial Fourier transform with respect to this coordinate. This leads to the spectral representation of the electromagnetic field, i.e.

$$\{E,H\}\ (x,y,z)\ =\ \frac{1}{2\pi}\int_{-\infty}^{+\infty}\{\widetilde{E},\widetilde{H}\}\ (x,y;k_z)\mathrm{e}^{-jk_z z}\mathrm{d}k_z\ ,\tag{2.3.1}$$

in which

$$\{\widetilde{E},\widetilde{H}\}\ (x,y;k_z)\ =\ \int_{-\infty}^{+\infty}\{E,H\}\ (x,y,z)\mathrm{e}^{+jk_z z}\mathrm{d}z\ ,\tag{2.3.2}$$

denotes the longitudinal spectrum of the electromagnetic field. In a subsequent spectral decomposition, one arrives at a modal description in which the electromagnetic field in a cross-section of the straight open waveguide is determined by the location and the nature of the singularities—poles and branch points—of the spectrum $\{\widetilde{E},\widetilde{H}\}\ (x,y;k_z)$, in so far as they are located on the physically acceptable, i.e. causal, sheet of a multi-valued Riemann surface that is representative for the complex propagation-coefficient plan (the k_z-plane). The contributions from the poles of Eq. (2.3.2)—discrete spectrum—, $k_z = \beta_\mu$ ($\mu = 1, 2, ..., M$) yield the guided (or surface-wave) modes with modal distribution functions $\{e_\mu^\pm, h_\mu^\pm\}(x,y)$ where the superscripts $+ / -$ denote propagation in the positive / negative z-direction. The contribution from the loop integrals around the branch cuts $k_z = \beta \in B_{1,2}$, corresponding to the chosen Riemann sheets—$B_{1,2}$ are the lines along which $\mathrm{Im}(k_{x,1,2}^2 - \beta^2)^{1/2} = 0$—, yield the radiation field—continuous superposition of radiation modes—with modal distribution functions $\{e^\pm, h^\pm\}(x,y;\beta)$. The resulting modal distribution in a cross-section of a straight open waveguide is then given by

$$E(x,y,z) = \sum_{\mu=1}^{M} \left\{ c_\mu^+ e_\mu^+(x,y)e^{-j\beta_\mu z} + c_\mu^- e_\mu^-(x,y)e^{+j\beta_\mu z} \right\} +$$

$$\sum_{i=1}^{2} \int_{\beta \in B_i} \left\{ c^+(\beta)e^+(x,y;\beta)e^{-j\beta z} + c^-(\beta)e^-(x,y;\beta)e^{+j\beta z} \right\} d\beta , \tag{2.3.3}$$

and a similar expression for $H(x,y,z)$. For an extensive discussion of the modal representation presented above see Blok [11][12] and de Ruiter [28]. Simple poles located on the nonphysically acceptable, i.e. noncausal, Riemann sheets—often referred to as improper poles—can be interpreted as leaky-wave poles; the corresponding field distributions are the leaky-wave modes. Leaky-wave modes can play a role in approximating the radiation field. Hessel [43] gives a thorough introduction to this delicate topic while Blok *et al.* [12] and Tamir *et al.* [49][61] [109] presented an intensive numerical investigation for the case of a slab wave-guide. Leaky-wave modes also play a role in understanding the prism coupler. Taking into account the similarity between the problem of the prism coupler and that of the dielectric bend [41], leaky waves will be calculated for bend problems after they have been transformed into an equivalent straight "guiding" structure (*See* section § 4.1.5).

The electric and the magnetic field strength $\left\{ e_\mu^+, h_\mu^+ \right\}(x,y)$ of the forward propagating mode with mode number μ, satisfy the equations

$$j\omega\mu_0 \begin{pmatrix} h_{x,\mu}^+ \\ h_{y,\mu}^+ \\ h_{z,\mu}^+ \end{pmatrix} = - \begin{pmatrix} \partial_y e_{z,\mu}^+ + j\beta_\mu e_{y,\mu}^+ \\ -j\beta_\mu e_{x,\mu}^+ - \partial_x e_{z,\mu}^+ \\ \partial_x e_{y,\mu}^+ - \partial_y e_{x,\mu}^+ \end{pmatrix}, \tag{2.3.4}$$

$$j\omega\varepsilon_0 n_i^2 \begin{pmatrix} e_{x,\mu}^+ \\ e_{y,\mu}^+ \\ e_{z,\mu}^+ \end{pmatrix} = \begin{pmatrix} \partial_y h_{z,\mu}^+ + j\beta_\mu h_{y,\mu}^+ \\ -j\beta_\mu h_{x,\mu}^+ - \partial_x h_{z,\mu}^+ \\ \partial_x h_{y,\mu}^+ - \partial_y h_{x,\mu}^+ \end{pmatrix}. \tag{2.3.5}$$

Similar relations exist for the radiation modes $\left\{ e^+, h^+ \right\}(x,y;\beta)$. It is easily shown that between modes propagating in the positive z-direction and modes propagating in the negative z-direction the following mutual relationships exist

$$e_x^+, e_y^+ = e_x^-, e_y^- \qquad , \qquad e_z^+ = -e_z^- ,$$
$$h_x^+, h_y^+ = -h_x^-, -h_y^- \quad , \qquad h_z^+ = h_z^- . \tag{2.3.6}$$

In each of the domains D_i, the refractive index n_i is assumed to be constant. Hence $\{e_\mu^\pm, h_\mu^\pm\}(x,y)$ satisfy the Helmholtz equations

$$\left(\partial_x^2 + \partial_y^2 + k_0^2 n_i^2 - \beta_\mu^2\right)\{e_\mu^\pm, h_\mu^\pm\}(x,y) = 0 . \tag{2.3.7}$$

For the existence of at least one guided mode in the modal representation, the condition $\max\{n_{substrate}, n_{cover}\} < \max\{n_{waveguide}\}$ must be satisfied and we might expect to have

$$\max\{k_0 n_{substrate}, k_0 n_{cover}\} < \beta_\mu < \max\{k_0 n_{waveguide}\} . \tag{2.3.8}$$

It is customary to introduce the dimensionless effective refractive index

$$N_{\mu,straight} \stackrel{\text{def}}{=} \frac{\text{Re}(\beta_\mu)}{k_0} = \frac{2\pi \text{Re}(\beta_\mu)}{\lambda_0} , \tag{2.3.9}$$

and the attenuation

$$\alpha_{\mu,straight} = \frac{0.2 \text{Im}(\beta_\mu)}{\ln 10} \text{ dB/cm} , \tag{2.3.10}$$

of the guided mode with mode number μ and complex propagation constant β_μ.

It can be shown that the discrete modes $\{e_\mu^+(x,y), h_\mu^+(x,y), \mu = 1, 2, ..., M\}$ and the continuous modes $\{e^+(x,y;\beta), h^+(x,y;\beta), \beta \in B_{1,2}\}$ form a complete set. In view of the analysis of the junction between a straight and a curved waveguide in section § 4.2, orthogonality relations for the modal constituents are required. The field orthogonality relations for straight open waveguides are well known [106] and will be presented without derivation. For two guided surface-wave modes we have

$$\int\limits_{-\infty}^{+\infty} dx \int\limits_{-\infty}^{+\infty} dy \; \hat{z} \cdot \left\{ e_\mu^+ \times h_\nu^+ \right\} = K_\mu \delta_{\mu,\nu} \,, \tag{2.3.11}$$

where K_μ denotes the norm of the guided mode with mode number μ. For a guided mode and a radiation mode we find

$$\int\limits_{-\infty}^{+\infty} dx \int\limits_{-\infty}^{+\infty} dy \; \hat{z} \cdot \left\{ e_\mu^+ \times h^+(\beta) \right\} = 0 \,, \tag{2.3.12}$$

where $\mu = 1, 2, ..., M$ and $\beta \in B_{1,2}$, while for two radiation modes we have

$$\int\limits_{-\infty}^{+\infty} dx \int\limits_{-\infty}^{+\infty} dy \; \hat{z} \cdot \left\{ e^+(\beta) \times h^+(\beta') \right\} = K(\beta)\delta(\beta-\beta') \,, \tag{2.3.13}$$

where $\beta, \beta' \in B_{1,2}$ and $K(\beta)$ denotes the norm of the radiation mode with $\beta \in B_{1,2}$. Leaky-wave modes are not orthogonal, although an orthogonality condition may be found by performing the integration on a complex cross-section [106]. Forward and backward propagating modes with identical propagating constants are not orthogonal to each other. In the case of degeneracy, it is possible to find linear combinations of the degenerate modes that are orthogonal to each other.

Apart from the *field* orthogonality relations, there are *power* orthogonality relations which will not be used in the thesis, because the problem of the junction can be solved by means of the field orthogonality relations. Power orthogonality is valid for the lossless case $\text{Im}(\varepsilon_r) = 0$ only and makes it possible to write a simple expression for the time average of the total power carried by a straight waveguide

$$<P>_T = \int\limits_{-\infty}^{+\infty} dx \int\limits_{-\infty}^{+\infty} dy \; \hat{z} \cdot \left\{ \tfrac{1}{2}\text{Re}(E \times H^*) \right\} =$$

$$= \frac{1}{2}\sum_{\mu=1}^{M} \left\{ |c_\mu^+|^2 - |c_\mu^-|^2 \right\} K_\mu + \frac{1}{2}\sum_{i=1}^{2} \int\limits_{\beta \in B_i} \left\{ |c^+(\beta)|^2 - |c^-(\beta)|^2 \right\} K(\beta) d\beta \tag{2.3.14}$$

This relation is used to evaluate the total power carried by the first and last straight section of a waveguide track, because the difference in power at the beginning and the end of the waveguide track represents the total loss of power.

Finally it is noted that the presence of a perfectly conducting screen, as discussed in section § 2.2.5, results in the disappearance of one of the branch-cut integrals in the field representation Eq. (2.3.3).

2.3.3　Curved waveguides

The invariance of the circularly curved waveguide structure with respect to rotation around the x-axis suggests the application of a Fourier representation in the axial direction. Then the electromagnetic field $\{E,H\}$ (x,r,φ) can be written as

$$\{E,H\}\,(x,r,\varphi) \;=\; \frac{1}{2\pi}\int_{-\infty}^{+\infty}\{\widetilde{E},\widetilde{H}\}\,(x,r;k_\varphi)e^{-jk_\varphi\varphi}dk_\varphi\,, \qquad (2.3.15)$$

in which

$$\{\widetilde{E},\widetilde{H}\}\,(x,r;k_\varphi) \;=\; \int_{-\infty}^{+\infty}\{E,H\}\,(x,r,\varphi)e^{+jk_\varphi\varphi}d\varphi\,, \qquad (2.3.16)$$

denotes the azimuthal spectrum of the electromagnetic field. It is noted that the integration with respect to φ is carried out over the interval $[-\infty, +\infty]$. In this respect we adopt a point of view that has proved its usefulness in diffraction and wave propagation problems associated with circular cylinders [33]. It might be useful to perform the integration with respect to φ over the section $\varphi_1 < \varphi < \varphi_2$ of the curved waveguide. Once the azimuthal spectrum of the electromagnetic field has been determined, a spectral decomposition similar to the one that has been discussed for the straight open waveguide section leads to the modal distribution. Such a modal description has been discussed for the case of a single concave reactive surface by Lewin *et al.* [65] and by Wasylkiwskyj [123]. The field representation for this configuration shows a contribution of a finite number of discrete modes due to—simple—poles and a branch-cut contribution. The discrete modes appear to be of the whispering-gallery type first discussed by Lord Rayleigh [95][96]. A similar discussion on electromagnetic waves in the neighborhood of curved structures by Lewin *et al.* [65], suggests that also in our problem the

electromagnetic field in a cross-section of the curved open waveguide is determined by the location of the singularities (poles and branch points) of the azimuthal spectrum $\{\widetilde{E},\widetilde{H}\}(x,r;k_\varphi)$, in so far as they are located on a physically acceptable sheet of a multi-valued Riemann surface that is representative for the complex k_φ-plane. The contribution from the poles of Eq. (2.3.16)—discrete spectrum—, $k_\varphi = \gamma_\mu$ ($\mu = 1, 2, ..., M$) yields modes of the whispering-gallery type with modal distribution functions $\{e_\mu^\pm, h_\mu^\pm\}(x,r)$, where the superscripts $+ / -$ denote propagation in the forward / backward φ-direction. The contribution from the branch-cut integral $k_\varphi = \gamma \in [0, j\infty]$, corresponding to the chosen Riemann sheet, yields the continuous spectrum with distribution functions $\{e^\pm, h^\pm\}(x,r;\gamma)$. The resulting modal distribution in a section of a curved open waveguide is then given by

$$
E(x,r,\varphi) = \sum_{\mu=1}^{M} \left\{ c_\mu^+ e_\mu^+(x,r)e^{-j\gamma_\mu\varphi} + c_\mu^- e_\mu^-(x,r)e^{+j\gamma_\mu\varphi} \right\} +
$$

$$
\int_0^{j\infty} \left\{ c^+(\gamma)e^+(x,r;\gamma)e^{-j\gamma\varphi} + c^-(\gamma)e^-(x,r;\gamma)e^{+j\gamma\varphi} \right\} d\gamma , \qquad (2.3.17)
$$

and a similar expression for $H(x,r,\varphi)$. In contrast to the modal representation in the straight open waveguide, the properties of the modal constituents presented in the representation Eq. (2.3.17) have not been investigated. The electric and the magnetic field strength $\{e_\mu^+, h_\mu^+\}(x,r)$ of the forward propagating discrete mode with mode number μ, satisfy the equations

$$
j\omega\mu_0 \begin{pmatrix} h_{x,\mu}^+ \\ h_{r,\mu}^+ \\ h_{\varphi,\mu}^+ \end{pmatrix} = - \begin{pmatrix} r^{-1}\partial_r r e_{\varphi,\mu}^+ + jr^{-1}\gamma_\mu e_{r,\mu}^+ \\ -jr^{-1}\gamma_\mu e_{x,\mu}^+ - \partial_x e_{\varphi,\mu}^+ \\ \partial_x e_{r,\mu}^+ - \partial_r e_{x,\mu}^+ \end{pmatrix}, \qquad (2.3.18)
$$

$$
j\omega\varepsilon_0 n_i^2 \begin{pmatrix} e_{x,\mu}^+ \\ e_{r,\mu}^+ \\ e_{\varphi,\mu}^+ \end{pmatrix} = \begin{pmatrix} r^{-1}\partial_r r h_{\varphi,\mu}^+ + jr^{-1}\gamma_\mu h_{r,\mu}^+ \\ -jr^{-1}\gamma_\mu h_{x,\mu}^+ - \partial_x h_{\varphi,\mu}^+ \\ \partial_x h_{r,\mu}^+ - \partial_r h_{x,\mu}^+ \end{pmatrix}. \qquad (2.3.19)
$$

Similar equations exist for the continuous modes $\{e^+, h^+\}(x,r;\gamma)$. It can be shown

that between modes propagating in the forward φ-direction and modes propagating in the backward φ-direction the following mutual relationships exist

$$
\begin{aligned}
e_x^+ , e_r^+ &= e_x^- , e_r^- \quad , \quad e_\varphi^+ = -e_\varphi^- , \\
h_x^+ , h_r^+ &= -h_x^- , -h_r^- \quad , \quad h_\varphi^+ = h_\varphi^- .
\end{aligned}
\tag{2.3.20}
$$

In each of the domains D_i, the refractive index n_i is assumed to be constant. Hence $\{e_\mu^\pm, h_\mu^\pm\}(x,r)$ satisfy the Helmholtz equations

$$
(\widetilde{\nabla}^2 + k_0^2 n_i^2) \{e_x, h_x\} = 0 ,
\tag{2.3.21}
$$

$$
(\widetilde{\nabla}^2 + k_0^2 n_i^2 - r^{-2}) \{e_r, h_r\} + j2r^{-2}\gamma_\mu \{e_\varphi, h_\varphi\} = 0 ,
\tag{2.3.22}
$$

$$
(\widetilde{\nabla}^2 + k_0^2 n_i^2 - r^{-2}) \{e_\varphi, h_\varphi\} - j2r^{-2}\gamma_\mu \{e_r, h_r\} = 0 ,
\tag{2.3.23}
$$

in which

$$
\widetilde{\nabla}^2 = \partial_x^2 + \partial_r^2 + r^{-1}\partial_r - \gamma_\mu^2/r^2 .
\tag{2.3.24}
$$

The azimuthal or angular propagation constants γ_μ are complex. In order to compare the field representation Eq. (2.3.17) with Eq. (2.3.3) on page 26, it can be useful to introduce

$$
k_\varphi' \overset{\text{def}}{=} \gamma R_t^{-1} , \quad \varphi' \overset{\text{def}}{=} R_t\varphi ,
\tag{2.3.25}
$$

in which R_t is an appropriately chosen radius of curvature. In analogy with the straight section, the effective refractive index can be introduced as

$$
N_{\mu,curved} \overset{\text{def}}{=} \frac{\text{Re}(\gamma_\mu)}{k_0 R_t} = \frac{2\pi\text{Re}(\gamma_\mu)}{\lambda_0 R_t} ,
\tag{2.3.26}
$$

and the attenuation can be introduced as

$$\alpha_{\mu,curved} \stackrel{\text{def}}{=} \frac{10\pi\text{Im}(\gamma_\mu)}{\ln 10} \text{ dB}/90° .$$

(2.3.27)

In contrast to the orthogonality conditions for straight open waveguides, little is found in the literature about orthogonality conditions of the field constituents in curved open waveguides. In the remaining part of this section, it will be indicated how this orthogonality can be derived. To this end we apply the reciprocity relation of Lorentz [23]

$$\oint_S \hat{n}\cdot(E_1\times H_2 - E_2\times H_1)dS = 0 ,$$

(2.3.28)

to the domain V, $[-x_\infty < x < x_\infty$, $R_{sc} < r < R_\infty$, $\varphi_1 < \varphi < \varphi_2$], that is enclosed by the surface S consisting of six parts as shown in Fig. 2.7. The contribution of the perfectly conducting screen at $r = R_{sc}$ will vanish because of the boundary conditions. In the x-direction away from the curved light channel, the field behavior is expected to be evanescent. Consequently, the contributions at the surfaces $[x \to \pm\infty, R_{sc} < r < R_\infty, \varphi_1 < \varphi < \varphi_2]$ will vanish. For large values of r, we might expect the electromagnetic field in the curved structure to behave as an outgoing cylindrical wave. Then also the contribution of the surface $[-\infty < x < \infty, r \to \infty, \varphi_1 < \varphi < \varphi_2]$ will vanish. The only two nonvanishing contributions to the surface integral then come from the interfaces $\varphi = \varphi_1$ and $\varphi = \varphi_2$. Hence from Eq. (2.3.28) we have

$$\int_{R_{sc}}^{+\infty} dr \int_{-\infty}^{+\infty} dx \, \hat{\varphi}\cdot \left\{E_1\times H_2 - E_2\times H_1\right\}_{\varphi=\varphi_2} - \int_{R_{sc}}^{+\infty} dr \int_{-\infty}^{+\infty} dx \, \hat{\varphi}\cdot \left\{E_1\times H_2 - E_2\times H_1\right\}_{\varphi=\varphi_1} = 0 .$$

(2.3.29)

When dealing with discrete modes, we first take for the states 1 and 2 in Eq. (2.3.29) two forward propagating modes,

$$\left\{E_1, H_1\right\} = \left\{e_\mu^+, h_\mu^+\right\}e^{-j\gamma_\mu\varphi} ,$$

(2.3.30)

$$\left\{E_2, H_2\right\} = \left\{e_\nu^+, h_\nu^+\right\}e^{-j\gamma_\nu\varphi} ,$$

(2.3.31)
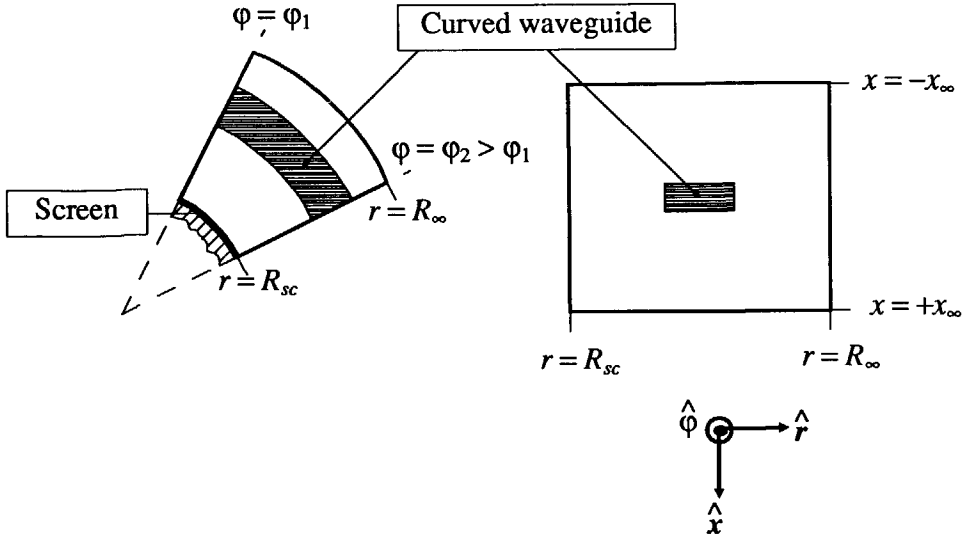
Fig. 2.7 *Cross-section* $x = $ constant *(left) and cross-section* $\varphi = \varphi_2$ *(right) of the curved waveguide. A volume V bounded by a surface S consisting of the six planes $x = \pm x_\infty$, $r = R_{sc}$, $r = R_\infty$, $\varphi = \varphi_1$ and $\varphi = \varphi_2$ is indicated. A perfect conductor that screens the origin is located at the interface $r = R_{sc}$.*

and insert them into the above integral to find

$$\int\limits_{R_{sc}}^{+\infty} dr \int\limits_{-\infty}^{+\infty} dx \; \hat{\varphi} \cdot \left\{ e_\mu^+ \times h_\nu^+ - e_\nu^+ \times h_\mu^+ \right\} \left\{ e^{-j(\gamma_\mu + \gamma_\nu)\varphi_2} - e^{-j(\gamma_\mu + \gamma_\nu)\varphi_1} \right\} = 0 \; . \qquad (2.3.32)$$

Since this has to be valid for any φ_1 and φ_2 it is found that

$$\int\limits_{R_{sc}}^{+\infty} dr \int\limits_{-\infty}^{+\infty} dx \; \hat{\varphi} \cdot \left\{ e_\mu^+ \times h_\nu^+ \right\} = \int\limits_{R_{sc}}^{+\infty} dr \int\limits_{-\infty}^{+\infty} dx \; \hat{\varphi} \cdot \left\{ e_\nu^+ \times h_\mu^+ \right\} , \text{ when } \gamma_\mu + \gamma_\nu \neq 0 \; . \qquad (2.3.33)$$

Next we take for solutions $\{E_1, H_1\}$ and $\{E_2, H_2\}$ a forward propagating mode and a backward propagating mode, respectively:

$$\left\{E_1, H_1\right\} = \left\{e_\mu^+, h_\mu^+\right\} e^{-j\gamma_\mu \varphi} , \tag{2.3.34}$$

$$\left\{E_2, H_2\right\} = \left\{e_\nu^-, h_\nu^-\right\} e^{+j\gamma_\nu \varphi} , \tag{2.3.35}$$

and find in a similar way

$$\int_{R_{sc}}^{+\infty} dr \int_{-\infty}^{+\infty} dx \,\hat{\varphi} \cdot \left\{e_\mu^+ \times h_\nu^-\right\} = \int_{R_{sc}}^{+\infty} dr \int_{-\infty}^{+\infty} dx \,\hat{\varphi} \cdot \left\{e_\nu^- \times h_\mu^+\right\} , \text{ when } \gamma_\mu - \gamma_\nu \neq 0 . \tag{2.3.36}$$

Using the relation Eq. (2.3.20) between backward and forward propagating modes, we find

$$\int_{R_{sc}}^{+\infty} dr \int_{-\infty}^{+\infty} dx \,\hat{\varphi} \cdot \left\{e_\mu^+ \times h_\nu^+\right\} = -\int_{R_{sc}}^{+\infty} dr \int_{-\infty}^{+\infty} dx \,\hat{\varphi} \cdot \left\{e_\nu^+ \times h_\mu^+\right\} , \text{ when } \gamma_\mu - \gamma_\nu \neq 0 . \tag{2.3.37}$$

If $\mu \neq \nu$, then $\gamma_\mu + \gamma_\nu \neq 0$ and $\gamma_\mu - \gamma_\nu \neq 0$. Both Eqs. (2.3.33) and (2.3.37) should hold, leading to *field orthogonality* of the discrete modes

$$\int_{R_{sc}}^{+\infty} dr \int_{-\infty}^{+\infty} dx \,\hat{\varphi} \cdot \left\{e_\mu^+ \times h_\nu^+\right\} = 0 , \text{ when } \mu \neq \nu . \tag{2.3.38}$$

A similar derivation might be given for the continuous modes.

The resulting orthogonality for the guided modes in a curved open structure can be written as

$$\int_{-R_{sc}}^{+\infty} dr \int_{-\infty}^{+\infty} dx \,\hat{\varphi} \cdot \left\{e_\mu^+ \times h_\nu^+\right\} = K_\mu \delta_{\mu,\nu} , \tag{2.3.39}$$

where K_μ denotes the norm of the discrete mode with mode number μ. For a discrete mode and a continuous mode, we have

$$\int_{-R_{sc}}^{+\infty} dr \int_{-\infty}^{+\infty} dx \; \hat{\phi} \cdot \left\{ e_\mu^+ \times h^+(\gamma) \right\} = 0 \, , \tag{2.3.40}$$

while for two continuous modes we have

$$\int_{-R_{sc}}^{+\infty} dr \int_{-\infty}^{+\infty} dx \; \hat{\phi} \cdot \left\{ e^+(\gamma) \times h^+(\gamma') \right\} = K(\gamma)\delta(\gamma-\gamma') \, , \tag{2.3.41}$$

where $\gamma, \gamma' \in [0,j\infty]$ and $K(\gamma)$ denotes the norm of the continuous mode with $\gamma \in [0,j\infty]$. We assume the discrete and continuous modes to form a complete set.

Chapter 3

Tackling the third dimension

The preceding chapter introduced basic definitions and relations, described the general configuration of the straight and the curved waveguide and formulated the electromagnetic problem. The next step is to find solutions for the given geometries. We adopt the well-known method of effective dielectric constant (EDC) or effective index method (EIM) to reduce the number of dimensions by one. The transversal or x-dependence will be taken care off. The two-dimensional cross-section is transformed into a one-dimensional problem, i.e. that of a planar straight or curved waveguide that depends only on the y- or r-coordinate respectively. This chapter deals with the method of effective dielectric constant and section § 3.2 gives a derivation of this method for both the straight and the curved waveguide. It is not evident at first sight that the method of effective dielectric constant—normally used for straight waveguides—can be used for bends as well. Section § 3.1 discusses some approximating techniques like the method of effective dielectric constant.

3.1 Overview of techniques

The classification of the available numerical modeling techniques for optical waveguides is a rather cumbersome process. In fact, there is a European initiative, the purpose of which is to survey and compare these techniques. This COST216 Working Group 1 recently published a study on different modeling techniques for

Table 3.1 *Overview of several modeling techniques. (WIM = weighted index method, BPM = beam propagating method, CEIM = corrected effective index method, EDC = method of effective dielectric constant, FEM and FDM = finite element or finite difference method respectively, DIM = domain integral equation method)*

Classification	Technique	References	Useful for bends	General comments
EDC method [57] [94] plus	Bessel functions	[81]	Yes	
	2-D BPM		Yes	See text
	Transformation and 2-D BPM	[7]	Yes	See text
	Transformation and WKB approximation	[40][41]	Yes	Breaks down at small radii of curvature.
	Transformation and matrix transfer method	[112]	Yes	
	Local modes	[100]	Yes	
Miscellaneous	WIM	[56][29]	Yes	Does not differentiate between HE/EH modes.
	CEIM	[121]	No	
Full 3-D methods	Method of lines	[36][37]	Yes	
	3-D BPM		Yes	See text
	Scalar FEM, Vector FEM, FDM, DIM	[29]	No	
Perturbation techniques	Volume Current Method	[62]	Yes	Perturbation techniques are not suited to calculating the coupling losses.
	Huygens-type formula	[8][51][52] [53][55][107]	Yes	

longitudinally invariant optical waveguides [29]. A similar survey has been done by Benson *et al.* [9]. The COST216 group is currently investigating the problem of the curved waveguide and the directional coupler, but the results of this investigation are not yet available (*See* also page 105).

Various modeling techniques discussed in these two surveys are listed in Table 3.1. Some methods, e.g. the method of effective dielectric method, can be applied in the modeling of straight as well as curved waveguides. As far as methods applicable to bends are concerned, the following problems can be mentioned:

- Perturbation techniques estimate radiation losses quite reasonably, because the radiation loss is related to the imaginary part of the angular propagation constant $\text{Im}(\gamma)$, which is much smaller than its real part $\text{Re}(\gamma)$, even when high radiation losses occur. However, these methods do not give field expressions, because the field of the curved waveguide is approximated by that of the straight waveguide. Knowledge of the fields is required for the full treatment of coupling losses at the junction. The reader is referred to the discussion in § 7.2 of Lewin *et al.* [65] on the use of perturbation theories.

- The beam propagating method (BPM) calculates the total loss of a given structure and it is difficult, though not impossible, to see how different loss mechanisms contribute to the total loss figure. This method gives limited insight into individual loss mechanisms and is for this reason less suited to the optimization of the bend than other techniques.

- The methods are either too slow on a computer or too cumbersome. In order to be able to carry out the modeling of curved waveguides efficiently, it must be possible to calculate the losses of a great number of structures within reasonable computing times. This puts limitations on both the required CPU time and on the friendliness of the interface between the user and the computer program.

3.2 The effective dielectric constant method

3.2.1 Introduction

The method of effective dielectric constant (EDC) or effective-index method (EIM) was introduced by Knox and Toulios [57] as an improvement on Marcatili's method [66]. It has found widespread acceptance due to its general applicability, ease of use and its accuracy. A derivation will be given here because, firstly, although widely used, little can be found in the literature and, secondly, because we are also going to use the method of effective dielectric constant for curved waveguides and to my knowledge, this topic has not been investigated elsewhere. We adopt Marcatili's line of reasoning [66]. An additional advantage of pursuing Marcatili's argument is the elucidation of the differences and the similarities between the methods.
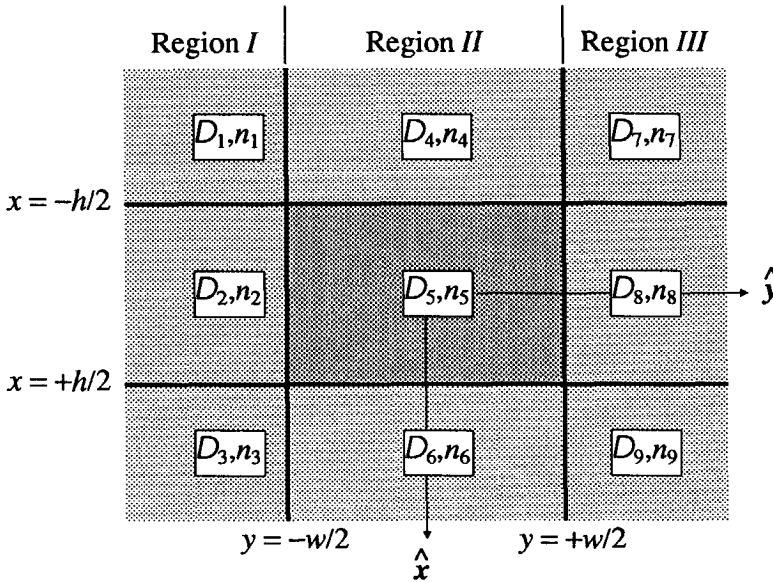
Fig. 3.1 *"Noughts and crosses" cross-section $z =$ constant of the straight waveguide. This generalized waveguide is used in the derivation of Marcatili's method and the method of effective dielectric constant. The central domain has the higher index of refraction and confines the larger part of the power flux. The outer domains are assumed to extend to infinity.*

The derivation will be restricted to the generalized waveguide structure shown in Fig. 3.1. This "noughts and crosses" structure has been used by both Marcatili and Knox *et al.*, and the corrected effective index method (CEIM) by van der Tol and Baken [121] discusses the same "noughts and crosses"[§] waveguide. The analysis is greatly simplified and made much clearer by confining ourselves to a configuration with 3×3 domains D_i.

It is not evident at first sight that this generalized structure encompasses the ridge guide. Ramaswamy [94] applied the method of effective dielectric constant to strip-loaded film waveguides and, therefore, to the similar ridge waveguide. The method of effective dielectric constant will be generalized in section § 3.2.7 in order to apply it to ridge waveguides and multilayer structures.

---

§ "Noughts and crosses" is a game which translates into "Boter, kaas en eieren" in the Dutch language.

3.2.2 Mode nomenclature

It appears that the solutions of the Maxwell equations fall into two groups. This separation originates in the polarization properties of light. The modal fields are generally classified according to the presence of the longitudinal field components; TEM modes have $e_z = h_z = 0$, TE—transverse electric—modes have $e_z = 0$ and $h_z \neq 0$ and TM—transverse magnetic—modes have $h_z = 0$ and $e_z \neq 0$. In open structures TEM-waves are only supported in the trivial case of an infinite uniform medium. Planar straight and curved waveguides support both TE and TM modes, numbered TE_μ or TM_μ with $\mu \geq 0$. But a mode confined in two dimensions in an open waveguide has a hybrid character, $e_z \neq 0$ and $h_z \neq 0$. The appearance of the hybrid modes is nevertheless TEM-like, in the sense that either e_y and h_x are dominant or e_x and h_y. We will use Unger's [117] convention throughout the thesis. His convention identifies TE_μ with H_μ and TM_μ with E_μ and defines a hybrid $HE_{\mu\nu}$-mode, in which μ refers to the transversal mode number and ν to the lateral mode number with $\mu, \nu \geq 0$, as the mode that corresponds to the planar H_μ-mode when the ridge height of a ridge waveguide approaches zero. $HE_{\mu\nu}$-modes may therefore be grouped together as quasi-TE_μ-modes. The nomenclature is summarized in Table 3.2.

Table 3.2 *Definition of the mode nomenclature. Unger's convention is used throughout the thesis. The x-components disappear by definition and this serves as the starting point in the derivation of the method of effective dielectric constant (See Eqs. (3.2.1), (3.2.23) and (3.2.37)). The coordinates x, y and r in Marcatili's nomenclature are the coordinates used in the thesis.*

Nomenclature			Definition (thesis)	
Unger [117]	Planar equivalent	Marcatili [66]	Straight	Curved
$HE_{\mu\nu}$	Quasi-TE_μ	$E^y_{\mu\nu}$, $E^r_{\mu\nu}$	$e_x \overset{\text{def}}{=} 0$ $\|h_x\| \gg \|h_z\| \gg \|h_y\|$ $\|e_y\| \gg \|e_z\| \gg \|e_x\|$	$e_x \overset{\text{def}}{=} 0$ $\|h_x\| \gg \|h_\varphi\| \gg \|h_r\|$ $\|e_r\| \gg \|e_\varphi\| \gg \|e_x\|$
$EH_{\mu\nu}$	Quasi-TM_μ	$E^x_{\mu\nu}$	$h_x \overset{\text{def}}{=} 0$ $\|h_y\| \gg \|h_z\| \gg \|h_x\|$ $\|e_x\| \gg \|e_z\| \gg \|e_y\|$	$h_x \overset{\text{def}}{=} 0$ $\|h_r\| \gg \|h_\varphi\| \gg \|h_x\|$ $\|e_x\| \gg \|e_\varphi\| \gg \|e_r\|$

$HE_{\mu\nu}$ h (transversal) e (lateral)

$EH_{\mu\nu}$ e (transversal) h (lateral)
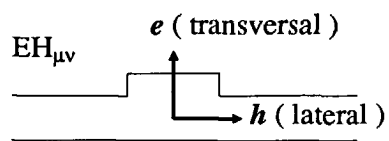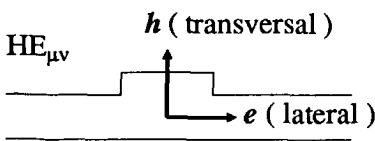
3.2.3 Straight waveguides; HE modes

We can now proceed to the explanation of the method of effective dielectric constant. We define the $HE_{\mu\nu}$ mode by the vanishing of the e_x component, i.e.

$$e_x^\pm \stackrel{\text{def}}{=} 0 .$$

(3.2.1)

The field component $e_y^\pm$ then satisfies the Helmholtz equation Eq. (2.3.7) everywhere

$$e_y^\pm(x,y) = \begin{cases} C_I e^{k_y(y+w/2)} \dfrac{\cos(-k_{yII}w/2+\theta)}{\cos(\varphi_2)} \begin{cases} \cos(-k_{x2}h/2+\varphi_2)e^{k_{x1}(x+h/2)} & r \in D_1 \\ \cos(k_{x2}x+\varphi_2) & r \in D_2 \\ \cos(k_{x2}h/2+\varphi_2)e^{-k_{x3}(x-h/2)} & r \in D_3 \end{cases} \\[4ex] C_{II} \dfrac{\cos(k_{yII}y+\theta)}{\cos(\varphi_5)} \begin{cases} \cos(-k_{x5}h/2+\varphi_5)e^{k_{x4}(x+h/2)} & r \in D_4 \\ \cos(k_{x5}x+\varphi_5) & r \in D_5 \\ \cos(k_{x5}h/2+\varphi_5)e^{-k_{x6}(x-h/2)} & r \in D_6 \end{cases} \\[4ex] C_{III} e^{-k_{yIII}(y-w/2)} \dfrac{\cos(k_{yII}w/2+\theta)}{\cos(\varphi_8)} \begin{cases} \cos(-k_{x8}h/2+\varphi_8)e^{k_{x7}(x+h/2)} & r \in D_7 \\ \cos(k_{x8}x+\varphi_8) & r \in D_8 \\ \cos(k_{x8}h/2+\varphi_8)e^{-k_{x9}(x-h/2)} & r \in D_9 \end{cases} \end{cases}$$

(3.2.2)

where C_I, C_{II}, C_{III}, φ_2, φ_5, φ_8 and θ are constants. The component $e_z^\pm$ is given by

$$e_z^\pm = \frac{\partial_y e_y^\pm}{\pm j\beta} .$$

(3.2.3)

The magnetic field $h^\pm$ is found from Maxwell's equation Eq. (2.3.4)

$$\begin{pmatrix} h_x^\pm \\ h_y^\pm \\ h_z^\pm \end{pmatrix} = \frac{1}{\pm\omega\mu_0\beta} \begin{pmatrix} \partial_y^2-\beta^2 \\ -\partial_x\partial_y \\ \pm j\beta\partial_x \end{pmatrix} e_y^\pm = \frac{1}{\pm\omega\mu_0\beta} \begin{pmatrix} -k_0^2 n_i^2-\partial_x^2 \\ -\partial_x\partial_y \\ \pm j\beta\partial_x \end{pmatrix} e_y^\pm .$$

(3.2.4)

The components of the wave vector k in Eq. (3.2.2) are interrelated by

$$
\begin{pmatrix} k_{x1} \\ k_{x2} \\ k_{x3} \end{pmatrix} = \begin{pmatrix} [(\beta^2-k_{yI}^2)-k_0^2 n_1^2]^{1/2} \\ [k_0^2 n_2^2-(\beta^2-k_{yI}^2)]^{1/2} \\ [(\beta^2-k_{yI}^2)-k_0^2 n_3^2]^{1/2} \end{pmatrix} \overset{\text{def}}{=} k_0 \begin{pmatrix} [N_I^2-n_1^2]^{1/2} \\ [n_2^2-N_I^2]^{1/2} \\ [N_I^2-n_3^2]^{1/2} \end{pmatrix},
\tag{3.2.5}
$$

$$
\begin{pmatrix} k_{x4} \\ k_{x5} \\ k_{x6} \end{pmatrix} = \begin{pmatrix} [(\beta^2+k_{yII}^2)-k_0^2 n_4^2]^{1/2} \\ [k_0^2 n_5^2-(\beta^2+k_{yII}^2)]^{1/2} \\ [(\beta^2+k_{yII}^2)-k_0^2 n_6^2]^{1/2} \end{pmatrix} \overset{\text{def}}{=} k_0 \begin{pmatrix} [N_{II}^2-n_4^2]^{1/2} \\ [n_5^2-N_{II}^2]^{1/2} \\ [N_{II}^2-n_6^2]^{1/2} \end{pmatrix},
\tag{3.2.6}
$$

$$
\begin{pmatrix} k_{x7} \\ k_{x8} \\ k_{x9} \end{pmatrix} = \begin{pmatrix} [(\beta^2-k_{yIII}^2)-k_0^2 n_7^2]^{1/2} \\ [k_0^2 n_8^2-(\beta^2-k_{yIII}^2)]^{1/2} \\ [(\beta^2-k_{yIII}^2)-k_0^2 n_9^2]^{1/2} \end{pmatrix} \overset{\text{def}}{=} k_0 \begin{pmatrix} [N_{III}^2-{}^2 n_7^2]^{1/2} \\ [n_8^2-N_{III}^2]^{1/2} \\ [N_{III}^2-n_9^2]^{1/2} \end{pmatrix},
\tag{3.2.7}
$$

in each domain D_i. All square roots $\sqrt{k_{xi}^2}$ have been chosen with $\text{Re}(k_{xi}) > 0$, $i = 1, 2, \ldots, 9$. The form into which the field component $e_y^{\pm}$, Eq. (3.2.2), has been put ensures its continuity across all horizontal interfaces $x = \pm h/2$. The continuity of the derivatives $\partial_y e_y$ and $\partial_y^2 e_y$ automatically follows from that of e_y and consequently the continuity of the field components e_z and h_x. By requiring the continuity of $\partial_x e_y$ all boundary conditions have been matched exactly at $x = \pm h/2$. This requirement leads to three dispersion relations

$$
\tan(k_{x2}h) = \frac{k_{x2}(k_{x1}+k_{x3})}{k_{x2}^2-k_{x1}k_{x3}}, \text{ when } y \leq -w/2 \text{ (Region } I\text{)},
\tag{3.2.8}
$$

$$
\tan(k_{x5}h) = \frac{k_{x5}(k_{x4}+k_{x6})}{k_{x5}^2-k_{x4}k_{x6}}, \text{ when } -w/2 \leq y \leq +w/2 \text{ (Region } II\text{)},
\tag{3.2.9}
$$

$$
\tan(k_{x8}h) = \frac{k_{x8}(k_{x7}+k_{x9})}{k_{x8}^2-k_{x7}k_{x9}}, \text{ when } +w/2 \leq y \text{ (Region } III\text{)}.
\tag{3.2.10}
$$

We now have to match the boundary conditions at the vertical interfaces $y = \pm w/2$, but it appears to be impossible to make any of the field components continuous along $y = \pm w/2$, because the x-dependence is different in every region

I, *II* and *III*. It is at this point that we are going to make an approximation. The essence of the method of effective refractive index is, in fact, that it gives the horizontal boundaries with the strong refractive index changes priority over the vertical interfaces (*See* also Fig. 3.2 on page 49).

Thus, instead of satisfying the boundary conditions along the entire vertical interfaces $y = \pm w/2$, we are going to match two field components at one point of the interface only, preferably a point where the magnitude of the fields is large, for example at $x = 0$. We will analyze now which boundary conditions can be fulfilled and to what extent. In order to do this we name the two field components that we choose to match $\Psi_1(x,y)$ and $\Psi_2(x,y)$ and we have

$$\Psi_1(x{=}0,y{=}w/2^-) = \Psi_1(x{=}0,y{=}w/2^+), \tag{3.2.11}$$

as the continuity requirement for Ψ_1 at $x = 0$ and $y = w/2$ plus similar requirements for Ψ_1 at $x = 0$ and $y = -w/2$ and for Ψ_2 at $x = 0$ and $y = \pm w/2$. Since Ψ_1 has been matched at $x = 0$ only and not along the entire interfaces $y = \pm w/2$, the continuity of the derivative $\partial_x \Psi_1$ across the interface does not automatically follow, i.e.

$$\left. \partial_x \Psi_1(x,y{=}w/2^-) \right|_{x=0} \neq \left. \partial_x \Psi_1(x,y{=}w/2^+) \right|_{x=0}, \tag{3.2.12}$$

as it did for the transversal boundary conditions. In order to label the extent to which the boundary conditions have been fulfilled, we introduce the difference

$$\Delta\{\Psi_1(x)\} = \Psi_1(x,w/2^-) - \Psi_1(x,w/2^+), \tag{3.2.13}$$

between the field component $\Psi_1(x,y)$ on both sides of the interface $y = w/2$. A similar expression holds for $\Psi_2(x,y)$ and it seems redundant to introduce still another expression for $y = -w/2$. Equation (3.2.11) leads to $\Delta\{\Psi_1(0)\} = 0$ and Eq. (3.2.12) can be written as $\Delta\{\partial_x \Psi_1(x)\} \neq 0$. We will now proceed to make a choice for the field components to be matched and will express the deviation from the continuity requirement by means of Eq. (3.2.13) (This discussion is continued in section § 3.2.8).

The choice of the field components that are going to be matched is inspired by the wish to express the result of the method of effective dielectric constant as a

laterally planar waveguide of width w and refractive indices N_I, N_{II} and N_{III} plus the corresponding TM boundary conditions. The planar lateral waveguide—i.e. without x-dependence—has $e_x = h_y = h_z = 0$, solves the Helmholtz equation for h_x and requires the continuity of h_x and $e_z \propto N_i^{-2}\partial_y h_x$. We choose to match these conditions and require the continuity of $\Psi_1 = h_x \propto N_i^2 e_y$ and $\Psi_2 = N_i^{-2}\partial_y h_x \propto \partial_y e_y$ at $y = \pm w/2$. Effecting these requirements yields

$$C_I(k_{yI}^2 - \beta^2) = C_{II}(-k_{yII}^2 - \beta^2),\qquad(3.2.14)$$

$$C_{II}(-k_{yII}^2 - \beta^2) = C_{III}(k_{yIII}^2 - \beta^2),\qquad(3.2.15)$$

$$k_{yI}C_I\cos(-k_{yI}w/2+\theta) = -k_{yII}C_{II}\sin(-k_{yII}w/2+\theta),\qquad(3.2.16)$$

$$-k_{yII}C_{II}\sin(k_{yII}w/2+\theta) = -k_{yIII}C_{III}\cos(k_{yIII}w/2+\theta),\qquad(3.2.17)$$

The deviation from the continuity requirement of h_x is now expressed as $\Delta\Psi_1$. The deviation from the continuity requirement of e_z is proportional to $\Delta\Psi_2$ since $e_z \propto \partial_y e_y = \Psi_2$, the deviation is proportional to $\Delta(\partial_x\Psi_2)$ for h_y since $h_y \propto \partial_x\partial_y e_y = \partial_x\Psi_2$ et cetera. Table 3.3 summarizes all boundary conditions and the degree to which they are satisfied. The reader will have noticed some arbitrariness, because we could have demanded the continuity of other field components that are equally important. The consequences of this arbitrariness are discussed in section § 3.2.8.

Table 3.3 *The boundary conditions for the HE-modes in straight waveguides using the EDC method. The table indicates which field components have to be continuous, the degree to which this requirement is fulfilled and how it is accomplished. The deviation Δ is explained in Eq. (3.2.13).*

Transversal conditions at $x = \pm h/2$				Lateral conditions at $y = \pm w/2$		
Field component	Relative magnitude	How continuity has been established	Degree of continuity	Field component	Relative magnitude	Degree of continuity. We require continuity of $\Psi_1 = h_x \propto N_i^2 e_y$ and $\Psi_2 = N_i^{-2}\partial_y h_x \propto \partial_y e_y$
d_x		$\stackrel{\text{def}}{=}0$	Exact	e_x		$\stackrel{\text{def}}{=}0$
e_y	**	Required	Exact	d_y	**	$\propto \Delta\{(n_i/N_i)^2\Psi_1\}$
e_z	*	$\Leftarrow e_y$	Exact	e_z	*	$\propto \Delta\Psi_2$
h_x	**	$\Leftarrow e_y$	Exact	h_x	**	$= \Delta\Psi_1$
h_y		$\Leftarrow h_z$	Exact	h_y		$\propto \Delta(\partial_x\Psi_2)$
h_z	*	Required	Exact	h_z	*	$\propto (N_i^{-2}\partial_x\Psi_1)$

An eigenvalue equation is obtained from Eqs. (3.2.14) through (3.2.17) by eliminating C_I, C_{II}, C_{III} and θ and by substituting the N_i from Eqs. (3.2.5) through (3.2.7)

$$\tan(k_{yII}w) = \frac{\dfrac{k_{yII}}{N_{II}^2}\left(\dfrac{k_{yI}}{N_I^2} + \dfrac{k_{yIII}}{N_{III}^2}\right)}{\left(\dfrac{k_{yII}}{N_{II}^2}\right)^2 - \dfrac{k_{yI}}{N_I^2}\dfrac{k_{yIII}}{N_{III}^2}} . \tag{3.2.18}$$

This equation is indeed the TM dispersion relation for a planar waveguide with width w, film index N_{II}, substrate index N_I and cover index N_{III}. The method of effective dielectric constant can now be summarized in the notation of van der Tol and Baken [121]. The propagation constant $\beta_{\mu\nu} = N_{\mu\nu}k_0$ for the $HE_{\mu\nu}$ modes is found by solving a set of four uncoupled equations

$$D_s(TE, n_1, n_2, n_3, h, \mu, N_I) = 0 , \tag{3.2.19}$$

$$D_s(TE, n_4, n_5, n_6, h, \mu, N_{II}) = 0 , \tag{3.2.20}$$

$$D_s(TE, n_7, n_8, n_9, h, \mu, N_{III}) = 0 , \tag{3.2.21}$$

$$D_s(TM, N_I, N_{II}, N_{III}, w, \nu, N_{\mu\nu}) = 0 . \tag{3.2.22}$$

3.2.4 Straight waveguides; EH modes

The derivation for the complementary polarization is very similar to the one just given. The Helmholtz equation is solved for $h_y^\pm(x,y)$ leading to a solution identical to Eq. (3.2.2). The other field components can be calculated from $h_y^\pm$

$$h_x^\pm \overset{\text{def}}{=} 0 \tag{3.2.23}$$

$$h_z^\pm = \frac{\partial_y h_y^\pm}{\pm j\beta} \tag{3.2.24}$$

$$\begin{pmatrix} e_x^\pm \\ e_y^\pm \\ e_z^\pm \end{pmatrix} = \frac{-1}{\pm\omega\varepsilon_0 n_i^2\beta}\begin{pmatrix} \partial_y^2 - \beta^2 \\ -\partial_x\partial_y \\ \pm j\beta\partial_x \end{pmatrix}h_y^\pm = \frac{-1}{\pm\omega\varepsilon_0 n_i^2\beta}\begin{pmatrix} -k_0^2 n_i^2 - \partial_x^2 \\ -\partial_x\partial_y \\ \pm j\beta\partial_x \end{pmatrix}h_y^\pm \tag{3.2.25}$$

The field h and the components d_x, e_y and e_z have to be continuous at the boundaries with the strong dielectric discontinuities $x = \pm h/2$. By requiring the continuity of h_y and $e_z \propto n_i^{-2} \partial_x h_y$ the exact fulfillment of all other conditions follows. These two requirements lead to three TM dispersion relations for $\mathrm{EH}_{\mu\nu}$ modes

$$D_s(\mathrm{TM}, n_1, n_2, n_3, h, \mu, N_I) = 0 , \tag{3.2.26}$$

$$D_s(\mathrm{TM}, n_4, n_5, n_6, h, \mu, N_{II}) = 0 , \tag{3.2.27}$$

$$D_s(\mathrm{TM}, n_7, n_8, n_9, h, \mu, N_{III}) = 0 . \tag{3.2.28}$$

It is not possible to satisfy the boundary conditions in the lateral direction, which are the continuity of h, e_x, d_y and e_z along the entire interfaces $y = \pm w/2$. The fields have different x-dependences in regions I, II and III. Continuity is therefore required along $x = 0$ only, and the reader is referred to page 44 for a discussion on the accompanying deviation. We try again to impose the TE-boundary conditions of a laterally planar waveguide of width w and refractive indices N_I, N_{II} and N_{III}. The laterally planar waveguide has $h_x = e_y = e_z = 0$, solves the Helmholtz equation for e_x and requires the continuity of e_x and $\partial_y e_x$. We impose the same conditions along $x = 0$ at $y = \pm w/2$ and since $e_x \propto (N_i/n_i)^2 h_y$. We have

$$\frac{C_I N_I^2}{n_2^2} = \frac{C_{II} N_{II}^2}{n_5^2} \tag{3.2.29}$$

$$\frac{C_{II} N_{II}^2}{n_5^2} = \frac{C_{III} N_{III}^2}{n_8^2} , \tag{3.2.30}$$

$$\frac{k_{yI} C_I N_I^2}{n_2^2} \cos(-k_{yI} w/2 + \theta) = -\frac{k_{yII} C_{II} N_{II}^2}{n_5^2} \sin(-k_{yII} w/2 + \theta) , \tag{3.2.31}$$

$$-\frac{k_{yII} C_{II} N_{II}^2}{n_5^2} \sin(k_{yII} w/2 + \theta) = -\frac{k_{yIII} C_{III} N_{III}^2}{n_8^2} \cos(k_{yIII} w/2 + \theta) . \tag{3.2.32}$$

We have summarized the boundary conditions in Table 3.4. An eigenvalue equation is obtained by eliminating C_I, C_{II}, C_{III} and θ from Eqs. (3.2.29) through (3.2.32)

Table 3.4 *The boundary conditions for the EH-modes in straight waveguides using the EDC method. The table indicates which field components have to be continuous, the degree to which this requirement is fulfilled and how it is accomplished. The deviation Δ is explained in Eq. (3.2.13).*

Transversal conditions at $x = \pm h/2$				Lateral conditions at $y = \pm w/2$		
Field component	Relative magnitude	How continuity has been established	Degree of continuity	Field component	Relative Magnitude	Degree of continuity We require continuity of $\Psi_1 = e_x \propto (N_i/n_i)^2 h_y$ and $\Psi_2 = \partial_z e_x \propto (N_i/n_i)^2 \partial_y h_y$
d_x	**	$\Leftarrow h_y$	Exact	e_x	**	$= \Delta \Psi_1$
e_y		$\Leftarrow e_z$	Exact	d_y		$\propto \Delta\{(n_i/N_i)^2 \partial_x \Psi_2\}$
e_z	*	Required	Exact	e_z	*	$\propto (N_i^2 \partial_x \Psi_1)$
h_x		$\stackrel{\text{def}}{=} 0$	Exact	h_x		$\stackrel{\text{def}}{=} 0$
h_y	**	Required	Exact	h_y	**	$\propto \Delta\{(n_i/N_i)^2 \Psi_1\}$
h_z	*	$\Leftarrow h_y$	Exact	h_z	*	$\propto \Delta\{(n_i/N_i)^2 \Psi_2\}$

$$\tan(k_{yII}w) = \frac{k_{yII}(k_{yI} + k_{yIII})}{k_{yII}^2 - k_{yI}k_{yIII}},$$
(3.2.33)

or

$$D_s(\text{TE}, N_I, N_{II}, N_{III}, w, v, N_{\mu v}) = 0,$$
(3.2.34)

thus reproducing the dispersion relations of the preceding section with TE and TM interchanged.

3.2.5 Comparison with Marcatili's method

The derivation of the method of effective dielectric constant is very similar to the derivation of Marcatili's method [66]. There are a few differences, however. One of them is unfortunate but cannot be circumvented. Marcatili defined $\text{HE}_{\mu v}$ modes by $h_y \stackrel{\text{def}}{=} 0$ and calculated h_x. The e_x component is proportional to $\partial_y \partial_x h_x$ which is of the second order and can be neglected. But the method of effective dielectric constant has to be exact for a planar waveguide. The approximation becomes worse when the actual structure deviates further from the planar case and the derivation should reflect this fact. It seems more natural to define the $\text{HE}_{\mu v}$ mode by the exact vanishing of $e_x \stackrel{\text{def}}{=} 0$ and to calculate e_y. This difference in starting point does not

have any serious consequences since in both cases e_x, $h_y \approx 0$ within a second-order approximation.

The main difference between Marcatili's method and the EDC method, however, involves the boundary conditions. Marcatili's solution of the field satisfies the scalar Helmholtz equation Eq. (2.3.7) everywhere and so does the solution Eq. (3.2.2) of the method of the effective dielectric constant. But not all boundary conditions can be simultaneously fulfilled. Marcatili's method gives priority to the boundary conditions at the interfaces between the central and the four adjacent regions and neglects the four corner areas. The method of the effective dielectric constant is best suited to a planar-like waveguide, where the largest refractive index changes occur at the horizontal interfaces $x = \pm h/2$, because it fulfills all transversal boundary conditions exactly and the lateral boundary conditions approximately. These differences are shown in Fig. 3.2.

Marcatili's method   EDC method
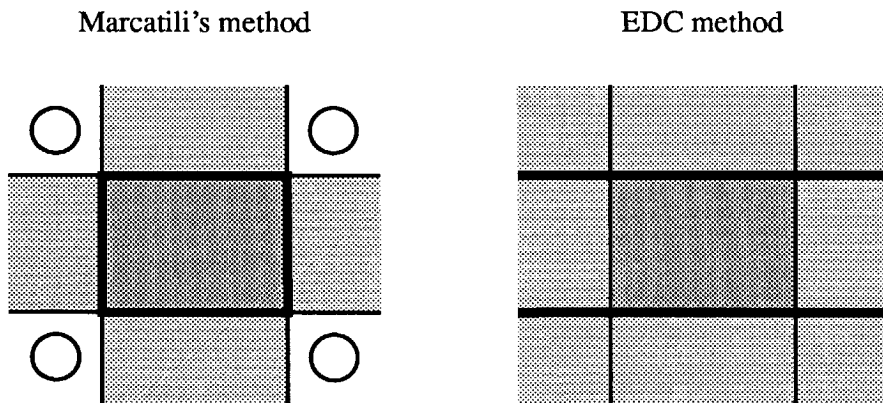
Fig. 3.2 *The differences between Marcatili's method and the method of the effective dielectric constant when they are applied to the generalized "noughts and crosses" cross-section of Fig. 3.1. Marcatili's method stresses the boundary conditions at the interfaces that bound the central domain, while the EDC method exactly fulfills all transversal boundary condition at the horizontal interfaces (thick lines). Marcatili's method neglects the fields in the four corner regions.*

3.2.6 Curved waveguides

We will now proceed to the derivation of the method of effective dielectric constant for curved waveguides and $HE_{\mu\nu}$ modes. The derivation is restricted to
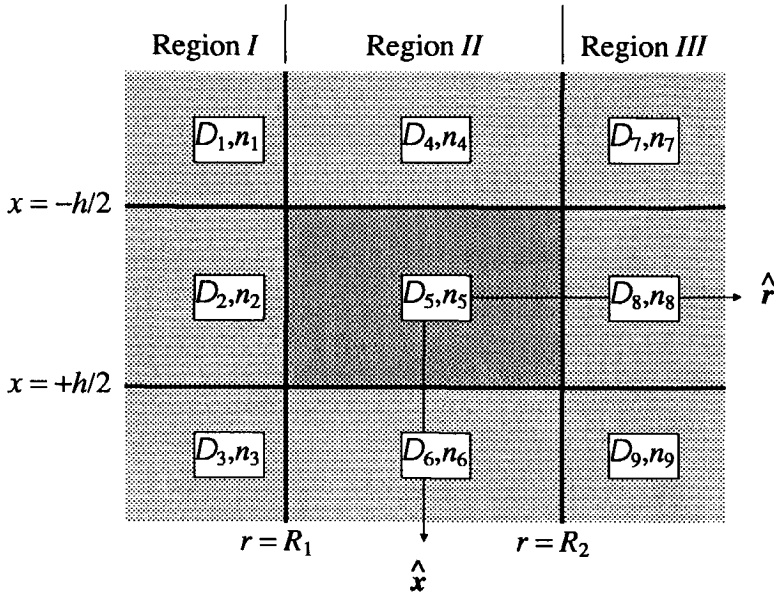
Fig. 3.3 *"Noughts and crosses" cross-section $\varphi = constant$ of the curved waveguide. The central domain has the higher index of refraction and confines the larger part of the power flux. The outer domains are assumed to extend to infinity. The perfectly conducting screen which was introduced in section § 2.2.5 has been left out of the discussion.*

the generalized waveguide cross-section shown in Fig. 3.3. The field component $e_r^\pm$ is written as

$$
e_r^\pm(x,r) = \begin{cases}
\dfrac{C_I e_{rI}(r)}{\cos(\varphi_2)} \begin{cases} \cos(-k_{x2}h/2+\varphi_2)e^{k_{x1}(x+h/2)} & r \in D_1 \\ \cos(k_{x2}x+\varphi_2) & r \in D_2 \\ \cos(k_{x2}h/2+\varphi_2)e^{-k_{x3}(x-h/2)} & r \in D_3 \end{cases} \\[2em]
\dfrac{C_{II} e_{rII}(r)}{\cos(\varphi_5)} \begin{cases} \cos(-k_{x5}h/2+\varphi_5)e^{k_{x4}(x+h/2)} & r \in D_4 \\ \cos(k_{x5}x+\varphi_5) & r \in D_5 \\ \cos(k_{x5}h/2+\varphi_5)e^{-k_{x6}(x-h/2)} & r \in D_6 \end{cases} \quad , \text{ for } r \in D_5, \\[2em]
\dfrac{C_{III} e_{rIII}(r)}{\cos(\varphi_8)} \begin{cases} \cos(-k_{x8}h/2+\varphi_8)e^{k_{x7}(x+h/2)} & r \in D_7 \\ \cos(k_{x8}x+\varphi_8) & r \in D_8 \\ \cos(k_{x8}h/2+\varphi_8)e^{-k_{x9}(x-h/2)} & r \in D_9 \end{cases}
\end{cases}
\tag{3.2.35}
$$

where the components of the wave vector k are defined by

$$\begin{pmatrix} k_{x1} \\ k_{x2} \\ k_{x3} \end{pmatrix} \stackrel{def}{=} k_0 \begin{pmatrix} [N_I^2 - n_1^2]^{1/2} \\ [n_2^2 - N_I^2]^{1/2} \\ [N_I^2 - n_3^2]^{1/2} \end{pmatrix}, \begin{pmatrix} k_{x4} \\ k_{x5} \\ k_{x6} \end{pmatrix} \stackrel{def}{=} k_0 \begin{pmatrix} [N_{II}^2 - n_4^2]^{1/2} \\ [n_5^2 - N_{II}^2]^{1/2} \\ [N_{II}^2 - n_6^2]^{1/2} \end{pmatrix}, \begin{pmatrix} k_{x7} \\ k_{x8} \\ k_{x9} \end{pmatrix} \stackrel{def}{=} k_0 \begin{pmatrix} [N_{III}^2 - n_7^2]^{1/2} \\ [n_8^2 - N_{III}^2]^{1/2} \\ [N_{III}^2 - n_9^2]^{1/2} \end{pmatrix}$$

$$(3.2.36)$$

in each domain D_i. All square roots $\sqrt{k_{xi}^2}$ have been chosen with $\mathrm{Re}(k_{xi}) > 0$ and $i = 1, 2, \ldots, 9$. We define

$$e_x^{\pm} \stackrel{def}{=} 0, \tag{3.2.37}$$

and find from the divergence relation

$$e_\varphi^{\pm} = \frac{\partial_r(r e_r^{\pm})}{\pm j\gamma} = \frac{(r^{-1} + \partial_r) e_r^{\pm}}{\pm j\gamma/r}. \tag{3.2.38}$$

The functions $e_{r,i}(r)$ are then seen to satisfy an uncoupled Helmholtz equation

$$\left(\frac{\partial^2}{\partial r^2} + \frac{3}{r} \frac{\partial}{\partial r} + k_0^2 N_i^2 - \frac{\gamma^2 - 1}{r^2} \right) e_{r,i}^{\pm}(r) = 0, \text{ with } i = I, II, III, \tag{3.2.39}$$

by the substitution of Eq. (3.2.38) into Helmholtz equation Eq. (2.3.22). The magnetic field can be found from Maxwell's equation Eq. (2.3.18)

$$\begin{pmatrix} h_x^{\pm} \\ h_r^{\pm} \\ h_\varphi^{\pm} \end{pmatrix} = \frac{1}{\pm\omega\mu_0\gamma/r} \begin{pmatrix} r^{-2}(\partial_r r)^2 - (\gamma/r)^2 \\ -r^{-1}\partial_x\partial_r r \\ \pm j\gamma r^{-1}\partial_x \end{pmatrix} e_r^{\pm} = \frac{1}{\pm\omega\mu_0\gamma/r} \begin{pmatrix} \partial_r^2 + 3r^{-1}\partial_r + r^{-2} - \gamma^2 r^{-2} \\ -\partial_x(r^{-1} + \partial_r) \\ \pm j\gamma r^{-1}\partial_x \end{pmatrix} e_r^{\pm} =$$

$$= \frac{1}{\pm\omega\mu_0\gamma/r} \begin{pmatrix} -k_0^2 N_i^2 \\ -\partial_x(r^{-1} + \partial_r) \\ \pm j\gamma r^{-1}\partial_x \end{pmatrix} e_r^{\pm}. \tag{3.2.40}$$

The continuity of d_x, e_r, e_φ and h is required at the interfaces $x = \pm h/2$. If e_r and $h_\varphi \propto \partial_x e_r$ are matched, then $\partial_r e_r$ and $\partial_r^2 e_r$ are also continuous and all continuity requirements are seen to have been fulfilled precisely. This leads to three dispersion equations for the $HE_{\mu\nu}$ modes, Eqs. (3.2.8) through (3.2.10), or equivalently

$$D_s(TE, n_1, n_2, n_3, h, \mu, N_I) = 0 , \tag{3.2.19}$$

$$D_s(TE, n_4, n_5, n_6, h, \mu, N_{II}) = 0 , \tag{3.2.20}$$

$$D_s(TE, n_7, n_8, n_9, h, \mu, N_{III}) = 0 . \tag{3.2.21}$$

The transversal boundary conditions, notably the continuity of e_x, d_r, e_φ and h at $r = R_1$ and $r = R_2$, are impossible to fulfill, but this is what the method of effective refractive index is about. The boundary conditions will be matched as far as possible along $x = 0$ as shown in the preceding sections for the straight waveguide. The freedom, obtained from the impossibility of matching all components, can be used to impose the HE boundary conditions for a laterally planar, curved waveguide with refractive indices N_I, N_{II} and N_{III}, bounded by $r = R_1$ and $r = R_2$. In the electromagnetic problem of the planar TM bend, we have $e_x = h_r = h_\varphi = 0$, solve the cylindrical Helmholtz equation for h_x and require the continuity of h_x and $N_i^{-2} \partial_r h_x$. Imposing these boundary conditions on the solution of the method of effective dielectric constant leads to the continuity requirement of $N_i^2 e_r$ and $\partial_r e_r$ and in this way all requirements are fulfilled along $x = 0$ to the second order. This is summarized for the reader's convenience in Table 3.5.

In conclusion it can be said that the HE-boundary conditions of the planar bend fulfill all lateral boundary conditions for $HE_{\mu\nu}$-modes at $x = 0$ to a second-order approximation and that we therefore find

$$D_c(TM, N_I, N_{II}, N_{III}, R_1, R_2, \nu, \gamma_{\mu\nu}) = 0 , \tag{3.2.41}$$

where $D_c(...) = 0$ denotes the dispersion relation for the curved slab waveguide with corresponding parameters. It is stated without much ado that for $EH_{\mu\nu}$ modes Eqs. (3.2.19), (3.2.20), (3.2.21) and (3.2.41) are recovered with TE and TM interchanged.

Note that Eq. (3.2.41) yields a propagation constant $\gamma_{\mu\nu}$ in place of an effective refractive index $N_{\mu\nu}$. Eq. (2.3.26) can be used to calculate an effective index of

refraction, but its value is not unambiguous because it involves division by an arbitrary radius R_t (*See* the discussion on page 64).

Section § 4.1 gives a number of solutions to the problem of the planar curved waveguide.

Table 3.5 *The boundary conditions for the HE-modes in curved waveguides using the EDC method. The table indicates which field components have to be continuous, the degree to which this requirement is fulfilled and how it is accomplished. The deviation Δ is explained in Eq. (3.2.13).*

Transversal conditions at $x = \pm h/2$				Lateral conditions at $r = R_1$ and $r = R_2$		
Field component	Relative magnitude	How continuity has been established	Degree of continuity	Field component	Relative magnitude	Degree of continuity We require continuity of $\Psi_1 = h_x \propto N_i^2 e_r$, and $\Psi_2 = N_i^{-2}\partial_x h_x \propto \partial_r e_r$
d_x		$\stackrel{\text{def}}{=} 0$	Exact	e_x		$\stackrel{\text{def}}{=} 0$
e_r	**	Required	Exact	d_r	**	$\propto \Delta\{(n_i/N_i)^2\Psi_1\}$
e_φ	*	$\Leftarrow e_r$	Exact	e_φ	*	$\propto \Delta(r^{-1}N_i^{-2}\Psi_1+\Psi_2)$
h_x	**	$\Leftarrow e_r$	Exact	h_x	**	$= \Delta\Psi_1$
h_r		$\Leftarrow h_\varphi$	Exact	h_r		$\propto \Delta(r^{-1}N_i^{-2}\partial_x\Psi_1+\partial_x\Psi_2)$
h_φ	*	Required	Exact	h_φ	*	$\propto (N_i^{-2}\partial_x\Psi_1)$

3.2.7 Ridge waveguides and multilayer structures

The derivation of the method of effective dielectric constant has been restricted to the "noughts and crosses" structure of Fig. 3.1, mainly because it simplifies the analysis considerably and because it is a common starting point for other techniques. The method of effective dielectric constant itself is not restricted to that configuration and it is easy to see that the four eigenvalue equations Eqs. (3.2.19) through (3.2.22) can also be applied to the ridge waveguide of Fig. 3.4 as follows

$$D_s(\text{TE},n_1,n_2,n_3,h_I,\mu,N_I) = 0 , \tag{3.2.42}$$

$$D_s(\text{TE},n_1,n_2,n_3,h_{II},\mu,N_{II}) = 0 , \tag{3.2.43}$$

$$D_s(\text{TE},n_1,n_2,n_3,h_{III},\mu,N_{III}) = 0 , \tag{3.2.44}$$

$$D_s(\text{TM},N_I,N_{II},N_{III},w,v,N_{\mu v}) = 0 . \tag{3.2.45}$$
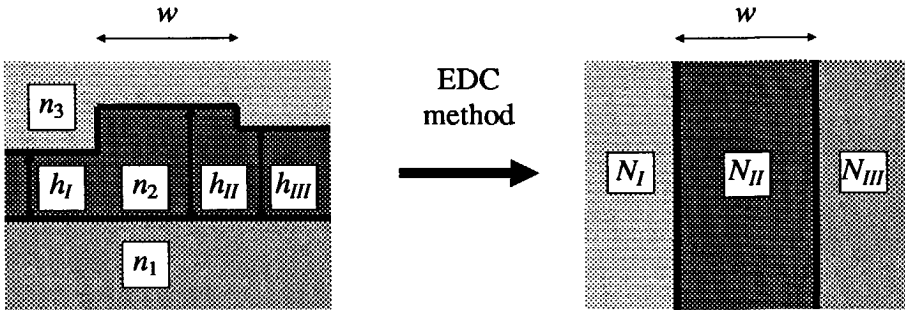
Fig. 3.4 *The method of effective dielectric constant for ridge waveguides. The ridge waveguide on the left is transformed into an effective slab waveguide with effective refractive indices on the right-hand side.*

Further, the applicability of the method of effective dielectric constant can be extended to include multilayer waveguides. Any region $y_i \leq y \leq y_{i+1}$ can consist of an arbitrary number of domains D_i, which leads us to a dispersion relation for the corresponding planar multilayer structure and results in an effective index of refraction. All effective refractive indices found in this way are used in an effective lateral planar multilayer waveguide.

We assume that the above generalization can be made for the curved waveguide as well.

3.2.8 Ambiguity, accuracy and trouble-shooting

The quantity $\Delta\Psi$, Eq. (3.2.13), has been introduced to describe the change of a field component on both sides of an interface, across which it should be continuous. If the three regions *I*, *II* and *III* are identical, the general noughts and crosses structure reduces to the cross-section of a transversally planar waveguide. The field solutions are equal in all three regions *I*, *II* and *III*, all deviations $\Delta\Psi$ become zero and the solution of the method of effective dielectric constant reduces to the exact solution of the transversally planar waveguide. We might, therefore, expect that the method of effective dielectric constant is good when the transversal refractive-index profiles in the regions *I*, *II* and *III* *resemble* each other very much as in the case of a ridge waveguide with a low ridge.

If, on the other hand, all outer regions are equal, i.e. we have a rectangular cross-section D_5 with refractive index n_5 in a homogeneous background, none of the quantities $\Delta\Psi$ become zero, because no solutions are found in regions *I* and

III. This configuration is, in practice, dealt with by taking N_I and N_{III} equal to the refractive index of the background. It would seem that the method of the effective dielectric constant is a poor approximation for such a geometry, but it was, in fact, this geometry that was discussed in the paper by Knox and Toulios [57] and for which they found the method of effective dielectric constant to be a good approximation.

The conclusion may, therefore, be drawn that the method of effective dielectric is exact for the transversally planar slab, that it is a good approximation to the solution for a rectangular waveguide cross-section in a homogeneous surrounding and that the approximation becomes poorer for geometries that do not resemble these two limiting cases.

There is some arbitrariness in the method of effective dielectric concerning the lateral boundary conditions. All transversal boundary conditions have been satisfied exactly as summarized in Table 3.3 and Table 3.4, but the lateral boundary conditions cannot be fulfilled exactly. In section § 3.2.3 we had to match e_x, d_y, e_z and h. We chose to match exactly $h_x \propto N_i^2 e_y$ and $e_z \propto \partial_y e_y$ at $y = \pm w/2$ and at $x = 0$, because this gave us the advantage of retaining the lateral eigenvalue equation

$$\tan(k_{yII}w) = \frac{\dfrac{k_{yII}}{N_{II}^2}\left(\dfrac{k_{yI}}{N_I^2} + \dfrac{k_{yIII}}{N_{III}^2}\right)}{\left(\dfrac{k_{yII}}{N_{II}^2}\right)^2 - \dfrac{k_{yI}}{N_I^2}\dfrac{k_{yIII}}{N_{III}^2}}, \tag{3.2.18}$$

which is equivalent to that of the planar waveguide with effective refractive indices N_I, N_{II} and N_{III} for the case of TM-polarization. But alternatively, requiring the continuity of the equally important $d_y = n_i^2 e_y$ component and $e_z \propto \partial_y e_y$ leads us to

$$\tan(k_{yII}w) = \frac{\dfrac{k_{yII}}{n_5^2}\left(\dfrac{k_{yI}}{n_2^2} + \dfrac{k_{yIII}}{n_8^2}\right)}{\left(\dfrac{k_{yII}}{n_5^2}\right)^2 - \dfrac{k_{yI}}{n_2^2}\dfrac{k_{yIII}}{n_8^2}}. \tag{3.2.46}$$

Within the second-order approximation, we have the proportionality $h_x \propto e_y$. The continuity of e_y and $e_z \propto \partial_y e_y$ might, therefore, just as well have been demanded, leading in turn to the TE-eigenvalue equation

$$\tan(k_{yII} w) = \frac{k_{yII} (k_{yI} + k_{yIII})}{k_{yII}^2 - k_{yI} k_{yIII}} . \tag{3.2.47}$$

Three dispersion relations are found instead of one and within a second-order approximation they are all equivalent. We adhere, however, to the original choice Eq. (3.2.18) for the straight waveguide and $HE_{\mu\nu}$ modes, but the other two equations may be taken as an estimate of the accuracy of the method of the effective dielectric constant. Briefly, the lateral boundary conditions cannot be fulfilled completely and within the order of the approximation used we can apply a laterally planar-waveguide dispersion relation with either TE conditions, Eq. (3.2.47), TM conditions with N_i^2, Eq. (3.2.18), or TM conditions with n_i^2, Eq. (3.2.46). (A numerical example is provided in Table 6.1 on page 159)

Chapter 4

Two-dimensional solutions

The previous chapter showed how the method of the effective dielectric constant can be used to eliminate the transversal coordinate. The result is a two-dimensional problem that depends on the lateral coordinate and the coordinate along which propagation takes place. This chapter is devoted to solving the curved open-waveguide problem and the corresponding junction problem for waveguides with a lateral dependence only. Section § 4.3 discusses how to deal with multimode waveguide tracks. Section § 4.4 introduces a conformal transformation to solve the two-dimensional problem of two coupled diverging bends with identical radii of curvature.

4.1 Curved waveguides

4.1.1 Introduction

Before giving solutions, we will briefly summarize the relevant configuration and equations for the reader's convenience. The three-dimensional bend described in section § 2.2.3 is transformed into the two-dimensional structure shown in Fig. 4.1. The perfectly conducting screen introduced in section § 2.2.5 is also indicated in this figure. The refractive indices indicated are the effective refractive indices that are found by solving the transversal problem first, as described in the previous
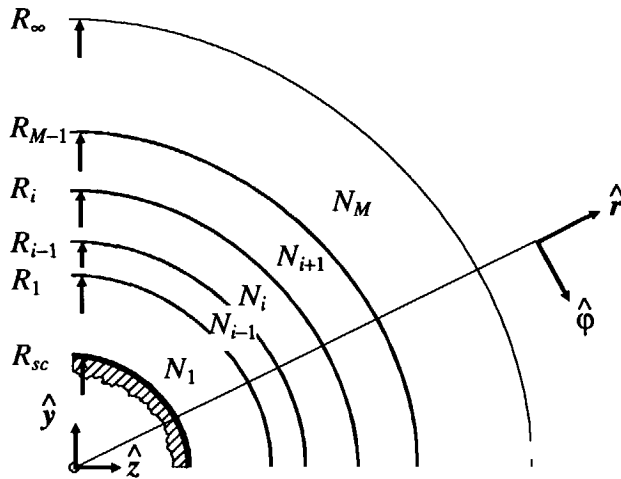
Fig. 4.1 *Two-dimensional curved waveguide structure. Multiple interfaces R_i are allowed to exist, either forming part of one complex waveguide or representing multiple coupled bends. The N_i are the effective refractive indices. A perfect conductor at $r = R_{sc}$ screens the origin.*

chapter. The subsequent lateral problem for $HE_{\mu\nu}$-modes consists of solving the equation

$$\left(\frac{\partial^2}{\partial r^2} + \frac{1}{r}\frac{\partial}{\partial r} + k_0{}^2 N_i{}^2 - \frac{\gamma^2}{r^2}\right) h_{x,i}(r) = 0 \ , \ i = 1, 2, \ldots, M \ , \tag{4.1.1}$$

plus the continuity of

$$h_x(R_i) \quad \text{and} \quad \frac{1}{N_i^2}\partial_r h_x\bigg|_{R_i} \ , \ i = 1, 2, \ldots, M{-}1 \ , \tag{4.1.2}$$

while at the screen we have

$$\partial_r h_x\bigg|_{R_{sc}} \propto N_i^2 \partial_r(r e_r)\bigg|_{R_{sc}} \propto e_\varphi\bigg|_{R_{sc}} \stackrel{\text{def}}{=} 0 \ . \tag{4.1.3}$$

The Helmholtz equation Eq. (4.1.1) does not seem to comply with Eq. (3.2.39) that was derived by means of the method of effective dielectric constant in the previous chapter. Equation (4.1.1) is found by substituting the proportionality $e_r^{\pm} \propto h_x^{\pm}/r$, obtained from Eq. (3.2.40), into Eq. (3.2.39).

In a similar way, the problem for $EH_{\mu\nu}$-modes consists of solving

$$\left(\frac{\partial^2}{\partial r^2} + \frac{1}{r} \frac{\partial}{\partial r} + k_0^2 N_i^2 - \frac{\gamma^2}{r^2} \right) e_{x,i}(r) = 0 \ , \ i = 1, 2, ..., M \ , \tag{4.1.4}$$

plus the continuity of

$$e_x(R_i) \text{ and } \partial_r e_x \Big|_{R_i} , \ i = 1, 2, ..., M-1 \ , \tag{4.1.5}$$

and the requirement at the screen

$$e_x \Big|_{R_{sc}} \stackrel{\text{def}}{=} 0 \ . \tag{4.1.6}$$

4.1.2 The Bessel-function approach

Equations (4.1.1) and (4.1.4) are differential equations of the Bessel type and their solutions are well known. Bearing in mind that γ is a complex quantity, the independent solutions are $J_\gamma(k_0 N_i r)$, the Bessel function of the first kind, and $Y_\gamma(k_0 N_i r)$, the Neumann function or Bessel function of the second kind, in which the complex order is understood to be $\gamma = \sqrt{\gamma^2}$ with $\text{Re}(\gamma) > 0$. The Bessel functions of the third kind, the Hankel functions, are defined as linear combinations of the first two, i.e. $H_\gamma^{(1)}(k_0 N_i r) = J_\gamma(k_0 N_i r) + jY_\gamma(k_0 N_i r)$ and $H_\gamma^{(2)}(k_0 N_i r) = J_\gamma(k_0 N_i r) - jY_\gamma(k_0 N_i r)$. These two Hankel functions form an independent set of solutions to the Bessel equation on their own. If the Bessel function of the first and second kinds are chosen as the independent set of solutions, then the field in every section can be expressed as

$$\begin{pmatrix} e_{x,i}^{\pm} \\ h_{x,i}^{\pm} \end{pmatrix} = A_i J_\gamma(k_0 N_i r) + B_i Y_\gamma(k_0 N_i r) \text{ , when } R_{i-1} < r < R_i \qquad (4.1.7)$$

for EH- and HE-modes respectively—except for the fact that the effective refractive indices are different—. The EH- and HE-modes behave quite similarly and it has proved to be worthwhile to introduce a special symbol $\aleph_i$ in order to deal with both polarizations simultaneously

$$\aleph_i \overset{\text{def}}{=} \begin{cases} 1 & \text{for EH modes ,} \\ \dfrac{N_{i+1}^2}{N_i^2} & \text{for HE modes .} \end{cases} \qquad (4.1.8)$$

If boundary conditions are matched at $r = R_i$ two equations are found that relate the coefficients $\{A_{i+1}, B_{i+1}\}$ and $\{A_i, B_i\}$ to each other in matrix notation

$$\begin{pmatrix} J_\gamma & Y_\gamma \\ N_{i+1}J_\gamma' & N_{i+1}Y_\gamma' \end{pmatrix}_{k_0 N_{i+1} R_i} \begin{pmatrix} A_{i+1} \\ B_{i+1} \end{pmatrix} = \begin{pmatrix} J_\gamma & Y_\gamma \\ N_i \aleph_i J_\gamma' & N_i \aleph_i Y_\gamma' \end{pmatrix}_{k_0 N_i R_i} \begin{pmatrix} A_i \\ B_i \end{pmatrix}, \qquad (4.1.9)$$

where the prime denotes differentiation of the Bessel function with respect to its argument $k_0 N_i r$. The determinant of the left-hand matrix is seen to be N_{i+1} times the Wronskian $W(J_\gamma, Y_\gamma)$ and is thus equal to $2/(\pi k_0 R_i)$. Since this Wronskian never vanishes, equation (4.1.9) can always be inverted to yield

$$\begin{pmatrix} A_{i+1} \\ B_{i+1} \end{pmatrix} = \frac{\pi k_0 R_i}{2} \begin{pmatrix} N_{i+1}Y_\gamma' & -Y_\gamma \\ -N_{i+1}J_\gamma' & J_\gamma \end{pmatrix}_{k_0 N_{i+1} R_i} \begin{pmatrix} J_\gamma & Y_\gamma \\ N_i \aleph_i J_\gamma' & N_i \aleph_i Y_\gamma' \end{pmatrix}_{k_0 N_i R_i} \begin{pmatrix} A_i \\ B_i \end{pmatrix}. \qquad (4.1.10)$$

Boundary conditions have to be imposed in the inner- and outermost region. The innermost is bounded by the screen and we impose condition Eq. (4.1.3) for the HE-modes

$$B_1 = -A_1 \left. \frac{J_\gamma'}{Y_\gamma'} \right|_{k_0 N_1 R_{sc}} , \tag{4.1.11}$$

and condition Eq. (4.1.6) for EH modes

$$B_1 = -A_1 \left. \frac{J_\gamma}{Y_\gamma} \right|_{k_0 N_1 R_{sc}} , \tag{4.1.12}$$

Note that both conditions can be approximated by $B_1 \approx 0$, i.e. the boundary condition without the screen, if $J_\gamma(k_0 N_1 r)$ and $Y_\gamma(k_0 N_1 r)$ have an exponentially decreasing and increasing character respectively when r decreases. The radiation condition must be imposed when $r \to \infty$, which means that, far enough from the origin, all solutions must exhibit the asymptotic behavior of an outgoing wave. The asymptotic form of the Hankel function of the second kind describes such an outgoing wave in combination with time dependence Eq. (2.1.1). When expressing solution Eq. (4.1.7) in terms of Hankel functions

$$\begin{pmatrix} e_{x,i}^\pm \\ h_{x,i}^\pm \end{pmatrix} = \frac{1}{2}(A_i - jB_i)H_\gamma^{(1)}(k_0 N_i r) + \frac{1}{2}(A_i + jB_i)H_\gamma^{(2)}(k_0 N_i r) , \tag{4.1.13}$$

the condition for the outermost region is found to be

$$A_M - jB_M = 0 . \tag{4.1.14}$$

Starting at the boundary conditions Eqs. (4.1.11) and (4.1.12) for HE and EH modes respectively, repeated application of transfer matrix Eq. (4.1.10) and imposing requirement Eq. (4.1.14), a lateral dispersion equation is found which leads to a finite set of discrete, complex values of the azimuthal propagation constant $\gamma_{\mu\nu}$ which is characterized by a transversal mode number $\mu = 0, 1, \ldots, M_\mu - 1$ and the lateral mode number $\nu = 0, 1, \ldots, M_\nu - 1$. To each $\gamma_{\mu\nu}$ corresponds a lateral modal distribution $h_{x;\mu\nu}(r)$ for HE$_{\mu\nu}$-modes or $e_{x;\mu\nu}(r)$ for EH$_{\mu\nu}$-modes.

The simplest curved waveguiding structure consists of a single boundary $r = R_1$ that separates a region with an effective refractive index N_1 from a region with N_2 and $N_1 > N_2$. Not only does such a curved interface constitute a waveguide

[95][102], its radiation losses are also either lower than or equal to that of a double-interface bend which makes it of practical importance. The dispersion relation of the single-boundary bend is $A_2/B_2 = j$ or

$$\frac{N_2 Y_\gamma'(k_0 N_2 R_1) J_\gamma(k_0 N_1 R_1) - N_1 \aleph_1 Y_\gamma(k_0 N_2 R_1) J_\gamma'(k_0 N_1 R_1)}{-N_2 J_\gamma'(k_0 N_2 R_1) J_\gamma(k_0 N_1 R_1) + N_1 \aleph_1 J_\gamma(k_0 N_2 R_1) J_\gamma'(k_0 N_1 R_1)} = j \,, \qquad (4.1.15)$$

where we have taken $B_1 = 0$, i.e. the boundary condition without the presence of the screen, which leads to a simplified equation that is a good approximation to the equation for the configuration with the screen. This is justified, if J_γ and Y_γ have an exponential character in the neighborhood of the screen, or, equivalently, by verifying that the solution found by solving Eq. (4.1.15) has a modal distribution with a negligible magnitude near the screen.

Although the Bessel function approach is straightforward, its numerical implementation is not. Lewin *et al.* [65] hint at the difficulties encountered in the calculation of these Bessel functions:

- The Bessel functions have to be evaluated in a region where they change in character from increasing exponentially to oscillating. In this *transition* region, the magnitude of the argument and the order are roughly equal. There are few accurate expressions for the Bessel functions in this region, the only useful ones are given by Olver [85][86].
- Both the magnitude of the argument and the order are large. Practical bends have a radii of curvature that range from $50\lambda_0$ to $50000\lambda_0$. Argument and order are thus at least of the order of 10^3 to 10^6.
- The order γ is complex and possibly the argument as well.
- High accuracy—at least six significant digits—is required. An attenuation of $\alpha = 0.01$ dB/90° corresponds to an imaginary part $\text{Im}(\gamma) \approx 10^{-3}$ by means of Eq. (2.3.27). This leads in combination with the above to $\text{Re}(\gamma)/\text{Im}(\gamma) > 10^6$.

We have implemented the Bessel functions with an accuracy of at least twelve digits in the range of arguments and orders as described above. The implementation has been based upon an article by Neumann and Richter [81]. Adjustments have been made to improve the accuracy and these are documented in Appendix A. Chapter 5 gives the numerical results of the calculations that have been done by using the Bessel-function approach.

4.1.3 The transformation to an equivalent straight waveguide

Although the Bessel function technique is the most direct approach, it has some disadvantages. It provides little insight into the mechanism of the radiation loss and its numerical evaluation is very time consuming on a computer, which is not convenient for modeling purposes. The transformation that will be discussed in this section gives more insight and lends itself to a variety of numerical implementations. The first reference to this transformation is in a report by Chang and Barnes [16], who used the Wentzel-Kramers-Brillouin approximation to find the solutions of the transformed curved waveguide problem, and later in Lewin, Chang and Kuester [65], § 7.7. But it is especially the paper by Heiblum and Harris [40] on this technique that received much attention. Heiblum and Harris showed that the transformation belongs to the class of conformal transformations. Conformal transformations are known to be applicable to the two-dimensional Helmholtz equation.

In cylindrical coordinates the conformal transformation of the Helmholtz equation is restricted to a transformation with respect to r

$$\begin{cases} r = R_t\, e^{u/R_t} \\ \\ \partial_r = e^{u/R_t}\, \partial_u \end{cases} \quad \Leftrightarrow \quad \begin{cases} u = R_t \ln(r/R_t) \\ \\ \partial_u = (R_t/r)\, \partial_r \end{cases} , \qquad (4.1.16)$$

that transforms

$$0 < R_{sc} < r < \infty , \qquad (4.1.17)$$

into

$$-\infty < U_{sc} < u < \infty . \qquad (4.1.18)$$

Application of this transformation to the Helmholtz equations (4.1.1) and (4.1.4) yields

$$\left(\frac{\partial^2}{\partial u^2} + k_0^2 N_i^2 e^{2u/R_t} - \frac{\gamma^2}{R_t^2} \right) \begin{pmatrix} e^{\pm}_{x,i}(u) \\ h^{\pm}_{x,i}(u) \end{pmatrix} = 0 \, , i = 1, 2, \dots, M \, , \qquad (4.1.19)$$

plus the continuity requirements of

$$\left\{ \begin{array}{ll} h_x(u) \ , \ N_i^{-2}\partial_u h_x(u) & \text{for HE modes} \\ e_x(u) \ , \ \ \ \partial_u e_x(u) & \text{for EH modes} \end{array} \right\} , \text{ at } u = u_i = u(r=R_i) , \qquad (4.1.20)$$

and the requirement at the screen

$$\left\{ \begin{array}{ll} \partial_u h_x(u) = 0 & \text{for HE modes} \\ \ \ e_x(u) = 0 & \text{for EH modes} \end{array} \right\} , \text{ at } u = U_{sc} = u(r=R_{sc}) . \qquad (4.1.21)$$

Inspection of the transformed Helmholtz equation Eq. (4.1.19) shows that it is equivalent to the Helmholtz equation for a straight waveguide in u-space with a transformed index of refraction $N_i e^{u/R_t}$ in place of N_i. Such a transformed index of refraction is shown in Fig. 4.2. The transformed index of refraction makes clear why curved waveguides radiate light. The transformed index of refraction is unbounded for large u and will, therefore, lead to an oscillating field at the outer side of the curved waveguide. The transformed problem of the curved waveguide is not completely identical to the problem of a straight waveguide in u-space, because of two reasons:

- the transformed index of refraction $N_i e^{u/R_t}$ ranges from the unphysical values zero to infinity, if $u \in [-\infty,\infty]$ and
- the refractive index that occurs in the boundary conditions for HE-modes in Eq. (4.1.20) is not the transformed index of refraction.

Discussion

It is very tempting to use the transformation in conjunction with a 3-D technique such as the finite element method (FEM) or the finite difference method (FDM). When using Eq. (4.1.16) to transform the Maxwell equations for a three-dimensional waveguiding structure, it is easily verified that no simple decoupled scalar Helmholtz equation results. It may, of course, be possible to find approximations that justify the direct application of the transformation to a three-dimensional geometry, but I have not investigated this.

I want to stress here that the parameter R_t is a parameter of the transformation and as such is not a *physical quantity*. It may, in principle, be chosen arbitrarily and should not influence the final result of the calculation. After calculation of the fields and propagation constants of the transformed bend in u-space, the results

have to be transformed back to r-space. There are good reasons, however, to choose the parameter R_t somehow proportional to the radius of curvature, but care has to be taken. If R_t is taken equal to the radius of curvature of the middle of a conventional two-boundary bend for example, the counter-intuitive result is obtained of an increasing effective refractive index $\text{Re}(\gamma)/(k_0 R_t)$ for smaller R_t. This problem can be avoided by letting R_t equal the radius curvature of the outer boundary R_2. The effective refractive index $\text{Re}(\gamma)/(k_0 R_t)$ is then bounded by the refractive indices of the film and the cladding (*See also* Eqs. (2.3.26) and (4.1.34)).

We have $r = R_t e^{u/R_t} \approx R_t + u$, when $u/R_t \ll 1$. The transformation of the field is then a translation and an appropriate choice of R_t makes the value $u = 0$ coincide with the value $y = 0$ for the straight waveguide at the junction. This plays a role when the problem of the curved waveguide is solved by means of the transformation in conjunction with the two-dimensional beam-propagating method (2-D BPM) [7][111]. The 2-D BPM is usually applied to a geometry of the transformed curved waveguide that is expressed in the y-coordinate of the straight waveguide plus the transformed index of refraction which is then written as $N_i e^{u/R_t} \approx N_i(1+u/R_t) = N_i(1+y/R_t)$.

4.1.4 WKB solution to the single-boundary bend

Heiblum and Harris [40][41] introduced the conformal transformation and solved it with the Wentzel-Kramers-Brillouin approximation. There would be no need to give a derivation here were it not for the fact that discrepancies are found between values based on their equations and those found with the transfer-matrix method, which is discussed in the following section. Table 5.1 gives numerical values that support this statement.

The WKB method is applied to the simplest of all curved waveguiding structures, i.e. the single-boundary bend. The single-boundary bend is of considerable interest because its radiation loss is either lower than or equal to that of the double-boundary bend, as will be discussed in section § 5.2.3. Secondly, the derivation of a dispersion relation by means of the WKB approximation becomes complicated when the number of interfaces grows beyond one or two. The transfer-matrix method or the Bessel function approach are better suited to curved structures with many interfaces.

The Wentzel-Kramers-Brillouin approximation is discussed in most textbooks on quantum mechanics and a summary of the solutions and the connection formulae is given in Appendix B for convenience. Two complications arise when

using the WKB approximation to solve the problem of the transformed curved waveguide. No information can be found on the application of the WKB approximation to a complex differential equation. The classical turning points, for example, have no meaning, because the function $f(u) = N_i^2 e^{2u/R_i} - \gamma^2/(k_0^2 R_i^2)$ in Eq. (4.1.19) has no zeros if γ is a complex quantity and if γ is the only complex quantity. *We will apply the WKB approximation to the Helmholtz equation as if it were a real equation and then use the analytic continuation of the solution into the complex γ-plane.* Secondly, the function $f(u)$ is not bounded. We will verify explicitly in Eq. (4.1.35), that the solution which is found by means of the WKB approximation shows the correct asymptotic behavior for $u \rightarrow \infty$.

The original and the transformed index of refraction are shown in Fig. 4.2. The value $u = u_{II}$ is the transformed radius of curvature $r = R_1$ and the values $u = u_I$ and $u = u_{III}$ are the turning points, where $N_i e^{u/R_i} = \mathrm{Re}(\gamma)/(k_0 R_i)$. Note that there are no actual turning points, because the function $f(u) = N_i^2 e^{2u/R_i} - \gamma^2/(k_0^2 R_i^2)$ has no zeroes. The values $u = u_I$ and $u = u_{III}$ do, however, mark the transition from a region where the solution has an oscillating character to a region where the solution has an exponential character. The WKB solutions given in Appendix B are directly applied to the transformed structure depicted in Fig. 4.2.
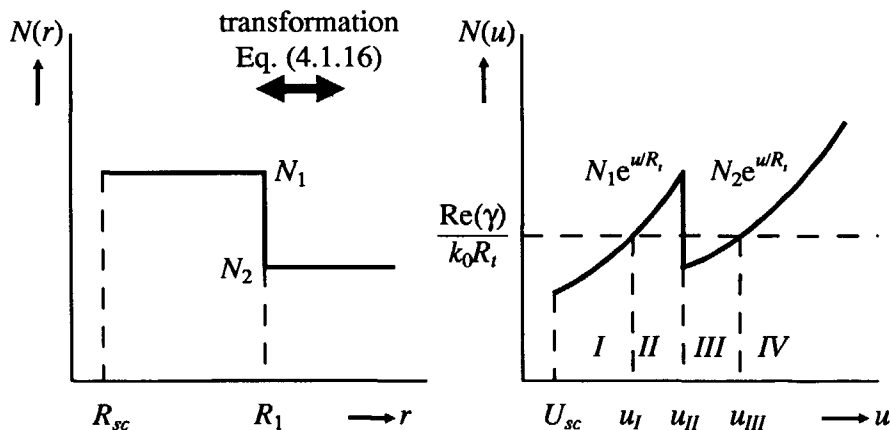

Fig. 4.2 *The original and the transformed index of refraction profile for the single-boundary bend that consists of two domains with refractive indices N_1 and N_2, separated by $r = R_1$. Four regions can be discerned according to whether the transformed index of refraction is larger or smaller than the effective index of refraction. The regions II and IV have oscillatory solutions.*

$$\begin{pmatrix} e_{x,i}^{\pm}(u) \\ h_{x,i}^{\pm}(u) \end{pmatrix} = \frac{A}{\sqrt{\kappa_I}} \exp\left(-\int_u^{u_I} \kappa_I(u')du' \right), \quad -\infty < U_{sc} < u \ll u_I \tag{4.1.22}$$

$$\begin{pmatrix} e_{x,i}^{\pm}(u) \\ h_{x,i}^{\pm}(u) \end{pmatrix} = \frac{2A}{\sqrt{k_{II}}} \cos\left(\int_{u_I}^{u} k_{II}(u')du' - \frac{\pi}{4} \right), \quad u_I \ll u \le u_{II} \tag{4.1.23}$$

$$\begin{pmatrix} e_{x,i}^{\pm}(u) \\ h_{x,i}^{\pm}(u) \end{pmatrix} = \frac{\frac{1}{2}B}{\sqrt{\kappa_{III}}} \exp\left(-\int_u^{u_{III}} \kappa_{III}(u')du' \right) + \frac{jB}{\sqrt{\kappa_{III}}} \exp\left(+\int_u^{u_{III}} \kappa_{III}(u')du' \right),$$

$$u_{II} \le u \ll u_{III} \tag{4.1.24}$$

$$\begin{pmatrix} e_{x,i}^{\pm}(u) \\ h_{x,i}^{\pm}(u) \end{pmatrix} = \frac{B}{\sqrt{k_{IV}}} \exp\left(-j\left\{ \int_{u_{III}}^{u} k_{IV}(u')du' - \frac{\pi}{4} \right\} \right), \quad u_{III} \ll u < \infty \tag{4.1.25}$$

with

$$u_I = R_t \ln\left\{ \frac{\operatorname{Re}(\gamma)}{N_1 k_0 R_t} \right\}, \tag{4.1.26}$$

$$u_{II} = R_t \ln\left\{ \frac{R_1}{R_t} \right\}, \tag{4.1.27}$$

$$u_{III} = R_t \ln\left\{ \frac{\operatorname{Re}(\gamma)}{N_2 k_0 R_t} \right\}, \tag{4.1.28}$$

and

$$\kappa_I \overset{\text{def}}{=} \sqrt{\frac{\gamma^2}{R_t^2} - k_0^2 N_1^2 e^{2u/R_t}}, \quad \operatorname{Re}(\kappa_I) > 0, \tag{4.1.29}$$

$$k_{II} \overset{\text{def}}{=} \sqrt{k_0^2 N_1^2 e^{2u/R_t} - \frac{\gamma^2}{R_t^2}}, \quad \operatorname{Re}(k_{II}) > 0, \tag{4.1.30}$$

$$\kappa_{III} \overset{\text{def}}{=} \sqrt{\frac{\gamma^2}{R_t^2} - k_0^2 N_2^2 e^{2u/R_t}}, \quad \operatorname{Re}(\kappa_{III}) > 0, \tag{4.1.31}$$

$$k_{IV} \stackrel{\text{def}}{=} \sqrt{k_0^2 N_2^2 e^{2u/R_t} - \frac{\gamma^2}{R_t^2}} , \quad \text{Re}(k_{IV}) > 0 .$$ (4.1.32)

The form in which the above equations have been written reflects the fact that we are looking for a solution in the form of a "guided" wave with oscillatory behavior in region II and an exponential character in region III. This requires that $\text{Re}(k_{II}^2) > 0$ for at least one value $u < u_{II}$ and that $\text{Re}(\kappa_{III}^2) > 0$ for at least one value $u > u_{II}$, or

$$\text{Re}\{N_2^2 e^{2u_{II}/R_t}\} < \text{Re}\left\{\frac{\gamma^2}{k_0^2 R_t^2}\right\} < \text{Re}\{N_1^2 e^{2u_{II}/R_t}\} .$$ (4.1.33)

Equation (4.1.33) can be simplified to

$$N_2 < \frac{\text{Re}(\gamma)}{k_0 R_1} = N_{eff} < N_1 ,$$ (4.1.34)

where γ has been replaced by $\text{Re}(\gamma)$ which is justified since $\text{Im}(\gamma) \ll \text{Re}(\gamma)$ as discussed on page 62. The above consideration shows that a useful effective refractive index is obtained from Eq. (2.3.26) by taking $R_t = R_1$ for the single-boundary bend and, at the same time, that the effective index of refraction is an ambiguous parameter for curved waveguides.

   The form of the solution in region I reflects the boundary conditions which is imposed by the screen Eq. (4.1.21). The WKB solution Eq. (4.1.22) decays exponentially and this means that both the field and its derivative are zero if the field decays fast enough and / or the screen is far enough away. The solution in region IV Eq. (4.1.25) reflects the outward radiation condition and is equal to $H_\gamma^{(2)}(k_0 N_2 r)$ for large values of the argument, which can verified by using the result Eq. (C.4) of Appendix C, by subsequently taking the limit when $u \to \infty$ and by transforming back to r

$$\lim_{u \to \infty} \begin{pmatrix} e_{x,i}^{\pm}(u) \\ h_{x,i}^{\pm}(u) \end{pmatrix} = B \sqrt{\frac{R_t}{k_0 N_2 r}} \exp\left\{-j\left(k_0 N_2 r - \gamma\frac{\pi}{2} - \frac{\pi}{4}\right)\right\} .$$ (4.1.35)

This limit Eq. (4.1.35) is indeed proportional to the asymptotic form of the Hankel function of the second kind $H_\gamma^{(2)}(k_0 N_2 r)$ (Eq. (9.2.4) in [1]).

The solutions in regions I and II on both sides of the turning point u_I have already been matched to each other by means of connection formula (B.11) and the fields in regions III and IV on both sides of the turning point u_{III} have already been matched through connection formulae Eqs. (B.11) and (B.12). The only solutions that have not yet been related to each other are the solutions in regions II and III. The connection between these two solutions is established by means of the boundary conditions Eqs. (4.1.2) and (4.1.5). Imposing these boundary conditions and some manipulation lead to the dispersion equation

$$
\sin\left\{\int_{u_I}^{u_{II}} k_{II}(u')du' - \frac{\pi}{4} - \tan^{-1}\left(\frac{\kappa_{III}(u_{II})}{\aleph_1 k_{II}(u_{II})}\right)\right\}
$$
$$
-\frac{j}{2}\sin\left\{\int_{u_I}^{u_{II}} k_{II}(u')du' - \frac{\pi}{4} + \tan^{-1}\left(\frac{\kappa_{III}(u_{II})}{\aleph_1 k_{II}(u_{II})}\right)\right\}\exp\left\{-2\int_{u_{II}}^{u_{III}} \kappa_{III}(u')du'\right\} = 0,
$$

$$(4.1.36)$$

in which

$$
\frac{\kappa_{III}(u_{II})}{k_{II}(u_{II})} = \frac{\gamma^2 - k_0^2 N_2^2 R_1^2}{k_0^2 N_1^2 R_1^2 - \gamma^2},
$$

$$(4.1.37)$$

and

$$
\int_{u_I}^{u_{II}} k_{II}(u')du' = \gamma\left[\sqrt{\frac{k_0^2 N_1^2 R_1^2}{\gamma^2} - 1} - \tan^{-1}\sqrt{\frac{k_0^2 N_1^2 R_1^2}{\gamma^2} - 1}\right],
$$

$$(4.1.38)$$

$$
\int_{u_{II}}^{u_{III}} \kappa_{III}(u')du' = \gamma\left[\frac{1}{2}\ln\left(\frac{1+\sqrt{1 - k_0^2 N_2^2 R_1^2/\gamma^2}}{1-\sqrt{1 - k_0^2 N_2^2 R_1^2/\gamma^2}}\right) - \sqrt{1 - \frac{k_0^2 N_2^2 R_1^2}{\gamma^2}}\right].
$$

$$(4.1.39)$$

The contributions to the above integrals from the points $u = u_I$ and $u = u_{III}$ are not exactly zero, but have been neglected with respect to the contribution from the

point $u = u_{II}$. The evaluation of integrals Eqs. (4.1.38) and (4.1.39) is discussed in Appendix C. The expressions in series, Eqs. (C.4) and (C.8), are to be preferred to the expressions in closed form whenever the dispersion equation (4.1.36) is solved numerically.

The lateral dispersion equation Eq. (4.1.36) can be compared to Eq. (4.1.15) and leads to a finite set of discrete, complex values of the azimuthal propagation constant $\gamma_{\mu\nu}$ with a transversal mode number $\mu = 0, 1, ..., M_\mu-1$ and a lateral mode number $\nu = 0, 1, ,..., M_\nu-1$. The corresponding modal field distributions are given by Eqs. (4.1.22) through (4.1.25).

Inspection of dispersion equation Eq. (4.1.36) shows that it is identical to the dispersion relation for the single-boundary bend Eq. (16) in Heiblum [41], except for a factor ½ that is missing in front of the second term in Heiblum's equation. This missing factor explains the discrepancies found between the values calculated by means of Eq. (16) in [41] or Eq. (20) in [40] and the values that have been calculated by means of the techniques that are discussed in the thesis. Numerical values are given in Table 5.1 and they show discrepancies of approximately a factor ½ for the radiation losses. It is unlikely that the missing factor ½ is caused by an editorial error since the factor is missing in both [41] and [40] and the equations are consistent with each other throughout both papers. Moreover it seems that a similar factor ½ is missing in the papers by Harris [38] and [39] (compare for example Eqs. (10) through (14) in [38], Eqs. (13) and (14) in [39], and Eq. (14) in [41]). It is my conviction that all the attenuation coefficients calculated by Heiblum and Harris in the above-mentioned papers are too large by a factor two.

A perturbation solution of Eq. (4.1.36) will be pursued, because the dispersion equation gives a number of solutions without advance knowledge as to which mode numbers they correspond. The perturbed solution, on the other hand, depends explicitly on the mode number. We then know with certainty which propagation constant corresponds to which mode number. The perturbation solution is also more accurate when the radiation losses are small and it leads to two convenient analytic expressions for the minimum width and the lateral offset, Eqs. (4.1.47) and (4.1.49).

To this end we write the original dispersion relation Eq. (4.1.36) as $D_{WKB}(\gamma) = 0$. The exponential term vanishes when there is no attenuation and the dispersion relation retains its first sine term

$$D_{WKB}^0(\gamma^0) = \sin\left\{\int_{u_I}^{u_{II}} k_{II}(u')du' - \frac{\pi}{4} - \tan^{-1}\left(\frac{\kappa_{III}(u_{II})}{\aleph_1 k_{II}(u_{II})}\right)\right\} = 0\,, \tag{4.1.40}$$

with a real solution γ^0. Equation (4.1.40) can be written in the form of

$$\int_{u_I}^{u_{II}} k_{II}(u')du' - \frac{\pi}{4} - \tan^{-1}\left(\frac{\kappa_{III}(u_{II})}{\aleph_1 k_{II}(u_{II})}\right) - \nu\pi = 0\,, \tag{4.1.41}$$

where ν is an integer and represents the mode number. The dispersion relation $D_{WKB}(\gamma) = 0$ can be expanded in a Taylor series around γ^0

$$D_{WKB}(\gamma) = D_{WKB}(\gamma^0) + \frac{\partial D_{WKB}}{\partial\gamma}\bigg|_{\gamma^0}(\gamma-\gamma^0) + \frac{\partial^2 D_{WKB}}{2\partial\gamma^2}\bigg|_{\gamma^0}(\gamma-\gamma^0)^2 + \ldots = 0\,. \tag{4.1.42}$$

The first-order correction $\gamma-\gamma^0$ to γ^0 is desired. Neglecting the second- and higher-order contributions, we find

$$(\gamma-\gamma^0) \approx \frac{-D_{WKB}}{\partial_\gamma D_{WKB}}\bigg|_{\gamma^0} \approx \frac{-D_{WKB}}{\partial_\gamma D_{WKB}^0}\bigg|_{\gamma^0}\,, \tag{4.1.43}$$

and a little algebra yields

$$\gamma-\gamma^0 \approx j\,\frac{\dfrac{\aleph_1 k_{II}\kappa_{III}}{\aleph_1^2 k_{II}^2 + \kappa_{III}^2}}{\tan^{-1}\left(\dfrac{k_{II}R_1}{\gamma^0}\right) + \dfrac{\aleph_1[k_{II}^2 + \kappa_{III}^2]}{\aleph_1^2 k_{II}^2 + \kappa_{III}^2}\dfrac{\gamma^0/R_1^2}{\kappa_{III}k_{II}}}\bigg|_{u_{II}}\,\exp\left\{-2\int_{u_{II}}^{u_{III}}\kappa_{III}(u')du'\right\}\,, \tag{4.1.44}$$

which is imaginary if the effective refractive indices N_1 and N_2 are real and which represents the attenuation. Equation (4.1.41) can be solved to find the real part of

the angular propagation constant $\gamma^0_{\mu\nu}$ for a given mode number ν, after which Eq. (4.1.44) can be used to find the first-order correction to $\gamma^0_{\mu\nu}$ that represents the radiation loss.

Expressions for the minimum width and the offset

The solution to the problem of the single-boundary bend that has been provided by the WKB approximation can be used to obtain two convenient expressions. One expression estimates the minimum width that a two-boundary curved wave-guide must have in order to be effectively a single-boundary bend. The minimum width is a useful parameter because the single-boundary bend has lower radiation losses than the double-boundary bend (*see* Fig. 7.7 and section § 5.2.3). A second expression gives the position of the maximum of the modal field distribution. Knowledge of the position of this maximum leads to a prediction of the lateral offset that must be applied at the junction between the straight and curved waveguide. The lateral offset is introduced to align the maxima of both field distributions and, thereby, to reduce coupling losses (See section § 5.2.4).

The expression for the minimum width of the double-boundary bend follows from the observation that the inner interface should lie sufficiently far away from the caustic $u = u_I$ in Fig. 4.2 where the field quantities decay exponentially and the presence of the inner interface will be unnoticed. A reasonably acceptable width Δu is found by requiring that

$$\text{Re}\left\{ \int_{u_{II}-\Delta u}^{u_I} \kappa_I(u')du' \right\} \geq 3 \, , \tag{4.1.45}$$

which means that the magnitude of the field at $u = u_{II}-\Delta u$ is approximately e^{-3} times the magnitude of the field at the caustic $u = u_I$. Condition Eq. (4.1.45) can be evaluated by using Eq. (C.8)

$$\text{Re}\left\{ \gamma\left[\frac{1}{2}\ln\left(\frac{1+\sqrt{1 - k_0^2 N_1^2 (R_1-w)^2/\gamma^2}}{1-\sqrt{1 - k_0^2 N_1^2 (R_1-w)^2/\gamma^2}} \right) - \sqrt{1 - \frac{k_0^2 N_1^2 (R_1-w)^2}{\gamma^2}} \right] \right\} \geq 3 \, . \tag{4.1.46}$$

In order to find a simpler expression for the minimal width[§] w, we replace γ by its real part $\mathrm{Re}(\gamma)$ which is justified since $\mathrm{Im}(\gamma) \ll \mathrm{Re}(\gamma)$ as discussed on page 62 and we keep the first term of the series Eq. (C.8) which is permitted for sufficiently small arguments of the square root. Equation (4.1.46) is thus simplified to

$$\frac{w}{R_1} \geq 1 - \left(\frac{\mathrm{Re}(\gamma)/(k_0 R_1)}{N_1}\right) \sqrt{1 - \left(\frac{9}{\mathrm{Re}(\gamma)}\right)^{2/3}} \tag{4.1.47}$$

Inequality (4.1.47) gives the minimum width that a curved waveguide should have in order to be effectively a single-boundary bend.

An approximate expression which gives the position $r = R_1 - \Delta r$ of the maximum field amplitude for the single-boundary bend can be found by requiring that the real part of the argument of the cosine in Eq. (4.1.23) be zero

$$\mathrm{Re}\left\{\gamma\left[\sqrt{\frac{k_0^2 N_1^2 (R_1 - \Delta r)^2}{\gamma^2} - 1} - \tan^{-1}\sqrt{\frac{k_0^2 N_1^2 (R_1 - \Delta r)^2}{\gamma^2} - 1}\right]\right\} = \frac{\pi}{4}, \tag{4.1.48}$$

in which the integral Eq. (C.4) has been used. A simpler form of Eq. (4.1.48) is found here as well by replacing γ by $\mathrm{Re}(\gamma)$ and by retaining the first term of the series Eq. (C.4),

$$\frac{\Delta r}{R_1} \approx 1 - \left(\frac{\mathrm{Re}(\gamma)/(k_0 R_1)}{N_1}\right) \sqrt{1 + \left(\frac{3\pi}{4\mathrm{Re}(\gamma)}\right)^{2/3}}. \tag{4.1.49}$$

Equation (4.1.49) gives the distance Δr between the outer interface and the maximum of the field distribution. The lateral offset that must be applied at the junction of a straight waveguide and a double-boundary bend of width w in order to minimize the transition losses is $w/2 - \Delta r$.

The WKB approximation is subject to inequality (B.10) for its validity. Direct substitution of $f(u) = N_i^2 e^{2u/R_i} - \gamma^2/(k_0 R_i)^2$ into Eq. (B.10) gives

---

[§] The minimum width is written as w instead of $R_2 - R_1$ in order to avoid confusion, because this section discusses the single-boundary bend.

$$\left| N_i^2 r^2 \left\{ \frac{N_i^2 r^2}{4} + \frac{\gamma^2}{k_0^2} \right\} \right| \ll \left| k_0^2 \left\{ N_i r^2 - \frac{\gamma^2}{k_0^2} \right\}^3 \right| . \tag{4.1.50}$$

Inequality (4.1.50) does not hold in the neighborhood of the two turning points $r = \mathrm{Re}(\gamma)/(k_0 N_1)$ and $r = \mathrm{Re}(\gamma)/(k_0 N_2)$ and in the limit $k_0 \to 0$. Expression Eq. (4.1.34) for the effective refractive index can be used to approximate inequality Eq. (4.1.50) by

$$k_0^2 R_1^2 \gg \frac{N_i^2 (\tfrac{1}{4} N_i^2 + N_{eff}^2)}{N_i^2 - N_{eff}^2} , \tag{4.1.51}$$

where the inequality has been evaluated for $r = R_1$ and where γ has been replaced by $\mathrm{Re}(\gamma)$. This condition fails when either $N_{eff} \approx N_1$ or when $N_{eff} \approx N_2$ where the mode is close to cutoff. The WKB approximation may also not be used when the radius of curvature is too small or equivalently when the wavelength is too large.

4.1.5 Staircase approximation plus transfer-matrix algorithm

A third technique to solve the problem of the transformed curved waveguide is to approximate the transformed index of refraction $N_i e^{u/R_i}$ by a large number of small steps of constant refractive index, called the staircase approximation, which is then solved by means of the transfer-matrix method. This method gives optimal results as far as accuracy, applicability and computing speed are concerned. There seems to be an abundant amount of literature on the transfer-matrix method and in general on the exact solution of multilayer structures. The best reference here is the work of Ghatak, Thyagarajan and Shenoy on the matrix approach [35], since they seem to be the only ones who published the application of this technique to the curved waveguide [112].

The staircase approximation

The starting point is the scalar Helmholtz equation

$$\left(\frac{\partial^2}{\partial u^2} + k_0^2 N_i^2 e^{2u/R_i} - \frac{\gamma^2}{R_i^2} \right) \begin{pmatrix} e_{x,i}^{\pm}(u) \\ h_{x,i}^{\pm}(u) \end{pmatrix} = 0 , \, i = 1, 2, ..., M , \tag{4.1.19}$$

which is reproduced here, including the boundary conditions

$$\left\{ \begin{array}{ll} h_x(u) \ , \ N_i^{-2}\partial_u h_x(u) & \text{for HE modes} \\ e_x(u) \ , \quad \partial_u e_x(u) & \text{for EH modes} \end{array} \right\}, \text{ at } u = u_i = u(r=R_i) \ , \qquad (4.1.20)$$

and the requirement at the screen

$$\left\{ \begin{array}{ll} \partial_u h_x(u) \ = \ 0 & \text{for HE modes} \\ e_x(u) \ = \ 0 & \text{for EH modes} \end{array} \right\}, \text{ at } u = U_{sc} = u(r=R_{sc}) \ . \qquad (4.1.21)$$

The staircase approximation replaces the transformed refractive index $N_i\exp(u/R_i)$ by another refractive index $N'(u)$, which consists of a large number of steps where the index of refraction is constant as shown in Fig. 4.3. We have adopted the following discretization where the transformed index $N_i\exp(u/R_i)$ in domain i, that is bounded by $[u_{i-1},u_i]$ and that corresponds to N_i in domain $[R_{i-1},R_i]$, is approximated by m_i partitions l of equal size $(u_i-u_{i-1})/m_i$ that are bounded by

$$[u_{i,l-1},u_{i,l}] \ = \ \left[u_{i-1} + (l-1)\frac{u_i-u_{i-1}}{m_i} \ , \ u_{i-1} + l\frac{u_i-u_{i-1}}{m_i} \right], \text{ with } l = 1, 2, ..., m_i \ ,$$

$$(4.1.52)$$

and characterized by constant refractive indices

$$N'_{i,l} \ = \ N_i \exp\left\{ \frac{u_{i-1} + (l-\frac{1}{2})\frac{u_i-u_{i-1}}{m_i}}{R_i} \right\} . \qquad (4.1.53)$$

The boundary u_{i,m_i} of the last partition i coincides with the original boundary u_i and equals the boundary $u_{i+1,0}$ of the first partition in domain $i+1$. The refractive index $N'_{i,l}$ has been evaluated at the middle of the partition $[u_{i,l-1},u_{i,l}]$. There is now a total of

$$M_{tot} \ = \ \sum_{i=1}^{M} m_i \qquad (4.1.54)$$

partitions bounded by $M_{tot}+1$ border. By omitting the first border $u_0 = u_{0,0}$ and the last border $u_M = u_{M-1,m_M}$ and letting $N'_{1,1}$ and N_{M,m_M} extend to infinity, we retain an approximation to the original refractive index profile that consists of M_{tot} partitions with a constant refractive index separated by $M_{tot}-1$ boundaries.

The original profile ranges from $u = U_{sc}$ to $u = +\infty$, but the number of steps cannot be infinite. There is a first partition at $u = u_0$ and a last partition at $u = u_M$. The refractive index before the first and after the last step of the staircase is approximated by one step only, i.e. the landing. The omission of the part of the refractive-index profile for small u does not lead to serious errors, because the field profile
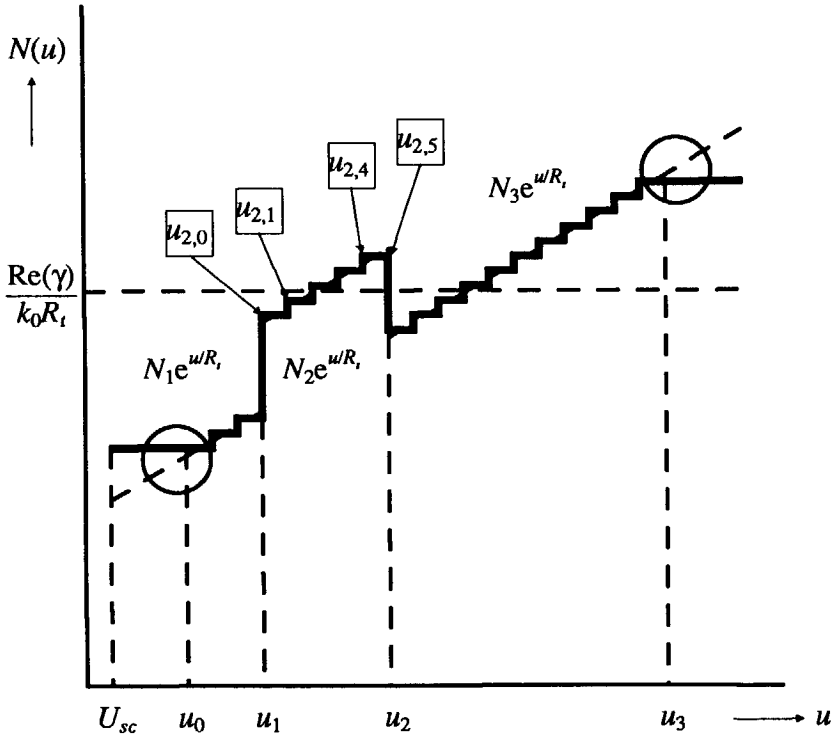
Fig. 4.3 *The staircase approximation. The original refractive-index profile is approximated by a large number of small steps with a constant index of refraction. In this example we have $m_1 = 3$, $m_2 = 5$ and $m_3 = 11$. The refractive-index profile before u_0 and beyond u_3 is approximated by one value only, being $N_{1,1}$ and $N_{3,11}$ respectively. The position of the screen is given by $u = U_{sc}$. The two circles mark the beginning and the end of the staircase, where the remaining parts of the transformed index of refraction are omitted.*

decays exponentially for small u and the point $u = u_0$ can be located at a point where the magnitude of the field is negligible. The omission of the refractive index beyond $u = u_M$ is not trivial, because the field decreases very slowly there. Consequently a larger error results and the point $u = u_M$ must be chosen much further away from the bend than the point $u = u_0$. The influence of these omissions is investigated numerically in Table 5.2 on page 104.

The transfer-matrix method

The solution to the scalar Helmholtz equation in partition l of domain i which is characterized by a constant index of refraction $N'_{i,l}$ and $u \in [u_{i,l-1}, u_{i,l}]$, can be written as

$$\begin{pmatrix} e^{\pm}_{x,i,l}(u) \\ h^{\pm}_{x,i,l}(u) \end{pmatrix} = A_{i,l}\cos\{k_{i,l}(u-u_{i,l-1})\} + \frac{B_{i,l}\sin\{k_{i,l}(u-u_{i,l-1})\}}{k_{i,l}} \quad , \quad \begin{cases} \text{EH modes} \\ \text{HE modes} \end{cases},$$

$$(4.1.55)$$

with

$$k_{i,l} = \sqrt{k_0^2 N_{i,l}^2 - \frac{\gamma^2}{R_t^2}} \; , \; \text{Re}(k_{i,l}) > 0 \, .$$

$$(4.1.56)$$

The solution is even in $k_{i,l}$ and moreover it behaves correctly for $k_{i,l} = 0$. A similar solution is found in partition $l+1$ and both solutions are interrelated through the application of the boundary conditions at $u = u_{i,l}$. The boundary conditions Eq. (4.1.20) are required at the "real" interfaces $u = u_i = u_{i,0} = u_{i-1,m_{i-1}}$. There are no real discontinuities in the refractive index at all other boundaries and normal continuity is thus required of the fields and their derivatives. A little algebra yields the transfer matrix relating the coefficients $\{A_{i,l}, B_{i,l}\}$ to $\{A_{i,l+1}, B_{i,l+1}\}$

$$\begin{pmatrix} A_{i,l+1} \\ B_{i,l+1} \end{pmatrix} = \begin{pmatrix} \cos\{k_{i,l}(u_{i,l}-u_{i,l-1})\} & k_{i,l}^{-1}\sin\{k_{i,l}(u_{i,l}-u_{i,l-1})\} \\ -k_{i,l}\sin\{k_{i,l}(u_{i,l}-u_{i,l-1})\} & \cos\{k_{i,l}(u_{i,l}-u_{i,l-1})\} \end{pmatrix} \begin{pmatrix} A_{i,l} \\ B_{i,l} \end{pmatrix}, \quad (4.1.57)$$

when $l \neq m_i$ and

$$\begin{pmatrix} A_{i+1,1} \\ B_{i+1,1} \end{pmatrix} = \begin{pmatrix} \cos\{k_{i,m_i}(u_{i,m_i}-u_{i,m_i-1})\} & k_{i,m_i}^{-1}\sin\{k_{i,l}(u_{i,m_i}-u_{i,m_i-1})\} \\ -\aleph_i k_{i,m_i}\sin\{k_{i,m_i}(u_{i,m_i}-u_{i,m_i-1})\} & \aleph_i\cos\{k_{i,m_i}(u_{i,m_i}-u_{i,m_i-1})\} \end{pmatrix} \begin{pmatrix} A_{i,m_i} \\ B_{i,m_i} \end{pmatrix},$$

(4.1.58)

when $l = m_i$, where

$$\aleph_i = \begin{cases} 1 & \text{HE modes}, \\ \dfrac{N_{i+1}^2}{N_i^2} & \text{EH modes}. \end{cases}$$

(4.1.59)

Note again that the transfer matrix is symmetric in $k_{i,l}$ and that its determinant never vanishes.

Boundary conditions

The transfer matrix can be used repeatedly to relate coefficients $\{A_{M,m_M}, B_{M,m_M}\}$, to $\{A_{1,1}, B_{1,1}\}$. Boundary conditions can be imposed on these four coefficients. To this end it is more convenient to write the general field Eq. (4.1.55) as

$$\begin{pmatrix} e_{x,i,l}^{\pm}(u) \\ h_{x,i,l}^{\pm}(u) \end{pmatrix} = (k_{i,l}A_{i,l}-jB_{i,l})\frac{e^{+jk_{i,l}(u-u_{i,l-1})}}{2k_{i,l}} + (k_{i,l}A_{i,l}+jB_{i,l})\frac{e^{-jk_{i,l}(u-u_{i,l-1})}}{2k_{i,l}}.$$

(4.1.60)

Inspection of Fig. 4.3 shows that we are looking for the solution that is leaky for $u > u_M$ and that represents an outgoing wave. This leads in combination with Eq. (4.1.60), the choice of the root $\text{Re}(k_{i,l}) > 0$ and the time dependence $e^{j\omega t}$ to

$$A_{M,m_M}k_{M,m_M}-jB_{M,m_M} = 0.$$

(4.1.61)

Inspection of Fig. 4.3 also shows that the solution must be bounded for $u < u_0$. This requires knowledge of the sign of $\text{Im}(k_{1,1})$, which is related to the sign of $\text{Re}(k_{1,1})$ by means of

$$\mathrm{Re}k_{i,l}\mathrm{Im}k_{i,l} = -\frac{\mathrm{Re}\gamma\mathrm{Im}\gamma}{R_t^2} > 0 \tag{4.1.62}$$

Inequality (4.1.62) follows from the imaginary part of the square of Eq. (4.1.56) under the assumption $\mathrm{Im}N_{i,l} = 0$. The greater than sign results from the requirement that both the forward and the backward propagating mode attenuate due to radiation. The boundary condition on the coefficients $\{A_{1,1}, B_{1,1}\}$ is thus seen to be

$$A_{1,1}k_{1,1}-jB_{1,1} = 0 , \tag{4.1.63}$$

The solutions to the problem of the transformed curved waveguide that have been found by means of the staircase approximation and the transfer-matrix method represent leaky waves. The leaky character, however, has been caused by chopping off the part of the transformed refractive index beyond $u > u_M$. The field that is calculated by means of the staircase approximation will deviate from the exact solution beyond $u > u_M$. The field remains bounded, on the other hand, when the transformed refractive index is not chopped and is allowed to go to infinity (*see also* the discussion on page 26).

4.2 The junction

4.2.1 Introduction

The junction of two straight waveguides has been studied by a number of authors. Clarricoats, Hockham and Sharpe [22][48] solved the problem of the straight waveguide junction by means of mode matching. Rozzi [99] used the complete orthogonal set of discrete and continuous modes and subsequent matching of these modes to find the scattering matrix of the junction. The study by Biehlig *et al.* [10] is similar to the work of Rozzi [99] but is of special interest because it uses a similar notation to the one that is used in this section. De Ruiter [27] developed a general theory for transmission and reflection at the straight waveguide junction which uses the Green's function integral approach.

The transmission of a junction of a straight and curved waveguide is calculated by means of the "overlap" integral in several papers. Heiblum and Harris [40] give an overlap integral with a factor which accounts for the Fresnel reflection and so do Chen and Unger [18]. Baets and Lagasse [7] give an overlap integral that includes the factor $1/r$ in the integrand.

In the following sections, a derivation will be given for the scattering matrix of the junction of two straight waveguides, the junction of the straight and the curved waveguide and the junction of two bends. The scattering matrix will be given for both HE and EH polarizations. The derivation includes the effect of reflection, it does not a priori neglect the continuous modes. Rozzi's approach [99] will be followed, i.e. the use of the complete orthonormal set of modes to match the boundary conditions at the junction. It will be shown that the resulting formulae can be considerably simplified and the final result consists of simple overlap integrals.

4.2.2 One-dimensional orthogonality relations

The coupling problem is treated here for straight and curved slab waveguides. It has been shown in the previous chapter that the method of the effective dielectric constant can be used to calculate approximate solutions for straight and curved waveguides with a two-dimensional cross-section and that the results of the EDC method are straight and curved slab waveguides with an effective refractive index profile. The junction will, therefore, be treated here for slab waveguides.

Orthogonality relations are required and the orthogonality relations given in Chapter 2 are explicitly written out here for slab waveguides. It is straightforward to show that for a straight slab waveguide and EH-polarization, Eq. (2.3.11) transforms into

$$\frac{\beta_\mu}{\omega\mu_0} \int_{y_{sc}}^{+\infty} e_{x,\mu}^+ e_{x,\nu}^+ \, dy = K_\mu \delta_{\mu,\nu} \,, \tag{4.2.1}$$

and for HE-polarization into

$$\frac{\beta_\mu}{\omega\varepsilon_0} \int_{y_{sc}}^{+\infty} \frac{h_{x,\mu}^+ h_{x,\nu}^+}{N_i^2} \, dy = K_\mu \delta_{\mu,\nu} \,. \tag{4.2.2}$$

The above equations may be compared with Eqs. (8.5-13) and (8.5-14) of Marcuse [70]. For the curved waveguide and EH-polarization, we have from Eq. (2.3.39)

$$\frac{\gamma_\mu}{\omega\mu_0} \int\limits_{R_{sc}}^{+\infty} \frac{e_{x,\mu}^+ e_{x,\nu}^+}{r} \, dr = K_\mu \delta_{\mu,\nu} \,, \tag{4.2.3}$$

and for HE-polarization

$$\frac{\gamma_\mu}{\omega\varepsilon_0} \int\limits_{R_{sc}}^{+\infty} \frac{h_{x,\mu}^+ h_{x,\nu}^+}{rN_i^2} \, dr = K_\mu \delta_{\mu,\nu} \,. \tag{4.2.4}$$

The dimension of K_μ is W m^{-1} in all four equations. Similar orthogonality relations exist for the continuous part of the spectrum.

4.2.3 Junction of two straight waveguides; EH-modes

We start with the junction of two different straight planar waveguides at $z = 0$ and EH modes. In the half-space $z < 0$ we have waveguide a and in the half-space $z > 0$ we have waveguide b. The electric field has only one component e_x, with $e_{x,\mu}^+ = e_{x,\mu}^-$. The electric field strength of mode μ will therefore be written as e_μ for short, without the subscript x or the superscripts $+$ or $-$. In order to minimize the details the total electric field Eq. (2.3.3) is written in shorthand notation as
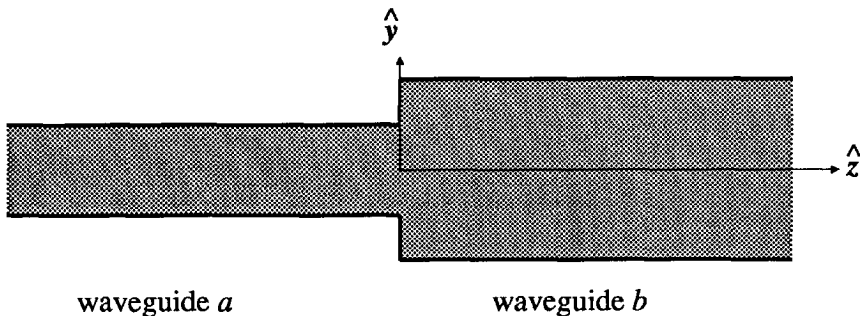

waveguide a waveguide b

Fig. 4.4 *The junction of two straight waveguides at $z = 0$.*

$$e_x = \sum_{\mu=1}^{M} \left\{ c_\mu^+ e_\mu^+ + c_\mu^- e_\mu^- \right\} + \int_B \left\{ c^+(\beta)e^+(\beta) + c^-(\beta)e^-(\beta) \right\} d\beta \stackrel{\text{def}}{=} |e_\mu\rangle (c_\mu^+ + c_\mu^-) , \quad (4.2.5)$$

where *Einstein's summation convention* is adopted for summing over all indices that appear twice. The indices refer to the mode number and range from 1 to M_a+1 when attached to a quantity that is labeled a and similarly from 1 to M_b+1 for a quantity that is labeled b. It is understood that the summation includes M discrete modes *plus* the contribution of the continuous part of the spectrum, which is labeled by the index $\mu = M+1$.

The fields $|e_\mu\rangle$ are normalized, i.e.

$$|e_\mu\rangle \stackrel{\text{def}}{=} \begin{cases} \dfrac{e_\mu(y)}{\sqrt{K_\mu}} & \text{with } K_\mu \delta_{\mu,\nu} = \int_{y_\infty}^{\infty} e_\mu(y)e_\nu(y)dy , \\[2em] \dfrac{e(y,\beta)}{\sqrt{K(\beta)}} & \text{with } K(\beta)\delta(\beta-\beta') = \int_{y_\infty}^{\infty} e(y,\beta)e(y,\beta')dy . \end{cases} \quad (4.2.6)$$

where *the Dirac notation* is used, i.e. the field of every mode has either a left or a right bracket and an integration is performed on closing the brackets. More information on Dirac's notation and some examples are presented in Appendix D. Such an integral $\langle e_\nu^a | e_\mu^b \rangle$ will be called *the overlap integral* and the $(M_a+1) \times (M_b+1)$ matrix that consists of all overlap integrals $\langle e_\nu^a | e_\mu^b \rangle$ will be called *the overlap matrix*. See Biehlig *et al.* [10] for a similar use of this notation. The dimension of $|e_\mu\rangle$ after normalization is $m^{-1/2}$ and the overlap integrals are dimensionless.

The continuity is required of e_x and h_y at the interface of the junction $z = 0$. The boundary condition on e_x at $z = 0$ can be conveniently written as

$$|e_\mu^a\rangle (c_{\mu a}^+ + c_{\mu a}^-) = |e_\mu^b\rangle (c_{\mu b}^+ + c_{\mu b}^-) . \quad (4.2.7)$$

The continuity requirement of $h_{y,\mu}^{\pm} = \pm\beta_\mu e_\mu/(\omega\mu_0)$ at $z = 0$ leads to

$$|e_\mu^a\rangle \beta_{\mu\nu}^a (c_{\nu a}^+ - c_{\nu a}^-) = |e_\mu^b\rangle \beta_{\mu\nu}^b (c_{\nu b}^+ - c_{\nu b}^-) , \quad (4.2.8)$$

where $\beta_{\mu\nu}^a$ is the square diagonal matrix $\beta_\mu^a \delta_{\mu,\nu}$ with the propagation constants on the diagonal. The eigenfunctions $|e_\mu^a\rangle$ and $|e_\mu^b\rangle$ satisfy orthogonality

$$\langle e_\nu^a | e_\mu^a \rangle = \delta_{\nu,\mu} , \tag{4.2.9}$$

$$\langle e_\nu^b | e_\mu^b \rangle = \delta_{\nu,\mu} . \tag{4.2.10}$$

Multiplying Eqs. (4.2.7) and (4.2.8) with M_a+1 functions $|e_\mu^a\rangle$ and M_b+1 functions $|e_\mu^b\rangle$, integrating and using the orthogonality conditions we find

$$c_{\xi a}^+ + c_{\xi a}^- = \langle e_\xi^a | e_\mu^b \rangle (c_{\mu b}^+ + c_{\mu b}^-) , \tag{4.2.11}$$

$$\langle e_\xi^b | e_\mu^a \rangle (c_{\mu a}^+ + c_{\mu a}^-) = c_{\xi b}^+ + c_{\xi b}^- , \tag{4.2.12}$$

$$\beta_{\xi\nu}^a (c_{\nu a}^+ - c_{\nu a}^-) = \langle e_\xi^a | e_\mu^b \rangle \beta_{\mu\nu}^b (c_{\nu b}^+ - c_{\nu b}^-) , \tag{4.2.13}$$

$$\langle e_\xi^b | e_\mu^a \rangle \beta_{\mu\nu}^a (c_{\nu a}^+ - c_{\nu a}^-) = \beta_{\xi\nu}^b (c_{\nu b}^+ - c_{\nu b}^-) . \tag{4.2.14}$$

The consistency of these equations requires

$$\langle e_\xi^b | e_\nu^a \rangle \langle e_\nu^a | e_\mu^b \rangle = \delta_{\xi,\mu} , \tag{4.2.15}$$

which is the requirement of completeness of the discrete and the continuous modes of waveguide a. The consistency of Eqs. (4.2.11) through (4.2.14) similarly yields the completeness requirement for the modes of waveguide b.

We can view $c_{\mu a}^+$ and $c_{\mu b}^-$ as the incoming waves and $c_{\mu a}^-$ and $c_{\mu b}^+$ as the outgoing waves. The outgoing waves can be related to the incoming waves by a *scattering matrix* S with the dimension M_a+M_b+2

$$\begin{pmatrix} c_{\mu a}^- \\ c_{\mu b}^+ \end{pmatrix} \stackrel{\text{def}}{=} S \begin{pmatrix} c_{\nu a}^+ \\ c_{\nu b}^- \end{pmatrix} \stackrel{\text{def}}{=} \begin{pmatrix} R_{\mu\nu}^{aa} & T_{\mu\nu}^{ab} \\ T_{\mu\nu}^{ba} & R_{\mu\nu}^{bb} \end{pmatrix} \begin{pmatrix} c_{\nu a}^+ \\ c_{\nu b}^- \end{pmatrix} , \tag{4.2.16}$$

where $R_{\mu\nu}$ and $T_{\mu\nu}$ are *the reflection and the transmission matrices* respectively. It is easily verified that the scattering matrix must satisfy Stokes' relations[§]

$$\begin{pmatrix} R^{aa}_{\tau\xi} & T^{ab}_{\tau\xi} \\ T^{ba}_{\tau\xi} & R^{bb}_{\tau\xi} \end{pmatrix} \begin{pmatrix} R^{aa}_{\xi\mu} & T^{ab}_{\xi\mu} \\ T^{ba}_{\xi\mu} & R^{bb}_{\xi\mu} \end{pmatrix} = \begin{pmatrix} \delta_{\tau,\mu} & 0 \\ 0 & \delta_{\tau,\mu} \end{pmatrix}. \tag{4.2.17}$$

The coefficients $c^-_{\mu a}$ are first eliminated from Eqs. (4.2.11) and (4.2.13) by adding $\beta^a_{\nu\xi}$ times Eq. (4.2.11) to Eq. (4.2.13) and some renaming

$$\beta^a_{\xi\nu}c^+_{\nu a} = \left\{\beta^a_{\xi\nu}\langle e^a_\nu|e^b_\mu\rangle + \langle e^a_\xi|e^b_\nu\rangle\beta^b_{\nu\mu}\right\}c^+_{\mu b} + \left\{\beta^a_{\xi\nu}\langle e^a_\nu|e^b_\mu\rangle - \langle e^a_\xi|e^b_\nu\rangle\beta^b_{\nu\mu}\right\}c^-_{\mu b}, \tag{4.2.18}$$

Similarly, the coefficients $c^+_{\mu b}$ can be eliminated from Eqs. (4.2.12) and (4.2.14)

$$\left\{\beta^b_{\xi\nu}\langle e^b_\nu|e^a_\mu\rangle - \langle e^b_\xi|e^a_\nu\rangle\beta^a_{\nu\mu}\right\}c^+_{\mu a} + \left\{\beta^b_{\xi\nu}\langle e^b_\nu|e^a_\mu\rangle + \langle e^b_\xi|e^a_\nu\rangle\beta^a_{\nu\mu}\right\}c^-_{\mu a} = \beta^b_{\xi\nu}c^-_{\nu b}, \tag{4.2.19}$$

These relations cannot yet be inverted since the matrices are not square. Square invertible matrices are obtained by multiplying Eq. (4.2.18) by $\langle e^b_\tau|e^a_\xi\rangle$ and Eq. (4.2.19) by $\langle e^a_\tau|e^b_\xi\rangle$. Inverting the relations and using completeness, the reflection and the transmission matrices are found to be

$$T^{ba}_{\kappa\mu} = \left\{\langle e^b_\tau|e^a_\sigma\rangle\beta^a_{\sigma\chi}\langle e^a_\chi|e^b_\kappa\rangle + \beta^b_{\tau\kappa}\right\}^{-1}2\langle e^b_\tau|e^a_\xi\rangle\beta^a_{\xi\mu}, \tag{4.2.20}$$

$$R^{bb}_{\kappa\mu} = -\left\{\langle e^b_\tau|e^a_\sigma\rangle\beta^a_{\sigma\chi}\langle e^a_\chi|e^b_\kappa\rangle + \beta^b_{\tau\kappa}\right\}^{-1}\left\{\langle e^b_\tau|e^a_\xi\rangle\beta^a_{\xi\nu}\langle e^a_\nu|e^b_\mu\rangle - \beta^b_{\tau\mu}\right\}, \tag{4.2.21}$$

$$T^{ab}_{\kappa\mu} = \left\{\langle e^a_\tau|e^b_\sigma\rangle\beta^b_{\sigma\chi}\langle e^b_\chi|e^a_\kappa\rangle + \beta^a_{\tau\kappa}\right\}^{-1}2\langle e^a_\tau|e^b_\xi\rangle\beta^b_{\xi\mu}, \tag{4.2.22}$$

$$R^{aa}_{\kappa\mu} = -\left\{\langle e^a_\tau|e^b_\sigma\rangle\beta^b_{\sigma\chi}\langle e^b_\chi|e^a_\kappa\rangle + \beta^a_{\tau\kappa}\right\}^{-1}\left\{\langle e^a_\tau|e^b_\xi\rangle\beta^b_{\xi\nu}\langle e^b_\nu|e^a_\mu\rangle - \beta^a_{\tau\mu}\right\}. \tag{4.2.23}$$

This scattering matrix is a complete expression in the sense that both reflection and the contribution of the continuous modes are included. Since the general structure of the above expressions for the reflection and the transmission matrices and the equivalent matrices for the other polarization and the other types of

---

[§] Stokes' treatment of reflection involves the argument that the incoming field must be recovered if the scattered wave is reversed in direction. G. Stokes: Mathematical and physical papers, **2**, pp. 89ff.

junction resemble each other, it will prove worthwhile to introduce two new symbols, i.e. one symbol for the overlap matrices

$$C_{\mu\nu} \stackrel{\text{def}}{=} \langle e_{\mu}^{b}|e_{\nu}^{a}\rangle , \tag{4.2.24}$$

$$\tilde{C}_{\mu\nu} \stackrel{\text{def}}{=} \langle e_{\mu}^{a}|e_{\nu}^{b}\rangle , \tag{4.2.25}$$

and one symbol for the diagonal matrix that contains the propagation constants

$$k_{\mu\nu}^{a} \stackrel{\text{def}}{=} \beta_{\mu\nu}^{a} , \tag{4.2.26}$$

plus an equivalent expression for $k_{\mu\nu}^{b}$. The reflection and the transmission matrices Eqs. (4.2.20) through (4.2.23) are summarized in the new notation in Table 4.1 on page 89 together with the scattering matrices for the other types of junction.

4.2.4 Junction of two straight waveguides; HE-modes

The derivation for HE-modes is very similar to the derivation for EH-modes. The only differences lie in the normalization and the overlap integrals. The magnetic field for HE-modes in planar straight waveguides has an x component only, where $h_{x,\mu}^{+} = h_{x,\mu}^{-}$. The total magnetic field is written as

$$h_{x}^{a} = |h_{\mu}^{a}\rangle(c_{\mu a}^{+}+c_{\mu a}^{-}) , \tag{4.2.27}$$

in Dirac's bracket notation (*see* Appendix D) and by means of Einstein's summation convention. The modes are normalized as

$$|h_{\mu}\rangle \stackrel{\text{def}}{=} \begin{cases} \dfrac{h_{\mu}(y)}{\sqrt{K_{\mu}}} & \text{with } K_{\mu}\delta_{\mu,\nu} = \displaystyle\int_{y_{sc}}^{\infty} \dfrac{h_{\mu}(y)h_{\nu}(y)}{N^{2}} \, dy , \\[4mm] \dfrac{h(y,\beta)}{\sqrt{K(\beta)}} & \text{with } K(\beta)\delta(\beta-\beta') = \displaystyle\int_{y_{sc}}^{\infty} \dfrac{h(y,\beta)h(y,\beta')}{N^{2}} \, dy , \end{cases} \tag{4.2.28}$$

and the orthogonality relation Eq. (4.2.2) is now expressed as

$$\langle h_\nu^a | N_a^{-2} | h_\mu^a \rangle = \delta_{\nu,\mu} \,, \tag{4.2.29}$$

$$\langle h_\nu^b | N_b^{-2} | h_\mu^b \rangle = \delta_{\nu,\mu} \,. \tag{4.2.30}$$

The magnetic field h_x must be continuous at the junction at $z = 0$ between waveguide a and b or

$$|h_\mu^a\rangle(c_{\mu a}^+ + c_{\mu a}^-) = |h_\mu^b\rangle(c_{\mu b}^+ + c_{\mu b}^-) \,. \tag{4.2.31}$$

The continuity requirement of e_y at $z = 0$ is formulated as

$$|h_\mu^a\rangle\frac{\beta_{\mu\nu}^a}{N_a^2}(c_{\nu a}^+ - c_{\nu a}^-) = |h_\mu^b\rangle\frac{\beta_{\mu\nu}^b}{N_b^2}(c_{\nu b}^+ - c_{\nu b}^-) \,, \tag{4.2.32}$$

because $e_{y,\mu}^\pm = -\pm\beta_\mu h_{x,\mu}/(\omega\varepsilon_0 N^2)$. Multiplication of the continuity relation Eq. (4.2.31) by $\langle h_\mu^a | N_a^{-2} |$ and $\langle h_\mu^b | N_b^{-2} |$ and Eq. (4.2.32) by $\langle h_\mu^a |$ and $\langle h_\mu^b |$, and using orthogonality yield

$$c_{\xi a}^+ + c_{\xi a}^- = \langle h_\xi^a | N_a^{-2} | h_\mu^b \rangle(c_{\mu b}^+ + c_{\mu b}^-) \,, \tag{4.2.33}$$

$$\langle h_\xi^b | N_b^{-2} | h_\mu^a \rangle(c_{\mu a}^+ + c_{\mu a}^-) = c_{\xi b}^+ + c_{\xi b}^- \,, \tag{4.2.34}$$

$$\beta_{\xi\nu}^a(c_{\nu a}^+ - c_{\nu a}^-) = \langle h_\xi^a | N_b^{-2} | h_\mu^b \rangle\beta_{\mu\nu}^b(c_{\nu b}^+ - c_{\nu b}^-) \,, \tag{4.2.35}$$

$$\langle h_\xi^b | N_a^{-2} | h_\mu^a \rangle\beta_{\mu\nu}^a(c_{\nu a}^+ - c_{\nu a}^-) = \beta_{\xi\nu}^b(c_{\nu b}^+ - c_{\nu b}^-) \,. \tag{4.2.36}$$

The consistency of these equations leads to the requirement of completeness

$$\langle h_\xi^b | N_b^{-2} | h_\nu^a \rangle\langle h_\nu^a | N_a^{-2} | h_\mu^b \rangle = \delta_{\xi,\mu} \,, \tag{4.2.37}$$

for the modes of waveguide a. A similar completeness relation is required for the modes of waveguide b and it follows from Eq. (4.2.37) by interchanging the labels a and b. All remaining steps can be copied from the derivation for the EH-modes and the resulting reflection and transmission matrices have been put together with the other results in Table 4.1. The main difference is that there are now two asymmetric coupling matrices $C_{\mu\nu} \overset{\text{def}}{=} \langle h_\mu^b | N_a^{-2} | h_\nu^a \rangle$ and $\tilde{C}_{\mu\nu} \overset{\text{def}}{=} \langle h_\mu^a | N_b^{-2} | h_\nu^b \rangle$ that are not

the transpose matrix of each other due to the asymmetric occurrence of the refractive index in the overlap integrals.

4.2.5 Straight-to-curved waveguide junction

The geometry of the junction of the bend and the straight waveguide has been discussed in section § 2.2.4 and Fig. 2.5. It is clear that an overlap integral can be expressed either in the lateral y-coordinate of the straight waveguide or in the radial r-coordinate of the bend. The straight waveguide is labeled a and the bend is labeled b. The electric field strength of the EH-modes in the curved slab waveguide has only one component

$$e_x^b = |e_\mu^b\rangle(c_{\mu b}^+ + c_{\mu b}^-) , \tag{4.2.38}$$

The modes of the bend are normalized as

$$|e_\mu^b\rangle = \begin{cases} \dfrac{e_\mu^b(r_b)}{\sqrt{K_\mu}} & \text{with } K_\mu\delta_{\mu,\nu} = \displaystyle\int_{R_{sc}}^\infty e_\mu^b(r_b)e_\nu^b(r_b)\dfrac{R_b}{r_b}\,dr_b \ , \\[4mm] \dfrac{e^b(r_b,\beta)}{\sqrt{K(\beta)}} & \text{with } K(\beta)\delta(\beta-\beta') = \displaystyle\int_{R_{sc}}^\infty e^b(r_b,\beta)e^b(r_b,\beta')\dfrac{R_b}{r_b}\,dr_b \ , \end{cases} \tag{4.2.39}$$

where the coordinate r_b has been labeled b in order to avoid confusion when discussing the bend-to-bend transition. An arbitrary radius R_b is included in the normalization integrals to keep track of dimensions. If a dimensionless scattering matrix Eq. (4.2.16) is desired, then the coefficients $c_\mu^\pm$ and consequently the fields should have identical dimensions for both the straight and the curved waveguides. Since the dimension of the field in the straight waveguide was $m^{-\frac{1}{2}}$—*see* page 82—, the normalization for the curved waveguide must be as in Eq. (4.2.39). The orthogonality relation Eq. (4.2.3) is now expressed as

$$\langle e_\nu^b|\frac{R_b}{r_b}|e_\mu^b\rangle = \delta_{\nu,\mu} , \tag{4.2.40}$$

which is dimensionless. The electric field e_x should be continuous at the junction between waveguide a and b or

$$|e_\mu^a\rangle(c_{\mu a}^+ + c_{\mu a}^-) = |e_\mu^b\rangle(c_{\mu b}^+ + c_{\mu b}^-) \; . \tag{4.2.41}$$

The continuity requirement of h_r leads to

$$|e_\mu^a\rangle\beta_{\mu\nu}^a(c_{\nu a}^+ - c_{\nu a}^-) = |e_\mu^b\rangle\frac{\gamma_{\mu\nu}^b}{r_b}(c_{\nu b}^+ - c_{\nu b}^-) \; , \tag{4.2.42}$$

because $h_{r,\mu}^\pm = \pm\gamma_\mu e_{x,\mu}/(\omega\mu_0 r)$. Multiplication of the continuity relation Eq. (4.2.41) by $\langle e_\xi^a|$ and $\langle e_\xi^b|R_b/r_b|$ and Eq. (4.2.42) by $\langle e_\xi^a|$ and $\langle e_\xi^b|$, and using orthogonality yield

$$c_{\xi a}^+ + c_{\xi a}^- = \langle e_\xi^a|e_\mu^b\rangle(c_{\mu b}^+ + c_{\mu b}^-) \; , \tag{4.2.43}$$

$$\langle e_\xi^b|\frac{R_b}{r_b}|e_\mu^a\rangle(c_{\mu a}^+ + c_{\mu a}^-) = c_{\xi b}^+ + c_{\xi b}^- \; , \tag{4.2.44}$$

$$\beta_{\xi\nu}^a(c_{\nu a}^+ - c_{\nu a}^-) = \langle e_\xi^a|\frac{R_b}{r_b}|e_\mu^b\rangle\frac{\gamma_{\mu\nu}^b}{R_b}(c_{\nu b}^+ - c_{\nu b}^-) \; , \tag{4.2.45}$$

$$\langle e_\xi^b|e_\mu^a\rangle\beta_{\mu\nu}^a(c_{\nu a}^+ - c_{\nu a}^-) = \frac{\gamma_{\xi\nu}^b}{R_b}(c_{\nu b}^+ - c_{\nu b}^-) \; . \tag{4.2.46}$$

The requirement of the consistency of these equations leads us to the completeness relation

$$\langle e_\xi^b|\frac{R_b}{r_b}|e_\nu^a\rangle\langle e_\nu^a|e_\mu^b\rangle = \delta_{\xi,\mu} \; . \tag{4.2.47}$$

for the modes of waveguide a. A similar relation is found for the modes of waveguide b by interchanging both labels. Writing out the reflection and the transmission matrices is straightforward now and the results are given in Table 4.1.

The discussion for HE-polarization and the junction of two bends is skipped. The arguments and conclusions are similar to the ones just given. The resulting scattering matrices are included, however, in Table 4.1.

Table 4.1 *The exact transmission and reflection matrices for the junction of straight and curved slab waveguides. Dirac's bracket notation and Einstein's summation convention have been used. Matrix C^T is the transpose of matrix C.*

$$T^{ba}_{\kappa\mu} = \left\{C_{\tau\sigma}k^a_{\sigma\chi}C^T_{\chi\kappa}+k^b_{\tau\kappa}\right\}^{-1}2C_{\tau\xi}k^a_{\xi\mu}$$

$$R^{bb}_{\kappa\mu} = -\left\{C_{\tau\sigma}k^a_{\sigma\chi}C^T_{\chi\kappa}+k^b_{\tau\kappa}\right\}^{-1}\left\{C_{\tau\xi}k^a_{\xi\nu}C^T_{\nu\mu}-k^b_{\tau\mu}\right\}$$

$$T^{ab}_{\kappa\mu} = \left\{\widetilde{C}_{\tau\sigma}k^b_{\sigma\chi}\widetilde{C}^T_{\chi\kappa}+k^a_{\tau\kappa}\right\}^{-1}2\widetilde{C}_{\tau\xi}k^b_{\xi\mu}$$

$$R^{aa}_{\kappa\mu} = -\left\{\widetilde{C}_{\tau\sigma}k^b_{\sigma\chi}\widetilde{C}^T_{\chi\kappa}+k^a_{\tau\kappa}\right\}^{-1}\left\{\widetilde{C}_{\tau\xi}k^b_{\xi\nu}\widetilde{C}^T_{\nu\mu}-k^a_{\tau\mu}\right\}$$

Waveguide junction $a \leftrightarrow b$		Propagation Matrices		Overlap Matrices			
				EH Polarization		HE Polarization	
a	b	$k^a_{\mu\nu}$	$k^b_{\mu\nu}$	$C_{\mu\nu}$	$\widetilde{C}_{\mu\nu}$	$C_{\mu\nu}$	$\widetilde{C}_{\mu\nu}$
straight	straight	$\beta^a_{\mu\nu}$	$\beta^b_{\mu\nu}$	$\langle e^b_\mu\|e^a_\nu\rangle$	$\langle e^a_\mu\|e^b_\nu\rangle$	$\langle h^b_\mu\|N^{-2}_a\|h^a_\nu\rangle$	$\langle h^a_\mu\|N^{-2}_b\|h^b_\nu\rangle$
straight	curved	$\beta^a_{\mu\nu}$	$\dfrac{\gamma^b_{\mu\nu}}{R_b}$	$\langle e^b_\mu\|e^a_\nu\rangle$	$\langle e^a_\mu\|\dfrac{R_b}{r_b}\|e^b_\nu\rangle$	$\langle h^b_\mu\|N^{-2}_a\|h^a_\nu\rangle$	$\langle h^a_\mu\|\dfrac{R_b}{r_bN^2_b}\|h^b_\nu\rangle$
curved	curved	$\dfrac{\gamma^a_{\mu\nu}}{R_a}$	$\dfrac{\gamma^b_{\mu\nu}}{R_b}$	$\langle e^b_\mu\|\dfrac{R_a}{r_a}\|e^a_\nu\rangle$	$\langle e^a_\mu\|\dfrac{R_b}{r_b}\|e^b_\nu\rangle$	$\langle h^b_\mu\|\dfrac{R_a}{r_aN^2_a}\|h^a_\nu\rangle$	$\langle h^a_\mu\|\dfrac{R_b}{r_bN^2_b}\|h^b_\nu\rangle$

- The overlap integral $\langle e^b_\mu\|\frac{R_a}{r_a}\|e^a_\nu\rangle$, for example, is written in Dirac's notation (*see* Appendix D). The integral is equal to $\int_{R_{sc}}^{\infty} e^b_{x,\mu}(r_a)\frac{R_a}{r_a}e^a_{x,\nu}(r_a)dr_a$, which has been expressed in the coordinate r_a of the bend a, but which could have been expressed in any other coordinate.

- The propagation matrices are square and diagonal. The diagonal elements are the respective propagation constants.

- The radius r_a is the radial coordinate in the coordinate system of waveguide a and r_b is similarly related to waveguide b. The index of refraction N_a is the lateral refractive-index profile of waveguide a, and N_b is similarly related to waveguide b.

- All fields have been normalized in such a way as to make the coupling integrals and hence the coupling matrix dimensionless. The parameter R_a originates in this normalization (*see* text) and the scattering matrix is independent of the parameter R_a.

- The overlap matrices satisfy the completeness relation of the modes of waveguide a, $C_{\mu\xi}\widetilde{C}_{\xi\nu} = \delta_{\mu,\nu}$ and similarly of waveguide b, $\widetilde{C}_{\mu\xi}C_{\xi\nu} = \delta_{\mu,\nu}$.

4.2.6 Neglecting the contribution of the continuous spectrum

A good criterion to evaluate the influence of the continuous spectrum on the analysis of the junction are the completeness relations (4.2.15), (4.2.37), (4.2.47) and their combination in Table 4.1. Completeness can be restated in the following way. The overlap integrals squared and summed along a column or row should equal one or

$$\langle e_\xi^b | e_\nu^a \rangle \langle e_\nu^a | e_\mu^b \rangle = \delta_{\xi,\mu} \Rightarrow \sum_\nu \langle e_\xi^a | e_\nu^b \rangle^2 = 1 \ \forall \xi \,. \tag{4.2.48}$$

If the contribution of the continuous spectrum is neglected, the sum given above only includes the guided modes. Consequently the deviation from unity in the right-hand side of Eq. (4.2.48) is then due to the missing contribution of the continuous modes. We have, therefore, a fairly accurate estimate of the amount of coupling from a guided mode to the continuous modes at the junction. What cannot be estimated is the propagation of these continuous modes and their subsequent recoupling to guided modes at the next junction. This leads to discrepancies when junctions are very close to each other in combination with considerable coupling of guided to continuous modes and vice versa.

The sum of all overlap integrals squared from one guided mode in waveguide a to all guided modes in waveguide b is usually very close to one. The representative example on page 119 mentions a sum of the squares of the overlap integrals for the guided modes of 0.9962. These considerations justify the omission of the contribution of the continuous modes to the coupling problem.

4.2.7 Simplification of the scattering matrix

The propagation constants of the guided modes satisfy Eq. (2.3.8) and are thus closely spaced if the difference between the refractive index of the waveguide and the refractive indices of both cover and substrate is small. If the propagation constants for the guided modes of waveguide a are approximated by the constant β^a and those of waveguide b by the constant β^b, then the transmission and reflection matrices for the EH-polarization and the junction of two straight waveguides simplify to

$$T_{\kappa\mu}^{ba} = \frac{2\beta^a}{\beta^a+\beta^b} \langle e_\kappa^b | e_\mu^a \rangle \, , \tag{4.2.49}$$

$$R_{\kappa\mu}^{bb} = \frac{\beta^b-\beta^a}{\beta^a+\beta^b} \, , \tag{4.2.50}$$

$$T_{\kappa\mu}^{ab} = \frac{2\beta^b}{\beta^a+\beta^b} \langle e_\kappa^a | e_\mu^b \rangle \, , \tag{4.2.51}$$

$$R_{\kappa\mu}^{aa} = \frac{\beta^a-\beta^b}{\beta^a+\beta^b} \, . \tag{4.2.52}$$

The transmission matrices Eqs. (4.2.49) and (4.2.51) are seen to be composed of overlap integrals in combination with a Fresnel transmission or reflection factor that takes the differences in refractive indices of the media a and b into account. The reflection matrices Eqs. (4.2.50) and (4.2.52) are diagonal and, consequently, they do not express the intermodal coupling. Its magnitude is determined by the Fresnel reflection factor.

The overlap integrals and normalization for the curved waveguide have been formulated in such a way that they become equal to the overlap integrals and normalization for the straight waveguide, when $r_a \approx R_a$ and $r_b \approx R_b$. This is true if the field distributions are peaked around R_a and R_b and if the peaks are so narrow that the relative changes in r_a and r_b are small, which is valid for all practical bends, and provided that R_a and R_b are chosen equal to the radii of curvature of waveguide a and b, respectively.

In order to simplify the reflection and the transmission matrices for the HE-polarization it must be assumed that the indices of refraction of medium a and b are approximately equal, because the refractive indices enter the overlap matrices. Applying this assumption leads to the even more reduced reflection and transmission matrices

$$T_{\kappa\mu}^{ba} = \langle e_\kappa^b | e_\mu^a \rangle \, , \tag{4.2.53}$$

$$R_{\kappa\mu}^{bb} = 0 \, , \tag{4.2.54}$$

$$T_{\kappa\mu}^{ab} = \langle e_{\kappa}^{a} | e_{\mu}^{b} \rangle , \tag{4.2.55}$$

$$R_{\kappa\mu}^{aa} = 0 . \tag{4.2.56}$$

All reflection is neglected in Eqs. (4.2.53) through (4.2.56) and the transmission matrices are equal to the coupling matrices.

It is not correct to relate the overlap matrix and the transmission matrix to power flow. It is nevertheless common practice to specify a "transition or coupling loss" in the following way

$$\eta_{\mu\nu}^{ba} = 10 \log \left| T_{\mu\nu}^{ba} \right|^{2} = 10 \log \left| \langle e_{\mu}^{b} | e_{\nu}^{a} \rangle \right|^{2} . \tag{4.2.57}$$

Whenever a transmission or coupling loss in dB is mentioned in the thesis, it is understood that Eq. (4.2.57) has been applied and that this is merely a way of specifying the magnitude of the overlap integral.

4.3 Multimode interference effects

We mean by multimode interference effects the interference between the guided modes exhibited in multimode waveguide tracks with multiple junctions and considerable intermodal coupling at these junctions. Multimode effects can be unwanted, because they can lead to the unpredictability of the performance of devices and they can also lead to enhanced scattering losses when the guided modes couple to higher-order modes or to continuous modes. Multimode effects can, on the other hand, be used in couplers such as the multi-mode interference coupler (see sections § 4.4 and § 5.3.1).

The prediction of the behavior of such a multimode waveguide track has to take care of the relative phases of all these modes. To calculate the total performance of a waveguide track we can use the tools developed in the preceding sections. The field in waveguide a can be represented by the vector $c_{\mu a}^{+}$ and the transmission matrix $T_{\nu\mu}^{ba}$ can be used to yield the corresponding vector $c_{\nu b}^{+}$ after the junction in waveguide b. The analysis can be completed by defining square diagonal propagation matrices for the straight waveguide

$$e^{-j\beta_{\mu}\Delta z} \delta_{\mu,\nu} , \tag{4.3.1}$$

and for the curved waveguide

$$e^{-j\gamma_\mu\Delta\varphi}\delta_{\mu,\nu} .$$ (4.3.2)

These two propagation matrices incorporate complex propagation constants and account for both the phase changes and the propagation losses. If the vector $c_{\mu a}^+$ is known in the first section of the waveguide track, repeated application of the propagation matrices Eqs. (4.3.1) and (4.3.2) and the appropriate transmission matrices yields a vector at the end of the circuit. Finally, equation (2.3.14) can be used to determine the power at the beginning and the end of the waveguide track and consequently the loss of power.

4.4 Conformal transformation for two diverging bends

Introduction

The theory and techniques that have been developed in the previous chapters and sections are applicable to curved multilayer waveguides, such as the curved 'double-ridge' waveguide or two coupled curved waveguides that have identical centers of curvature. A more frequently encountered situation is the geometry of two coupled oppositely curved waveguides, such as the curved access waveguides of the multi-mode-interference coupler shown in Fig. 5.8. Three points are of interest. Firstly, the modal field distribution of the coupled bends at the junction can be used to determine the coupling efficiency with which the field of the straight section is transmitted to the access waveguides. Secondly, the coupling between the two bends gives an extra phase contribution in addition to the phase difference that occurs in the straight section of the coupler. In the third place, the diverging coupled waveguides exhibit radiation loss which degrades the performance of the coupler.

Coupled waveguides have been analyzed by means of the method of effective dielectric constant in combination with the beam propagation method [21][98]. A technique which is commonly applied to the two-dimensional problem of coupled diverging waveguides is the staircase approximation, which approximates the diverging waveguides by a large number of short straight waveguide sections, in combination with the local coupled-mode theory or the more rigorous mode-matching technique. The local coupled-mode theory can be used to give simple expressions for the extra phase contribution [89] or can be applied to the problem where more than two modes couple [108], but it does not account for the radiation

loss nor for the change in the modal field distribution due to the curvature. The coupling between bends can, however, be larger than the coupling between straight waveguides because the curvature leads to a smaller distance between the two modal field distributions. The staircase approximation in combination with a rigorous mode-matching technique [124] takes all these effects into account. The COST216 Working Group 1 is currently surveying and comparing the techniques that are available for the analysis of complete couplers including the curved sections (*see also* page 105).

In this section, a conformal transformation will be introduced that transforms two coupled curved waveguides into an equivalent straight waveguide with a transformed index of refraction. The reader is referred to Marcatili [68] where the technique of conformal mapping is applied to tapers.

The conformal transformation

In order to apply the technique of conformal mapping, three assumptions have to be made:

- It is assumed that the problem is either two-dimensional or is translated to a two-dimensional problem, e.g. by means of the method of effective dielectric constant, because conformal-mapping techniques are applicable to two-dimensional problems only.
- It is assumed that the two coupled curved waveguides have equal radii of curvature which is not a necessary assumption.
- It is assumed that each curved waveguide is or can be represented by a single-boundary bend. This is a sensible assumption because the guides modes of the single-boundary bend exhibit smaller radiation losses than those of the corresponding double-boundary bend as explained in section § 5.2.3.

The mapping properties of conformal transformations are well known [64]. The analytic function that transforms the $(y+jz)$-plane into the $(u+jv)$-plane also transforms the two-dimensional scalar Helmholtz equation

$$\left(\frac{\partial^2}{\partial y^2} + \frac{\partial^2}{\partial z^2} + k_0^2 N_i^2\right)\begin{pmatrix} H_{x,i}(y,z) \\ E_{x,i}(y,z) \end{pmatrix} = 0, i = 1, 2, \tag{4.4.1}$$

for the HE- and the EH-modes, respectively, into

$$\left(\frac{\partial^2}{\partial u^2} + \frac{\partial^2}{\partial v^2} + k_0^2 N_i^2 \left|\frac{\partial(u+jv)}{\partial(y+jz)}\right|^{-2}\right)\begin{pmatrix} H_{x,i}(u,v) \\ E_{x,i}(u,v) \end{pmatrix} = 0, i = 1, 2. \tag{4.4.2}$$

We consider the following conformal mapping

$$(u+jv) = R_1 \sqrt{\frac{y_0-R_1}{y_0+R_1}} \ln\left\{\frac{\sqrt{y_0^2-R_1^2} + (y+jz)}{\sqrt{y_0^2-R_1^2} - (y+jz)}\right\},$$
(4.4.3)

and it can be verified that Eq. (4.4.3) maps the two circles in the $(y+jz)$-plane

$$y + jz = \pm\left\{y_0-R_1e^{-\pm j\theta}\right\}, -\pi < \theta < \pi,$$
(4.4.4)

where the $+$ and the $-$ sign are for the upper and the lower circle respectively, where the upper circle is traversed counterclockwise and the lower circle clockwise, onto the two straight lines in the $(u+jv)$-plane. We have

$$u = \pm u_0 = \pm R_1 \sqrt{\frac{y_0-R_1}{y_0+R_1}} \ln\left\{\frac{y_0}{R_1} + \sqrt{\left(\frac{y_0}{R_1}\right)^2 -1}\right\},$$
(4.4.5)

with

$$-\pi R_1 \sqrt{\frac{y_0-R_1}{y_0+R_1}} = -v_0 < v < v_0 = \pi R_1 \sqrt{\frac{y_0-R_1}{y_0+R_1}},$$
(4.4.6)

as indicated in Fig. 4.5. The two points that are given by $\theta = 0$, i.e. $y = \pm(y_0-R_1)$, are mapped onto the two points $u = \pm u_0$. A conformal mapping preserves the magnitude of the angle between two intersecting lines. This implies that the transforms of the lines $v = constant$ intersect the two circles defined by Eq. (4.4.4) perpendicularly. A consequence of this property is that the transformed boundary conditions are the continuity requirement of

$$H_{x,i}(u,v) \text{ and } N_i^{-2}\partial_u H_{x,i}(u,v),$$
(4.4.7)

for the HE-modes and the requirement of the continuity of

$$E_{x,i}(u,v) \text{ and } \partial_u E_{x,i}(u,v),$$
(4.4.8)

at the interfaces $u = \pm u_0$.

From Eq. (4.4.2), we can see that a transformed index of refraction in u,v-space may be introduced

$$N_i'(u,v) \stackrel{\text{def}}{=} N_i \left| \frac{\partial(u+jv)}{\partial(y+jz)} \right|^{-1} = N_i \frac{y_0/R_1+1}{\cosh\left(\dfrac{u}{R_1}\sqrt{\dfrac{y_0+R_1}{y_0-R_1}}\right)+\cos\left(\dfrac{v}{R_1}\sqrt{\dfrac{y_0+R_1}{y_0-R_1}}\right)}. \quad (4.4.9)$$

It is now seen that the normalization constant in the conformal mapping Eq. (4.4.3) has been chosen such as to yield

$$N_i'(\pm u_0,0) = N_i. \quad (4.4.10)$$

The original and the transformed refractive-index profile are shown in Fig. 4.6. The figure illustrates several properties of the transformed refractive-index profile, which will be discussed below.
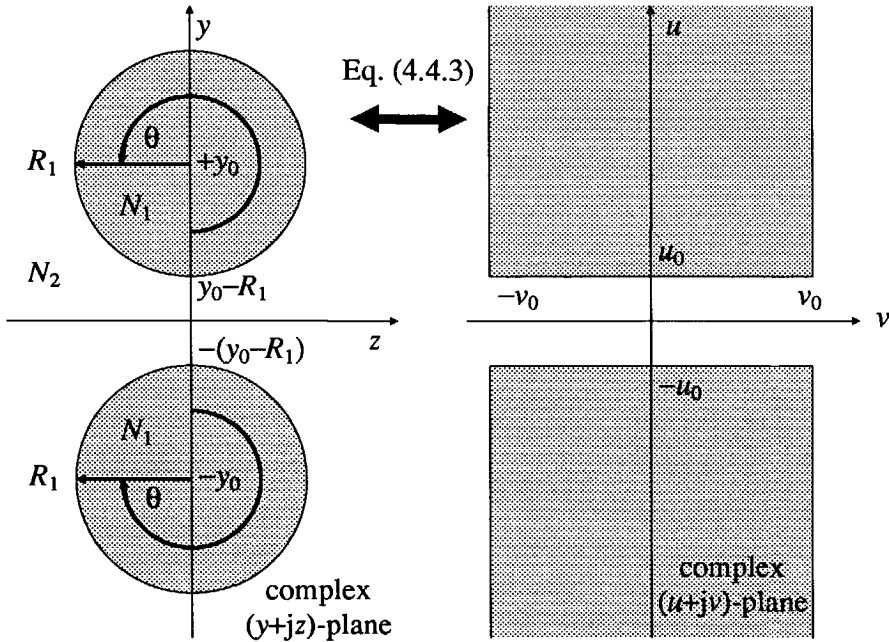

Fig. 4.5 *The conformal mapping Eq. (4.4.3) is used to transform two coupled bends into a straight waveguiding structure.*

For constant v, the transformed profile $N_i'(u,v) \to 0$, when $u \to \pm\infty$. The transformed profile may be thought of as 'guiding' in the sense that the profile becomes smaller for values of u far away from $u = \pm u_0$.

The transformed profile $N_i'(0,v) \to \infty$, when $\theta \to \pm\pi$. This transformed refractive-index profile at $u = 0$ eventually becomes larger than the value of the profile at $u = \pm u_0$. It seems inappropriate to discuss the radiation losses for the waveguiding structure, which is represented by the transformed refractive-index profile, because the transformed index of refraction approaches zero away from the central region. Instead, we might think of the bulge at $u = 0$ in the transformed refractive-index profile as representing a 'third waveguide', in addition to the two waveguides at $u = \pm u_0$. The power that is lost by the coupled bends can be thought of as being coupled to this 'third waveguide' in the middle.

The value of the transformed refractive-index profile increases for increasing v. This is due to the fact that the transform of line $v = constant$ connects the two points $y = \pm\sqrt{y_0^2 - R_1^2}$ and this line becomes larger for increasing v. In other words, the transformed waveguiding structure has a constant width of $2u_0$, but this constant width corresponds to an ever-larger distance in the y,z-space, which is compensated by the increase of the transformed refractive index. Alternatively, this effect may be compensated for by defining a local wave number
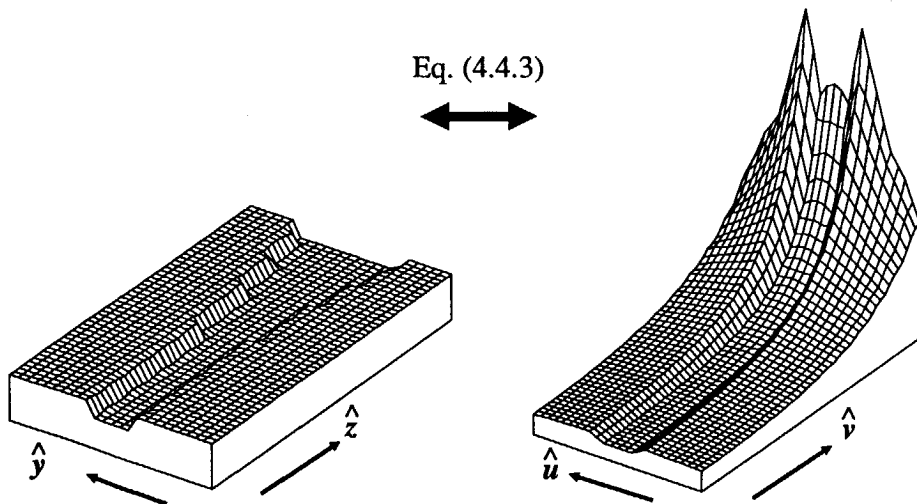
Eq. (4.4.3)

Fig. 4.6 *The index of refraction profile $N_i(y,z)$ (left) and the transformed index of refraction profile $N_i'(u,v)$ given by Eq. (4.4.9) (right). The parameters for this example have been chosen as $R_1 = 200\ \mu m$, $y_0 = 202\ \mu m$, $N_1 = 1.5$ and $N_2 = 1.0$. The two circles on the left are not smooth and the discontuity in the refractive-index profile is not sharp due to discretization.*

$$k(v) \stackrel{\text{def}}{=} k_0 \frac{N_i'(u_0,v)}{N_i'(u_0,0)} \quad \text{and} \quad N_i''(u,v) \stackrel{\text{def}}{=} N_i'(u,v) \frac{N_i'(u_0,0)}{N_i'(u_0,v)} . \tag{4.4.11}$$

or

$$k(v) = k_0 \frac{y_0/R_1+1}{y_0/R_1+\cos\left\{\dfrac{v}{R_1}\sqrt{\dfrac{y_0+R_1}{y_0-R_1}}\right\}} , \tag{4.4.12}$$

$$N_i''(u,v) = N_i \frac{\cosh\left\{\dfrac{u_0}{R_1}\sqrt{\dfrac{y_0+R_1}{y_0-R_1}}\right\}+\cos\left\{\dfrac{v}{R_1}\sqrt{\dfrac{y_0+R_1}{y_0-R_1}}\right\}}{\cosh\left\{\dfrac{u}{R_1}\sqrt{\dfrac{y_0+R_1}{y_0-R_1}}\right\}+\cos\left\{\dfrac{v}{R_1}\sqrt{\dfrac{y_0+R_1}{y_0-R_1}}\right\}} . \tag{4.4.13}$$

The transformed refractive-index profile $N_i''(u,v)$ is shown in Fig. 4.7.

Numerical calculations of the properties of the transformed index of refraction profile are not presented in the thesis. These calculations might, however, be pursued on the basis of a local coupled-mode theory or a mode-matching technique.
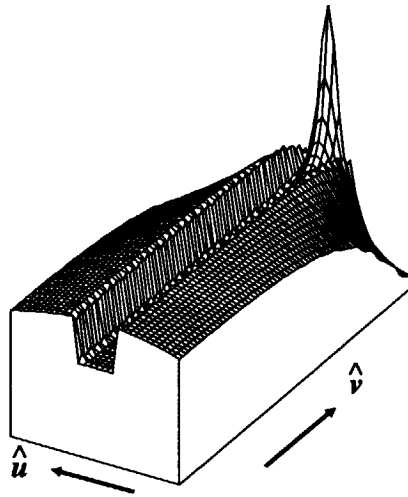

Fig. 4.7 *The transformed index of refraction $N_i''(u,v)$, Eq. (4.4.13) for the set of parameters given in the caption of Fig. 4.6.*

Chapter 5

Numerical results

This chapter contains numerical calculations that are based on the theory developed in the previous chapters. Comment is given with respect to the accuracy and numerical details of the Bessel function approach, the WKB approximation and the staircase / transfer-matrix method. Modeling has been done for the curved waveguide and the junction and the modeling results in design parameters.

Applications of curved waveguides will be discussed. The program that has been developed to simulate the transmission of waveguide tracks containing bends and straight waveguides has been applied to model multi-mode-interference couplers. A second example is an integrated planar Fabry-Pérot cavity where the cavity consists of a folded waveguide track and where gratings act as mirrors. Some work has been done to realize such a Fabry-Pérot cavity [120], but it will not be discussed in the thesis.

5.1 Assessment

5.1.1 Introduction

This section compares the numerical results of three techniques; the Bessel-function approach of section § 4.1.2, the WKB approximation of the transformed bend discussed in section § 4.1.4 and the staircase approximation plus transfer-matrix

algorithm for the transformed bend as discussed in section § 4.1.5. These techniques will be referred to simply as the "Bessel function approach", the "WKB approximation" and the "staircase approximation".

The main conclusion is that the three techniques are generally in good agreement with each other, which is illustrated in Fig. 5.1. The WKB approximation deviates significantly from the other two techniques for short radii of curvature, although the deviation starts at losses above 10 dB/90°. But even for larger radii of curvature, the agreement between the Bessel function approach and the staircase approximation is better than between the WKB method and the other two. The maximum that occurs in the results of the WKB-approximation is an artifact, because the assumption Eq. (4.1.50) on which the WKB approximation is based is no longer valid at those radii of curvature. This contradicts the suggestion presented in [41].

The values of Table 5.1 provide a better means of comparison than Fig. 5.1. The first two columns list values that were calculated according to the equations given by Heiblum and Harris [40][41]. The second column represents the full WKB approximation and the first column represents a perturbation solution to it. These
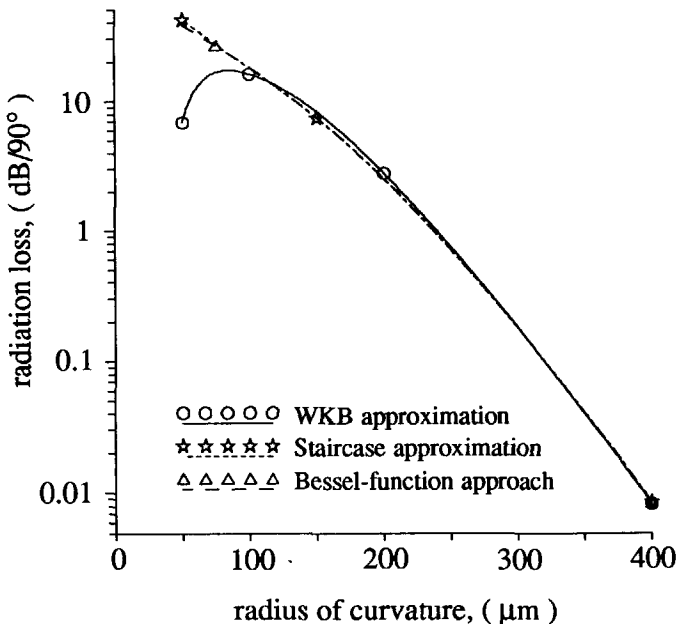

Fig. 5.1 Comparison between the three techniques discussed in the thesis to calculate radiation losses. The calculations were done for the waveguide parameters described in [119] or in section § 7.1. This graph applies to single-boundary bends.

Table 5.1 *Comparison between the numerical results of the three techniques discussed in the thesis and the equations given by Harris and Heiblum. Results are for the parameters of section § 7.1, i.e.* $\lambda_0 = 1.3\ \mu m$, $N_1 = 3.26106$, $N_2 = 3.22000$ *and* EH_{00}*-mode. The staircase approximation used a transformed profile with 500 partitions that range from 5 μm before the radius of curvature R_1 to 30 μm beyond it.*

R_1 (μm)	Heiblum and Harris Eq. (20) in [40]	Heiblum Eq. (16) in [41]	This thesis WKB approximation Eq. (4.1.36)	This thesis Staircase approximation § 4.1.5	This thesis Bessel functions Eq. (4.1.15)
	Effective refractive indices Re(γ)/($k_0 R_1$)				
400	3.2467743	3.2467743	3.2467743	3.2469051	3.2469052
300	3.2441917	3.2441919	3.2441918	3.2444898	3.2444899
200	3.2399003	3.2399379	3.2399098	3.2407551	3.2407555
150	3.2363855	3.2367812	3.2364948	3.2378996	3.2379020
100	3.2308681	3.2326711	3.2314391	3.2333018	3.2333062
75	3.2267697	3.2291088	3.2273953	3.2293963	3.2293403
50	3.2216610	3.2199147	3.2211261	3.2200978	3.2222268
	Radiation loss (dB/90°) $10\pi\mathrm{Im}(\gamma)/\ln(10)$				
400	0.01666	0.01666	0.00833	0.00863	0.00861
300	0.36671	0.36669	0.18335	0.18182	0.18205
200	5.66323	5.60041	2.82363	2.55695	2.56052
150	17.17608	15.78301	8.39062	7.54774	7.53796
100	34.99719	27.91642	16.33074	18.34612	18.46396
75	34.70509	30.18608	16.91188	27.58126	27.11798
50	12.83208	20.78638	6.99150	42.74666	38.31256

two columns are in agreement with each other especially for larger radii of curvature. The radiation losses in columns one and two, on the other hand, disagree by an approximate factor two from the columns three, four and five. The differences between the results of the three methods discussed in the thesis and the methods presented in [40][41] have already been discussed on page 70. The respective merits of the WKB approximation, the Bessel function approach and the staircase approximation are the topics of the following sections.

5.1.2 WKB approximation

The Wentzel-Kramers-Brillouin approximation of the transformed profile is the technique which is easiest to implement on a computer. The numerical implemen-

tation is fast and rigorous and it gives us the advantage that a mode number can be specified. It can be stated with confidence whether a solution exists and to which mode number that solution corresponds. The WKB approximation yields expressions for the field distributions but care must be taken near the "classical turning points", where a linear approximation must be used.

The WKB approximation is clearly the least accurate technique, especially for small values of the radius of curvature, where the approximation is no longer valid. The perturbation version, on the other hand, is accurate when dealing with very small loss figures, where $Im\gamma/Re\gamma$ becomes of the same order as the computer accuracy, i.e. 10^{-15} when using DOUBLE PRECISION data type in FORTRAN. Concerning the accuracy, it should be noted that the integrals derived in Appendix C have to be evaluated in the form of the series unless the arguments are not small compared to unity. The value of ξ, however, is in the range of $[0.015, 0.4]$ for all realistic applications. The ratio of the first non-vanishing term to the vanishing lowest-order term, thus, varies between 5×10^{-2} and 7.5×10^{-5}, which implies the loss of two to four significant figures if the series is not used.

5.1.3 The Bessel-function approach

The use of Bessel functions is straightforward since an exact analytical solution is known which is expressed in terms of these functions. The difficulties which are encountered are in the implementation of these functions for which asymptotic expansions can be used. *See also* Appendix A. The algorithm can be rigorously tested, on the other hand, throughout the complex γ-plane by evaluating Wronskians and recursion relations. The relative accuracy was found to be better than 10^{-12} for all orders and arguments of practical importance. The values of the radiation loss that have been calculated by means of this technique are the most trustworthy. The Bessel function approach becomes more accurate when the losses increase and / or the radii of curvature decrease, which is in contrast to the behavior shown when using the other two techniques.

The algorithm tends to become time consuming when many iterations are required to find the complex roots of the dispersion relation or when the number of interfaces grows. Such a situation can occur for a diffused LiNbO$_3$ waveguide if the diffused refractive index profile is discretized. The staircase approximation is by nature suited to such a refractive index profile. One evaluation of both Bessel functions plus their derivatives consumes approximately one second of CPU-time on a microVax II. The determination of the field profiles by means of the Bessel functions becomes, therefore, elaborate. The modal field distribution has usually

been approximated by an array of 600 or more values, the evaluation of which involves an equal number of evaluations of the Bessel functions.

5.1.4 Staircase approximation plus transfer-matrix algorithm

This method is, in my opinion, optimal insofar as numerical accuracy, required CPU-time, ease of implementation and applicability are concerned. The method can be applied to a wide variety of geometries, is reasonably fast and accurate as shown in Table 5.1.

It is nevertheless clear that deviations occur for parameters that result in very high losses, i.e. more than 10 dB/90°. This is partly caused by the discretization. The influence of the discretization is indicated in Table 5.2 which shows the influence of the total number of partitions (or subdomains) and the influence of the inner and outer boundary which correspond to $u = u_0$ and $u = u_M$ in Fig. 4.3. The initial size of the partitions was chosen equal to 1 µm, because the size of every region is a multiple of this value. This gives us the advantage that doubling the number of partitions halves the size of the partition and does not change the discretization. Table 5.2 lists the results of the calculations and these values show that a reasonably accurate value of the radiation loss is obtained for 160 partitions and that no significant improvement is found for more than 640 partitions. Most of the modeling of curved waveguides was performed using the staircase approximation and a total number of partitions of 500.

The inner boundary R_0, corresponding to u_0 in Fig. 4.3, has no influence whatsoever, provided it is located at a point where the fields are negligible. Since the field distribution decays exponentially at the inner side, a distance of several microns is adequate. The outer boundary R_2, corresponding to the point u_3 in Fig. 4.3, presents more difficulties. The field distribution is proportional to $H_\gamma^{(2)}(k_0 N_2 r)$, which oscillates and decreases very slowly, because the Bessel functions behave as $r^{-1/2}$, when $r \to \infty$. This explains, firstly, why $R_2 - R_1 >> R_1 - R_0$ and, secondly, why there is so little improvement when the value of the outer boundary is increased. Table 5.2 shows the radiation loss for the same single-boundary bend, when the position of the outer boundary is located further away from the bend without changing the size of the partition. Increasing the number of partitions might eventually lead to inaccuracy as well, because the multiplication of a large number of matrices results in numerical inaccuracy as the coefficients grow in size.

Table 5.2 *The influence of the discretization in the staircase approximation. The results do not change significantly for more than 640 partitions. The inner boundary R_0 has no influence at all, while the outer boundary does matter. There is no improvement for boundaries beyond 225 μm. The Bessel function approach gives $N_{eff} = 3.2407555$ and $\alpha = 2.5605223$ dB/90°.*

R_0 (μm)	R_1 (μm)	R_2 (μm)	Total number of partitions	$N_{eff} = \dfrac{\text{Re}\gamma}{k_0 R_1}$	$\alpha = \dfrac{10\pi\text{Im}\gamma}{\ln 10}$
Doubling the number of partitions					
195.0	200.0	235.0	40	3.2405833	2.0149450
195.0	200.0	235.0	80	3.2407416	2.2742282
195.0	200.0	235.0	160	3.2407497	2.5585156
195.0	200.0	235.0	320	3.2407541	2.5633978
195.0	200.0	235.0	640	3.2407551	2.5637523
195.0	200.0	235.0	1280	3.2407554	2.5636696
195.0	200.0	235.0	2560	3.2407554	2.5635717
195.0	200.0	235.0	5120	3.2407554	2.5635091
Varying the inner boundary R_0 of the transformed index of refraction.					
193.0	200.0	235.0	5376	3.2407554	2.5635091
Varying the outer boundary R_2 of the transformed index of refraction.					
195.0	200.0	205.0	1280	3.2407511	2.5372589
195.0	200.0	210.0	1920	3.2407541	2.5566201
195.0	200.0	215.0	2560	3.2407547	2.5634718
195.0	200.0	220.0	3200	3.2407557	2.5545878
195.0	200.0	225.0	3840	3.2407552	2.5640735
195.0	200.0	230.0	4480	3.2407557	2.5583989
195.0	200.0	240.0	5760	3.2407553	2.5615035
195.0	200.0	245.0	6400	3.2407555	2.5627988
195.0	200.0	250.0	7040	3.2407554	2.5588452
195.0	200.0	255.0	7680	3.2407554	2.5593863

5.1.5 The COST216 Working Group 1

It has proved to be quite interesting that the COST 216 Working Group 1[§] is currently performing a study on the modeling of optical waveguides. In it first session, the working group compared different modeling techniques for straight waveguides and couplers [29]. The current session is comparing the modeling techniques for curved waveguides and couplers including bends. The work on waveguide modeling by Baken and van der Tol of the PTT Research Neher Laboratories, Leidschendam, has been combined with our work on bends as a joint contribution to the COST 216 working group. The modeling techniques for the bends which are compared include, apart from our contribution, a number of contributions that use the method of effective dielectric constant in combination with the two-dimensional beam-propagating method, and the recently published method of lines by Gu *et al.* [36]. The S-bend losses predicted by the BPM method are in good agreement with each other, but differ as a whole from our results and the results of Gu[¶].

It is my opinion that the different modeling techniques give similar values for the radiation loss of a curved slab waveguide. The observed differences between the values of the total loss for S-bends are instead due to the way that the two-dimensional cross-section of the waveguide has been handled, such as the application of the method of effective dielectric constant (effective-index method). The differences in the predicted losses might also be caused by the way that the transition losses at the junction have been calculated and by the fact whether or not the multimode interference effects for multimode waveguides have been included in the analysis. From the comparison and the evident differences in predictions, the conclusion may be drawn that although the experiments described in the thesis show that the accuracy of the modeling is adequate to design very low-loss curved waveguides, it is difficult to obtain a very accurate agreement between the observed and the predicted losses for S-bends.

[§] COST is acronym for 'coopération Européenne dans le domaine de la science et de la technologie' and is an EEC initiative. The present study on curved waveguides and couplers of COST216 Working Group 1 includes contributions from the University of Gent (Belgium), the Heinrich Hertz Institut Berlin (F.R.G.), University of Twente (Netherlands), Technical Research Center of Finland Espoo (Finland), the Deutsche Bundespost TELEKOM Darmstadt (F.R.G.), the Swiss Federal Institute of Technology Zürich (Switzerland), Plessey Research Caswell Limited (U.K.), GEC-Marconi Research Centre Chelmsford (U.K), University of Padova (Italy), CSELT Torino (Italy) and the joint contribution from the PTT Research Neher Laboratories Leidschendam and the Delft University of Technology (the Netherlands).

[¶] Minutes of the 7th COST-216 Working Group 1 which met on November 9th, 1989, Berlin (F.R.G.). A paper with the results of the comparison is to be submitted to ECOC '90.

5.2 Optimizing bends

The study of the properties of curved waveguides and the minimization of the losses are closely linked. The numerical models will now be used to give general graphs and to analyze in more detail how the losses depend on waveguide parameters. The conclusions of the modeling automatically yield the design rules for low-loss bends.

5.2.1 Dimensionless formulation

The general two-boundary bend is characterized by a set of six variables, but the width of a curved waveguide should always be large enough to make the bend effectively operate as a single-boundary bend as explained in section § 5.2.3. The discussion will, therefore, be confined to single-boundary bends and values will be given for the minimal width for which the two-boundary bend operates as a single-boundary bend[§]. This has the additional advantage of reducing the number of parameters by two. The single-boundary slab bend is characterized by a set of four variables $\{N_1 ; N_2 ; \lambda_0 ; R_1\}$. Closer inspection of the Maxwell equations shows that a consistent dimensionless formulation can be given in terms of two dimensionless parameters $\{N_2/N_1 ; k_0 R_1 N_1\}$. We choose the equivalent parameters $1-N_2^2/N_1^2$ and $k_0 R_1 N_1$ to describe the single-boundary bend, because the difference of the refractive indices proves to be a more critical parameter than just their ratio.

5.2.2 Influence of the lateral refractive-index contrast

The largest influence on the radiation loss is due to the refractive-index contrast and the radius of curvature. Decreasing the radius of curvature and / or the contrast in the refractive index leads to an exponential increase in the radiation loss as shown in Fig. 5.2. The values of the radiation loss shown in the graph have been calculated by means of the Bessel-function approach for large radiation losses and by means of the WKB approximation for losses smaller than 10^{-5} dB/90°.

The apparent simplicity of Fig. 5.2 proves to have some interesting consequences. The "wall" is diagonal across the radius-contrast plane which suggests that the contours of constant radiation loss form straight lines in the radius-contrast plane. The accompanying contour plot Fig. 5.3 shows, indeed, a number of parallel straight lines for constant radiation loss. The contour plot is given for EH-polarization only, because the results for the HE-polarization are similar. If the radiation

---

§ The reader should be alert not to confuse the parameters of the two-boundary bend, radius R_2 and width R_2-R_1, and the parameter of the single-boundary bend, radius R_1.
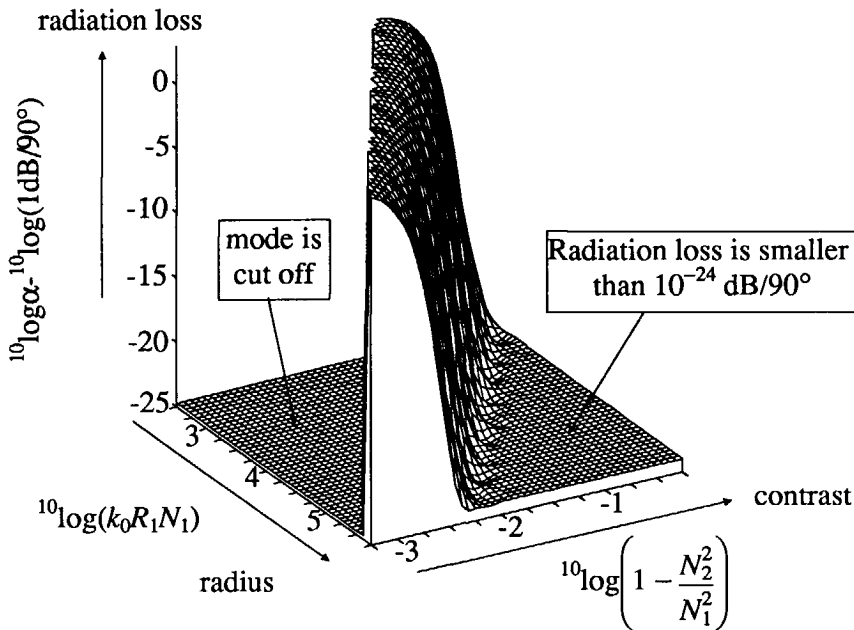
Fig. 5.2 *Radiation loss as a function of the normalized radius of curvature and the refractive-index contrast. The fundamental mode is cut off to the left of the 'wall' and the radiation losses are smaller than 10^{-24} dB/90° on the right-hand side of the 'wall'. The radiation loss increases almost exponentially for decreasing radius of curvature and refractive-index contrast.*

losses depend significantly on the polarization as demonstrated in section § 7.1, then these differences must be ascribed to differences in the effective refractive indices. The straightness of the contour lines in Fig. 5.3 can be used to obtain a useful interpolation. The contour line, which is labeled -3, corresponds to a radiation loss $\alpha = 10^{-3}$ dB/90° and can be approximated linearly by

$$\log\left\{1 - \frac{N_2^2}{N_1^2}\right\} = -0.65 \log(k_0 R_1 N_1) + 0.88 , \qquad (5.2.1)$$

or

$$k_0 R_1 N_1 \left\{1 - \frac{N_2^2}{N_1^2}\right\}^{1.54} = 22.7 = C(\alpha) . \qquad (5.2.2)$$
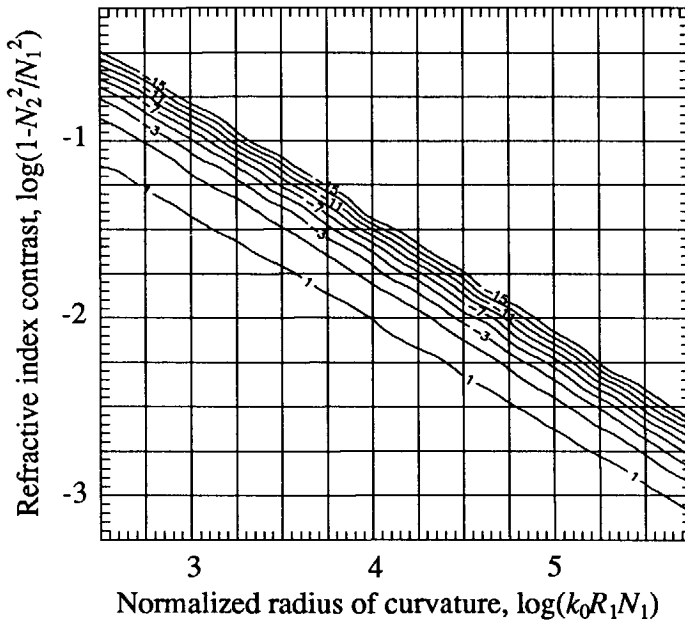
Fig. 5.3 Contour plot of the radiation loss in relation to the refractive-index contrast and the normalized radius of curvature. The losses have been computed for the EH$_{00}$-mode of the single-boundary bend. The curve labeled -3 corresponds to a radiation loss of 10^{-3} dB/90°. The losses for the HE$_{00}$-mode are very similar.

Since all contour lines seem to be parallel, they are described by equations similar to Eq. (5.2.2). All contour lines can be described by one equation and a parameter $C(\alpha)$ which depends on the radiation loss only. The dependence of $C(\alpha)$ on α has been evaluated for the data shown in Fig. 5.1 and the result is shown in Fig. 5.4. This graph too can be approximated by a straight line

$$C(\alpha) = 13.7 - 3.72 \log\left(\frac{\alpha}{1\mathrm{dB}/90°}\right), \tag{5.2.3}$$

for losses below $\alpha = 10^{-2}$ dB/90°. Equation (5.2.2) shows that $C(\alpha)$ is proportional to R_1 and Eq. (5.2.3) is, therefore, the well-known exponential relation $\alpha = A \exp(-BR_1)$ between the radius of curvature and the radiation loss. The straight interpolation is shown as the dashed line in Fig. 5.4 and it deviates from the
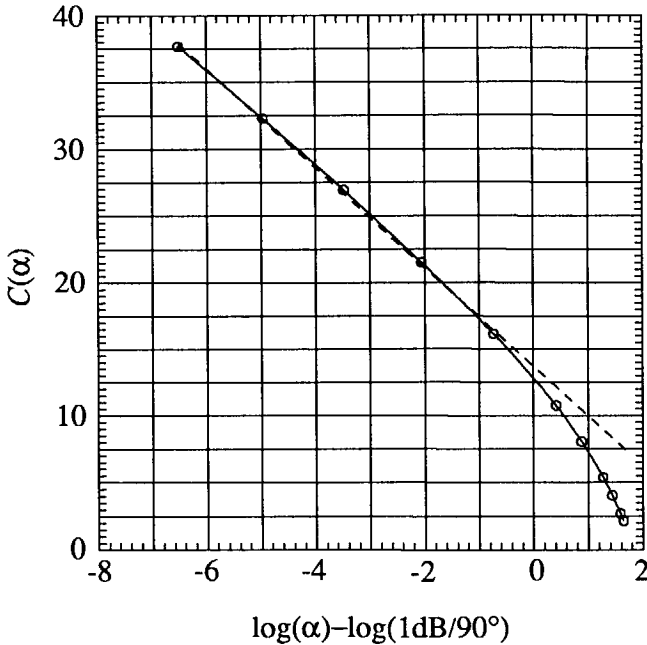
Fig. 5.4 *Curve relating the constant $C(\alpha)$ in Eq. (5.2.2) to the radiation loss. The dashed line is the straight interpolation Eq. (5.2.3) and is valid for small losses only. A value -4, for example, on the abscissa corresponds to a radiation loss $\alpha = 10^{-4}$ dB/90°.*

calculated curve for $\alpha > 0.1$ dB/90°. Kendall, Stern and Robson [55] have shown that a more accurate dependence is given by $\alpha = AR_1^{-3/2}\exp(-BR_1)$.

Optimization

Appendix E provides an example how to use the graphs and equations presented in this section in order to choose an optimized radius of curvature for a given refractive-index contrast.

The optimization strategy that presents the greatest conflict with other require-ments is the maximization of the lateral refractive index contrast. The other requirements are usually twofold; single-mode operation and low scattering losses both require small refractive-index contrasts. The ideal solution is to combine the large and the small refractive-index contrast.

One solution is the introduction of a new type of waveguide that combines a low and a high ridge and which we, therefore, have named the 'double-ridge wave-guide'. The idea behind the 'double-ridge' waveguide is that the radiation losses

are determined by the refractive-index contrast that corresponds to the total height of both ridges and that the scattering losses, on the other hand, are mainly determined by the scattering at the inner lower ridge. This waveguide, therefore, provides a compromise to the conflicting requirements of both low scattering and low radiation losses. The 'double-ridge' waveguide is the subject of section § 6.4.

A second solution is provided by the 'self-aligned doubly etched bends', where a self-aligned photolithographic step is used to etch a higher ridge at the site of the bend. This technique combines single-mode waveguides with low-loss bends on a single wafer. A price is paid in the form of additional transition losses at the junction of the low- and high-contrast waveguides. The 'self-aligned doubly etched' bends are discussed in section § 6.5.

5.2.3 Width of the curved waveguide[§]

All graphs of the radiation loss versus the width of the bend are similar in character. A representative example is given in Fig. 7.7 on page 189. The radiation losses increase exponentially without limit below a certain value of the width. Above this threshold value the radiation losses are completely independent of the width. This formulation is not entirely correct, because the width is not the parameter that is being varied, but the inner radius of curvature, while the outer radius is fixed. A better way of saying this is to state that the field distribution becomes independent of the inner boundary. The mode is guided by the outer interface alone and is not influenced by the presence of the inner interface. Such a mode bounded by one curved interface is called a whispering-gallery mode[¶] after Lord Rayleigh [95][96]. The application of these modes in integrated optics has been discussed in two papers by Sheem and Whinnery [102][103]. In the first of these two papers Sheem and Whinnery use ray optics to explain the phenomenon of the whispering-gallery modes. According to this picture, rays are reflected successively by the outer interface without encountering the inner interface. The point on the ray path nearest to the origin equals the caustic corresponding to u_t in Fig. 4.2. A mode is effectively a whispering-gallery mode if the inner interface is far away from the caustic.

Equation (4.1.47) has been derived to estimate the minimum width that a two-boundary bend should have in order to be in the whispering-gallery mode

---

[§] This section does not discuss the properties of double-boundary bends in general, which would be in contradiction to the statements made in the introduction § 5.2.1.

[¶] The phrase whispering-gallery mode (WGM) was originally applied by Lord Rayleigh to acoustic waves guided by a single curved surface, of which he found a good example in St. Paul's cathedral.
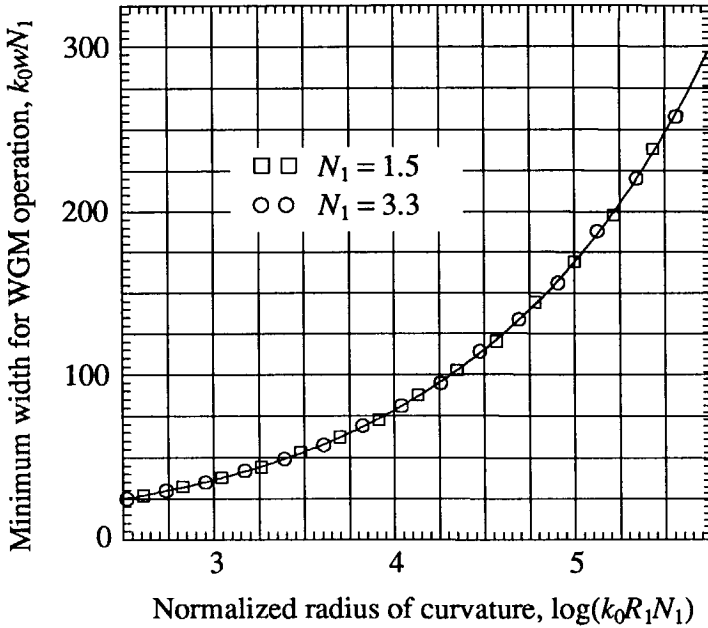
Fig. 5.5 *Minimum width w that the corresponding double-boundary curved waveguide should have in order to be in the WGM regime and thus to be effectively a single-boundary bend. The markers refer to calculations for different N_1 and show that the curve is independent of N_1.*

regime and thus to be effectively a single-boundary bend. This equation has been evaluated for the same range of normalized radii of curvature as in Fig. 5.3 and the results are shown in Fig. 5.5. The refractive index contrast at each normalized radius is chosen such that it yields a radiation loss of 0.001 dB/90°, although the refractive index contrast is not critical.

A useful interpolating formula can be found here too. The curve in Fig. 5.5 is accurately described by

$$k_0 w N_1 \geq 3.66 \sqrt[3]{k_0 R_1 N_1} \,. \tag{5.2.4}$$

This inequality has a general applicability. It is valid for all radii of curvature, refractive indices and wavelengths and, although calculated for refractive-index contrasts that lead to a radiation loss of 0.001 dB/90°, it is quite insensitive to the refractive-index contrast.

Optimization

Optimization with respect to the width of the curved waveguide is simple. *Make it as wide as possible*. Make it at least wider than the minimum required to reach the regime of the whispering-gallery mode. There is no penalty whatsoever in following this strategy. Even if the straight waveguides are monomode, no harm is done by allowing the bends to be multimode. The higher-order modes show increasing radiation losses and the influence of these higher-order modes is practically eliminated at the next junction.

See Appendix E for an example of the optimization of the width of a curved waveguide.

5.2.4 Transition losses at the junction

The theory of junctions has been discussed in section § 4.2, where it has been shown that the transmission matrix, which determines the excitation coefficients of the modes after a junction, is determined mainly by the overlap integral. Good coupling requires, therefore, that the modal field distribution in the straight waveguide and in the bend resemble each other as much as possible in order to maximize this overlap integral. The field profile in a bend changes considerably when the radius of curvature decreases, which is illustrated in Fig. 5.6. The field distribution shifts outward and "sticks" to the outer interface. This shift can be considerable even when the radiation losses are small such as for curves 2 and 3. The overlap integral decreases because of this shift, which can be compensated for by the application of a complementary shift of the curved waveguide with respect to the straight waveguide as in Figs. 2.2, 2.5, 7.4 and photograph 6.3. The concept of the offset was introduced in several papers and a patent by Neumann [80][82].

Apart from the outward shift of the maximum, the form of the field profile also changes. It becomes narrower and more asymmetric when the radius decreases as shown in Fig. 5.6. The width of the field distribution of a single-boundary bend is determined by the radius of curvature and the refractive-index contrast. The width of the field profile in a straight waveguide, on the other hand, is to a large extent determined by the width of the waveguide. A second reason why the overlap integral is not optimal is the difference in shapes of the modal field distributions. The fact that the shape of the field distribution in the straight waveguide is influenced by the width of the waveguide can be used to our advantage. The overlap integral can be further optimized by varying the width of the straight waveguide. Typical graphs of coupling loss versus lateral offset and width of the straight waveguide are Figs. 6.2 and 7.8, which are quite similar. The coupling
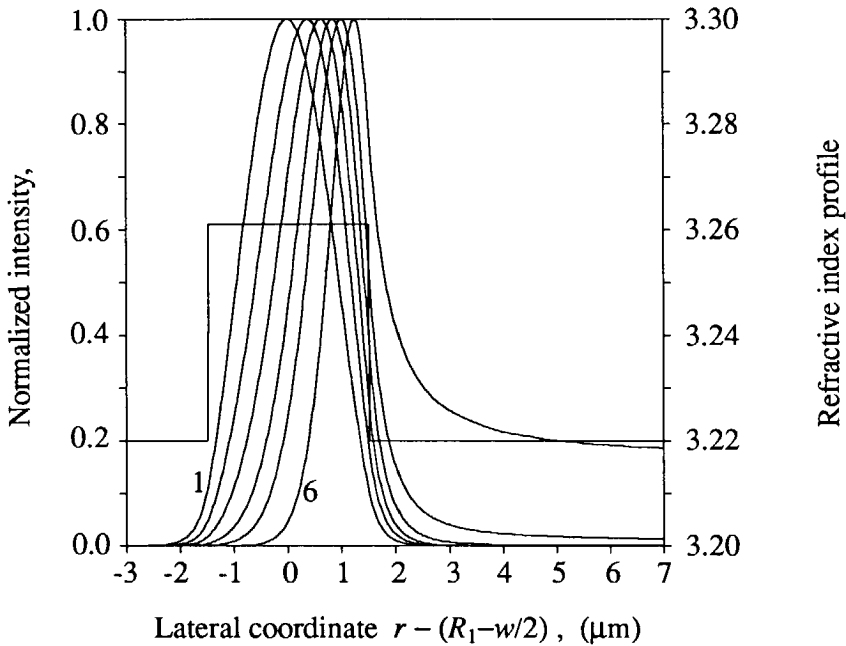
Fig. 5.6 The intensity $e_x(r)e_x^*(r)$ of the EH$_{00}$-mode versus coordinate r relative to the middle of the two-boundary bend. The width is constant $w = 3$ μm. The wavelength is $\lambda_0 = 1.3$ μm. The field profile shifts outward and becomes narrower for smaller radii of curvature. The legend to the graph is given below.

Curve	R_1 μm	α dB/90°	Center μm	FWHM μm
1	∞	0.00	0.00	1.90
2	1000	0.00	0.38	1.78
3	500	0.01	0.63	1.60
4	300	0.19	0.85	1.48
5	200	2.56	1.00	1.20
6	100	18.35	1.25	1.13

loss in dB is a parabolic function of the offset. The width of the straight waveguide influences the height of the minimum and the width of the parabola, but not the offset at which the minimum is reached. The influence of the width of the straight waveguide on the coupling loss is considerable. The coupling loss decreases by approximately 1 dB when going from a width of 4 μm to 2 μm in the example shown in Fig. 6.2.
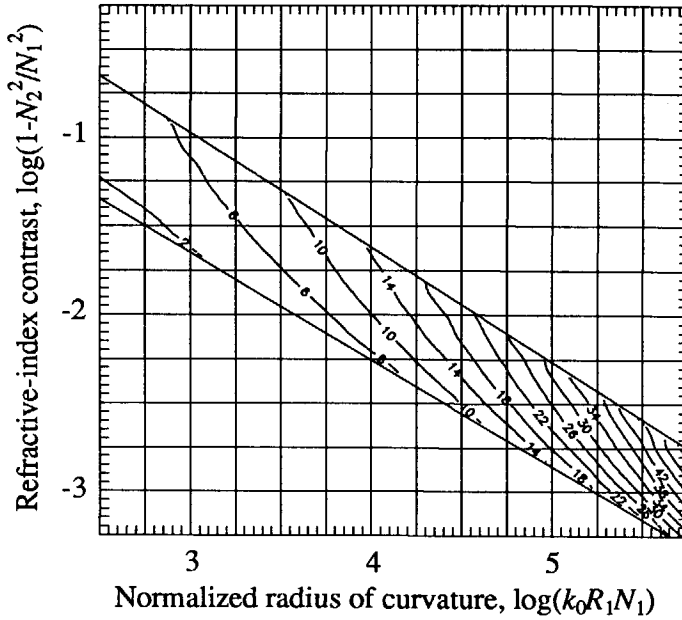
Fig. 5.7 Contour lines of the normalized distance $k_0\Delta rN_1$ between the radius R_1 and the maximum of the field distribution, which is based on Eq. (4.1.49). An estimate for the optimum offset between the straight and curved waveguide follows as $w/2 - \Delta r$. The values are for the EH_{00} mode of the single-boundary bend. The values for the HE_{00}-mode are very similar.

Lateral offsets at the junction have been applied by Döldissen *et al.* [31] to LiNbO$_3$ curved waveguides, but apart from their paper it seems that the application of offsets is not widespread. Equation (4.1.49) has been derived from the WKB approximation and gives the distance Δr between the maximum of the field distribution for the single-boundary bend and the guiding outer interface with radius R_1. An approximation to the optimum lateral offset is found from the distance Δr by means of the relation

$$offset = \frac{w}{2} - \Delta r.$$

(5.2.5)

for a curved waveguide with width w. The distance Δr has been evaluated for a wide range of parameters and the results are given in Fig. 5.7. However, all lateral

offsets that have been used in the thesis have been found by maximizing the overlap integral with respect to offset and straight-waveguide width.

There is some confusion with respect to the definition of *offset*. Curved waveguides are of the two-boundary type when they are actually fabricated and from the point of view of the mask design, *offset* is the distance between the center of the straight waveguide and the center of the bend. However, the single-boundary bend has no width and the practical definition of *offset* is useless. Even in the case of a two-boundary bend that is in the regime of the whispering-gallery mode, the meaning of *offset* is unclear, since it depends on an arbitrary width. The parameter that emerges from the analysis of the curved waveguide is the previously defined distance Δr between the maximum of the field distribution and the radius R_1 of the single-boundary bend. The relation between Δr and *offset* is given by Eq. (5.2.5).

Optimization

The use of an optimum lateral offset between the curved and the straight waveguide to match the positions of both field distributions is strongly recommended. There are no disadvantages to the application of such an offset. Optimizing the width of the straight waveguide is a very useful second strategy, but this can be in conflict with other requirements. However, all S-bends described in the thesis appeared to have optimized widths around the convenient values of 2 to 3 μm which implies that the optimization of the width of the straight waveguide with respect to the transition losses at the junction does not have to be in conflict with other requirements.

An example of the optimization of the junction is given in Appendix E.

5.3 Using bends

5.3.1 The multi-mode-interference coupler

Curved waveguides can be used in the input and output sections of directional couplers and the computer program developed to analyze multimode-waveguide tracks can also be used to analyze such couplers. Although the tools can be used to study the properties of both the directional (or synchronous) and the multi-mode-interference coupler, the discussion here is confined to the multi-mode-interference coupler, because the experimental program at the Delft University of Technology includes the fabrication of multi-mode-interference couplers.

The couplers of this type are known in the literature as two-mode-interference couplers (TMI) or as the optically active bifurcation coupler (BOA) [87]. The analysis presented in this section, however, considers couplers that guide an unlimited number of modes and it seems, therefore, more appropriate to talk about the multi-mode-interference coupler (MMI).

Principle

The structure of the multi-mode interference coupler is depicted in Fig. 5.8. Two input waveguides combine in one broad multimode waveguide. A fundamental mode arriving in one of the input waveguides equally excites the two lowest-order modes in the broad section. Since these two modes have different propagation constants their phase difference will change with propagation distance. If the phase difference has changed π during the total length of the broad section

$$L_{MMI} = L_{\pi} \overset{\text{def}}{=} \frac{\pi}{\beta_{00} - \beta_{01}} , \tag{5.3.1}$$

then the opposite output waveguide will be excited. The coupler is then in the cross state. The coupler is in the bar state when the phase difference is 2π at the coupler length $L_{MMI} = 2L_{\pi}$, and the output on the same side as the input is excited. The beat of the two modes leads to an amount of power in each output port that is
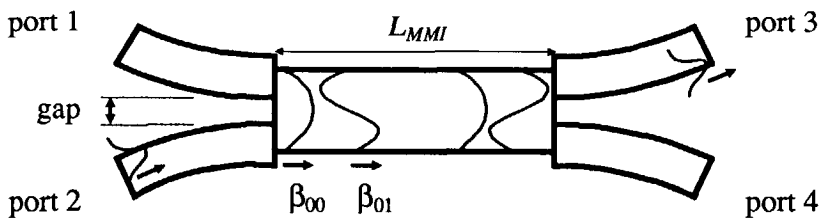

Fig. 5.8 *Schematic picture of the multi-mode interference coupler with curved input and output sections. The field distributions of the two lowest-order modes have been inserted in the figure. The ports 1 and 4 and the ports 2 and 3 are connected in the cross-state $L_{MMI} = (2m+1)L_{\pi}$. The ports 1 and 3 and the ports 2 and 4 are connected in the bar-state $L_{MMI} = 2mL_{\pi}$ ($m = 0, 1, \dots$). At lengths $L_{MMI} = (m+\frac{1}{2})L_{\pi}$ the coupler functions as a 3-dB splitter, where the power from port 1, for example, is divided equally between port 3 and port 4.*

proportional to $\sin^2(\pi/2 L_{MMI}/L_\pi)$ and to $\cos^2(\pi/2 L_{MMI}/L_\pi)$ respectively [97][24]. The maximum transmission or minimum loss from an input port to an output port equals the insertion loss. The minimum transmission or the maximum loss represents the cross-talk.

MMI couplers have been applied as wavelength demultiplexers [21][24][97] [98] and polarization splitters [84]. They offer compactness and improved reproducibility, because the difference $(\beta_{00}-\beta_{01})$ is much larger for MMI couplers than for directional couplers, and because multi-mode interference couplers lack the narrow gap between the coupled straight waveguides that is characteristic of directional couplers and which is subject to tight fabrication tolerances. The input and output sections usually consist of two straight waveguides with an angle of 1° - 4° between them. The use of curved input and output waveguides offers us the advantage of a faster separation between the access ports than can be achieved with tilted straight waveguides, and the lateral offset required to provide optimal coupling leads to a natural separation between the two waveguides at the beginning and the end of the MMI section as shown in Fig. 5.8.

Modeling

The multi-mode-interference coupler with curved input and output sections is made suitable to modeling by splitting it in two and ignoring one input and one output section as shown in Fig. 5.9. The MMI coupler reduces to a normal waveguide track and can be modeled with the tools developed in chapter 4 and especially as explained in section § 4.3. The omission of two sections from the MMI coupler is allowed if the extra coupling between the two bends is negligible compared to the total phase change in the MMI section. The coupling between the two bends leads to different coupling efficiencies at the beginning and the end of the MMI section and to an additional phase contribution. We make the assumption that the extra coupling between the two bends can be neglected if the radiation loss is small, because this implies that the modes are well confined by the curved waveguide. The coupling between oppositely curved bends was investigated in section § 4.4.

Two dielectric Al_2O_3/SiO_2 ridge waveguides have been modeled, one with a small ridge height of $H = 20$ nm and the other with a large ridge height of $H = 100$ nm. The cross-section of the ridge waveguides is given in Fig. 5.9 and the waveguides operate at a wavelength of 632.8 nm. The insertion loss and the cross-talk of the waveguide track have been calculated, where the width of the MMI section w_{MMI}, the size of the gap between the bends and the length of the MMI coupler L_{MMI} have been varied. The results of the modeling are summarized in Table 5.3 and this table shows some interesting things. The values marked by thick lines in
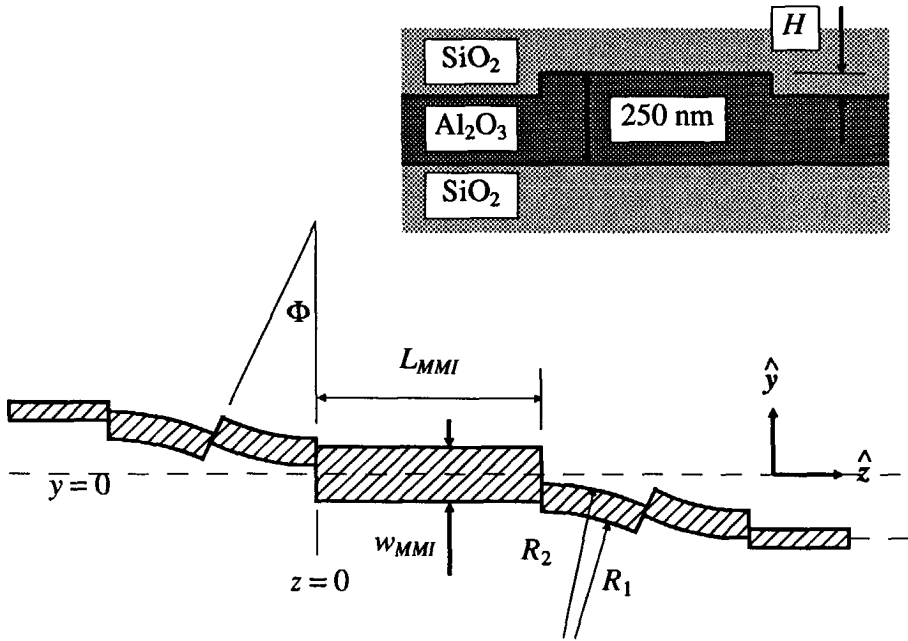
Fig. 5.9 *Cross-section and layout of waveguide used to model the MMI coupler. By omitting one input and one output section, the coupler reduces to a waveguide configuration that can be modeled by means of the tools developed in the previous chapters. Omitting two access waveguides is justified when the additional coupling between the two bends can be neglected.*

Table 5.3 correspond to multi-mode-interference couplers that show simultaneous-ly

- an insertion loss lower than 1 dB,
- a cross-talk of approximately 25 dB or better,
- a gap between the two access bends of 1.2 - 1.6 μm, which is wide enough to be fabricated reproducibly by standard lithography and
- short coupler lengths, i.e. shorter than 1 mm which includes the input and the output sections.

It is interesting to note that all waveguides are multimode. However, the MMI couplers that are reported in the literature always have bimodal MMI sections and monomode access waveguides. The presented calculations even predict that the MMI couplers function better when they become broader. The 7 μm wide MMI section, for example, guides four lateral modes that have all been included in the analysis. The squares of the overlap integrals from the fundamental mode of the

Table 5.3 *Insertion loss and cross-talk for the MMI coupler of Fig. 5.9. The ridge height H is 20 nm. The straight access ports are 2 μm wide and guide two modes $N_{HE00} = 1.57036$ and $N_{HE01} = 1.56474$. The curved waveguides are 3 μm wide, have $R_2 = 1300$ μm and also guide two modes with, $N_{HE00} = Re(\gamma)/(k_0 R_2) = 1.56994$, $\alpha_{HE00} = 0.079$ dB/90° and $N_{HE01} = 1.56534$, $\alpha_{HE01} = 66.6$ dB/90°. The second-order mode in the bend is thus of little influence. The curved waveguides subtend an angle $\Phi = 5°$ and accomplish a separation between the access ports of 11.1 μm within a distance of 226.4 μm. The total length of the coupler is twice this value plus L_{MMI}. The lateral offset is 0.7 μm at the bend-bend junction and 0.4 μm at the straight-to-curved waveguide junction. The 4- and 5-μm wide MMI-sections guide three modes, the other two MMI-sections four modes.*

gap μm	$w_{MMI} = 4$ μm		$w_{MMI} = 5$ μm		$w_{MMI} = 6$ μm		$w_{MMI} = 7$ μm	
	insertion loss, dB	cross-talk, dB	insertion loss, dB	cross-talk, dB	insertion loss, dB	cross-talk, dB	insertion loss, dB	cross-talk, dB
0.8	0.88	17.63	0.63	17.80	0.60	14.08		
1.0	1.05	21.66	0.71	22.96	0.64	17.51	0.64	14.06
1.2	1.25	24.63	0.81	24.62			0.76	17.08
1.4					0.77	26.89	0.79	21.74
1.6							0.80	28.73
1.8					0.96	18.20	0.83	25.46
2.0							0.90	20.09
L_π μm	97		133		177		227	
$2L_\pi$ μm		193		266		353		454

bend to the four modes of the 7-μm wide MMI section plus 1.6 μm gap are 0.4986, 0.4175, 0.751 and 0.0005 respectively, amounting to a total of 0.9962. The completeness relation Eq. (4.2.48) shows that the difference 0.0038 between the sum 0.9962 and unity is due to the contribution of the continuous modes[§].

Single-mode operation is an unnecessary requirement for the operation of MMI couplers and it seems that they function even better with multimode waveguides. A second simulation has, therefore, been done for a MMI coupler with a ridge height of $H = 100$ nm. The large ridge height leads to a multimode waveguide, but it also permits the use of short radii of curvature. A width of 3 μm and a radius of curvature of $R_2 = 150$ μm lead to a radiation loss of 6.7×10^{-6}, 9.3×10^{-3} and

---

[§] The values shown in Table 5.3 have been computed by F.B. Veerman, Delft University of Technology.

2.3 dB/90° for the HE_{00}- to HE_{02}-mode respectively. The fundamental mode is well confined and this reduces excessive coupling in the curved input and output sections. The straight access waveguides are 2 μm wide and guide three modes. An optimized offset of 0.7 μm leads to a transition loss of -0.06 dB at the junction of the straight and the curved waveguide for the fundamental modes. A transition loss of -0.16 dB occurs at the junction of the two bends when an offset of 1.5 μm is applied. The small radius of curvature leads to a fast separation of the output waveguides. The application of an arbitrarily chosen section angle $\Phi = 45°$ leads to a separation of 176.3 μm between the two output waveguides within a distance of 211.1 μm. The insertion loss and the cross-talk for several configurations are listed in Table 5.4.

The conclusions are similar to the conclusions for the MMI coupler with $H = 20$ nm. The cross-talk is below -20 dB for MMI couplers with a width of 7 μm or larger. The insertion losses are better than 0.7 dB which includes the radiation losses of the four curved waveguide sections with $R_2 = 150$ μm and a section angle of 45° and all six junctions. Table 5.4 shows that the performance of multimode MMI couplers becomes better for wider MMI sections. The only disadvantage of ever wider MMI sections seems to be the increasing length of the coupler. The length L_π increases because β_{00} and β_{01} approach each other as they both come nearer to the effective index of the film for wider waveguides.

The power in both output ports is shown in Fig. 5.10 as a function of the coupler length for the 9 μm wide MMI coupler and a gap of 1.6 μm. The coupler is in the cross state at $L_{MMI} = (2m+1)L_\pi$ and in the bar state for $L_{MMI} = 2mL_\pi$. The coupler

Table 5.4 Calculated insertion losses and cross-talk for the MMI-coupler with a ridge height $H = 100$ nm and access bends with $R_2 = 150$ μm. Indicated are $L_\pi = \pi(\beta_{00}-\beta_{01})^{-1}$ and the lengths L_{MMI} for which the minimum and maximum transmission loss have been computed.

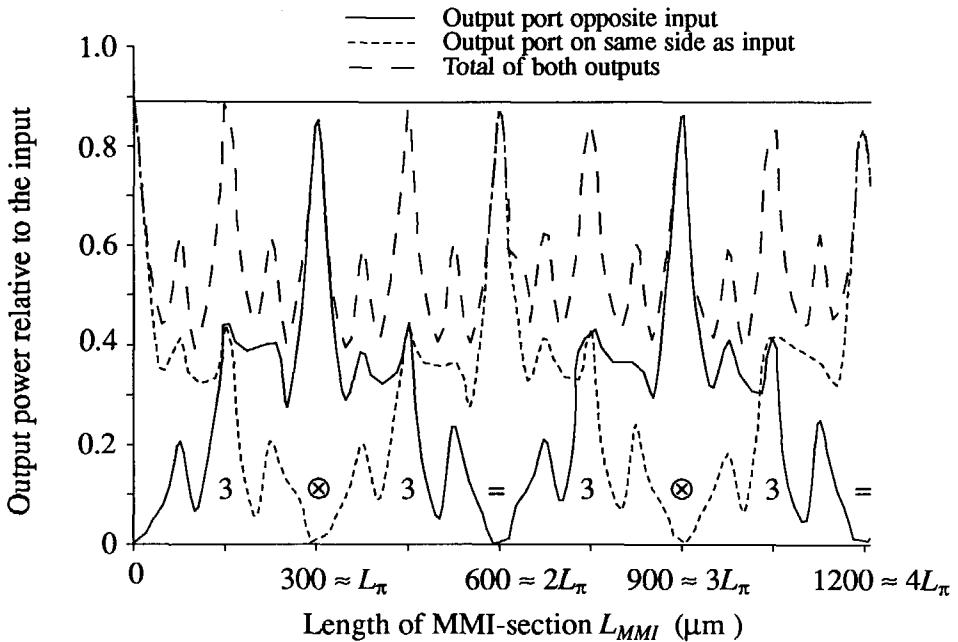| w_{MMI}, μm	gap μm	L_π μm	insertion loss, dB	@ L_{MMI} μm	cross-talk dB	@ L_{MMI} μm
4	0.4	66.9	0.88	67	13.97	137
5	0.6	99.8	0.67	104	15.10	204
6	0.8	139.3	0.54	141	17.20	278
7	1.0	185.6	0.57	188	21.40	368
8	1.2	238.4	0.68	240	28.71	472
	1.4		0.58		26.62	470
9	1.4	297.9	0.83	300	33.34	590
	1.6		0.66		29.61	

Fig. 5.10 *Output power versus coupler length, for the 9 μm wide MMI coupler and a gap size of 1.6 μm. The solid horizontal line denotes the loss at zero length and is due to radiation in the bends and to transition losses. The labels '3','=' and '⊗' denote the 3-dB splitter state, the bar-state and the cross-state respectively.*

functions as a 3-dB splitter when $L_{MMI} = (m+\frac{1}{2})L_{\pi}$. The losses of the coupler itself are very small (0.00 dB - 0.22 dB) because the larger part of the insertion loss (0.51 dB) is due to radiation losses in the bends and to transition losses at the junctions other than the junction of the access waveguides and the MMI section (this part of the insertion loss has been marked by the horizontal line in Fig. 5.10).

The curves in Fig. 5.10 do not resemble the simple $\cos^2$ and $\sin^2$ relationships at all. A complex interference pattern is seen instead of the simple relations. This is also exemplified in Fig. 5.11, where the field intensity $|h_y(x)|^2$ is shown along a total length of $L_{MMI} = 2L_{\pi}$. The field distribution at the beginning is the field distribution of the bend. This distribution is clearly reproduced at $L_{\pi} = 300$ μm, where it is shifted to the other side of the coupler. The field distribution recovers its original form at twice this length, $L_{MMI} = 2L_{\pi}$.
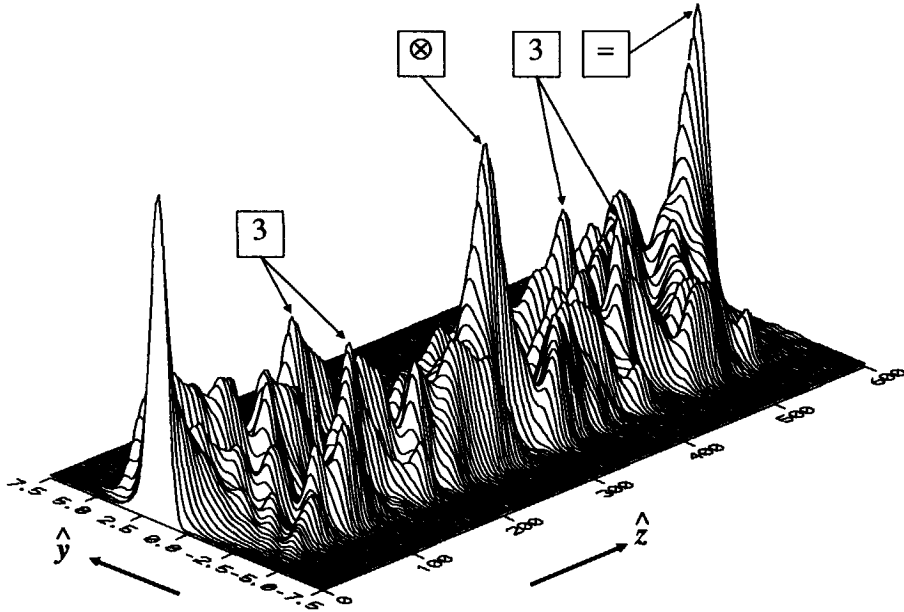
Fig. 5.11 *The total intensity distribution for the 9 μm-wide MMI coupler with a gap size of 1.6 μm and HE-polarization. The labels '3', '=' and '⊗' denote the 3-dB splitter state, the bar-state and the cross-state respectively.*

An important question should now be discussed. Why does the MMI coupler work? The MMI coupler that we have been discussing guides eleven modes and one would expect that the coherence between all modes is lost right after the point where the MMI coupler is excited. But the Figures 5.10 and 5.11 suggest that at lengths that are a multiple of $L_\pi/2$ all eleven modes interfere constructively.

Explanation

For the bimodal MMI coupler, the phase difference between both modes is a multiple of π, when the coupler is in the cross-state. It seems that for the MMI coupler, the phase differences between all modes become a multiple of π simultaneously in the cross-state. This happens indeed in a good approximation and is due to the 'self-imaging' properties of multimode waveguides, that have been studied previously by Ulrich and Kamiya [116] and by Chang and Kuester [17].

The 'self-imaging' character of multimode waveguides can be explained in the following way. The guided modes of a multimode slab waveguide that has a width w_{MMI} and is represented by an effective index of refraction N, are characterized by propagation constants that are approximately given by

$$\beta_{0v}^2 = k_0^2 N^2 - \frac{\pi^2(v+1)^2}{w_{MMI}^2}, v = 0, 1, 2, \dots, \tag{5.3.2}$$

which follows from $k_y^2 + k_z^2 = k_0^2 N^2$ with $k_z = \beta_{0v}$ and $k_y \approx (v+1)\pi/w_{MMI}$. Since β_{0v} is close to $k_0 N$, Eq. (5.3.2) may be approximated by

$$\beta_{0v} \approx k_0 N - \frac{\pi^2(v+1)^2}{2k_0 N w_{MMI}^2}. \tag{5.3.3}$$

The combination of Eqs. (5.3.1) and (5.3.3) yields

$$\frac{\pi}{L_\pi} = \beta_{00} - \beta_{01} \approx \frac{3\pi^2}{2k_0 N w_{MMI}^2}, \tag{5.3.4}$$

which can be used to rewrite Eq. (5.3.3)

$$\beta_{0v} \approx k_0 N - \frac{\pi(v+1)^2}{3L_\pi}. \tag{5.3.5}$$

The field in the MMI-section is written as a sum of the guided modes only for, say, the HE-polarization

$$h_x(y,z) = \sum_{v=0}^{M-1} c_v^+ h_{x,v}^+(y) e^{-j\beta_v z}, \tag{5.3.6}$$

where the coordinate system of the multi-mode-interference coupler is given in Fig. 5.9. The field at the entrance $z = 0$ of the MMI section is thus

$$h_x(y,0) = \sum_{v=0}^{M-1} c_v^+ h_{x,v}^+(y). \tag{5.3.7}$$

and the field at the end of the MMI section is

$$h_x(y,L_{MMI}) = e^{-jk_0NL_{MMI}} \sum_{v=0}^{M-1} c_v^+ h_{x,v}^+(y) \exp\left\{ j \frac{\pi L_{MMI}(v+1)^2}{3L_\pi} \right\}.$$

(5.3.8)

Inspection of the phase factor in Eq. (5.3.8) leads to

$$h_x(y,L_{MMI}) = \begin{cases} \sum c_v^+ h_{x,v}^+(y) \\ \sum (-1)^{v+1} c_v^+ h_{x,v}^+(y) \\ \sum_{v\ even} j(-1)^m c_v^+ h_{x,v}^+(y) + \sum_{v\ odd} c_v^+ h_{x,v}^+(y) \end{cases} \quad , \text{for}\ \frac{L_{MMI}}{3L_\pi} = \begin{cases} 2m \\ 2m+1 \\ m+\tfrac{1}{2} \end{cases}$$

(5.3.9)

where the overall phase factor $\exp\{-jk_0NL_{MMI}\}$ has been dropped. The symmetry properties of the modes

$$h_{x,v}(y) = \begin{cases} h_{x,v}(-y) & \text{for even } v \\ -h_{x,v}(-y) & \text{for odd } v \end{cases},$$

(5.3.10)

can be used to rewrite the result Eq. (5.3.9) as

$$h_x(y,L_{MMI}) = \begin{cases} h_x(y,0) \\ -h_x(-y,0) \\ \frac{j(-1)^m+1}{2}h_x(y,0) + \frac{j(-1)^m-1}{2}h_x(-y,0) \end{cases} \quad , \text{for}\ \frac{L_{MMI}}{3L_\pi} = \begin{cases} 2m \\ 2m+1 \\ m+\tfrac{1}{2} \end{cases}$$

(5.3.11)

The field at the end of the MMI section reproduces the field at the beginning for $L_{MMI}/(3L_\pi) = 2m$ and this represents the bar state. When $L_{MMI}/(3L_\pi) = 2m+1$, an exact mirror image is produced at the end of the MMI section and this is the cross state. When $L_{MMI}/(3L_\pi) = m+\tfrac{1}{2}$, a linear combination of the original field and its mirror image is obtained. The fields in both output ports have equal magnitudes and a relative phase of $\pi/2$, which means that the MMI coupler operates as a 3 dB splitter.

There is a second class of resonances, i.e. the resonances that coincide with those that have been calculated before and that occur at lengths of the MMI section L_{MMI} that are multiples of L_π instead of $3L_\pi$. Inspection of the phase factor in Eq. (5.3.8) shows that this second class of resonances does, indeed, occur provided that the following coefficients are not excited

$$c_v^+ = 0 \,, v = 2, 5, 8, \ldots \tag{5.3.12}$$

Eq. (5.3.12) shows that the optimization of the multi-mode-interference coupler that has been described at the beginning of this section consists, in fact, of trying to match Eq. (5.3.12).

Verification

These conclusions may be verified in two ways. Condition Eq. (5.3.12) must be fulfilled in order to have resonances at $L_{MMI} = L_\pi$ and this suggests a check of the overlap integrals for the junction of the MMI section and the bend for the case of an optimum MMI coupler. The squares of the overlap integrals for the fundamental mode of the bend to the modes $v = 0, 1, 2, \ldots$ of the MMI-coupler with a width of 9 μm and a gap of 1.6 μm, are 0.3531, 0.3317, 0.0010, 0.1513, 0.1061, 0.0001, 0.0384, 0.0128, 0.0025, ... respectively. The modes $v = 2, 5$, and 8 are seen to be significantly less excited than the other modes.

The existence of the super-resonances can be verified by considering the multi-mode-interference coupler that performed least optimally with respect to the optimization at $L_{MMI} = L_\pi$ and $L_{MMI} = 2L_\pi$, and by calculating the insertion loss at $L_{MMI} = 3L_\pi$ and the cross-talk at $L_{MMI} = 6L_\pi$. A good example is a multi-mode-interference coupler with $w_{MMI} = 4$ μm and a total gap of 1.0 μm. This coupler showed an insertion loss of 1.90 dB at $L_{MMI} = L_\pi$ and a cross-talk of -11.05 dB at $L_{MMI} = 2L_\pi$. But this same coupler has an insertion loss of 0.63 dB at $L_{MMI} = 3L_\pi$ plus a cross-talk of -24.49 dB at $L_{MMI} = 6L_\pi$, which shows that the super-resonances indeed occur.

The self-imaging properties of multimode waveguides make the optimization of the coupling of the MMI-section and the access waveguides redundant. When the super-resonances are concerned, the insertion loss is determined by the accuracy with which the image is reproduced and not by the excitation. The fact that an image can be better represented in terms of more modes explains why MMI sections that guide ever more modes show improved characteristics. The improved

properties of MMI-couplers permits us to use high-contrast waveguides for the design of the MMI-coupler. Very short bends can, therefore, be used that yield a fast separation between the access waveguides. The absence of the excitation problem allows us to optimize the size of the gap with respect to cross-talk only.

Chapter 6

Al$_2$O$_3$/SiO$_2$ ridge waveguides; experiments

This chapter is devoted to experimental work on dielectric curved waveguides. Section § 6.1 provides the introduction, and the sections § 6.2 on S-bend measurements and § 6.4 on the 'double-ridge' waveguide contain two papers that have been published in Electronics Letters. Additional material is presented in the two respective addenda. Section § 6.3 describes the experiments done to measure the losses of S-bends, where the lateral offset at the junction was varied. The 'self-aligned doubly etched' bends are the topic of section § 6.5, in which a new technique to combine waveguides with a low ridge and waveguides with a high ridge on one substrate is presented. Finally, section § 6.6 reports on experiments where the losses of S-bends in Al$_2$O$_3$/SiO$_2$ waveguides at a wavelength of 1300 nm were determined.

6.1 Technology and measurement setup

This chapter describes the experiments on and the fabrication of bends in dielectric buried ridge waveguides. Most of these waveguides have been operated at a wavelength of 632.8 nm and their cross-section is shown in Fig. 6.1. These waveguides consist of a sputtered Al$_2$O$_3$ film, which is approximately 250 nm thick, on a silicon substrate that has been thermally oxidized in order to form a

SiO$_2$ cladding layer. The SiO$_2$ layer, which is approximately 2 μm thick prevents the light from leaking into the silicon substrate. After the definition of the waveguides by photolithography and the subsequent etching by means of Argon beam milling, an SiO$_2$ cover is sputtered on top of the processed wafer which protects the waveguides and permits the use of a prism coupling to excite the waveguides. The SiO$_2$ cover layer is usually 650 nm thick, which gives an optimal coupling efficiency of the laser beam and the ridge waveguide. An annealing treatment is applied of 55 min at 800 °C which results in a low attenuation of the planar waveguide of approximately 1 dB/cm. This low value of the propagation loss of the Al$_2$O$_3$/SiO$_2$ waveguides makes them useful in integrated optics. The fabrication of these waveguides and the properties of sputtered Al$_2$O$_3$ with respect to integrated optics have been reported by Smit, Acket and van der Laan [105].

A chromium layer is sometimes sputtered on top of the SiO$_2$ cover in order to enhance the accuracy of the loss measurements (*see* Fig. 6.1). The chromium layer is subjected to photolithography and etched in order to form narrow gaps (grooves) above the waveguide channels. A large fraction of the light that is lost by the waveguide channel remains confined in the planar film. The chromium mask so formed is located at the site of the output coupling prism and permits the coupling of light out of the waveguide channels but prevents this for the rest of the planar film.
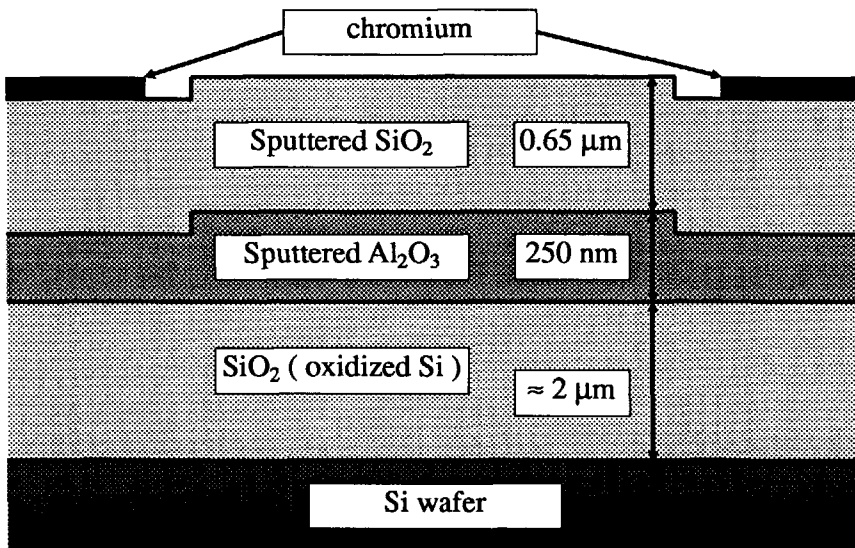

Fig. 6.1 *The straight-waveguide cross-section for operation at a wavelength of 632.8 nm.*

All measurements of the losses of S-bends in Al_2O_3/SiO_2 waveguides that are described in the thesis have been made using prisms to couple light into and out of the waveguides and by detection of that light with a photodiode. The technique of coupling light into a planar waveguide by means of a prism is well known. See, for example, the chapter by Tamir in [110], Tien [113] or Pasmooij et al. [88]. There are many advantages to prism-coupling. It permits an accurate determination of losses with an accuracy of approximately 0.1 dB. The light couples out of the film under a well-defined angle that is related to the propagation constant $\beta = Nk_0$ of the mode which propagates in the waveguide by means of

$$N = n_{prism} \sin\left\{ \theta_{prism} + \sin^{-1}\left\{ \frac{n_{air}}{n_{prism}} \cos(\theta_{prism} + \theta_{coupling}) \right\} \right\}, \tag{6.1.1}$$

where $n_{air} = 1.00028$ is the refractive index for air, $n_{prism} = 1.7356$ is the refractive index of the prism at a wavelength of 632.8 nm, $\theta_{prism} = 60°$ is the prism angle and $\theta_{coupling}$ is the coupling angle between the laser beam and the plane of the wafer. The accuracy with which the coupling angle can be determined is approximately 0.005°, leading to 5 significant digits for the effective refractive index [88].

Prism couplers can be used to excite a specific mode in a waveguide by giving the input beam of light the appropriate angle. The measured coupling angles $\theta_{coupling}$ can, in combination with Eq. (6.1.1), be used to calculate the effective refractive indices and, therefore, to calculate the properties of the waveguide such as the refractive index of the guiding film, its height, and the width of a two-dimensional waveguide by using the method of effective dielectric constant (see Table 6.1 for example).

The laser light is coupled directly into the straight waveguide by placing the prism on top of the waveguide and by using a cylindrical lens with a focus of 75 mm, which leads to a lateral spot size of the order of 50 µm. This spot size is much wider than the waveguide, which improves the coupling efficiency and leads to an improved stability of the measurement setup [88]. A contacting liquid (CH_2I_2 , $n \approx 1.74$) is used to reduce the influence of the gap between the prism and the cover layer, since its index of refraction is almost equal to that of the prism.

6.2 Losses in S-bends

The following section contains the manuscript that we sent to Electronics Letters and which was subsequently published [90]. Experimental material that is not covered by the letter will be given in the addendum.

6.2.1 Manuscript Electronics Letters

Low-loss Bends In Planar Optical Ridge Waveguides

E.C.M. PENNINGS, G.H. MANHOUDT[§] and M.K. SMIT

Laboratory of Telecommunication and Remote Sensing Technology
Faculty of Electrical Engineering
Delft University of Technology
P.O. Box 5031, 2600 GA Delft, the Netherlands

Abstract

Bending losses lower than 0.7 dB for 90°-bend sections with radii of curvature as small as 75 μm were measured on silicon-based Al$_2$O$_3$ ridge waveguides with SiO$_2$ cladding layers at a wavelength of 632.8 nm. These values, which are close to the calculated values, are the lowest thus far reported.

Introduction

In optoelectronic integrated circuits, waveguide bends play an important role in connecting components. The size of these bends eventually determines the maximum density with which components can be integrated on a single chip. Waveguide bends may also enable long components such as external cavities and phase modulators to be folded and miniaturized.

The only previous results on submillimeter bends in ridge waveguides seem to be those of Austin [6], where 1 dB/90°loss has been reported for GaAs/GaAlAs bends with $R = 300$ μm. Realization of directional changes with totally reflecting corner mirrors has not yet yielded losses below 1.5 dB per mirror [15].

We investigated bending losses in very short bends with radii of curvature from 50 to 200 μm in 3 μm wide ridge waveguides, etched in SiO$_2$ cladded Al$_2$O$_3$ films on silicon substrates. Measurements and calculations were performed at a wavelength of 632.8 nm.

Bending loss mechanisms

The total loss of a waveguide bend of finite length is due to radiation loss, field mismatch at the transition between the straight and curved waveguide and increased scattering caused by roughness of the outer edge. We will discuss these mechanisms subsequently.

---

§ Present address: A.T. & T. and Philips Telecommunication, P.O. Box 18, 1270 AA Huizen, the Netherlands
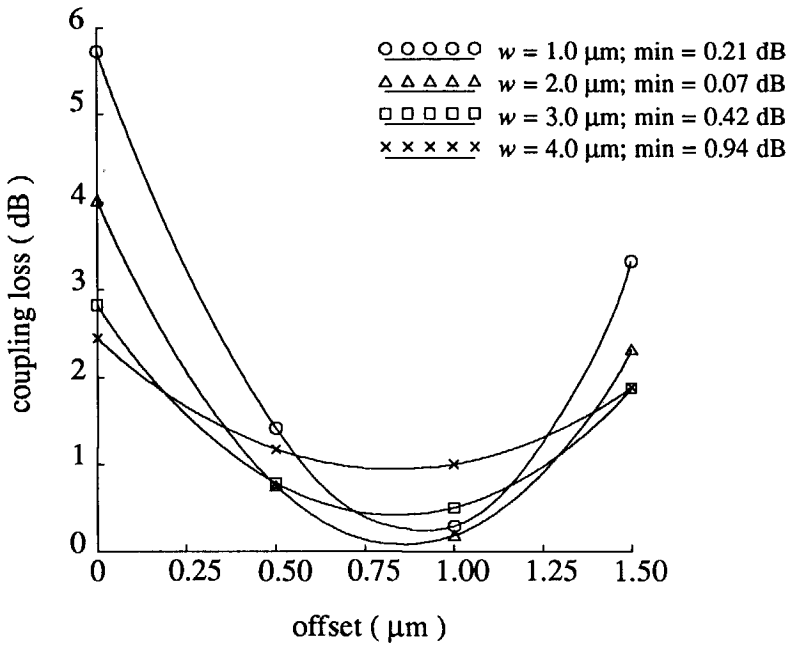
Fig. 6.2 *Calculated coupling losses for the HE$_{00}$-mode as a function of lateral offset for different widths of the straight waveguide. The width of the waveguide bend is 3 μm and R = 100 μm.*

(i) Every curved structure exhibits losses in the form of radiation, because of the finite speed of light in the cladding material. The radiation losses can be reduced either by increasing the radius of curvature or by introducing a large refractive-index contrast. In our case, we created a large contrast by etching a high ridge, the price of which is paid by increased propagation losses of the straight sections due to scattering by edge roughness. The calculation of the radiation losses involved the effective-index method. The resulting two-dimensional bend is transformed into an equivalent straight structure by means of a conformal transformation [40], which is then solved by means of the staircase approximation [19].

(ii) In a curved waveguide the intensity distribution shows a shift of its maximum towards the outer edge. For small radii of curvature the mode is guided by the outer edge alone (like a whispering gallery mode). The shape of this mode profile is, therefore, not determined by the width of the waveguide bend but mainly by the refractive-index contrast and the radius of curvature, whereas the shape of the straight-waveguide mode profile strongly depends on the width of the waveguide.
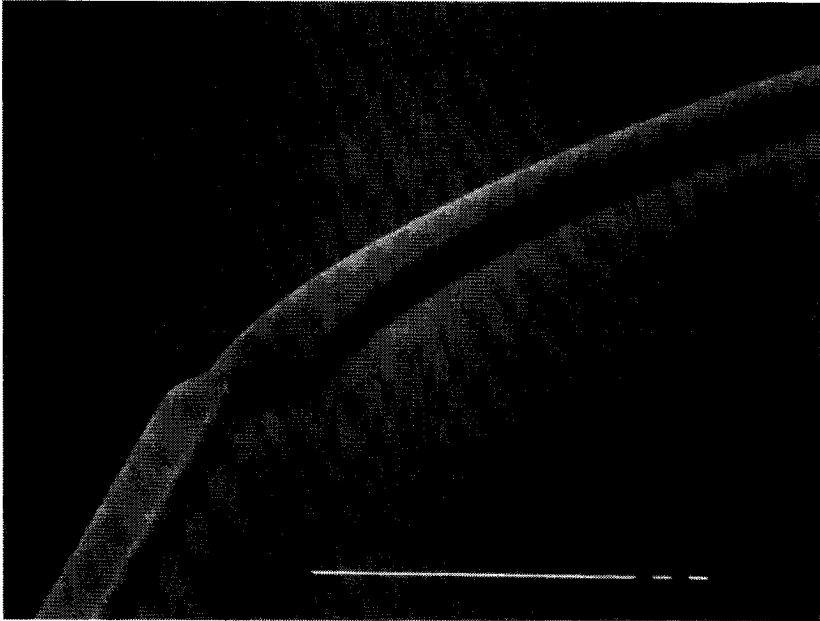
Fig. 6.3 *SEM photograph of a ridge waveguide bend with R = 50 μm defined in photoresist.*

At the transition between the straight and the curved waveguide, conversion losses will occur because of the mismatch between the two field distributions. These conversion losses can be minimized by introducing a lateral offset between the straight and the curved waveguide in order to align the field maxima [80], and by optimizing the width of the straight waveguide in order to match the widths of both field distributions, as exemplified in Fig. 6.3. The conversion losses have been estimated by applying overlap integrals [40]. The improvement in coupling efficiency can be substantial as can be seen in Fig. 6.2. For a 3-μm-wide straight waveguide the coupling loss improves by 2.4 dB if a 0.85-μm offset is introduced. An additional 0.35 dB is gained by changing to a 2-μm-wide straight waveguide. The applied waveguides are multimode and the resulting coherent effects were all taken into account in the calculations. We optimized all offsets and the straight-waveguide width for the lowest-order mode.

(iii) The scattering losses depend on the edge roughness of the ridge waveguide. We found that an optical pattern generator (ASET COMBO 250) with rotating head in combination with a 4× reduction camera gives an edge quality superior to
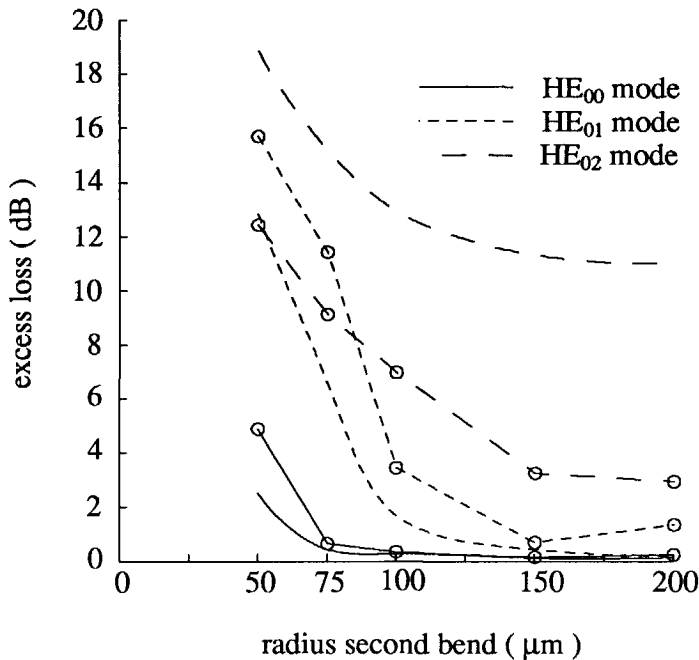
Fig. 6.4 *Measured (lines with markers) and predicted (lines without markers) losses for five different S-bends. The markers denote the measured values, for which the typical error is 0.2 dB. (See the addendum) (R = 50, 75, 100, 150, and 200 μm)*

electron-beam generated patterns, that often exhibit a step-like pattern due to electron-beam quantization. This may be solved by choosing a very small spot size, but at the price of excessive writing time. Figure 6.3 demonstrates the edge quality of the optically generated pattern.

Experiments and results

We designed and fabricated two wafers with five identical sets, each set containing five different S-bends and several straight reference waveguides. Each S-bend starts with a 200-μm 90° bend and is followed by a second 90° bend with R = 50, 75, 100, 150 and 200 μm respectively. Waveguides were formed by atom-beam milling a 100-nm step in a 250-nm-thick sputtered Al_2O_3 layer (n = 1.69) through a photoresist mask and by covering the circuit with a sputtered SiO_2 layer (n = 1.457) [105]. The 100-nm step creates a lateral effective-index contrast of $\Delta n/n \approx 3.4\%$. Light from a He-Ne laser (λ_0 = 632.8 nm) was coupled into and out

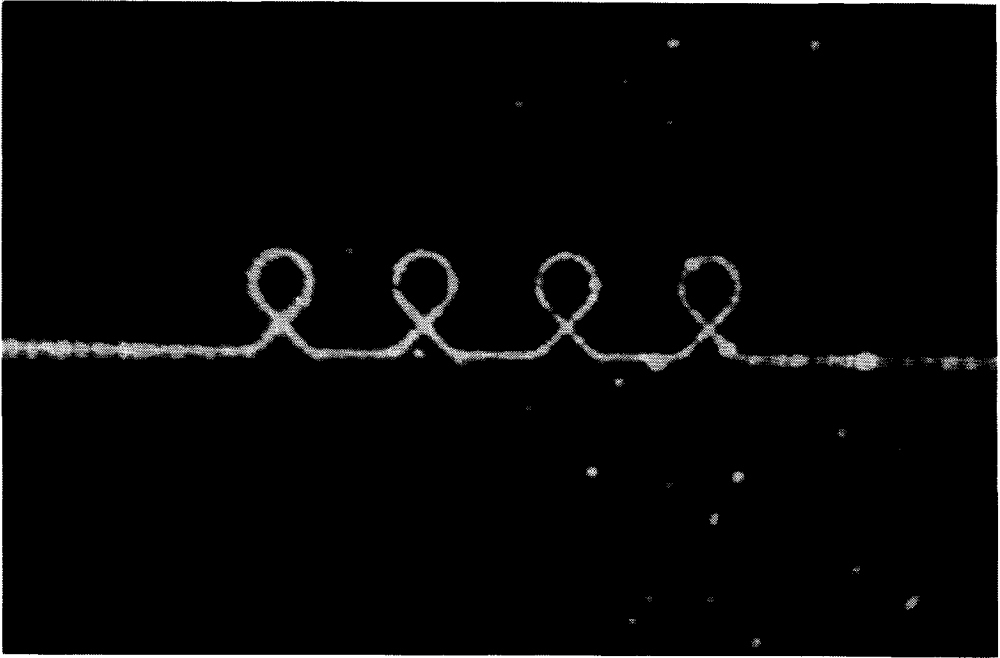***Fig. 6.5*** *Four loops with R = 150 μm.*

of the waveguides by means of the two-prism configuration enabling the selective excitation of all modes [88].

A silicon photodiode detected the power of all modes coupled out of the waveguide by the prism. We measured the total additional power loss occurring in the S-bend sections by comparing the power coupled out of them and out of the straight reference waveguides. The agreement between theory and experiment is quite good as can be seen in Fig. 6.4, in which the total additional power loss is plotted as a function of the radius of curvature of the second bend. The HE_{00} mode (notation of Unger [117]) in the 75-μm S-bend has a loss of 0.7 dB, which is the lowest value reported thus far. The loss of 0.2 dB for the 200-μm S-bend is within the measurement accuracy. This low loss enabled us to make the more complex waveguide structure shown in Fig. 6.5, which contains four loops with $R =$ 150 μm and shows negligible bending losses.

Because of the selective excitation, we could measure the bending losses for the HE_{01} and the HE_{02} mode as well. The offsets between straight and curved waveguides have not been optimized for these modes and consequently there is considerable intermodal conversion at the transitions. Despite the increased con-

tribution of multimode interference, effects the qualitative agreement between measured and predicted results remains quite good. The crossing of the HE_{01} and HE_{02} attenuation curves as predicted by theory is indeed measured.

Conclusions

We have fabricated ridge waveguide S-bends with radii of curvature as small as 75 μm and measured a total loss of 0.7 dB, which is very close to the calculated value. These low values were obtained by introducing a large lateral effective-index contrast and a lateral offset at the transition and by optimizing the width of the straight waveguide. The low losses made it possible to cascade a considerable number of bends with negligible bending losses, thus demonstrating the feasibility of folding and miniaturizing long components such as external cavities and phase modulators.

6.2.2 Addendum

A complete set of five S-bends and four straight reference waveguides is shown in Fig. 6.6. The radii of curvature of the first 90° bend of every S-bend are equal and amount to 200 μm. The radii of curvature of the second 90° bend vary between 50 μm and 200 μm. This mask design improves the resolution of the measurements, because the light is mainly radiated from the second 90° bend in a 'downward' direction and this light, therefore, does not reach the output coupling prism. The resolution has also been enhanced by the application of an extra chromium layer as explained in section § 6.1. The accuracy of the loss figures of 15 dB or larger is, nevertheless, reduced despite these precautions.

The manuscript has been corrected in two places with respect to the published version. Firstly, the correct radius of curvature of the four loops is 150 μm as indicated in the caption of Fig. 6.5. Secondly, the predicted excess losses that are shown in Fig. 6.4 have been corrected for the fact that the first and the second bend are oppositely curved. This results in a noticeable correction for the $R = 50$ μm S-bend and a better agreement between the measured and the predicted excess losses, especially for the first-order modes. The crossing that is found for the measured excess losses for the HE_{01}-mode and the HE_{02}-mode as shown in Fig. 6.4, does, however, not occur for the predicted values now. The fact that the measured excess losses increase sharply for the HE_{01}-mode and increase slowly for the HE_{02}-mode, is in agreement with the predicted values and it is this fact that leads to the 'crossing'. The excess losses that are shown in Fig. 6.4 should not be seen as giving the relation between the radiation loss and the radius of curvature for each mode, because the excess loss represents the total loss for the complete
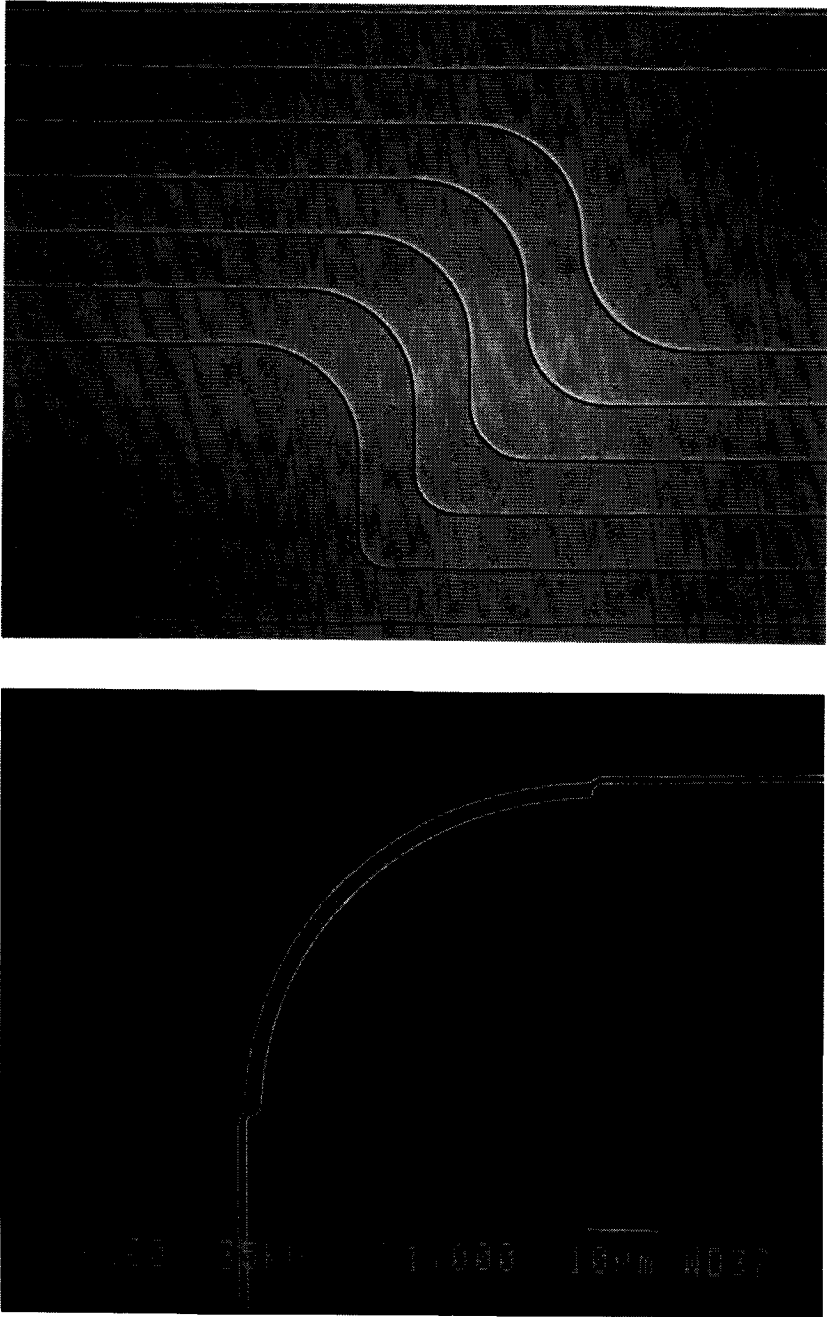
Fig. 6.6 *A set of five S-bends plus four straight reference waveguides (top) and a scanning electron micrograph of the bend with a radius of curvature of 50 μm (bottom).*
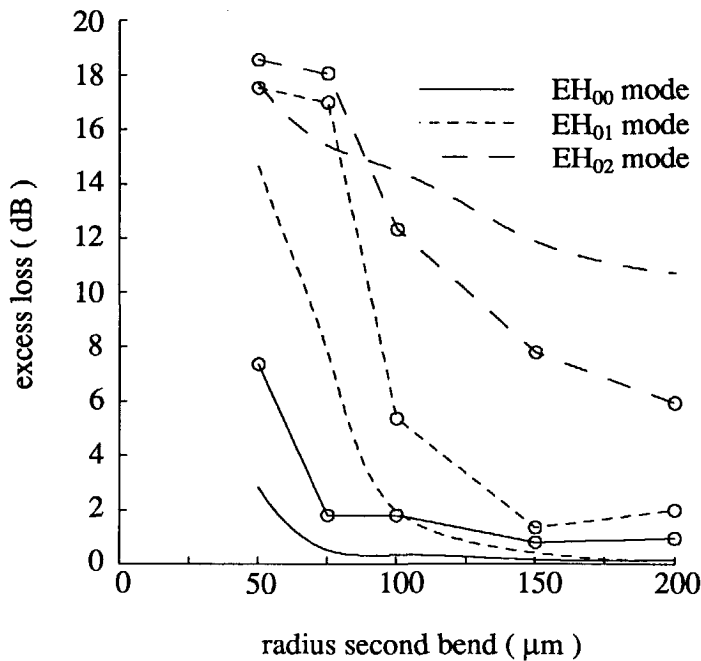
Fig. 6.7 *The measured (markers) and the predicted (curves without markers) losses for the same S-bends as in Fig. 6.4 and EH-polarization. The excess loss is the total loss of the S-bend relative to the straight reference waveguides. The ridge height of the waveguides is 100 nm.*

S-bend and this loss may quite easily be caused by transition losses at the junctions. If the HE_{02}-mode couples to the HE_{00}-mode at the first junction for example, then the excess loss will be dominated by the propagation properties of the HE_{00}-mode instead of the HE_{02}-mode.

The manuscript includes one graph with excess S-bend losses. These losses have also been determined for the EH-polarization and for a second wafer, which contains waveguides with a ridge height of 110 nm. These values are shown in Fig. 6.7 and Fig. 6.8. From these graphs, we see that the agreement between the predicted and the experimental values is better for the lowest- and first-order modes than for the second-order mode. The predicted losses are generally smaller than the measured losses. It should be noted, however, that the method of the effective dielectric constant has been used for a waveguide where the ridge height equals approximately half the thickness of the guiding film and a reduced accuracy of the EDC method is to be expected.
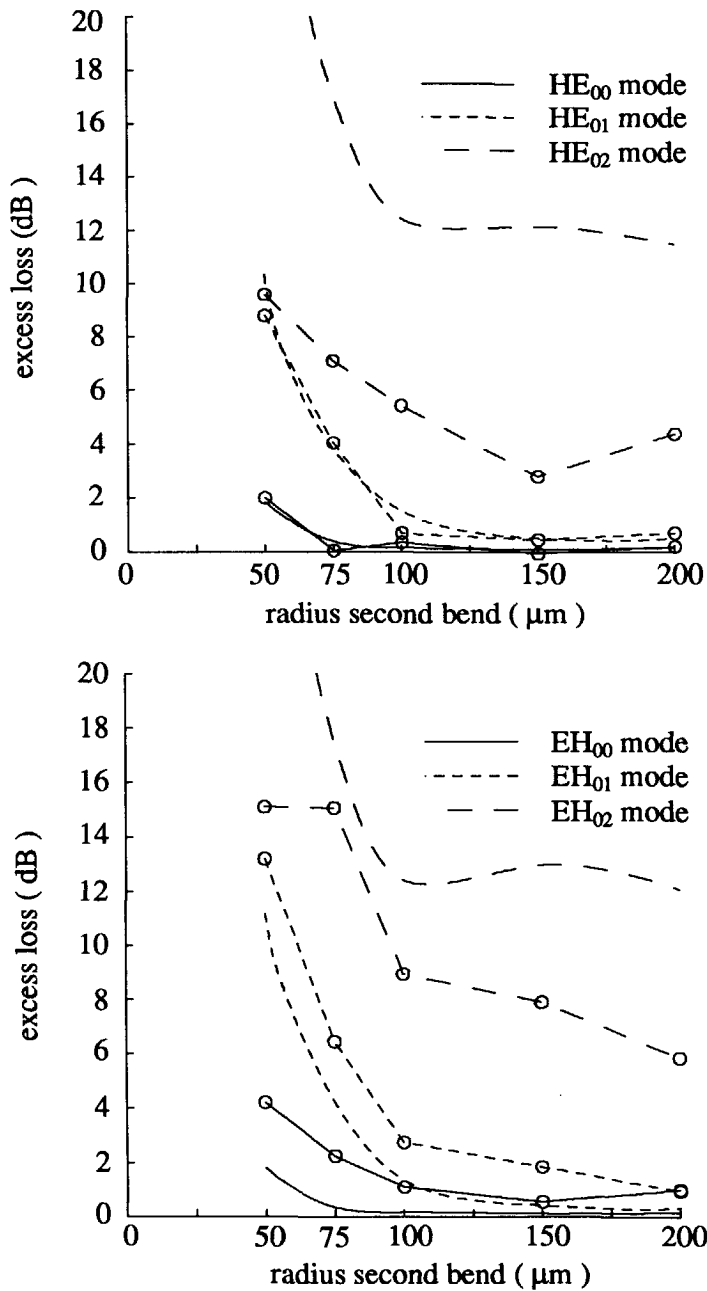
Fig. 6.8 *The measured (markers) and the predicted (curves without markers) losses for five different S-bends. The ridge height of the waveguides is* 110 nm.

The measured excess losses for the HE-modes are smaller than those for the EH-modes. This measured difference is not in agreement with the predictions, which yield almost equal values for both polarizations, and it cannot be accounted for by differences in propagation losses. The measured propagation losses for the HE-modes are even slightly larger than for the EH-modes, which is in agreement with the character of the source of the scattering, i.e. the roughness of the ridge. The scattering of light is largest when the electric field is oriented along the lateral direction in which the deviations from the perfectly smooth ridge geometry occur.

The mask included four waveguide tracks with one, two, three or four loops respectively, as shown for example in Fig. 6.5. The total excess loss for the HE_{00}-mode is 0.50, 2.55, 2.80 and 3.85 dB for these loops, respectively for the waveguides with a ridge height of 100 nm. The loss figure does not increase linearly with the number of loops, which is due to multimode interference effects. All light enters the first loop in the form of the HE_{00}-mode. After the first loop, some part of the remaining light has been converted to higher-order modes that show higher losses than the lowest-order mode. A least-squares approximation leads to an excess loss of 0.98 dB per loop and this value consists of the transition losses of four junctions, the transmission loss of one waveguide crossing, the radiation losses of bends with $R = 150$ μm and a total section angle of 360° and the propagation losses along a waveguide track that is 1.12 mm longer that the straight reference waveguide.

6.3 The influence of the offset

6.3.1 Introduction

The theory of waveguide junctions has been discussed in section § 4.2. It was shown in section § 5.2.4 that two strategies are available to reduce the transition losses at a junction of a straight and a curved waveguide. Firstly, a lateral offset may be applied to match the position of the maxima of the field distributions [80]. Secondly, the width of the straight waveguide can be varied in order to optimize the widths of the modal field distributions in both sections. Döldissen et al. [31] performed experiments to test the influence of the offset at the junctions in S-bends in LiNbO$_3$ at $\lambda_0 = 1.3$ μm and showed a loss reduction of up to 2 dB.

In this section, experiments will be described for the purpose of testing the influence of the lateral offset in S-bends in Al$_2$O$_3$/SiO$_2$ at a wavelength of 632.8 nm. The results of these experiments were presented at the European Conference on Optical Integrated Systems at Amsterdam [93].

6.3.2 Experiments

A mask has been designed that contains U-bends or 'chicanes' with identical radii of curvature but varying lateral offsets at the junctions, straight reference waveguides and several straight sections with a width of 40 μm which can be considered as equivalent to a planar film. The mask layout of the U-bends is shown in Fig. 6.9 and it closely resembles the layout shown in Fig. 7.4. Every U-bend consists of four curved sections with a section angle of 90° each. The first and third 90°-bend have a radius of curvature of 200 μm and the second and fourth 90°-bend have a radius of curvature of 100 μm, the purpose of which is to reduce the amount of light that emanates from the waveguide track in a forward direction where the output coupling prism is located. The width of the straight waveguides is 2 μm and the width of the curved waveguides is 3 μm. The offset at the junction of the straight waveguide and the 90°-bend with a radius of curvature of 200 μm has the constant optimized value of 0.73 μm. The offset at the junction of the straight waveguide and the 90°-bend with a radius of curvature of 100 μm has been varied between 0.6 μm and 1.5 μm in ten steps of 0.1 μm and between 0.55 μm and 1.55 μm in five steps of 0.25 μm. The range of offsets did not include zero because the straight and curved waveguides have different widths. The outer side of the ridge of the curved waveguide is aligned with the outer side of the ridge of the straight waveguides for an offset of 0.5 μm.

The U-bends have been manufactured in the form of 'standard' waveguides as explained in the introduction to this chapter § 6.1. The waveguides are created by Ar-ion- beam milling 100 nm away from a sputtered Al$_2$O$_3$ film with a thickness of 250 nm. A cover layer of 600 nm SiO$_2$ is sputtered on top and an annealing treatment is applied of 55 min at 800 °C. A chromium mask on top of the SiO$_2$ cover layer permits the coupling of light from the waveguide to the output coupling prism but prevents this for light that is guided in the planar film. The scanning electron micrograph that is shown in Fig. 6.9, gives an example of a lateral offset at the junction of the straight and curved waveguide.

6.3.3 Results and discussion

The light from an He-Ne laser with $\lambda_0 = 632.8$ nm was coupled into the etched film and into the 40 μm wide waveguide and the resulting coupling angles can be related to the effective refractive indices by means of Eq. (6.1.1). These values have been used, in turn, to yield the thickness of the as-deposited Al$_2$O$_3$ film (255 nm) and the thickness of the etched Al$_2$O$_3$ film (157 nm). The difference of these thicknesses gives a manufactured ridge height of 98 nm. The coupling angles for
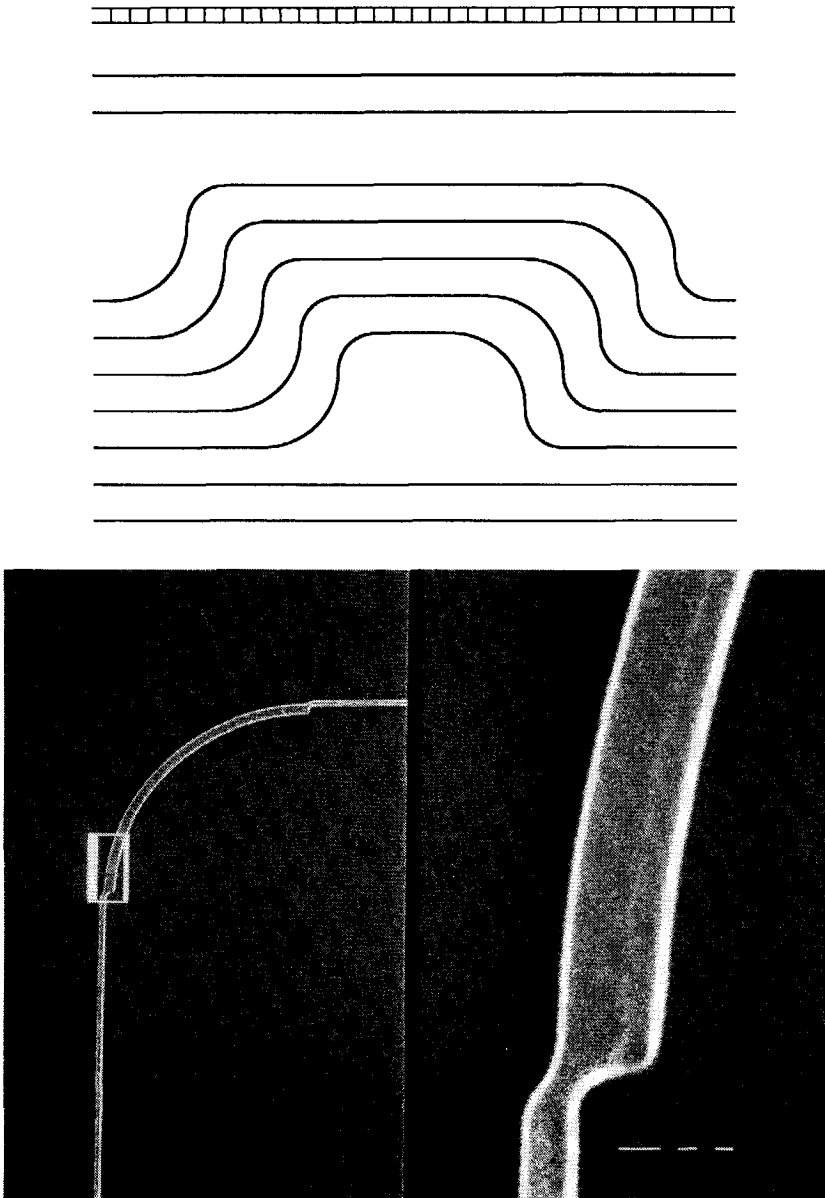
Fig. 6.9 *Mask layout of a set of five U-bends, four straight reference waveguides and a 40 μm-wide waveguide (top). Example of the use of a lateral offset at the junction (bottom). The scanning electron micrograph shows a junction of a 2 μm-wide straight waveguide and a 3 μm-wide curved waveguide with a radius of curvature of 50 μm, which are defined in photoresist.*

the HE$_{00}$-mode and the EH$_{00}$-mode have been used in combination with the method of effective dielectric constant to yield the width of the fabricated straight waveguide being 1.95 μm.

The excess loss of several of the fabricated sets of U-bends has subsequently been measured for the HE$_{00}$- and the EH$_{00}$-mode and the results of the measurements are shown in Fig. 6.10. Two parabola have been fitted to these measurements that reveal a relationship between the losses and the offset similar to the one shown in Fig. 6.2. The dashed vertical line indicates an offset of 0.88 μm, which gives a maximum overlap integral for the lowest-order modes in the straight and the curved waveguide. The optimum offset is equal for the HE$_{00}$- and the EH$_{00}$-mode. The minima for the fitted parabolae occur at 0.92 μm and 0.90 μm respectively, which is close to the predicted value of the optimum offset. The calculated excess losses for the HE$_{00}$-mode have been included in Fig. 6.10.

The experimental values shown in Fig. 6.10 are based on three fabricated sets of U-bends. Preliminary measurements of other sets indicates that the experimental values might show a large variation from set to set, which is due to multimode interference effects. The total U-bend with optimized offsets is a waveguide track that guides light with minimal losses from the first to the last section. If the offsets are far from being optimized, it may be more appropriate to look upon the U-bend as consisting of three multi-mode-interference couplers. The transmission of such a coupler varies considerably with the length and other parameters of the straight coupler section. In order to estimate this variation, the transmission of five U-bends has been calculated for the HE$_{00}$-mode for different ridge heights and waveguide widths. The ridge height has been varied between 97 $\pm$ 10 nm and the width of the straight waveguide has been varied between 2.0 $\pm$ 0.5 μm. The results of this analysis are indicated in Fig. 6.10 by means of the error bars that mark the minimum and the maximum calculated excess loss. The influence of the ridge height depends on the length of the straight 'coupler' sections in the sense that the ridge height becomes more critical for longer lengths of the straight section. The largest change in excess U-bend loss is caused by the variation of the width. This is due to the fact that when the width of the straight and the curved sections change simultaneously, both the properties of the 'coupler' section and the value of the offset change. The offset, i.e. the distance between the center of the straight and curved waveguides, does not depend on the width, but it is the distance between the outer side of the curved waveguide ridge and the center of the straight waveguide that determines the transition loss at the junction, and this distance depends on the width of the straight waveguide. A width variation of 0.5 μm changes the effective offset by 0.25 μm. The analysis reveals another important advantage offered by the use of an optimized offset. Not only are the losses minimal
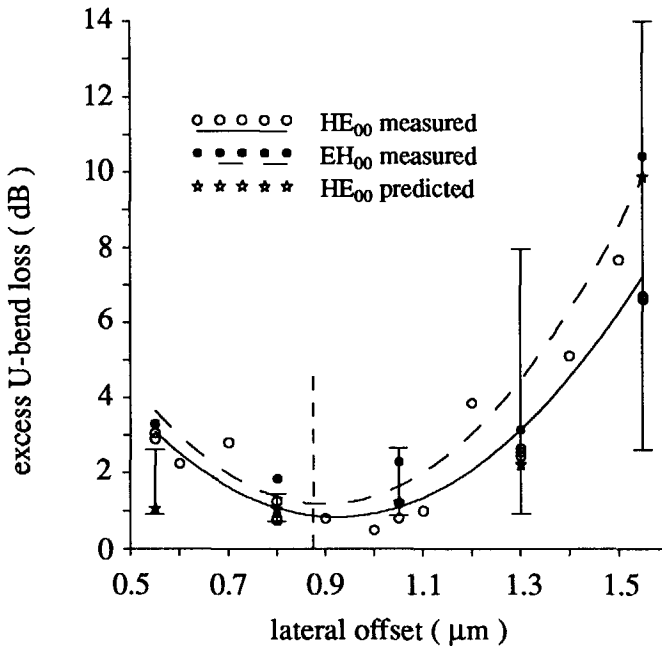
Fig. 6.10 *Total loss of the U-bend relative to the straight reference waveguides in relation to the lateral offset. The solid and dashed parabola are fitted to the measured values and indicate dependences similar to the one shown in Fig. 6.2. The vertical dashed line marks the optimum offset for both the* HE_{00}- *and the* EH_{00}-*mode. The error bars give the variation in predicted losses, when the ridge height is varied between* 97 ± 10 nm *and the width of the straight waveguide is varied between* 2.0 ± 0.5 µm *(the width of the bend is varied in accordingly).*

but this minimal loss is also the least susceptible to changes in the fabricated geometry.

The excess losses are larger for the EH_{00}-mode than for the HE_{00}-mode and the loss values for the EH_{00}-mode do not become smaller than 1 dB as the loss values for the HE_{00}-mode do. This has been observed before and is discussed on page 139.

6.3.4 Conclusions

The experiments show a minimum loss of the U-bends for an offset, which is very close to the predicted offset. The excess losses for the U-bend with an optimized offset and 'without an offset' differ by more than 2 dB (the offset of

0.5 μm is viewed as 'without offset', since this offset aligns the outer sides of the ridges). The calculations predict a considerable variation in transmission if the offset is not optimized which is due to multimode interference effects. An optimized offset minimizes the excess loss of the S-bends and this loss value is also the least susceptible to changes in the fabricated geometry.

6.4 The double-ridge waveguide

The following section contains the manuscript that we sent to Electronics Letters and which was subsequently published [92]. The addendum gives more details of the modeling of the scattering losses in ridge waveguides.

With respect to the 'double-ridge' waveguide, the following remarks are made concerning the nomenclature. Referring to Fig. 6.11, we can look upon the waveguide cross-section as consisting of one ridge (width: 2.7 μm + $2D$ and height: 130 nm $- H$) with a second ridge on top (width: 2.7 μm and height: H). The first ridge is referred to in the manuscript as the 'outer' and or 'high' ridge while the second ridge is referred to as the 'inner' and or 'low' ridge. A statement like "the inner ridge is monomode" is shorthand for "the waveguide whose cross-section consists of a planar film of height 250 nm $-H$ with a ridge on top of this film of width 2.7 μm and height H operates in the monomode regime".

6.4.1 Manuscript Electronics Letters

Reduced bending and scattering losses in new optical 'double- ridge' waveguide

E. C. M. PENNINGS, J. VAN SCHOONHOVEN,
J. W. M. VAN UFFELEN and M. K. SMIT
Department of Electrical Engineering
Delft University of Technology
PO Box 5031, 2600 GA, the Netherlands

Abstract

A new type of waveguide is proposed combining a low and a high ridge. Experiments at λ = 632.8 nm show an excess loss of 0.6 dB for a 90°-bend with R = 50 μm in SiO₂ cladded Al₂O₃, while showing reduced scattering losses compared with a conventional ridge waveguide.

Introduction

The successful development of optoelectronic integrated circuits depends largely on the ability to miniaturize components and to reduce their losses. A necessary ingredient of these circuits are curved waveguides with small radii of curvature and low losses. These bends not only provide directional changes, which can also be supplied by corner mirrors [2], but they separate waveguides in directional couplers, are used in ring lasers and they enable the miniaturization of long components such as phase modulators and external cavities by folding them onto a small area.

Attenuation of light in a waveguide bend is caused by radiation, by roughness scattering and by transition losses at the junction of the straight and curved sections. The radiation losses decrease with increasing difference in refractive index. In ridge waveguides the radiation losses can therefore be reduced by etching a high ridge. But this has two important drawbacks. First, a large refractive index contrast causes the waveguide to become multimode, whereas most applications require monomode waveguides. Secondly imperfections in the mask and etching processes lead to edge roughness coupling the bound mode to the continuum of unguided modes [69]. These scattering losses increase with refractive-index difference and with ridge height.

The ideal solution would be to use a local increase of the etched step as several authors [70][81] have suggested. For straight waveguides, a low ridge could be used that leads to a low-loss monomode waveguide while a high ridge at the bends reduces the radiation losses. Such a scheme, however, needs two different masks and leads to problems with the required submicron alignment.

In this letter we propose a new type of waveguide called 'double-ridge guide' as shown in Fig. 6.11 that combines a low inner and a high outer ridge in a self-aligned procedure. In straight waveguides the field is mainly confined by the inner ridge. The height of this ridge can be chosen to yield a monomode waveguide with low scattering losses. In a tight waveguide bend the field profile shifts outward to the high ridge thus preventing radiation of light out of the waveguide.

Modeling

Theoretical predictions for the radiation losses in curved waveguides have been made by applying the effective dielectric constant (EDC) method, after which a conformal transformation was used [70]. The solution of the transformed scalar wave equation was then found by numerical integration.

The scattering losses in a planar slab waveguide [69][47] are proportional to the square of the power-normalized electric field, to the square of the dielectric-constant difference and to λ^{-k} where k varies from two to four depending on the

statistical model of the roughness. These proportionalities and the EDC method
have been used in a semi-empirical formula for the scattering losses,

$$\alpha = \alpha_0 + \alpha_1 \sum_i \frac{(\Delta N_i^2)^2 |E(x_i)|^2}{\int |E(x)|^2 dx} \tag{6.4.1}$$

in which α represents the total loss in dB/cm, α_0 is the attenuation for the planar
waveguide without lateral confinement, ΔN_i is the difference in effective refractive
index at interface i, $E(x_i)$ is the electric field at interface i, x is a lateral coordinate
and the contributions are summed over all interfaces, which is justified if the
roughness in different ridges is not correlated. α_0 and α_1 have been fitted to
experimental values yielding $\alpha_0 = 1$ dB/cm and $\alpha_1 = 0.14$ dB for our waveguides
assuming that the correlation length and the rms value of the roughness are a
constant of the process.

The calculated radiation and scattering losses for Al₂O₃ ($n = 1.690$) and SiO₂
($n = 1.457$) at $\lambda_0 = 632.8$ nm are given in Fig. 6.12, while the relevant parameters
of the double-ridge waveguide are explained in Fig. 6.11. For $D = 0.2$ μm the
radiation curve is nearly flat, indicating that for small ridge separations the
radiation loss depends on the sum of both ridge heights and not on the individual
ridge heights. The scattering loss in the straight waveguide, on the other hand,
strongly depends on the way the total ridge height is divided and it shows a
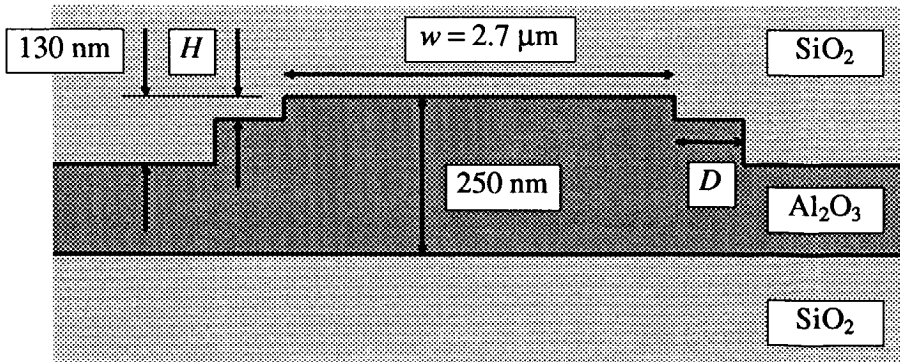minimum between $H = 20$ nm and $H = 40$ nm. For $H = 0$ and for $H = 130$ nm the

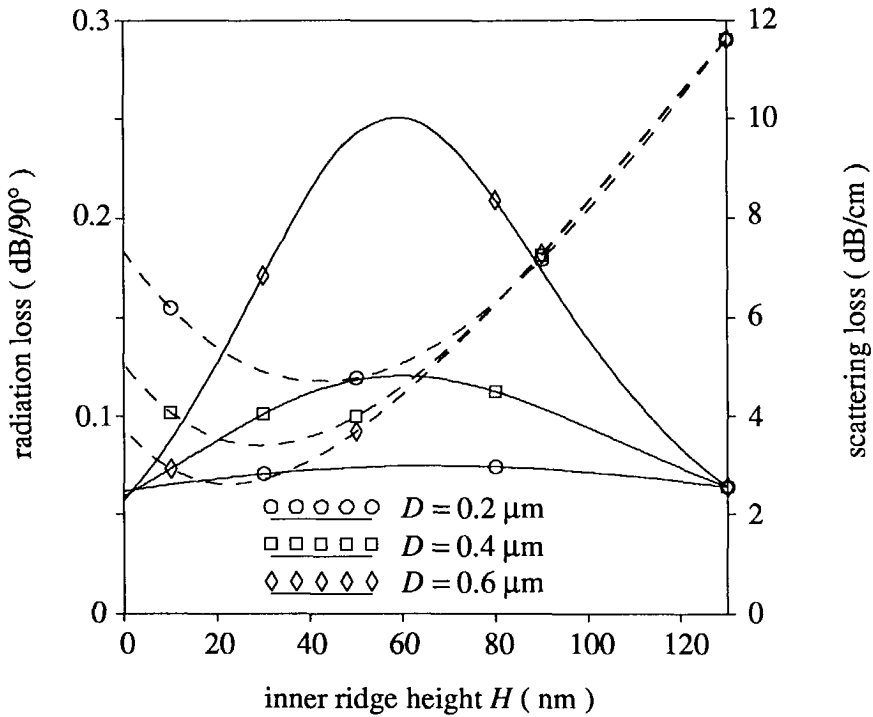**Fig. 6.11** *The geometry of the double-ridge guide (curved section).*

Fig. 6.12 *Calculated radiation loss the curved waveguide (solid curves, R = 50 μm, w = 2.7 μm) and calculated scattering loss for the straight waveguide (broken curves, w = 1.7 μm). The sum of both ridge heights is constant, i.e. 130 nm.*

waveguide is single-ridge and asymmetry in the scattering curves stems from the fact that at $H = 0$ nm the waveguide has become wider by an amount $2D$. The inner ridge will be single mode for ridge heights H smaller than 25 nm.

Experiments

Waveguides have been fabricated in 250 nm thick sputtered Al_2O_3 films on oxidized silicon wafers. We reported previously [90] on conventional ridge waveguides in the same material system, which allows us a comparison with the present results. The double-ridge waveguide was dimensioned such as to keep the scattering loss in the straight waveguides approximately equal to those of the single-ridge case and to reduce the radiation losses. This led to a total ridge height of 130 nm, an inner ridge height of 40 nm and a distance $D = 0.4$ μm. To create
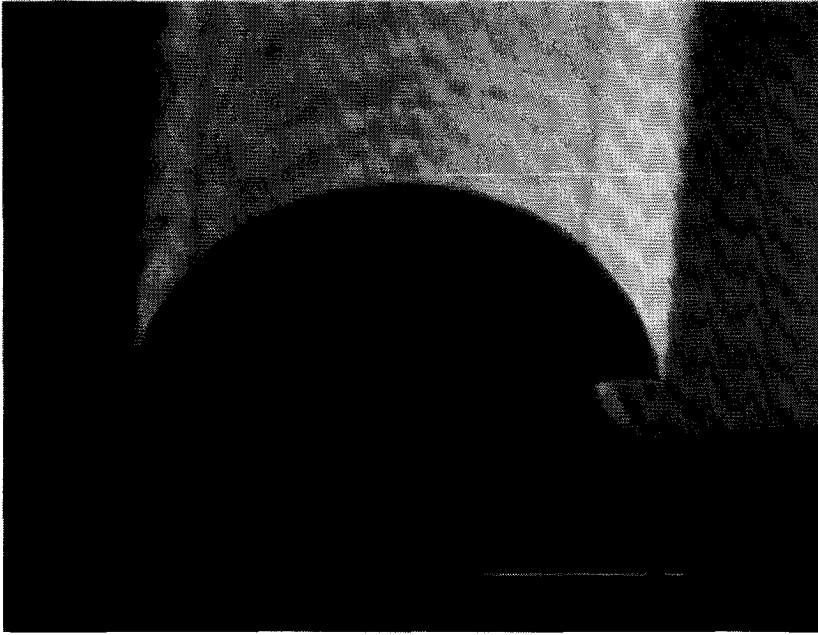
Fig. 6.13 *SEM photograph showing controlled underetch in photoresist covered SiO_2 on Al_2O_3 (bar represents 1 μm).*

the double-ridge guide we used a self aligned process that creates both ridges in one photolithographic step. On top of the Al_2O_3 film we sputtered 400 nm SiO_2, on which photoresist was applied, patterned and developed. Buffered HF was then used to etch the SiO_2 film. Due to the isotropic nature of this etch a large underetch developed (*See* Fig. 6.13), the amount of which could be controlled by varying the etching time. The photoresist defined the 90 nm high outer ridge that was etched by atom beam milling and after stripping the photoresist the remaining SiO_2 served to mask the inner ridge of 40 nm height. The SiO_2 mask was then etched away and a cladding layer of 650 nm SiO_2 was sputtered as a cover.

The same mask was used to pattern both the single and the double-ridge waveguide. Since the straight single-ridge waveguides were 2.5 μm wide, the inner ridge of the straight double-ridge waveguides was 1.7 μm wide.
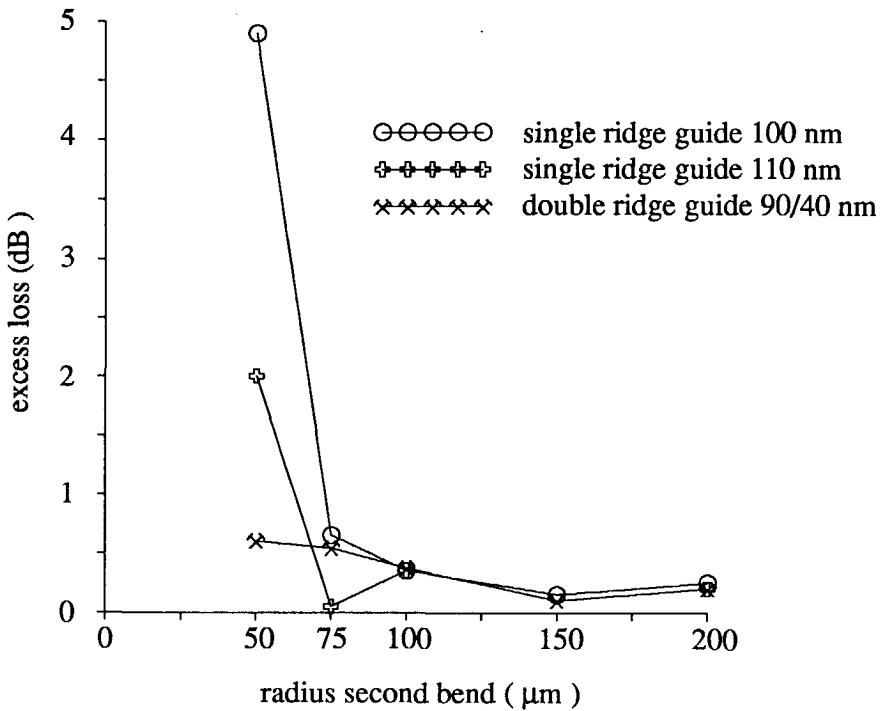
Fig. 6.14 *Measured S-bend losses for the HE$_{00}$ mode (The markers denote the measured values which have been connected by straight lines for convenience).*

Results

We fabricated five different S-bends, where every S-bend started with a 90° $R = 200$ µm bend and the second 90° bend had $R = 50, 75, 100, 150$ and 200 µm respectively. All S-bends had optimized offsets at the junctions between straight and curved sections in order to reduce the transition losses [90]. Light from a He-Ne laser was coupled into and out of the waveguides by means of prisms [88]. The attenuation for the straight waveguides was measured by sliding the output prism along the waveguide and was found to be 3.8±0.5 dB/cm for a 100 nm single-ridge guide and 4.4±0.4 dB/cm for a 110 nm single-ridge guide. The 130 nm double-ridge guide had only 4.7±0.3 dB/cm attenuation. This value of 4.7 dB/cm is slightly higher than the predicted reduction from 11.6 dB/cm to 3.6 dB/cm as can be seen from Fig. 6.12. This deviation may be due to extra roughening of the SiO$_2$ mask during the buffered HF etch. The total attenuation of these S-bends was compared with four straight reference waveguides. Figure

6.14 shows the results for 100 nm and 110 nm single-ridge guides and a double-ridge guide with 130 nm total ridge height (i.e. 90 + 40 nm). The double-ridge guide showed a total excess loss of 0.6 dB for the $R = 50$ μm 90° S-bend, which is the lowest value for bending losses reported thus far.

Conclusions

The double-ridge waveguide offers a solution to the conflicting requirements for short bends and for low scattering losses. A self aligned procedure has been used to create this waveguide. Experiments show a simultaneous reduction in bending and scattering losses. A total bending loss as low as 0.6 dB has been measured for a 90° S-bend with a radius of curvature of 50 μm.

6.4.2 Modeling of the scattering losses

This addendum discusses the modeling of the scattering losses in more detail. The propagation losses of waveguides are due to the absorption of light, to Rayleigh scattering in the bulk medium, and to scattering that is caused by the roughness of the interfaces and the sides of the ridge. The contribution of the absorption, the Rayleigh scattering and the scattering caused by the roughness of the transversal interfaces is assumed to be independent of the width and height of the ridge and is accounted for by the constant α_0 in Eq. (6.4.1). This constant is equal to the propagation loss of the planar waveguide without a ridge. The scattering loss of a planar slab waveguide has been discussed by Marcatili [69], by Tien [114] and by Hinken and Unger [47][117].

An expression is desired that gives the additional scattering loss caused by the ridge, which is usually the dominant loss. We combine equations (3a), (13) and (90) of Marcuse [69] for a symmetric slab waveguide with film index N_2, cladding index N_1, width w and for the fundamental mode of the EH-polarization with propagation constant β_0. We find

$$\alpha = \left\{ \frac{|e_x(y=w/2)|^2(N_2^2-N_1^2)^2}{\int_{-\infty}^{\infty} |e_x(y)|^2 dy} \right\} \cdot \left\{ \frac{A^2 k_0^2}{2\pi B} \right\} \cdot$$

$$\left\{ \int_{-N_1 k_0}^{N_1 k_0} \frac{\rho/\beta_0}{(\beta_0^2-\beta)^2+B^{-2}} \left[\frac{\cos^2\sigma w/2}{\rho^2\cos^2\sigma w/2+\sigma^2\sin^2\sigma w/2} + \frac{\sin^2\sigma w/2}{\rho^2\sin^2\sigma w/2+\sigma^2\cos^2\sigma w/2} \right] d\beta \right\}$$

$$\overset{def}{=} \left\{ \frac{|e_x(y=w/2)|^2(N_2^2-N_1^2)^2}{\displaystyle\int_{-\infty}^{\infty}|e_x(y)|^2dy} \right\} \cdot \alpha_1 , \tag{6.4.2}$$

where $\rho = \sqrt{N_2^2 k_0^2 - \beta^2}$, $\sigma = \sqrt{N_1^2 k_0^2 - \beta^2}$, A is the rms deviation of the interface from perfect straightness and B is the correlation length. Equation (6.4.2) has a form which suggests that the first factor describes the main influence of the waveguide parameters and the second and the third factor describe the influence of the roughness on the propagation losses. The second and third factor in Eq. (6.4.2) are thus replaced by a constant α_1 which depends on the material system and the fabrication process. Equation (6.4.2) gives the propagation loss for the interface $y = w/2$ only. The propagation loss doubles if the roughness on both interfaces $y = \pm w/2$ is not correlated. We, thus, take it for granted that the propagation loss for multiple interfaces is given by the sum of all the contributions of the individual

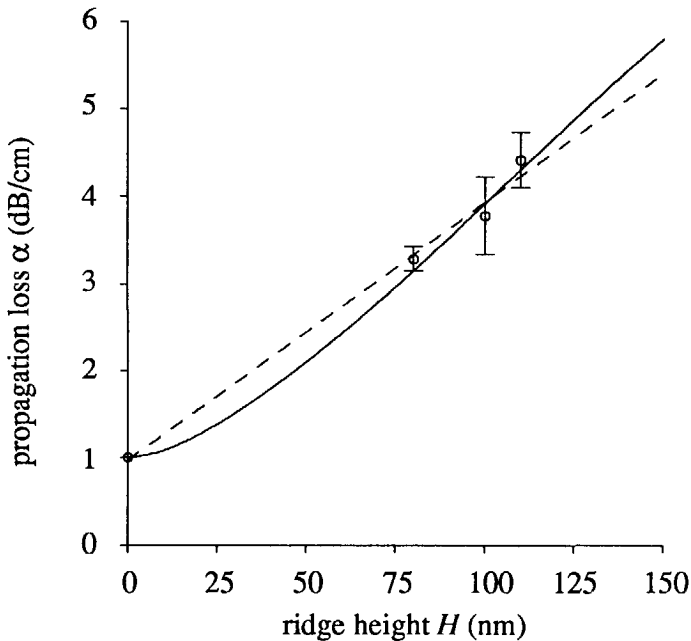**Fig. 6.15** *The propagation losses in relation to the etched ridge height for a 2.5 μm wide waveguide. The solid curve has been calculated by means of Eq. (6.4.1) plus $\alpha_0 = 1$ dB/cm and $\alpha_1 = 0.141$ dB. The dashed curve is the linear interpolation $\alpha = 1.0 + 0.03H$.. The markers denote measured values and the error bars give the standard error of the mean.*

interfaces where the field is evaluated. It is also assumed that the method of effective dielectric constant may be applied. A relation similar to Eq. (6.4.2) is given by Eq. (11) in Hinken [47]. Equation (6.4.2) corresponds to the fill factor Eq. (1) in Deri *et al.* [26] or Eq. (2) in Seto *et al.* [101]

Figure 6.15 gives the propagation losses as a function of the ridge height for an Al_2O_3/SiO_2 waveguide with a film thickness of 250 nm at a wavelength of 632.8 nm and a width of 2.5 μm. The calculated losses, a linear interpolation, and the measured propagation losses are indicated in the figure.

One interesting result of the calculations by means of Eq. (6.4.1) is that the scattering loss in curved waveguides can be either larger or smaller than the value for the corresponding straight waveguides. If the curved waveguide has a large radius of curvature and it is wide enough to operate in the whispering-gallery mode regime, then the scattering losses are lower than those of a straight waveguide because there is only one interface that scatters the light. If, on the other hand, we have a curved waveguide with a small radius of curvature, then the scattering loss of the bend is larger than that of the straight waveguide, because the field intensity at the interface is much larger for the curved than for the straight waveguide. This difference can be quite significant. The scattering losses for the waveguides that we have been discussing in this chapter with a ridge height of 100 nm and the radii of curvature that we fabricated are approximately two times larger than the scattering losses for the straight waveguides. It seems unlikely that these differences can be verified experimentally.

6.5 Self-aligned doubly etched bends

6.5.1 Introduction

The radiation losses of a curved waveguide can be reduced by the application of a large lateral refractive-index contrast as discussed in section § 5.2.2. A large lateral refractive-index contrast is achieved by a high ridge in the case of ridge waveguides, but the high ridge may have effects that are in conflict with the correct operation of other devices. The natural solution seems to be the etching of a high ridge at the sites where the high ridge is needed, i.e. around the curved waveguides only as illustrated in Fig. 6.16. This poses two problems. Firstly, a self-aligned technique must be used because our photolithography is not capable of aligning a mask with the required accuracy of approximately 0.1 μm. Secondly, transition losses occur at the junction of the low-ridge waveguide and the high-ridge waveguide, because the field distributions of the modes differ in each waveguide.

The location of this junction should not coincide with the junction of the bend and the straight waveguide, because high losses might result if a part of the curved waveguide has a small ridge. It is better to locate the junction of the low-ridge and the high-ridge waveguide approximately 10 μm or more away from the curved waveguide as indicated in Fig. 6.16.

6.5.2 Modeling

The strategy of the 'self-aligned doubly etched' (SADE) bends creates new junctions where the low-ridge waveguide and the high-ridge waveguide meet. The cross-sections of the low-ridge and high-ridge waveguides are shown in Fig. 6.17. The transition losses at this junction have been estimated by applying the one-dimensional overlap integral that has been derived in section § 4.2. The numerical results for the transition losses are also shown Fig. 6.17. From the plot, we can draw the conclusion that the transition losses increase with increasing ridge-height difference $h_2 - h_2'$ and with decreasing width w of the straight waveguides. The transition losses increases sharply when the lateral field distribution in the low-ridge section broadens, i.e. when the low-ridge waveguide becomes monomode. Monomode operation is achieved at ridge heights of 67 nm, 18 nm, 8 nm and 4 nm for widths of 1 μm, 2 μm, 3 μm and 4 μm, respectively. The transition losses are 0.07 dB, 0.50 dB, 0.74 dB and 0.97 dB for these four widths, respectively, which means that they are sufficiently low for the 1-μm wide waveguide only. The
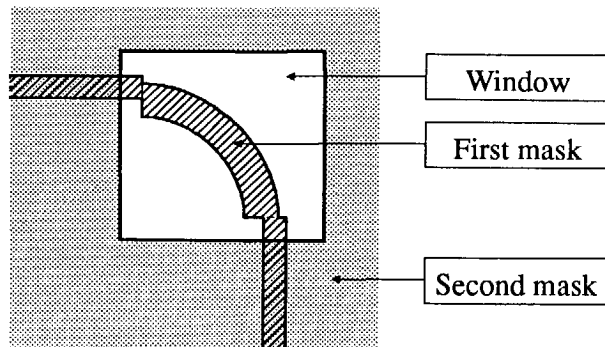
Fig. 6.16 *The self-aligned doubly etched (SADE) bend is fabricated by means of two masks and a self-aligned technique. The first mask defines the waveguiding structure and a low ridge is etched. The second mask defines a window around the curved waveguide. The region within this window is etched again which results in a high ridge. The alignment of the second mask is not critical if the size of the window is at least 10 μm more larger than the bend.*

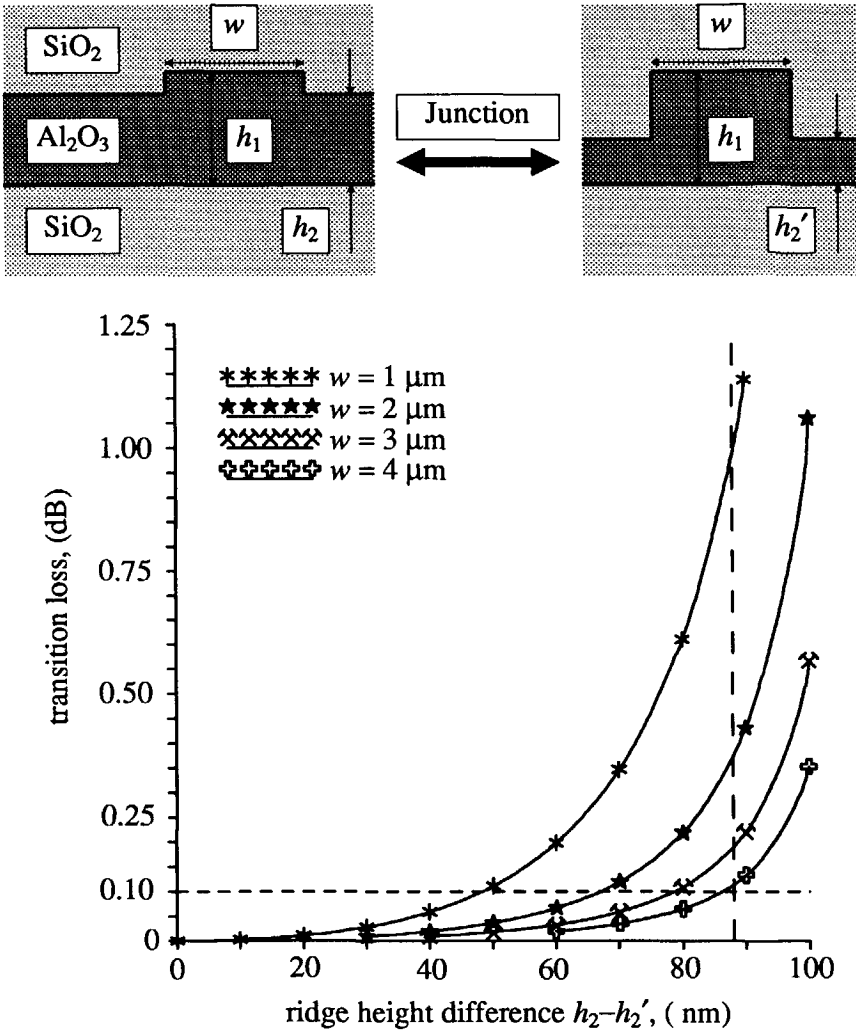***Fig. 6.17*** *Cross-section of the low-ridge and the high-ridge waveguide (top) and the transition losses at the junction of these two waveguides (below). The wavelength is 632.8 nm, the film thickness h_1 is 250 nm and the thickness h_2' is 140 nm. The horizontal dashed line marks a transition loss of 0.1 dB and the vertical dashed line marks the realized difference of 88 nm. The calculations have been done for the HE$_{00}$-modes.*

losses are more acceptable if the waveguide is bimodal, where the HE_{01} mode is close to cutoff. The asymmetric HE_{01}-mode is relatively unimportant then because the scattering and the radiation losses are high.

The transition losses depend strongly on the abruptness of the transition. For the 2-μm wide waveguide, for example, the transition loss is 0.50 dB at the junction where the ridge height changes 18 nm to 110 nm. If there is an intermediate section with a ridge height of 40 nm, the transition losses reduces to 0.26 dB and they vanish altogether when the change in ridge height is adiabatic.

A correct prediction of the transition losses is crucial to the modeling of the self-aligned doubly etched bends. We have, therefore, compared the result of a one-dimensional overlap integral for a field distribution that has been calculated by means of the effective-dielectric-constant method with the value of a two-dimensional overlap integral for a field distribution that has been calculated by means of the numerically accurate domain-integral-equation[§] method [59]. For a junction of two straight waveguides with a width of 2.1 μm, a film thickness of 260 nm, a low ridge height of 22 nm and a high ridge height of 110 nm, the first technique results in a value for the transition loss of 0.36 dB while the latter technique results in a value of 0.40 dB. These values show that the results of the one-dimensional overlap integral in combination with the effective-dielectric-constant method are accurate enough for our purposes.

The aforementioned transition losses are based on the overlap integral for the fundamental modes in the low-ridge waveguide and in the high-ridge waveguide. A more complete analysis has to include the multimode-interference effects and these effects have been taken into account in the predicted losses shown in Table 6.2.

Secondly, we have to know the minimum size of the window shown in Fig. 6.16, because the radiation losses of the curved waveguide are not sufficiently reduced if the window is too small. Figure 6.18 shows the radiation loss in relation to the size of the gap between the outside of the bend and the point where the singly-etched film begins. Figure 6.18 shows that the radiation losses increase very fast for gaps that are smaller than 1 μm and that the radiation loss is already close to the limiting value of 1.67 dB/90° for gap sizes greater than 4 μm. Note that the radiation loss oscillates when the size of the gap is varied, which is caused by the interference between the light that is radiated outward and its reflection at the singly-etched film with a higher effective index of refraction. The resulting

---

§   These calculations have been performed by N.H.G. Baken and J.J.G.M. van der Tol of the PTT
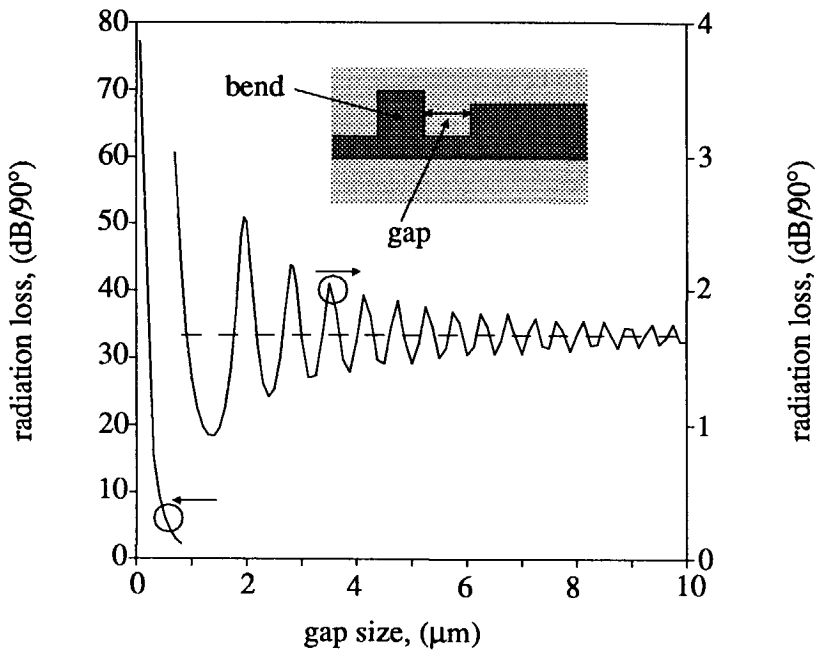   Research Neher Laboratories, Leidschendam, the Netherlands.

Fig. 6.18 *Radiation loss in relation to the gap size for the HE$_{00}$-mode in a 3-µm wide bend with a radius of curvature of 50 µm . The as-deposited Al$_2$O$_3$ film is 250 nm thick and the etched part is 150 nm thick. The dashed horizontal line indicates a radiation loss of 1.67 dB/90°, which is reached when the gap size becomes infinite. The vertical axis on the left-hand side refers to gap sizes smaller than 1 µm and the vertical axis on the right-hand side refers to gap sizes larger than 1 µm.*

interference pattern either enhances or reduces the radiation loss with an estimated period

$$\lambda_{\Delta R} \approx \frac{\pi}{k_r} \approx \frac{\lambda_0}{2\sqrt{N_{gap}^2 - \left\{\dfrac{\text{Re}(\gamma)}{k_0 r}\right\}^2}} \, , \tag{6.5.1}$$

where k_r is the radial component of the wave number (*see* Eq. (4.1.1)). This local period depends on r and the substitution of the effective refractive index $N_{gap} = 1.52317$, the wavelength $\lambda_0 = 632.8$ nm and the real part of the angular propagation constant $\text{Re}(\gamma) = 768.61$ yield a period of 0.54 µm for $r = 55$ µm and 0.39 µm for

$r = 60$ μm. Just outside of the bend we have the caustic (corresponding to $u = u_{II}$ in Fig. 4.2) where $k_r \rightarrow 0$ and consequently, the oscillation disappears.

These calculations show that a window whose border is at least 10 μm separated from the curved waveguide everywhere, performs satisfactorily.

6.5.3 Experiments

The self-aligned doubly etched bends have been fabricated by means of the same mask with five different S-bends, with radii of curvature of 50 μm, 75 μm, 100 μm, 150 μm and 200 μm, that had been used for the experiments described in the sections § 6.2 and § 6.4. This mask defines straight waveguides that are 2-μm wide and become monomode for a ridge height of 18 nm. A new mask was fabricated to define the windows. A layer of 250 nm Al_2O_3 was sputtered on a 2 inch (100) silicon wafer with 2.1 μm thermal oxide SiO_2 on top of it.

A self-aligned technique has been used by Albrecht *et al.* [2] and by Niggebrügge *et al.* [83] to make totally-reflecting corner mirrors, where a 200-nm thick SiO_2 layer defined the waveguides and an AZ-type photoresist defined the windows. We[§] have used two layers of AZ-5214E reversal photoresist on top of each other to define both the waveguides and the windows, which eliminates the extra step required to make the SiO_2 mask. A first layer of AZ-5214E photoresist defined the waveguides. Argon beam milling was used to etch 18 nm away from the 250-nm thick Al_2O_3 film. The photoresist was then subjected to a post-bake treatment of 5 times 5 min at 110 °C, 120 °C ..150 °C respectively plus 15 min at 160 °C. A second layer of AZ 5214E photoresist was spun on top of the previous layer. Subsequent illumination and development opened the windows around the bends. Argon-beam milling was used to remove another 80 nm from the Al_2O_3 film within the windows. A 600-nm SiO_2 cover layer was sputtered on top after the removal of the photoresist. A standard annealing treatment of 55 min at 800 °C was given and a chromium coating was applied and etched open around the waveguides with the purpose to improve the sensitivity of the attenuation measurements. Two photographs of the fabricated curved waveguides are shown in Fig. 6.19.

The light from an HeNe laser, $\lambda_0 = 632.8$ nm, was coupled into the singly etched and into the unetched Al_2O_3 film. The measured coupling angles are given in Table 6.1 and can be related to waveguide parameters which yield a thickness of 260 nm for the as-deposited Al_2O_3 film and a thickness of 238 nm for the singly-etched Al_2O_3 film, which means that the fabricated ridge height is 22 nm. The coupling

---

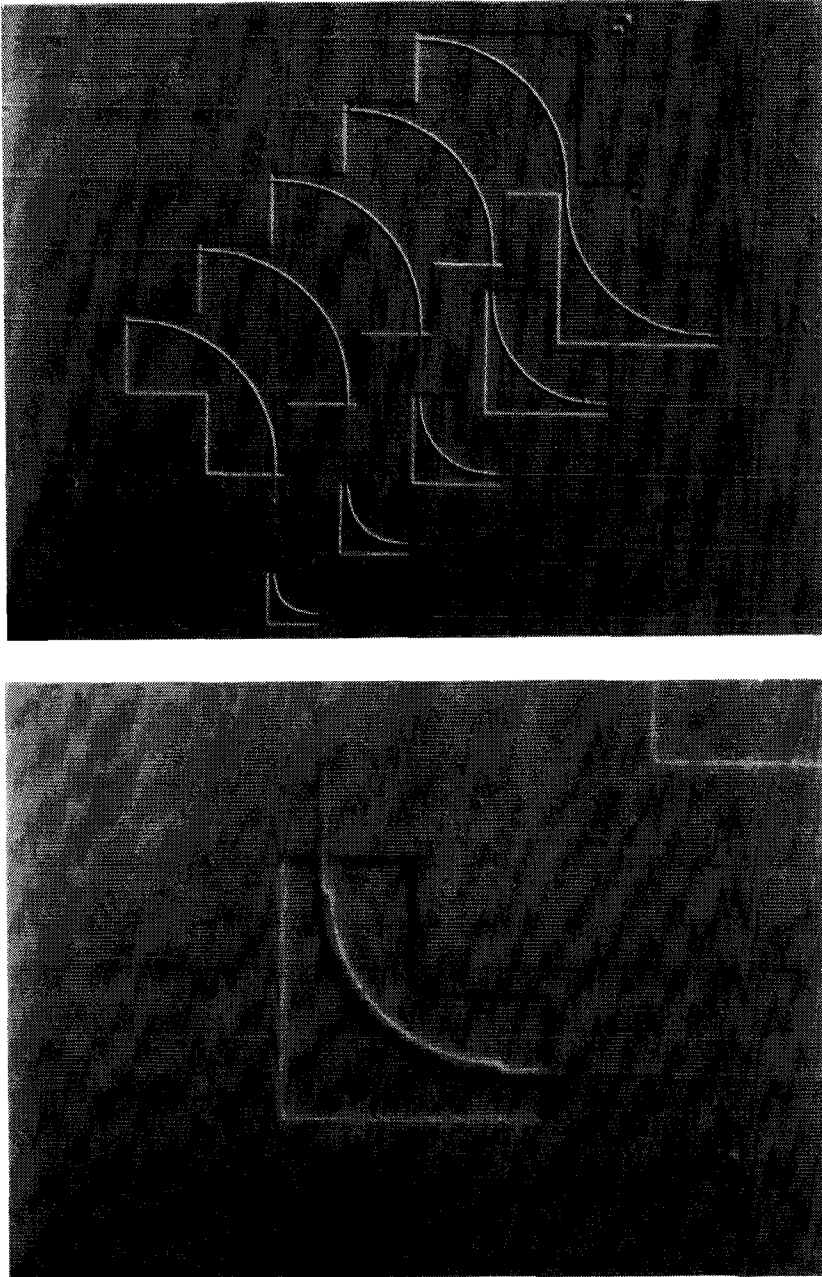[§] J.W.M. van Uffelen, Delft University of Technology, is accredited for his idea of this self-aligned technique.

Fig. 6.19 *Two photographs of the 'self-aligned doubly etched' bends. A set of five S-bends (top)
and a magnification of the R = 50 μm bend (bottom) are shown. The straight waveguides are
more difficult to discern because of the smaller ridge height.*

Table 6.1 *Measured coupling angles and the parameters that have been calculated from these angles (indicated by means of a tinted background). The angle θ_coupling is the angle between the laser beam and the plane of the wafer.*

mode	$\theta_{coupling}$	N_{eff}	$N_{cover} = N_{substrate}$	N_{film}	thickness width	comment
TE_0	20.727°	1.57717	1.457	1.6897	260.3 nm	unetched Al_2O_3 film
TM_0	23.364°	1.55754				
TE_0	21.915°	1.56847		1.6906	237.5 nm	etched Al_2O_3 film
TM_0	24.621°	1.54776				
TE_0	20.727°	1.57717		1.690	259.7 nm	unetched Al_2O_3 film
TM_0	23.364°	1.55754			259.8 nm	
TE_0	21.915°	1.56847			238.6 nm	etched Al_2O_3 film
TM_0	24.622°	1.54776			238.3 nm	
HE_{00}	21.114°	1.57436	1.56847	1.57717	2.08 µm	Calculated with TM-boundary conditions
					2.07 µm	Calculated with TE-boundary conditions
EH_{00}	23.740°	1.55464	1.54776	1.55754	2.11 µm	See above
					2.12 µm	

angles of the HE_{00}- and EH_{00}-mode can be used to estimate the width of the waveguide by means of the method of effective index of refraction, which results in a width of $w = 2.1$ µm.

The total loss was then determined for every S-bend relative to the straight reference waveguides and for both polarizations. The processed wafer contained a total of ten sets of waveguides and each set consists of five S-bends plus four straight reference waveguides. Four sets have been measured and the values of the total loss are listed in Table 6.2 together with the predicted values, which have been calculated as explained in the previous chapters and which include the effects of all junctions and the radiation losses.

6.5.4 Discussion and conclusions

From Table 6.2, we see that the losses for the four S-bends with the larger radii of curvature are dominated by transition losses that occur at the junction of the low-ridge and the high-ridge waveguide. The loss of the $R = 50$ μm S-bend, on the other hand, is dominated by the radiation losses. The total loss of the $R = 200$ μm S-bend is smaller than the losses of the other S-bends, because the $R = 200$ μm S-bend contains two junctions of the low-ridge and the high-ridge waveguide, whereas the other S-bends contain four of these junctions. This indicates that the S-bend losses are, indeed, dominated by the transition losses at the junction.

The large variation in the measured values of the excess loss is probably due to the multimode interference effects. The fundamental mode in the monomode low-ridge waveguide excites several modes (with an even mode number) in the multimode high-ridge waveguide. The interference effects become manifest at the last junction where the total field has to be coupled back to the fundamental mode of the low-ridge waveguide.

The loss figures for the EH-polarization are higher than the losses for the HE-polarization, which is in contradiction to the predicted values, but which is in agreement with other experiments in Al₂O₃/SiO₂ waveguides. This phenomenon seems to defy any explanation.

The best loss figures are 1.0 dB for the $R = 200$ μm S-bend and 2.3 dB for the $R = 150$ μm S-bend both in upper set 5. This corresponds to 0.5 dB per 90° for the $R = 200$ μm S-bend and 1.15 dB for the $R = 150$ μm S-bend. These values are higher than the S-bend losses that have been reported in the sections § 6.2 and § 6.4 but this is not a fair comparison. The losses for the self-aligned doubly etched S-bends have to be compared to the losses of totally-reflecting corner mirrors, 1 dB/mirror [2] or 1.5 dB/mirror [83], that have also been fabricated with a self-aligned technique and that also contain low-ridge waveguides and high-contrast mirrors. Secondly, a curved waveguide with a ridge height of 22 nm must have a radius of curvature of the order of 1 mm in order to obtain a similar loss of 0.5 dB/90°. The technique of the 'self-aligned doubly etched' (SADE) bends is, thus, very promising if looked upon in this way. Furthermore, the transition loss of the junction of the low-ridge and the high-ridge waveguides can be reduced if it is split in two smaller steps, which requires an extra photolithographic step or, by making the transition gradual or adiabatic. The latter could be accomplished by allowing the border of the window to make a small skew angle between the border and the waveguide instead of perpendicular to the waveguide.
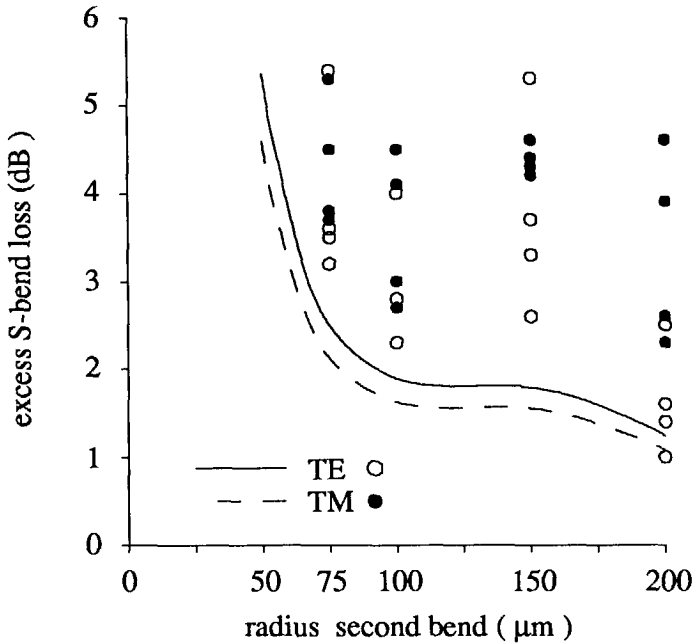
Fig. 6.20 *The measured (markers) and the predicted (curves) excess S-bend losses for the 'self-aligned doubly etched' bends. The measured loss values for the R = 50 μm S-bend do not fit in the graph. (See also Table 6.2)*

Table 6.2 *Total measured and calculated loss figure in dB for SADE S-bends relative to straight reference waveguides. The indicated radius of curvature is the radius of the second 90° bend. The first 90° bend of every S-bend has a radius of curvature of 200 μm. The error σ_{n-1} for the loss of straight reference waveguides is approximately 0.3 dB.*

R	Upper set 5		Lower set 2		Lower set 4		Lower set 5		Predicted	
μm	HE_{00}	EH_{00}	HE_{00}	EH_{00}	HE_{00}	EH_{00}	HE_{00}	EH_{00}	HE_{00}	EH_{00}
200	1.0	3.9	2.5	4.6	1.6	2.3	1.4	2.6	1.24	1.08
150	2.6	4.4	5.3	4.2	3.7	4.3	3.3	4.6	1.79	1.55
100	2.3	4.1	4.0	4.5	2.8	2.7	2.3	3.0	1.89	1.62
75	3.5	4.5	5.4	5.3	3.2	3.7	3.6	3.8	2.49	2.12
50	15.7	16.1	17.0	12.0	22.4	22.4	~	~	5.36	4.59

6.6 Experiments at a wavelength of 1300 nm

The use of Al_2O_3/SiO_2 waveguides at wavelengths of 1.3 μm or 1.55 μm is preferred to a wavelength of 632.8 nm, because glass fibers are operated at these wavelengths. In order to use the Al_2O_3/SiO_2 based waveguides at wavelengths of 1.3 μm or 1.55 μm, adaption of the measurement setup was required. This adaption and the subsequent experiments are the subjects of the following sections.

6.6.1 Adaption of the measurement setup

Up to now, all our experimental setups used one type of laser, i.e. the He-Ne laser which produced light with a wavelength of 632.8 nm. It was desirable that the prism-coupling setup could still be used at 632.8 nm after the adaption to infrared wavelengths and that switching between these wavelengths could be done efficiently. This has been accomplished by using monomode polarization-maintaining glass fibers, that guide the light from the laser to the measurement setup. The use of glass fibers in optical measurement setups has many advantages. The setup becomes modular in the sense that lasers, detectors, modulators, et cetera, can be separated from the 'actual' setup around the chip, which leads to a simpler setup. Most measurement setups are constructed around the source of light instead of around the chip, since the laser is the largest and least flexible part of the setup. Secondly, the adaption of the measurement setup can be done by merely disconnecting a fiber and replacing it by another one. A schematic picture of the new setup is given in Fig. 6.21.

Laser and power supplies

The source of light for the adapted prism-coupling setup is a GaInAsP Fabry-Pérot laser (Philips 503CQF #1983[§], 2 mW) with a fiber pigtail and a mode-gravity wavelength of $\lambda_0 = 1.303$ μm at a temperature of 20 °C. A power supply has been designed and built that can house this laser as well as several other types of lasers, such as an AlGaAs power laser that is used in a new type of measurement setup that determines the propagation losses of GaInAsP/InP waveguides by means of the twin guide [4]. The power supply is able to generate a constant threshold current with a pulsed current on top of it. The maximum value of the pulsed current is 500 mA and the minimum pulse time that can be generated is 60 ns. An internal 1-2 kHz modulator is used to modulate the laser which permits the detection of the signal by means of a lock-in amplifier. The power supply protects the laser

---

[§] This laser was obtained by courtesy of Philips Research Laboratories, Eindhoven, the Netherlands.
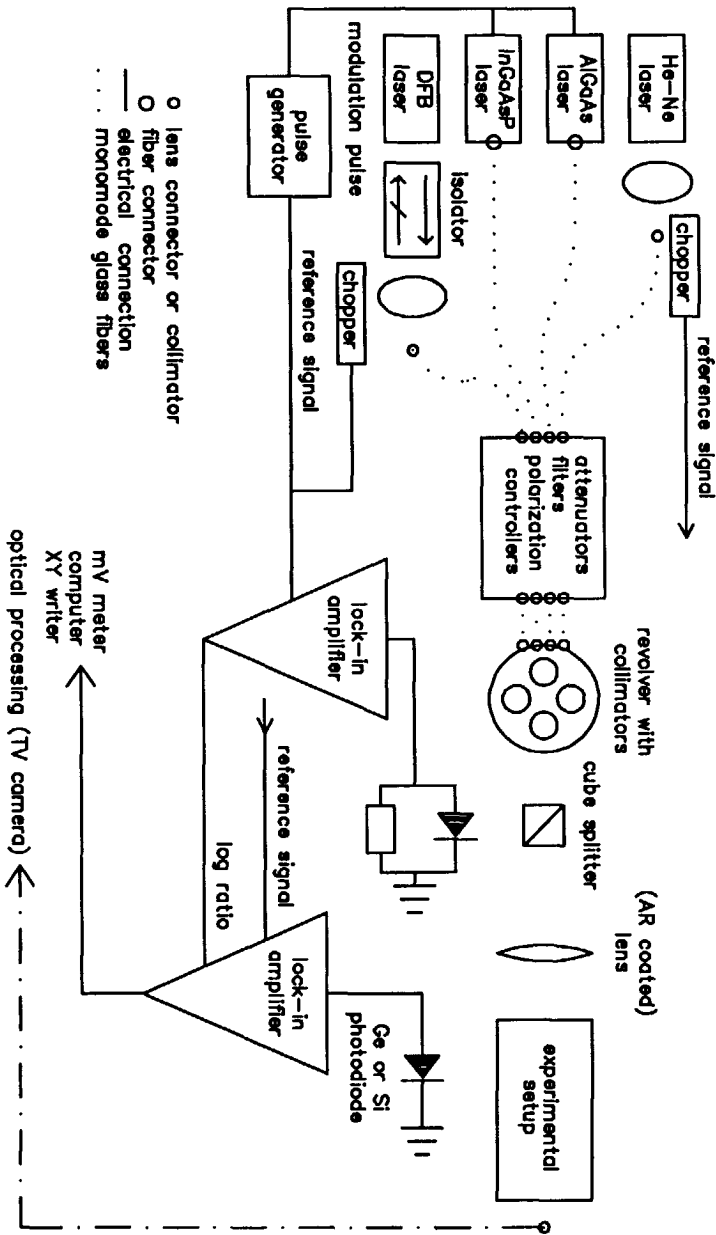
Fig. 6.21 *Schematic drawing of the adapted measurement setup. It gives an impression how glass fibers have been used to connect the lasers to the actual measurement setup. The lasers do not have to form part of the actual setup. The light is carried instead from the laser to the setup by means of monomode glass-fibers, connectors and collimators.*

against large forward currents, against a reverse bias and against fluctuations in the mains supply. The 1.3 μm laser is housed in the power supply and is connected to the setup by means of a fiber jumper and an adapter.

Fiber connectors

The Seiko FC-type connector has been chosen by us to connect all glass fibers. This fiber connector was chosen by NTT as the Japanese standard, it is suited to connect monomode polarization-maintaining fibers and it comes in one version which makes it more flexible than connectors that come in two complementary versions. Mounting the fiber into the connector (ferrule) is a precise and time-consuming job which requires special polishing equipment. An FC-type connector has been mounted to the fiber pigtail of the 1.3-μm laser by Seiko who provide this service.

The interface fiber-measurement setup

The glass fiber is usually cleaved and placed in an x, $,y$, z, φ, θ manipulator in front of a microscope objective. If the fiber is correctly cleaved, a good parallel beam is obtained by placing the fiber end in the focus of the objective. This is not a mechanically rigorous interface and it requires frequent adjustment and aligning, especially when the sources are regularly interchanged. A more elegant approach is provided by using lens collimators. We acquired jumpers that consist of a monomode polarization-maintaining fiber with an FC-type connector at one end and a collimator at the other end. The collimator (OZ-optics) itself consists of an AR-coated GRIN lens in a φ, θ manipulator that could be made to fit in the applied Spindler and Hoyer mounts.

Polarization

The polarization state of the light that emanates from a glass fiber is unknown and it may change completely if the fiber is moved or bent. A few precautions are, therefore, necessary. A polarization controller can be used such as the fiber squeezer [58]. Secondly, polarization-maintaining fibers can be used to eliminate changes of the polarization. A third option is the use of a polarizer in front of the fiber collimator. The changes in polarization are then manifested as power fluctuations, but these can in turn be eliminated by using a cube splitter and by measuring the power ratio of the input and output beam as indicated in Fig. 6.21. The second and the third option have been used in the adapted prism-coupling setup.

Detector

A Germanium photodiode (Germanium Power Devices, GM8CS) has been used to detect the light. The photodiode has a diameter of 5mm and is mounted on a ceramic substrate, which has been glued to the prism that is used to couple the light out of the waveguide. It is important that the active area of the photodiode is large in order to detect all the light that is coupled out of the waveguide.

6.6.2 Experiments[§]

Fabrication of the slab waveguide

Before the fabrication of S-bends, the planar slab waveguide has been designed, fabricated and measured and optimized with respect to the annealing treatment, that we apply to reduce the propagation losses. The slab waveguides have been fabricated on thermally oxidized silicon wafers. The resulting SiO_2 layer has a thickness of 4.15 μm, which is thick enough to prevent leakage of light to the silicon substrate. A layer of Al_2O_3 of 500 nm thickness was sputtered on top of the wafer (*See also* Fig. 6.23). This thickness has been chosen such that the resulting slab waveguide is well in the monomode regime. The thickness of the Al_2O_3 layer of 250 nm at $\lambda_0 = 632.8$ nm can, in fact, be scaled directly to a thickness of 500 nm at $\lambda_0 = 1.3$ μm.

The alignment of the fiber collimator and the emanating beam of light has been achieved by first coupling the light of the He-Ne laser ($\lambda_0 = 632.8$ nm) into the slab waveguide. Two pinholes could then be aligned to the He-Ne beam and finally the light from the fiber collimator could be aligned by means of the two pinholes. No subsequent optimization was necessary. The coupling angle of the TE_0-mode was found to be $\theta_{coupling} = 20.313°$ and the coupling angle of the TM_0-mode was found to be $\theta_{coupling} = 23.056°$. These two coupling angles can be used to give both the index of refraction and the thickness of the sputtered Al_2O_3 film, provided that the indices of refraction of the SiO_2 layer and the prism are known for a wavelength of 1.3 μm. The index of refraction of SiO_2 (fused silica) is $n(SiO_2) = 1.447$ for a wavelength of 1.3 μm ($n(SiO_2) = 1.457$ at a wavelength of 632.8 nm) [3]. The prism has been fabricated from SF13 glass (Schott, melt nr. 13028). Measurements[¶] indicated that the specification of the index of refraction by the manufacturer has to be augmented by 0.00022. This resulted in an index of refraction $n_{prism} = 1.7356$ at a wavelength of 632.8 nm and $n_{prism} = 1.7088$ at a wavelength

---

[§] The measurements have been performed by E.G. Wienke, Delft University of Technology.
[¶] F.H. Groen, Delft University of Technology. Private communication.

of 1.3 µm, where the dispersion equation has been interpolated outside the specified range of 356 - 1014 nm. The use of $n(\text{SiO}_2) = 1.447$, $n_{prism} = 1.7088$ and the measured coupling angles leads to an index of refraction $n(\text{Al}_2\text{O}_3) = 1.677$ and a thickness of 494 nm of the sputtered Al$_2$O$_3$ film.

Propagation loss of the slab waveguide

The propagation loss was subsequently measured by sliding the output prism over the waveguide and simultaneously monitoring the output power. A propagation loss of 0.68 dB/cm was found for the TE$_0$-mode and a propagation loss of 0.61 dB/cm was found for the TM$_0$-mode. These values are lower than the value of 1.0 dB/cm which is found for 250 nm thick Al$_2$O$_3$ films at a wavelength of 632.8 nm. Previous experiments have shown that the propagation loss of 250 nm thick Al$_2$O$_3$ films at a wavelength of 632.8 nm is considerably reduced by an annealing treatment of one hour at a temperature of 800 °C. An identical annealing treatment has been given to the 500 nm thick slab waveguide but it was to be expected that this treatment could be optimized. The second slab waveguide was fabricated and subjected to an annealing treatment[§] of 30 min at a temperature of 700 °C. After the determination of the propagation loss, the wafer was subjected to an annealing treatment of another 30 min at a temperature of 725 °C. This procedure was repeated several times and Fig. 6.22 shows the influence of the annealing treatment on the propagation loss. A minimum propagation loss of 0.35 dB/cm is obtained after the annealing treatment at a temperature of 825 °C. The total annealing treatment of several times 30 min is equivalent to one treatment of an hour at a constant temperature of 825 °C, because previous experiments have shown that an increase in annealing temperature of 25 °C increases the reaction rate by an approximate factor of two [105].

The propagation loss of 0.35 dB/cm of the slab waveguide is an improvement to the value of 1.0 dB/cm at a wavelength of 632.8 nm and this increases the applicability of the Al$_2$O$_3$/SiO$_2$ waveguide system for telecommunication-oriented optical integrated circuits. A reduction of the propagation loss might have been expected on account of the λ_0^{-4}-dependence of the Rayleigh scattering. The absorption of light in bulk Al$_2$O$_3$ at a wavelength of 1.3 µm, on the other hand, seems to increase by a factor of four with respect to the absorption at 632.8 nm [20]. The measured decrease of the propagation loss of the slab waveguide by an

---

[§] The optimization of the annealing treatment has been performed by A.H. de Vreede, Delft University of Technology.
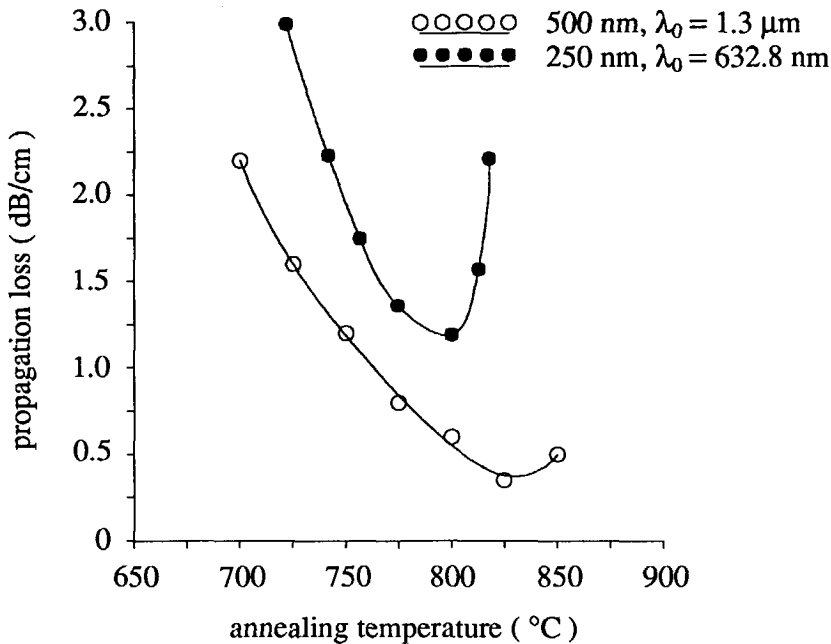
Fig. 6.22 *The effect of the annealing treatment of the wafer on the propagation loss. Every measured point represents a consecutive annealing treatment of 30 min to the same wafer at an elevated temperature. The data on the influence of the annealing treatment at a wavelength of 632.8 nm are shown for comparison [105].*

approximate factor of three seems to indicate that both the increased absorption and the reduced Rayleigh scattering apply.

Fabrication and measurement of S-bends

Little has been reported in the literature on the fabrication of curved waveguides in dielectric materials at wavelengths around 1.3 μm or 1.55 μm. Himeno, Terui and Kobayashi, however, have fabricated reflecting mirrors in high-silica waveguides, that consist of a SiO_2-TiO_2 core and a SiO_2 cladding on a silicon substrate and operate at a wavelength of 1.3 μm [44][45], and reported the fabrication of curved waveguides with radii of curvature in excess of 5 mm [46].

We will now describe the fabrication and subsequent measurement of S-bends in the form of buried waveguides. The cross-section of the straight waveguides is shown in Fig. 6.23. Buried waveguides provide a maximum lateral refractive-index contrast, which permits the fabrication of very small bends (*see* section § 5.2.2). Five S-bends have been designed and these S-bends resemble the set

shown in Fig. 6.6 very much. Each S-bends has first a curved-waveguide section with a section angle of 90° and a radius of curvature of 200 μm, which is followed by a small straight section and a second curved-waveguide section with a section angle of 90° and a radius of curvature of 50, 75, 100, 150 and 200 μm, respectively, for the five S-bends (the radius of curvature corresponds to the outer side of the waveguide). The curved sections have a width of 6 μm, which is large enough to permit the guidance of whispering-gallery modes (*see* section § 5.2.3). The subsequent optimization of the junction as described in section § 5.2.4 led to a width of the straight waveguide of 3 μm and lateral offsets of $\Delta r = 0.75, 0.98, 1.13,$ 1.33 and 1.50 μm for the five aforementioned radii of curvature, respectively (*offset* = $w_{curved}/2 - \Delta r$). The straight waveguides that interconnect both curved section of every S-bend are 162.3, 137.5, 112.6, 62.8 and 13.0 μm long, respectively, for the five S-bends.

The adapted prism coupling setup has then been used to couple light with a wavelength of 1.3 μm in a 40 μm-wide waveguide that may be considered as being equivalent to the slab waveguide without lateral confinement. The measured coupling angles of 20.212° and 22.886° for the TE_0- and the TM_0-mode respectively lead to a thickness of 507 nm and an index of refraction of 1.675 for the Al_2O_3 film. The coupling angles of 21.751° for the HE_{00}-mode and 24.112° for the EH_{00}-mode lead, by means of the method of effective dielectric constant, to a
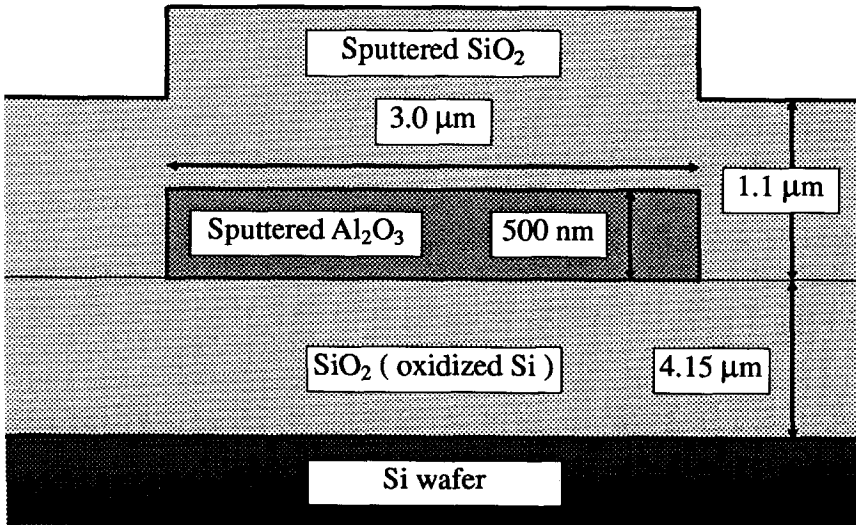

Fig. 6.23 The straight-waveguide cross-section for operation at a wavelength of 1.3 μm.

fabricated width of the straight waveguide of 2.9 μm and 3.0 μm, respectively. The excess loss has subsequently been determined for the S-bends, which is interpreted as the difference in power of the light that is coupled out of the last straight section of the S-bend and the average power of four straight reference waveguides. Three fabricated sets of S-bends have been measured and the resulting loss values are shown in Fig. 6.24 together with the predicted values.

From Fig. 6.24, we can see a sharp increase of the loss for the $R = 50$ μm S-bend. The excess loss of the $R = 75$ μm S-bend and the HE_{00}-mode amounts to the very low value of 0.23 dB, which indicates a correct optimization of these bends. The predicted values for the losses of the S-bends are too small, which seems to be due to a too large lateral refractive-index contrast that follows from the method of effective dielectric constant. The calculated losses are larger for the EH_{00}-mode than for the HE_{00}-mode, which is in agreement with the observations and the calculations for the EH_{00}-mode give the correct threshold radius of curvature of 75 μm.
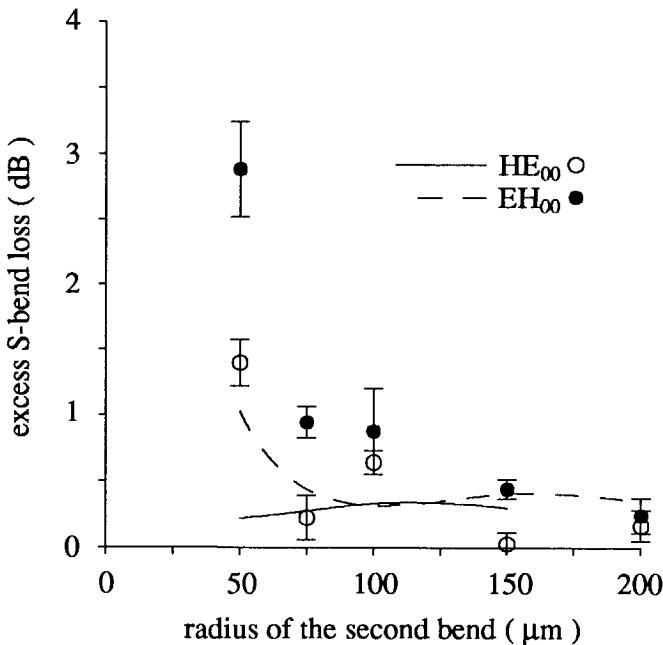

Fig. 6.24 *The excess loss of the five S-bends relative to the average loss value of the straight reference waveguides for the two fundamental modes. The solid and dashed line connect predicted values. The error bars indicate standard errors of the mean.*

Conclusions

It has been shown in this section that stable waveguides can be fabricated that consist of a 500 nm thick Al$_2$O$_3$ layer sandwiched between thermally oxidized and sputtered SiO$_2$ on a silicon substrate. A propagation loss of 0.35 dB/cm was obtained at a wavelength of 1.3 µm after an annealing treatment of one hour at a temperature of 825 °C. S-bends have been fabricated in the form of buried waveguides and an excess loss of 0.23 dB has been measured for the S-bend, which contains a 90°-bend with a radius of curvature of 75 µm. This value is lower than any published value for the losses of S-bends. The predicted losses of the S-bends are too low, which indicates that the method of the effective dielectric constant gives a value for the lateral refractive-index contrast which is too large. These experiments demonstrate the suitability of Al$_2$O$_3$/SiO$_2$-based waveguides for optical integrated circuits at a wavelength of 1.3 µm.

Chapter 7

GaInAsP/InP waveguides; experiments

This chapter describes the design and fabrication of curved ridge or rib waveguides in GaInAsP lattice-matched to InP at wavelengths of 1.3 and 1.52 μm and the subsequent measurement of the losses of these bends. The measurements show that the modeling and loss-reduction techniques described in the preceding chapter are also applicable to curved waveguides in III-V semiconductors. These experiments have been published in the form of a letter to Electronics Letters and a presentation at ECOC '89. This chapter contains both manuscripts plus two addenda.

7.1 S-bends in LPE-grown GaInAsP

The following manuscript has been published by Electronics Letters [119]. It is a joint publication by the Research Neher Laboratories and the Departments of Electrical Engineering and Applied Physics, Delft University of Technology. This work was the subject of a conference presentation by Doeksen at ECOISA '89 [30] and was presented in a talk at SIOE '89 [91].

7.1.1 Manuscript Electronics Letters

Low-loss Straight and Curved Ridge Waveguides in LPE-grown GaInAsP

H. VAN BRUG[‡], F.H. GROEN[‡], J.W. PEDERSEN[‡§], Y.S. OEI[†], E.C.M. PENNINGS[†], D.K. DOEKSEN[¶], J.J.G.M. VAN DER TOL[¶]

[‡]*Delft University of Technology, Department of Applied Physics, Optics Research Group, Lorentzweg 1, 2628 CJ Delft, the Netherlands*
[†]*Delft University of Technology, Department of Electrical Engineering, the Netherlands*
[¶]*PTT Research Neher Laboratories, Leidschendam, the Netherlands*

Abstract

Loss measurements on ridge waveguides in LPE-grown GaInAsP at a wavelength of 1.3 μm are presented. An attenuation of 4.5 dB/cm has been obtained for straight waveguides and for curved waveguides an excess loss as low as 0.7 dB was found for a 20.8° S-bend with a radius of 300 μm ($\approx$ 1.5 dB/90°).

Introduction

The development of fiber based telecommunication demands cheap, reliable and small optoelectronic integrated circuits (OEIC). These circuits will operate at a wavelength of 1.3 μm or 1.55 μm. The only material suitable for the integration of both passive and active components on one wafer is GaInAsP lattice matched to InP.

Low-loss straight and curved waveguides are essential to achieve the required optoelectronic circuits. Optical losses in straight waveguides are due to absorption and to scattering by interface roughness and can therefore be reduced by lowering the background doping level, by using small refractive index contrasts and by using reactive ion etching (RIE) to produce smooth edges [25]. The losses in curved waveguides are due to radiation and to transitions between straight and curved sections (conversion losses). Radiation losses decrease with increasing lateral refractive index contrast. Conversion losses are caused by mode mismatch and can be reduced by offsetting the curved waveguide with respect to the straight

---

§ permanent address: Laboratory for Semiconductor Technology, Electronics Institute, the Technical University of Denmark, DK-2800 Lyngby, Denmark.

waveguide. It is obvious that concerning refractive index contrast there is a trade off between scattering losses in straight waveguides and radiation losses in curved waveguides.

To our knowledge no experimental results on bending losses have been published so far for InP-based curved waveguides. Austin and Flavin [6], however, found 1 dB/90° for GaAs/AlGaAs ridge waveguides with a radius of curvature of 300 μm at a wavelength of 1.15 μm. In this letter we report on bending losses for curved ridge waveguides in GaInAsP on InP, etched by RIE. Theoretical calculations have been done to find the optimal offsets and to verify the experimental results. The bending losses have been determined for both polarizations.

Table 7.1 *Measured and calculated excess loss due to S-bends. The given angle is for one curve of an S-bend. The excess loss is taken as ½($\alpha_1+\alpha_2$) minus 7.1 dB and 4.8 dB for TE- and TM-polarization respectively.*

R	Angle	Offset	TE polarization				TM polarization			
			Insertion loss		Excess loss	Cal-cu-lated	Insertion loss		Excess loss	Calcu-lated
			α_1	α_2			α_1	α_2		
μm	°	μm	dB	dB	dB	dB	dB	dB	dB	dB
∞			8.6	8.6			7.0	4.8		
∞			7.1	7.1			5.5	5.1		
700	13.4	0.13	8.4	6.9	0.5±0.2	0.08	6.9	5.8	1.5±0.4	0.05
500	16.0	0.18	7.2	7.7	0.3±0.1	0.26	5.0	5.1	0.2±0.3	0.12
300	20.8	0.30	11.2	12.8	4.8±0.2	2.86	5.5	5.6	0.7±0.5	0.71
200	25.2	0.48	18.6	19.2	11.8±0.6	12.98	8.8	9.5	4.3±0.3	4.77

Experiments

A number of straight waveguides together with four different S-bends have been fabricated in a double hetero (DH) structure with a width of 1.9 μm and a ridge height of 0.24 μm (*See* Fig. 7.1a). These S-bends had different radii of curvature (R = 200, 300, 500 and 700 μm) but the same lateral displacement of 44 μm. Between the two curved sections of an S-bend a straight section has been inserted. Optimized lateral offsets were introduced at the connections between curved and straight waveguides (*See* Fig. 7.1b and Table 7.1) to reduce the conversion losses [80]. This technique has been used successfully by us to form very low-loss bends
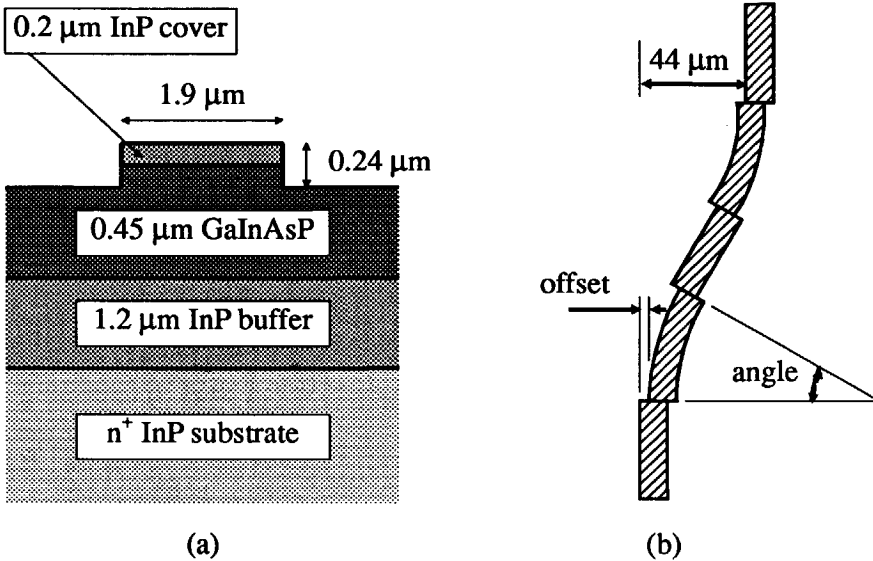
Fig. 7.1 *Cross-section of ridge waveguide (a), and layout of S-bends (b).*

in Al_2O_3/SiO_2 at a wavelength of 632.8 nm [90]. Due to a mask error one of the offsets was missing which has been taken into account in the calculations.

The double heterostructure, consisting of 1.2 μm InP-buffer, 0.45 μm GaInAsP-film, and 0.2 μm InP top layer, was grown by LPE on an n^+-InP substrate (MCP). The lattice matching of the quaternary layer was $\Delta a/a = -4 \times 10^{-4}$ and the band gap was determined by room-temperature photoluminescence as $\lambda_g = 1112 \pm 5$ nm. A background doping level of $n = 3 \times 10^{16}$ cm^{-3} was measured by a Polaron PN4200 Profile Plotter.

The waveguide structures were defined on a chromium mask by optical lithography and reproduced on the substrate by projection illumination, reduction factor 1:4, using the image reversal AZ 5214 E photoresist (Hoechst). Etching of the ridge was performed by Reactive Ion Etching, Plasmalab RIE 80 (Plasma Technology) using CH_4/H_2 (1:4) at 0.5 W/cm^2.

We measured the insertion losses, i.e. the change in the throughput of the measuring set-up due to the insertion of the waveguide in the light path, by coupling light from a $\lambda_0 = 1.3$ μm DH laser into the waveguide with a 50× / 0.85 microscope objective—butt-end coupling—and then measuring the emanating light power as a function of waveguide length (cut-back method). The excitation of waveguide modes is checked visually by imaging the near field distribution at

the outcoupling side onto an infrared camera. The waveguides were observed to be monomode although calculations revealed the presence of two modes. Owing to the multimode character of the laser, modulation in the attenuation of the transmitted power as a function of length did not occur—as is used in the Fabry-Pérot technique—and the measured attenuation can therefore be directly related to loss per unit length. The normal polarization state of the output beam of the laser is TE. To obtain TM polarized light a ½ plate is inserted in the light path.

Results and discussion

A: straight waveguides

The result of the loss measurements for straight waveguides is shown in Fig. 7.2. The loss was measured for 20 different waveguides. Some of the waveguides showed defects and were not included in the analysis. A line has been fitted by applying the least squares method to all 47 measured points. The fitted line through our data yields a propagation loss of 4.5 dB/cm and an interception of 5.8 dB. This value for the propagation loss is among the best figures for LPE-grown GaInAsP waveguides [32] and is very close to the attenuation of the planar film demonstrating the small contribution of the ridge to the losses. The loss at zero length, the coupling loss, can be found by extrapolating the data to zero lengths. The coupling loss is caused by (i) reflection at the front and end face of the waveguide and by (ii) mode mismatch. The loss due to (i) is taken to be 2.9 dB, as calculated from the Fresnel reflection formula, and the loss due to (ii) is 2.9 dB, being the difference between the measured interception and the reflection-loss, and they are independent of the cleave.

B: S-bends

Insertion losses have been determined for two different sets of waveguides, α_1 and α_2, each set containing four different S-bends and two straight reference waveguides, and are given in Table 7.1. The insertion loss of every waveguide is an average over several measurements and over both the forward and the backward direction and it has been determined for both polarizations. The difference in insertion loss between S-bend and reference waveguide is interpreted as the excess bending loss, where the lowest insertion loss was taken as the reference value (7.1 dB for TE and 4.8 dB for TM polarization).

Table 7.1 also gives the theoretical predictions for the excess bending losses for which the refractive indices had to be known. Using the modified Single Oscillator Model [34] it was found that $\lambda_g = 1112 \pm 5$ nm implies a refractive index $n_Q = 3.352 \pm 0.004$ at $\lambda_0 = 1.3$ µm. The refractive index of InP was determined as n_{InP}
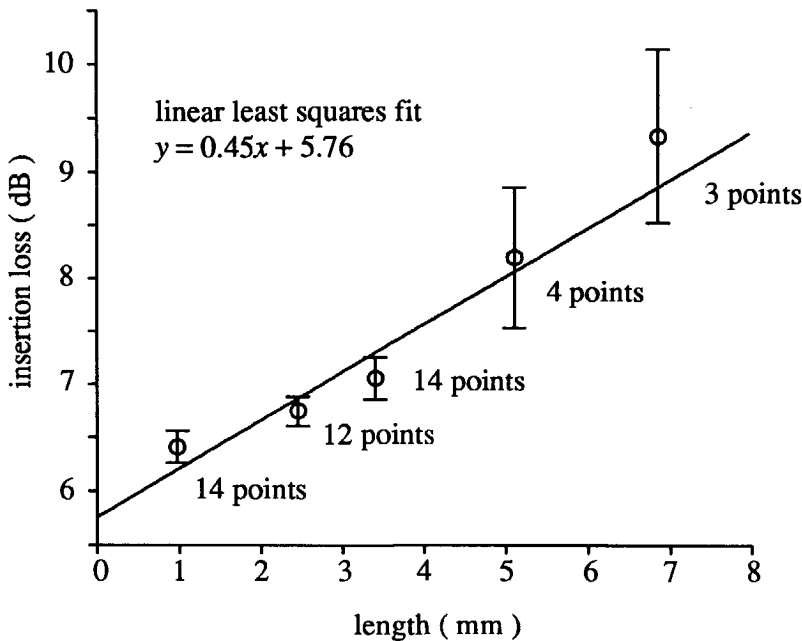
Fig. 7.2 *Insertion loss vs. length for TE mode. The labels denote the number of measured waveguides.*

= 3.209. For the calculations a conformal transformation [40] and a staircase approximation were used in conjunction with the effective dielectric constant (EDC) method as described before [90]. Results for both calculations and measurements are plotted for comparison in Fig. 7.3.

The S-bend with two 20.8° sections and $R = 300$ μm showed an excess loss of only 0.7 dB being in good agreement with the predicted loss and amounting to approximately 1.5 dB/90°. The lower loss for the TM mode can be explained by a better lateral confinement. The relative lateral contrast for the TM mode is 1.26% whereas it is 1.04% for the TE mode.

Conclusions

This letter is the first to report on experimental results for bending losses in curved ridge waveguides in GaInAsP lattice matched to InP. Low losses were found for the S-bends because of a large lateral contrast and because of the introduction of optimized lateral offsets at the transition between the straight and curved waveguide sections. Bending losses have been determined for both polarizations. The
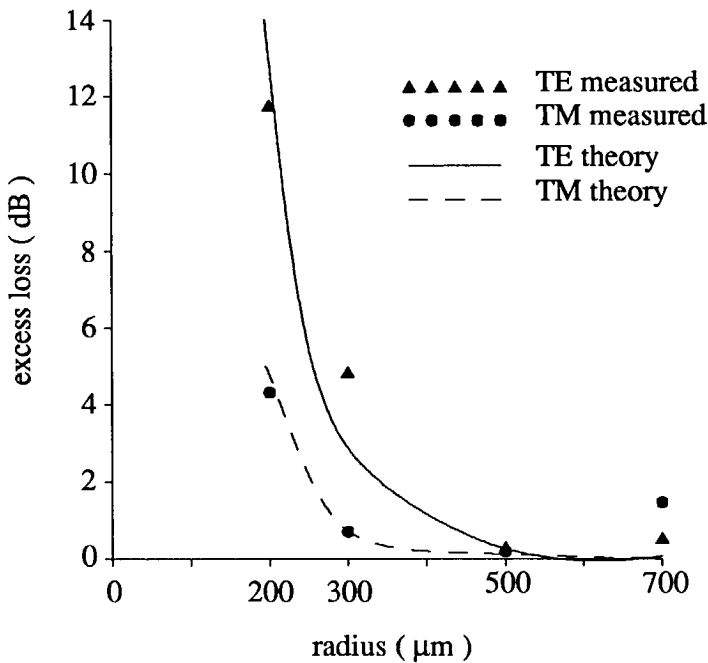
Fig. 7.3 *Excess S-bend losses as a function of radius for both polarizations.*

quasi-TM modes showed significantly lower bending losses than the quasi-TE modes. This is in perfect agreement with theoretical predictions and is caused by a larger lateral difference in effective refractive index. The straight waveguides on the other hand were observed to be monomode and had propagation losses of 4.5 dB/cm, which is close to the film attenuation.

7.1.2 Addendum

A first remark concerns the analysis of the insertion losses shown in Fig. 7.2. The values of the insertion loss seem less reliable for the waveguide lengths of 5.1 mm and 6.85 mm than for the other lengths. Leaving these values out of the analysis altogether gives a propagation loss of 2.6 dB/cm. On the other hand, by fitting a straight line to the five average values of the insertion loss a value of 5.1 dB/cm is found for the propagation loss. At the time of the preparation of the manuscript, the best way to analyze the measurements seemed the application of the least-squares method to all 47 measured values of the insertion loss. A smaller weight

is automatically given to the loss values for waveguide lengths of 5.1 and 6.85 mm, because there are fewer measured values for these lengths of the substrate. A propagation loss of 4.5 dB/cm results when the least-squares method is applied, which is the value that has been published. This procedure, however, treats all 47 measured values equally accurate. The loss values at the lengths of 5.1 and 6.85 mm are not only smaller in number but also less accurate which is shown by the larger standard error. The correct analysis of the data is, therefore, to use a weighted least-squares method[§] and apply it to 47 measured values, where the weight for each measured value is based on the standard error of the ensemble of measured values at that length. Application of the weighted least-squares method yields a propagation loss of 3.5 dB/cm, which seems to be a more correct value than the published value of 4.5 dB/cm.

A second remark concerns the refractive indices which have been used to in the modeling of the bending losses. In the above experiments we used the model of Fiedler and Schlachetzki [34] for the index of refraction of $Ga_xIn_{1-x}As_yP_{1-y}$. This model is first given by Utaka, Kobayashi and Suematsu [118] as an interpolation between data on GaInP and GaInAs and is given by

$$n^2 = 1 + \frac{E_b}{E_a} + \frac{E_b}{E_a^3} E_0^2 + \frac{E_b}{2E_a^3(E_a^2-E_g^2)} E_0^4 \ln\left\{\frac{2E_a^2-E_g^2-E_0^2}{E_g^2-E_0^2}\right\},$$ (7.1.1)

where

$$E_a = 3.391 - 1.652y + 0.863y^2 - 0.123y^3,$$ (7.1.2)

$$E_b = 28.91 - 9.278y + 5.626y^2,$$ (7.1.3)

$$E_g = \frac{hc}{e\lambda_g} \approx 1.35 - 0.72y + 0.12y^2 \text{ eV}.$$ (7.1.4)

The matching of both lattices requires $y = 2.197x$ and $E_0 = hc/(e\lambda_0)$ is the photon energy in eV. An extra contribution to the refractive index results from free carriers. This free-carrier plasma effect is more pronounced for electrons than for holes because their effective masses are much smaller. Free electrons with concentration

---

§ J. Mähnß, Technische Universität Braunschweig. Private communication.

N_e and effective mass $m_{e,eff} \approx m_e$ (0.07–0.0308y) decrease the refractive index by an amount

$$2n\Delta n = \frac{\Delta\varepsilon}{\varepsilon_0} = -\frac{e^2 N_e}{\varepsilon_0 \omega^2 m_{e,eff}}.$$ (7.1.5)

It appeared within the context of the COST 216 project (see page 105) that the refractive indices of the above model are inaccurate near the band edges, i.e. for small fractions y. The model of Henry *et al.* [42] for the refractive indices of GaInAsP is based on the accurate determination of the refractive indices by measuring the angle of the light which is coupled out of a waveguide by means of a grating. Their model for the refractive index is

$$n^2 = 1 + \frac{13.3510 - 5.4554 E_g + 1.2332 E_g^2}{1 - \left(\dfrac{E_0}{E_g + 2.5048\text{eV}}\right)^2} + \frac{0.7140 - 0.3606 E_g}{1 - \left(\dfrac{E_0}{E_g + 0.1638\text{eV}}\right)^2},$$ (7.1.6)

which yields more accurate values for the refractive index near the band edges. A value of $E_g = 1.32$ eV is given for InP which differs significantly from the widespread 1.35 eV. If we apply Eq. (7.1.6) to the measured absorption wavelength of $\lambda_g = 1112$ nm and the vacuum wavelength of $\lambda_0 = 1300$ nm, the values of $n_Q = 3.3408$ and $n_{InP} = 3.2022$ are found instead of $n_Q = 3.3520$ and $n_{InP} = 3.2091$. The refractive-index contrast that is calculated by means of Eq. (7.1.6) is thus slightly smaller. The differences in refractive indices, however, are not large enough to have significant consequences for the calculations and the modeling that have been performed.

7.2 'Chicanes' in MOVPE-grown GaInAsP

The following manuscript was accepted as a post-deadline paper PDB-9 at the 15th European conference on optical communication (ECOC '89) on September 10-14, 1989, Gothenburg, Sweden [122]. The paper reports on experiments with low-loss small-radii bends in MOVPE-grown GaInAsP ridge waveguides at $\lambda_0 = 1.52$ µm. These experiments are the result of the cooperation between B.H. Verbeek of Philips Research Laboratories, Eindhoven, who performed the measurements and wrote the paper, P.J.A. Thijs of Philips Research Laboratories,

Eindhoven, who grew the double-hetero structure, Y.S. Oei and J.W.M. van Uffelen of Delft University of Technology, who are responsible for the etching and the photolithography. My contribution consisted of the modeling of the S-bends, mask design and calculation of the losses.

7.2.1 Manuscript ECOC '89

Fabrication And Analysis Of Low-loss GaInAsP/InP Optical Waveguides With Extremely Small Bends

B.H. VERBEEK[§&], E.C.M. PENNINGS[&], Y.S. OEI[&],
J.W.M. VAN UFFELEN& AND P.J.A. THIJS§

[§]*Philips Research Laboratories Eindhoven,*
PO Box 80.000, 5600 JA Eindhoven, The Netherlands

[&]*Delft University of Technology, Dept. of Electrical Engineering,*
PO Box 5031, 2600 GA Delft, The Netherlands.

Abstract

MOVPE-grown GaInAsP/InP strip waveguide bends ($4 \times 90°$) with radii of curvature R between 100 - 400 μm have been fabricated. An excess loss of 0.5 (0.6) dB/90° for $R = 150$ μm and 1.52 μm TM (TE)-light is in agreement with our theoretical analysis.

Introduction

Low-loss optical waveguides in InP play an essential role in optoelectronic circuits when various optical components will be integrated on a single chip. Straight passive waveguides of GaInAsP/InP with propagation losses as low as 0.18 dB/cm have recently been fabricated using MOVPE-growth technique [5][13] and optimized for minimum losses. However, low-loss lightguide bends with small radius of curvature R are a prerequisite for implementation of integrated optical devices with practical dimensions. Until now, bends have been employed in integrated devices with R exceeding several mm's and only very recently the first results have been obtained on S-bends using submillimeter radii of curvature [104][119]. An excess loss of 1.1 dB/90° for $R = 200$ μm has been reported for TE polarized light [104], but that result seems in contradiction with our calculations for that structure yielding 26.2 dB/90°. In this paper we report the results of an experimental and theoretical study on the optical losses of $4 \times 90°$ ("chicane"-

testpattern) GaInAsP/InP waveguide bends with very small radii of curvature. The optical losses in bends are caused by radiation and by mode mismatch between straight and curved sections. In our calculations, these effects have been taken into account and also coherent effects were included since our waveguides are multi-mode. For the first time an excess bend loss as low as 0.5 (0.6) dB/90° for $R =$ 150 µm for TM (TE resp.) polarized light has been measured which is in agreement with our theoretical predictions.

Bend-loss analysis

The properties of curved waveguides can be calculated by the conformal trans-formation technique [40] which has the form[§]: $x + jy = re^{j\varphi} = Re^{(u+jv)/R}$ and transforms the curved waveguide scalar wave equation into an equivalent straight structure:

$$\left[\frac{\partial^2}{\partial u^2} + \frac{\partial^2}{\partial v^2} + k_0^2 \tilde{n}^2 \right] \Psi_z(u,v) = 0 , \tag{7.2.1}$$

with a transformed index of refraction profile

$$\tilde{n}(u) = n(u(r))e^{u/R} \tag{7.2.2}$$

and $\Psi_z(u,v)$ the transformed field in the bend. A numerical evaluation of the transformed problem has been adopted using a discretized refractive index profile (staircase approximation) and applying a transfer-matrix method plus appropriate boundary conditions to the resulting field solution [112]. A discrete eigenvalue for the complex angular propagation constant is obtained, the imaginary part of which represents the attenuation due to radiation.

The field profile in the bend is used to calculate the conversion losses at the junctions between straight and curved waveguides. The conversion loss is mi-nimized by a lateral offset to compensate for the outward shift of the curved waveguide mode profile (the Whispering Gallery Mode (WGM), *see* Fig. 7.4 and Table 7.2). Additional loss-optimization can be obtained by adjusting the width of the straight waveguide to match both field profile widths. A very important feature of bends is that radiation losses decrease exponentially with increasing width, eventually reaching a lower limit. In this limit, the mode becomes a WGM

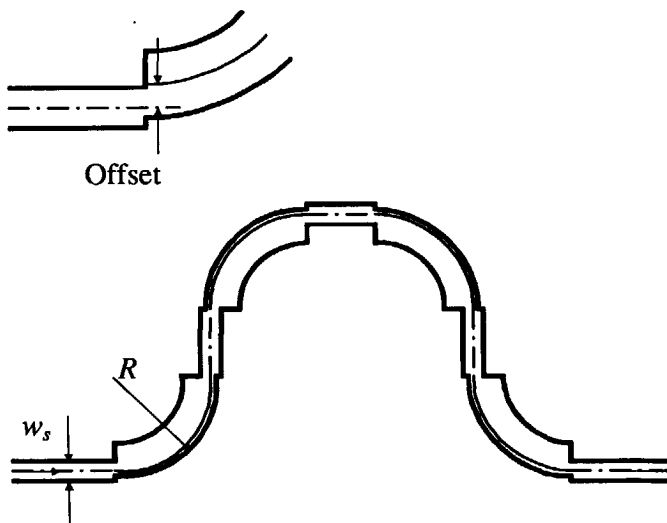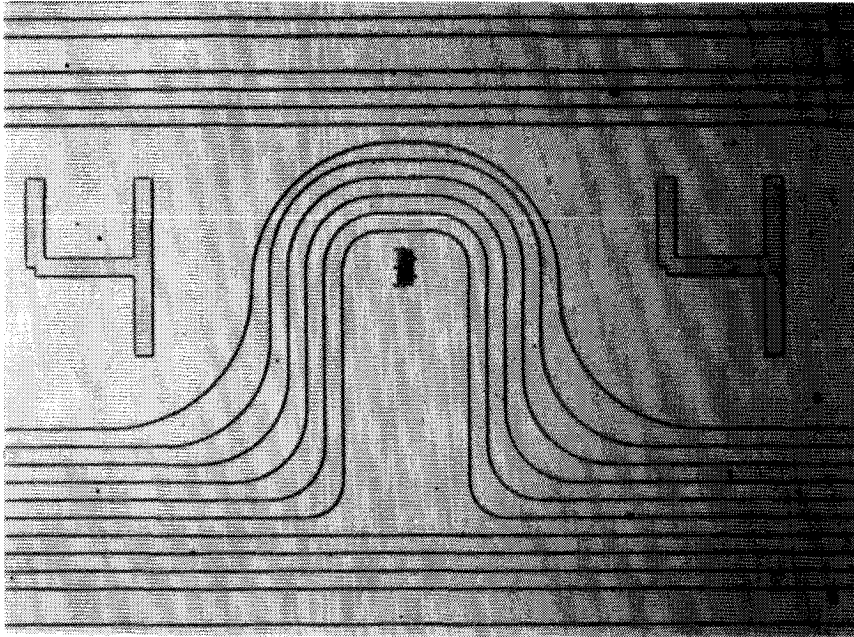§ This notation is in slight disagreement with the notation in the rest of the thesis.

Fig. 7.4 *Layout of "Chicane"-test structure 90° including offsets between straight and curved waveguide sections. Dashed curve indicates the maximum intensity of the fundamental mode and demonstrates clearly the necessity of the offset. The waveguide width is 3.0 and 3.4 μm for straight and curved parts resp.*

Table 7.2 *Calculated excess loss for the TE- and the TM-polarization without and with offset correction.*

R	Offset	no offset TE	+ offset TE	no offset TM	+ offset TM
μm	μm	dB/90°	dB/90°	dB/90°	dB/90°
100	1.05	11.82	**2.68**	3.69	**0.78**
150	0.80	2.85	**0.45**	3.70	**0.23**
200	0.65	0.69	**0.13**	0.16	**0.15**
250	0.55	0.27	**0.08**	0.27	**0.11**
300	0.48	0.07	**0.10**	0.26	**0.08**
400	0.38	0.19	**0.05**	0.11	**0.07**

which is guided by the outer optical contrast only. The large lateral contrast ΔN_e = 0.075 ((TE) calculated via the effective index method) necessary to minimize the radiation losses made the waveguide multimode and there exists some inter-modal coupling at the junctions. Straight and curved waveguide field profiles have been calculated for all allowed modes. The transmission of the full test-structure follows by multiplying the vector representing the amplitude of these modes by propagation and coupling matrices. The excess loss for a multimode structure may be either higher or lower than for monomode waveguides depending on the amount of intermodal coupling and the relative phases of the modes.

Fabrication and Measurements

The waveguides were fabricated from LPMOVPE-grown epilayers of undoped InP/GaInAsP on a SI-InP substrate. The GaInAsP guiding layer has a gap wave-length of 1320 nm. The top InP layer was etched by RIE using CH_4/H_2 (1:4) slightly into the guiding layer for a large optical contrast ΔN_e = 0.075. The structure of the waveguide, its dimensions and a SEM micrograph are shown in Fig. 7.5. The optimal width of the rib was 3.0 μm in the straight sections and 3.4 μm in the bends. The "chicane" waveguide test pattern consisted of four 90° bends connected with straight waveguides with the optimal offsets for each R (*see* Fig. 7.4 and Table 7.2). A set of "chicanes" with R ranging between 100 - 400 μm was defined on the mask together with reference straight waveguides by optical lithography giving very smooth curved patterns. The excess bend loss per 90° at λ_0 = 1.52 μm was obtained as the difference between the total insertion loss of the chicane and the straight waveguides and dividing by 4. Fiber polarization controllers were used for TE and TM excitation.
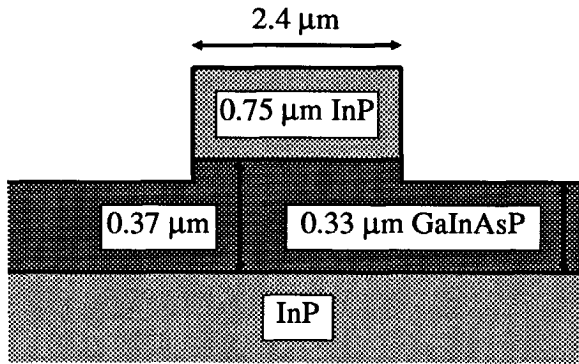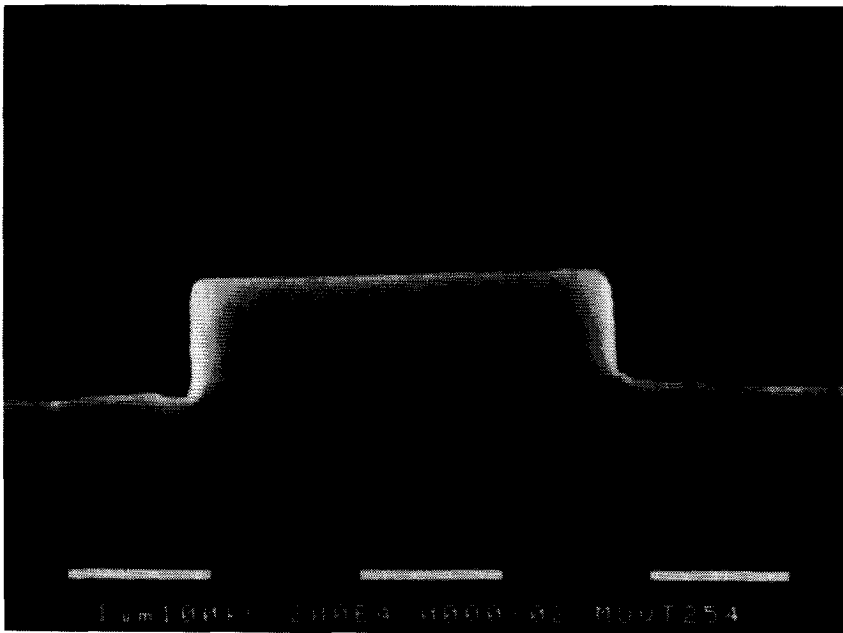
(a)

Fig. 7.5 *Structure and SEM micrograph of straight waveguides cross section.*
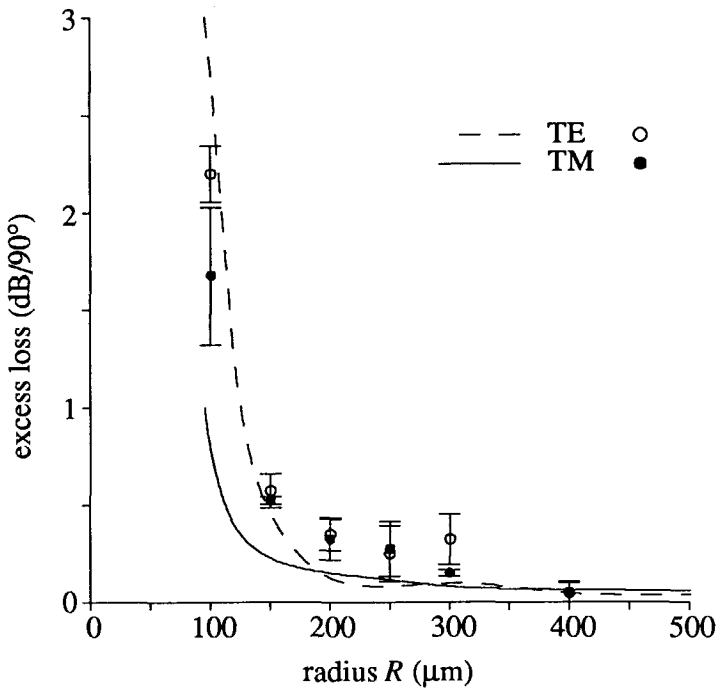
Fig. 7.6 *Excess bend loss per 90° versus radius of curvature R at λ₀ = 1.52 µm for TE and TM polarization. Dots give measured average values with standard deviation indicated by bars. The full and dashed curves represent our theoretical calculations.*

Results

The excess loss of 90° bends for different R is shown in Fig. 7.6 for TE and TM polarized light. The data have not been corrected for propagation losses (< 1 dB/cm [5]) since the maximum additional length was 1.4 mm for $R = 100$ µm. The losses for TE polarization are consistently higher than those of the TM data as a result of a 22 % lower contrast than for TM modes. Also shown are the calculated curves for TE and TM mode propagation. Both results show that the excess bend loss depends critically on the radius R. A steep increase of the bend losses is observed between 100 and 200 µm in very good agreement with the calculations for the high contrast waveguides.

Summary

We have presented the results of an analysis of $4 \times 90°$ "chicane" bend losses of MOVPE-grown GaInAsP/InP waveguides. Using lateral offsets and optimized widths of straight and curved waveguides, excess losses for 90° bends as low as 0.5 (0.6) dB/90° for $R = 150$ μm and TM (TE) have been realized. These loss-figures for bends are the best values published so far and they are in very good agreement with theory. Our results show that with proper design, extremely small, practical waveguide bends with low excess loss can be fabricated and are essential for implementation in integrated optical devices with practical dimensions.

7.2.2 Addendum

One of the reactions to the presentation of this work at ECOC '89 came from E.-G. Neumann[§], who rightly reminded us that we had forgotten to refer to his work, most notably [80] that first describes the lateral offset at the junction to reduce transition losses. Neumann also mentioned the fact that the principle of the offset has been patented by him [82]. The work of Neumann is referred to in the thesis.

More details are given here of the loss calculations that we performed for the S-bends as reported by Singh *et al.* [104], because the ECOC manuscript mentions discrepancies that are found between our calculations and the loss values reported in [104]. The curved waveguides that are reported in [104] have radii of curvature in the range of 100 μm to 400 μm and have been fabricated in MOVPE-grown GaInAsP. These waveguides have very small widths of 0.27 μm, 1 μm and 1.8 μm, which is contrary to the guidelines developed in chapter 5. The calculations are based on the parameters reported in [104], being TE-polarized light with $\lambda_0 = 1.553$ μm, a GaInAsP film of height 0.22 μm and a band gap wavelength $\lambda_g = 1.28$ μm and for the widths and radii given above. The Utaka model, [118] and Eqs. (7.1.1) through (7.1.4), yields the refractive indices $n_Q = 3.3787$ and $n_{InP} = 3.1690$. The effective refractive index is $N = 3.21242$ and the S-bend losses that have been calculated from these parameters are summarized in Table 7.3. The calculated losses differ a factor 10 to 25 from the experimental values. A radiation loss of 84.3 dB/90° is found when $w = 0.27$ μm and 0.4 dB/90° when $w = 3$ μm, both for a radius of curvature of $R = 300$ μm, which shows that the width of the curved waveguide is not optimal with respect to the radiation losses.

---

§ Private communication.

Table 7.3 *Losses calculated for the S-bends reported by Singh et al. [104]. We denote the total S-bend loss by α_{tot}, the radiation loss by α, the radius of curvature by R, and η is the coupling loss at the junction between the straight and curved waveguide or at the junction between two oppositely curved bends.*

R μm	Calculated $w = 1$ μm				Calculated $w = 3$ μm		Calculated $h = 0.3$ μm		α_{tot} [104] dB
	α_{tot} dB	α dB/90°	$\eta_{s \to c}$ dB	$\eta_{c \to c}$ dB	α_{tot} dB	α dB/90°	α_{tot} dB	α dB/90°	
400	4.7	2.6	0.5	1.2	2.4	0.0	0.1	0.0	0.8
300	11.2	6.4	1.1	2.6	4.4	0.4	0.2	0.0	0.3
200	26.2	14.4	2.8	6.2	15.3	3.7	1.1	0.3	1.1
100	63.9	30.8	8.0	17.2	63.2	20.8	12.9	5.5	7.8

The discrepancies between the calculated and the experimental values suggest the variation of the parameters that are used for the calculations. A larger width of $w = 3$ μm does not lead to significant differences in the calculated losses as shown in Table 7.3, because small widths lead to large radiation losses and large widths lead to increased transition losses. Another set of calculations has been done for a film height $h = 0.3$ μm instead of 0.22 μm in combination with the original width of 1 μm and the refractive indices $n_Q = 3.3858$ and $n_{InP} = 3.1641$ that have been calculated by means of Eq. (7.1.6). The resulting values of this set of calculations are in good agreement with the experimental values. The larger film height leads to a larger effective index $N = 3.23696$, which leads in turn to a better confinement of the light and thus to reduced radiation losses.

I. Henning[§], who is one of the authors of [104], revealed that the very high losses, that have been calculated for the 0.27 μm wide S-bends, have been observed, indeed. The refractive indices calculated by means of both the Utaka and the Henry model, Eqs. (7.1.1) and (7.1.6) respectively, are in agreement with the values $n_Q = 3.38$ and $n_{InP} = 3.17$, that have been used by I. Henning. The thickness of the quaternary film is 0.22 ± 10 % according to SEM photographs and this excludes the value of 0.3 μm. The geometry the waveguides can vary locally, however, due to the anisotropic character of the chemical etch that has been used and due to a possibly incomplete overgrowth leading to a cover which consists partially of air.

The measured losses of the S-bends in [104] are for S-bends that have no lateral offset at the junction of the straight and the curved waveguides. The optimal offset,

---

§ Private communication.

however, happens to be zero for a width of approximately 1 μm, which can be seen as follows. An optimal lateral offset, *offset* = $w/2-\Delta r$ Eq. (5.2.5), is found by aligning the maxima of the straight and the curved waveguide profiles, where Δr is the distance between the maximum of the field distribution and the outer edge of the bend. This distance Δr is of the order of the wavelength and varies, in practice, between zero and 1.0 μm for small bends. The resulting offset will, therefore, be close to zero when the width of the bend w equals twice the distance Δr.

The two figures, that are shown on page 189, give results of the modeling of the bends that are described in the ECOC manuscript. Fig. 7.7 shows the radiation loss as a function of the width of the curved waveguide. The regime of whispering-gallery mode operation, where the radiation losses are minimal, is reached for widths that are larger than 2.5 μm. A value of 3.0 μm has been chosen for the width of our bends and SEM photographs of the manufactured curved waveguides revealed a fabricated width of 3.4 μm.

The transition loss of the junction of the straight and the curved waveguide is shown in Fig. 7.8. The transition loss is minimal for an offset of 0.7 μm and a straight-waveguide width of 2 μm. A width of 2.6 μm has been chosen instead, which is a compromise between the optimization of the transition losses and the minimization of the scattering losses.
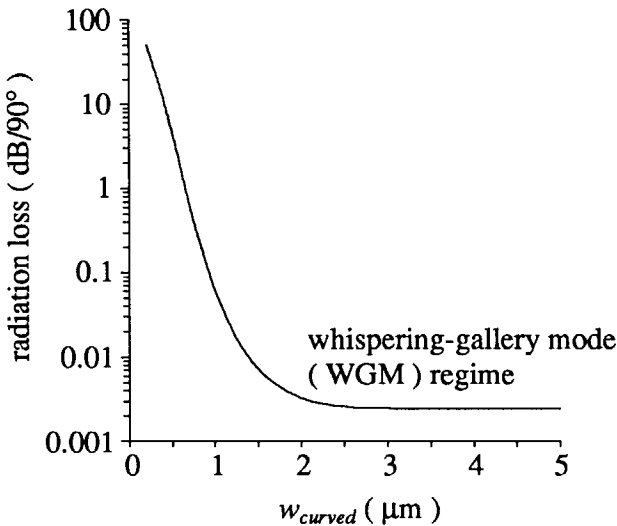
Fig. 7.7 *Calculated radiation losses versus width for a bend with R = 150 μm and parameters as given in the ECOC manuscript. The asymptotic limit reached for widths greater that 2.5 μm is the WGM regime where the inner side of the bend has no influence on the modal field distribution.*
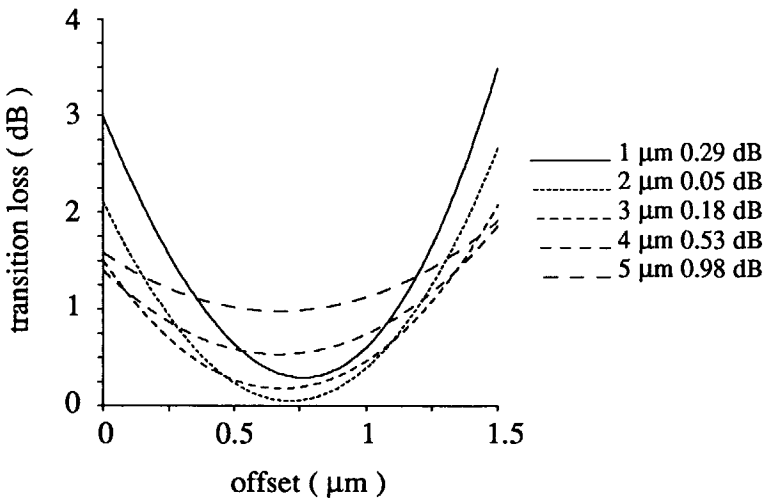
Fig. 7.8 *Calculated transition losses at the junction for the HE$_{00}$-mode, R = 150 μm and w$_{curved}$ = 3 μm. The width of the straight waveguide has been varied from 1 to 5 μm. The corresponding minimum transition losses are indicated in the legend.*

Appendix A

Implementation of the Bessel functions

This appendix discusses the numerical implementation of Bessel functions with large arguments and large complex orders. The implementation is based on information found in a paper by Neumann and Richter [81] and uses Airy functions and asymptotic expansions that are listed by Abramowitz and Stegun [1]. The asymptotic expansions for the Bessel functions are those of Olver [85][86].

Since the asymptotic expansions for the Bessel functions of the first and the second kind and their derivatives use similar expansion coefficients and since the transfer-matrix needs both the Bessel functions and their derivatives, an implementation has been adopted in the form of a subroutine that evaluates both the Bessel functions and their derivatives simultaneously for the same argument and order.

Is is noted that the accuracy of an asymptotic expansion is always better than the next term in the expansion that has not yet been included in the sum. This implies that the summation must be stopped before the smallest term in order to obtain the maximum accuracy.

The expansions for the Bessel functions have been based on the Airy functions and these have, therefore, been implemented first.

Ai(z), Bi(z), Ai$'$(z), Bi$'$(z) =

$$\begin{cases} \text{Eqs. (10.4.2)} - \text{(10.4.5)} & , |z| \le 6 & \text{COMPLEX}*16 \\ \text{Eqs. (10.4.2)} - \text{(10.4.5)} & , \text{Re}(z) > 3.75 \text{ and } |z| < 6.5 & \text{REAL}*16 \\ \text{Eqs. (10.4.59)} - \text{(10.4.68)} & , |z| > 6 & \text{COMPLEX}*16 \end{cases} ,$$

$$(A.1)$$

where the equation numbers correspond to those of Abramowitz and Stegun [1]. The REAL*16 data type has been used in order to achieve the required accuracy. The numerical implementation has been done for the real and imaginary parts separately which implies an effective accuracy which is equal to that of an COMPLEX*32 data type. The coefficients Eqs. (10.4.4) and (10.4.5) of [1] have been recalculated

$$c_1 = \frac{3^{-\frac{2}{3}}}{\Gamma(2/3)} = 0.335028053887817239260063186 04 , \tag{A.2}$$

$$c_2 = \frac{3^{-\frac{1}{3}}}{\Gamma(1/3)} = 0.258819403792806798405183560 17 , \tag{A.3}$$

and have an adequate accuracy of 28 digits. The accuracy of the calculated values of the Airy functions and their derivatives has been estimated by means of

$$accuracy = \pi \left\{ \text{Ai}(z)\text{Bi}'(z) - \text{Ai}'(z)\text{Bi}(z) \right\} - 1 , \tag{A.4}$$

where Eq. (10.4.10) of [1] has been used for the Wronskian of the Airy functions. The accuracy is better than 10^{-12} everywhere in the complex z-plane. An accuracy of 10^{-8} for $z = 6$ would have resulted if 'normal'COMPLEX*16 had been used for this value of the argument. The implementation of the Airy functions and their derivatives has also been tested with respect to the relations between the Airy functions Eqs. (10.4.6) through (10.4.9) of [1], with respect to complex conjugates Ai(z^*) = Ai*(z) et cetera, and by means of the Table (10.11) in [1].

The evaluation of the coefficients Eq. (10.4.58) in [1] can be simplified and made faster by using

$$\frac{c_k}{c_{k-1}} = \frac{k-1}{2} + \frac{5}{72k} , \tag{A.5}$$

and similarly

$$\frac{d_k}{d_{k-1}} = \frac{k-1}{2} - \frac{7}{72k}.$$ (A.6)

The Debye's asymptotic expansions, Eqs. (9.3.7) and (9.3.8) of [1], may not be used, since we have to evaluate the Bessel functions in the transition region where the order and argument are almost equal. Setting $\operatorname{sech} \alpha = 1$ results in $\coth \alpha \rightarrow \infty$ and we find that the terms in the Debye's asymptotic expansion then do not converge. The asymptotic expansion in the transition region Eqs. (9.2.23) through (9.3.30) cannot be used either since too few expansion coefficients are given to obtain the desired accuracy. The evaluation of extra expansion coefficients soon turned out to be a hazardous enterprise.

We have, therefore, adopted the option of always using Eqs. (9.3.35) through (9.3.46) in [1]. There is a problem, however, because the expressions, Eqs. (9.3.40) and (9.3.46) in [1], for the expansions are numerically not stable near $\zeta = 0$, although the expansion coefficients themselves are well behaved. The wanted relative accuracy for the Bessel functions of at least 10^{-12} leads to an accuracy requirement for the expansion coefficients of 16 significant digits for $a_0(\zeta \approx 0)$, 10 significant digits for $a_1(\zeta \approx 0)$, five significant digits for $a_2(\zeta \approx 0)$ and one digit for $a_3(\zeta \approx 0)$ and similar requirements for the coefficients b_i, c_i and d_i. The values for the coefficients at $\zeta = 0$ are related to the given coefficients below Eq. (9.3.34) in [1], whose accuracy is adequate. The coefficients $a_k(\zeta)$, $b_k(\zeta)$, $c_k(\zeta)$ and $d_k(\zeta)$ have, therefore, been calculated by means of a twenty-point Lagrangian interpolation (Eq. (25.2.1) in [1]) within the circle $|\zeta - 1| < 0.1/1.001$ for $k = 0, 1, 2, 3$, respectively, whereas the coefficients have been approximated by zero within the circle $|\zeta - 1| < 0.2/1.001$ for $k = 4, 5, 6$, respectively, and within the circle $|\zeta - 1| < 0.4/1.001$ for $k \geq 7$. The twenty-point Lagrangian interpolation has been based on the given values of the coefficients for $\zeta = 0$, supplemented by values of the coefficients which have been calculated with high precision.

The polynomials $u_k(t)$, Eq. (9.3.10) in [1], and $v_k(t)$, Eq. (9.3.14) in [1], have been evaluated by means of

$$u_k(t) = \sum_{i=0}^{3k} U_{k,i} t^i,$$ (A.7)

where

$$U_{k,i} = U_{k-1,i-1}\left\{\frac{k-1}{2} + \frac{1}{2k}\right\} + U_{k-3,i-1}\left\{\frac{-5}{8k} - \frac{k-3}{2}\right\} \text{ and } U_{0,0} = 1 , \qquad \text{(A.8)}$$

and

$$v_k(t) = \sum_{i=0}^{3k} V_{k,i} t^i , \qquad \text{(A.9)}$$

where

$$V_{k,i} = U_{k-1,i-1}\left\{\frac{-k}{2} + \frac{1}{8k}\right\} + U_{k-3,i-1}\left\{\frac{-5}{8k} + \frac{k-2}{2}\right\} \text{ and } U_{0,0} = 1 . \qquad \text{(A.10)}$$

The accuracy of the numerical implementation of the Bessel functions and their derivatives, $J_v(z)$, $Y_v(z)$, $J_v'(z)$ and $Y_v'(z)$ has been assessed by calculating the Wronskian, Eq. (9.1.16) in [1], and the recursion relations, Eqs. (9.1.27) in [1]. The precision is twelve significant digits for $|v| > 100$. The precision is nine significant digits for $v \approx 5$. Our implementation of the Bessel functions can be used for all z and $|\text{Arg}(v)| < \pi/2$.

Appendix B

The WKB approximation

The WKB approximation is named after Wentzel, Kramers and Brillouin [60]. The WKB method provides an approximation to the one-dimensional Schrödinger equation

$$\frac{\partial^2 \psi(u)}{\partial u^2} + k_0^2 f(u)\psi(u) = 0.$$ (B.1)

Many textbooks on quantum mechanics discuss the WKB method. In the elegant derivation by Landau and Lifschitz [63], the wave function $\psi(u)$ is expanded in powers of Planck's constant. This is equivalent to an expansion in inverse powers of the wave number in vacuum k_0

$$\psi(u) = e^{jk_0\eta(u)},$$ (B.2)

$$\eta(u) = \eta_0(u) + \eta_1(u)\left(\frac{j}{k_0}\right) + \eta_2(u)\left(\frac{j}{k_0}\right)^2 + \dots.$$ (B.3)

Quantum mechanics becomes classical when the de Broglie wavelength becomes small in respect to the characteristic dimensions or in the limit when Planck's constant becomes zero. Similarly, wave optics becomes geometrical in the limit

of a a very small wavelength. The first-order approximation to $\psi(u)$ is found by substituting Eq. (B.2) with $\eta = \eta_0$ into Eq. (B.1)

$$-\left(\frac{\partial \eta_0}{\partial u}\right)^2 + \left(\frac{j}{k_0}\right)\frac{\partial \eta_0}{\partial u} + f(u) = 0, \tag{B.4}$$

and neglecting the term which contains j/k_0

$$\eta_0(u) = \pm \int^u \sqrt{f(u')}\, du'. \tag{B.5}$$

The second-order contribution to $\psi(u)$ is found by substitution of $\eta = \eta_0 + j\eta_1/k_0$ into Eq. (B.1) and dropping the terms that contain j/k_0

$$\partial_u\eta_0\partial_u\eta_1 - \tfrac{1}{2}\partial_u^2\eta_0 = 0. \tag{B.6}$$

The solution of Eq. (B.6) is

$$\eta_1(u) = \frac{1}{2}\int^u \frac{\partial_{u'}(\partial_{u'}\eta_0(u'))}{\partial_{u'}\eta_0(u')}\,du' = \frac{1}{2}\ln\sqrt{\partial_u\eta_0(u)} = \frac{1}{2}\ln\sqrt{f(u)}, \tag{B.7}$$

and we find for $\psi(u)$ to the second order

$$\psi(u) = \frac{C}{\sqrt[4]{f(u)}}\exp\left\{\pm jk_0\int_{u_0}^u \sqrt{f(u')}\,du'\right\}. \tag{B.8}$$

The second-order solution Eq. (B.8) satisfies

$$\partial_u^2\psi + \left\{k_0^2 f + \frac{1/4}{f}\partial_u^2 f - \frac{5/16}{f^2}(\partial_u f)^2\right\}\psi = 0, \tag{B.9}$$

exactly and is a good approximation to Eq. (B.1) when

$$\left| \frac{\frac{1}{4}}{f} \partial_u^2 f - \frac{5\!\!/\!\!16}{f^2} (\partial_u f)^2 \right| \ll \left| k_0^2 f \right| .$$ (B.10)

Inequality Eq. (B.10) fails
  - in the neighborhood of a zero, $f(u) = 0$,
  - when the wave number of vacuum becomes very small, $k_0 \!\downarrow\! 0$,
  - when the derivatives $\partial_u f$ and $\partial_u^2 f$ are large with respect to f or equivalently when the relative change in f is large in a distance k_0^{-1}.

  The approximation can, therefore, not be used in the neighborhood of a zero of $f(u)$. This zero is called the classical turning point, because it marks a region that is inaccessible according to classical mechanics. Far away from the turning point, the approximations are good and the approximations on both sides of the turning point can be related to each other. A proper treatment involves the approximation $f(u) \approx C(u - u_0)$ in the neighborhood of the turning point $u = u_0$ and the integration along a "proper path"—*see* §1.4 in [73]—. The results are the connection formulas, which are neatly summarized by Merzbacher [74]. In Fig. B.1 where the turning point is to the left of the classical region, the solutions are connected by

$$\frac{1}{\sqrt[4]{-f(u)}} \exp\left(-\int_u^{u_0} \sqrt{-f(u')}\, du' \right) \longleftrightarrow\!\!\!\rightarrow \frac{2}{\sqrt[4]{f(u)}} \cos\left(\int_{u_0}^u \sqrt{f(u')}\, du' - \frac{\pi}{4} \right), \quad \text{(B.11)}$$

$$\frac{-1}{\sqrt[4]{-f(u)}} \exp\left(+\int_u^{u_0} \sqrt{-f(u')}\, du' \right) \longleftarrow\!\!\!\rightarrow \frac{1}{\sqrt[4]{f(u)}} \sin\left(\int_{u_0}^u \sqrt{f(u')}\, du' - \frac{\pi}{4} \right), \quad \text{(B.12)}$$
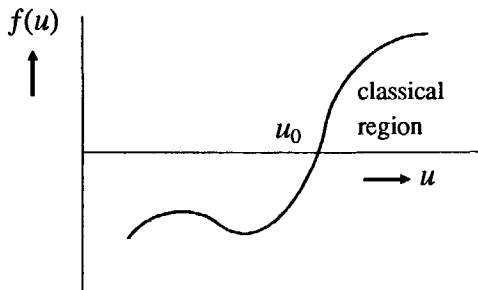
Fig. B.1 *The classical region is to the right of the turning point $u = u_0$.*

and in the opposite case shown shown in Fig. B.2, the connection formulas are given by

$$\frac{2}{\sqrt[4]{f(u)}}\cos\left(\int_u^{u_1}\sqrt{f(u')}\,du' - \frac{\pi}{4}\right) \longleftrightarrow \frac{1}{\sqrt[4]{-f(u)}}\exp\left(-\int_{u_1}^u\sqrt{-f(u')}\,du'\right), \quad (B.13)$$

$$\frac{1}{\sqrt[4]{f(u)}}\sin\left(\int_u^{u_1}\sqrt{f(u')}\,du' - \frac{\pi}{4}\right) \longleftrightarrow \frac{-1}{\sqrt[4]{-f(u)}}\exp\left(+\int_{u_1}^u\sqrt{-f(u')}\,du'\right), \quad (B.14)$$
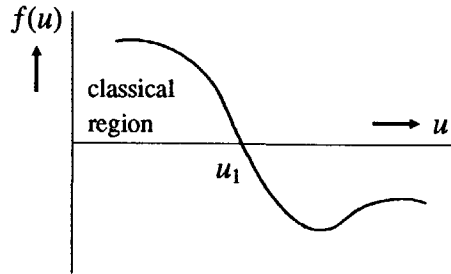
Fig. B.2 *The classical region is to the left of the turning point $u = u_1$.*

The connection formulas are to be used in the direction of the double arrow only.

Appendix C

WKB integrals

The WKB solution to the transformed curved slab waveguide of § 4.1.4 involves two integrals that can be evaluated in closed form. The first integral is

$$\int_{u_1}^{u_2} \sqrt{k_0^2 N_i^2 e^{2u'/R_t} - \frac{\gamma^2}{R_t^2}}\, du' \, , \tag{C.1}$$

and is solved by means of the substitution

$$\xi = \sqrt{\frac{k_0^2 N_i^2 R_t^2 e^{2u'/R_t}}{\gamma^2} - 1} = \sqrt{\frac{k_0^2 N_i^2 r^2}{\gamma^2} - 1} \, , \tag{C.2}$$

$$d\xi = \frac{\xi^2 + 1}{\xi} \frac{du'}{R_t} \, . \tag{C.3}$$

Effecting the substitution yields

$$\int_{u_1}^{u_2} \sqrt{k_0^2 N_i^2 e^{2u'/R_t} - \frac{\gamma^2}{R_t^2}}\, du' = \gamma \int_{\xi_1}^{\xi_2} \frac{\xi^2}{\xi^2+1}\, d\xi = \gamma\left(\xi - \tan^{-1}\xi\right)\Bigg|_{\xi_1}^{\xi_2} =$$

$$= \gamma\left(\tfrac{1}{3}\xi^3 - \tfrac{1}{5}\xi^5 + \tfrac{1}{7}\xi^7 - \,....\right)\Bigg|_{\xi_1}^{\xi_2}. \tag{C.4}$$

The integral has been expressed in the form of a series because the integral appears in a dispersion relation that has to be solved numerically. Since the quantity ξ is small and the two contributions to ξ^1 cancel, a reduced numerical accuracy results if the closed expression is used. The second integral

$$\int_{u_1}^{u_2} \sqrt{\frac{\gamma^2}{R_t^2} - k_0^2 N_i^2 e^{2u'/R_t}}\, du', \tag{C.5}$$

is very similar to the first one. The substitution

$$\xi = \sqrt{1 - \frac{k_0^2 N_i^2 R_t^2 e^{2u'/R_t}}{\gamma^2}} = \sqrt{1 - \frac{k_0^2 N_i^2 r^2}{\gamma^2}}, \tag{C.6}$$

$$d\xi = \frac{\xi^2 - 1}{\xi}\frac{du'}{R_t}. \tag{C.7}$$

leads to

$$\int_{u_1}^{u_2} \sqrt{\frac{\gamma^2}{R_t^2} - k_0^2 N_i^2 e^{2u'/R_t}}\, du' = \gamma \int_{\xi_2}^{\xi_1} \frac{\xi^2}{1-\xi^2}\, d\xi = \gamma\left(\frac{1}{2}\ln\frac{1+\xi}{1-\xi} - \xi\right)\Bigg|_{\xi_2}^{\xi_1} =$$

$$= \gamma\left(\tfrac{1}{3}\xi^3 + \tfrac{1}{5}\xi^5 + \tfrac{1}{7}\xi^7 + \,....\right)\Bigg|_{\xi_2}^{\xi_1}. \tag{C.8}$$

Appendix D

Dirac's notation

Dirac's notation is used in section § 4.2 and its first occurrence is in Eq. (4.2.5). The normalized fields $|e_\mu\rangle$ and $|h_\mu\rangle$ are appropriately defined in each section and we have $\langle e_\mu| = |e_\mu\rangle$ and $\langle h_\mu| = |h_\mu\rangle$. The overlap integral has the following form

$$
\langle e_\mu^a | e_\nu^b \rangle \stackrel{\text{def}}{=}
\begin{cases}
\displaystyle\int_{y_{sc}}^{\infty} \frac{e_\mu^a(y)e_\nu^b(y)}{\sqrt{K_\mu^a K_\nu^b}}\, dy & \mu = 1, \ldots, M_a \text{ and } \nu = 1, \ldots, M_b \ , \\[2ex]
\displaystyle\int_{y_{sc}}^{\infty} \frac{e^a(y;\beta^a)e_\nu^b(y)}{\sqrt{K^a(\beta^a)K_\nu^b}}\, dy & \mu = M_a+1 \text{ and } \nu = 1, \ldots, M_b \ , \\[2ex]
\displaystyle\int_{y_{sc}}^{\infty} \frac{e_\mu^a(y)e^b(y;\beta^b)}{\sqrt{K_\mu^a K^b(\beta^b)}}\, dy & \mu = 1, \ldots, M_a \text{ and } \nu = M_b+1 \ , \\[2ex]
\displaystyle\int_{y_{sc}}^{\infty} \frac{e^a(y;\beta^a)e^b(y;\beta^b)}{\sqrt{K^a(\beta^a)K^b(\beta^b)}}\, dy & \mu = M_a+1 \text{ and } \nu = M_b+1 \ ,
\end{cases}
\tag{D.1}
$$

when the EH-polarization is considered and when the two waveguides a and b are both straight. Similar definitions apply to the HE-polarization and to the other types of junction. The norm of the discrete mode K_μ and the norm of the continuous

mode $K(\beta)$ are defined together with the normalization of the field, as in Eq. (4.2.6) for example.

Writing out all equations is a straightforward but arduous task. The completeness requirement Eq. (4.2.6), i.e. $\langle e_\xi^b | e_\nu^a \rangle \langle e_\nu^a | e_\mu^b \rangle = \delta_{\xi,\mu}$, for example, is shorthand for

$$\sum_{\nu=1}^{M_a} \left\{ \int_{y_{sc}}^\infty \frac{e_\xi^b(y)e_\nu^a(y)}{\sqrt{K_\xi^b K_\nu^a}} \, dy \int_{y_{sc}}^\infty \frac{e_\nu^a(y')e_\mu^b(y')}{\sqrt{K_\nu^a K_\mu^b}} \, dy' \right\} +$$

$$\int_{\beta^a \in B^a} \left\{ \int_{y_{sc}}^\infty \frac{e_\xi^b(y)e^a(y;\beta^a)}{\sqrt{K_\xi^b K^a(\beta^a)}} \, dy \int_{y_{sc}}^\infty \frac{e^a(y';\beta^a)e_\mu^b(y')}{\sqrt{K^a(\beta^a)K_\mu^b}} \, dy' \right\} d\beta^a = \delta_{\xi,\mu}, \qquad \text{(D.2)}$$

when $\xi, \mu \neq M_b+1$, and it is shorthand for

$$\sum_{\nu=1}^{M_a} \left\{ \int_{y_{sc}}^\infty \frac{e^b(y;\beta^b)e_\nu^a(y)}{\sqrt{K^b(\beta^b)K_\nu^a}} \, dy \int_{y_{sc}}^\infty \frac{e_\nu^a(y')e^b(y';\beta^{b'})}{\sqrt{K_\nu^a K^b(\beta^{b'})}} \, dy' \right\} +$$

$$\int_{\beta^a \in B^a} \left\{ \int_{y_{sc}}^\infty \frac{e^b(y;\beta^b)e^a(y;\beta^a)}{\sqrt{K^b(\beta^b)K^a(\beta^a)}} \, dy \int_{y_{sc}}^\infty \frac{e^a(y';\beta^a)e^b(y';\beta^{b'})}{\sqrt{K^a(\beta^a)K^b(\beta^{b'})}} \, dy' \right\} d\beta^a = \delta(\beta^b-\beta^{b'}), \text{(D.3)}$$

when $\xi = \mu = M_b+1$, and it equals zero either when $\xi \neq M_b+1$ and $\mu = M_b+1$ or when $\xi = M_b+1$ and $\mu \neq M_b+1$.

Appendix E

Recipe

Two examples are given in which a curved waveguide and the accompanying junction are optimized. One example concerns Al_2O_3/SiO_2 waveguides at a wavelength of 1300 nm and the second example optimizes a GaInAsP/InP curved waveguide for a wavelength of 1520 nm. The lateral refractive-index contrast must be as large as possible in order to reduce the radiation losses and we begin the optimization procedure with a fixed maximized lateral refractive-index contrast.

We consider the waveguide cross-section of Fig. 6.23, the HE_{00}-mode and a wavelength of 1300 nm. The refractive index of SiO_2 at this wavelength is $n = 1.447$ while the refractive index of Al_2O_3 is $n = 1.677$. Neglecting the influence of the air cover and the silicon substrate on the calculations, we find the effective refractive indices $N_{II} = 1.5580$ for the guiding layer and $N_I = N_{III} = 1.4470$ for the two cladding layers. A corresponding single-boundary bend with $N_1 = N_{II}$ and $N_2 = N_{III}$ has a lateral refractive-index contrast $\log(1 - N_2^2/N_1^2) \approx -0.86$. From Fig. 5.3, we find that a bend with a normalized radius of $\log(k_o R_1 N_1) \approx 2.68$ and a contrast of -0.86 exhibits a radiation loss of 1×10^{-3} dB/90°. We, thus, have $R_1 \approx 64$ μm. Alternatively, a value $C(\alpha) \approx 25$ can be obtained from Fig. 5.4 and substitution of this value into Eq. (5.2.2) yields a radius of curvature of $R_1 \approx 71$ μm. From Fig. 5.5, we find a normalized width of at least $k_0 w N_1 \geq 30$, or $w \geq 4$ μm, in order to be in the whispering-gallery-mode regime. Finally, from Fig. 5.7

can be found that $2 < k_0 \Delta r N_1 < 6$ for the parameters given. We take $k_0 \Delta r N_1 \approx 5$ and find a value for the offset of $0.6 \, \mu m < \Delta r < 0.7 \, \mu m$.

A more precise analysis by means of the staircase approximation and the transfer-matrix method results in a radiation loss of 1.1×10^{-3} dB/90° for a radius of curvature of $R_1 = 67 \, \mu m$ and a width of $w = 4 \, \mu m$, which is indeed in the whispering-gallery-mode regime. The maximization of the overlap integral, results in an minimum transmission loss of 0.05 dB for a parameter $\Delta r = 0.95 \, \mu m$ and a width of the straight waveguide $w_{straight} = 2.5 \, \mu m$.

We actually measured an excess loss of 0.23 dB for an S-bend with a curved section with $R_1 = 75 \, \mu m$, $w_{curved} = 6 \, \mu m$ and $\Phi = 90°$, joined to a straight waveguide with $w_{straight} = 3 \, \mu m$ and $\Delta r = 0.98 \, \mu m$.

As a second example, we consider the cross-section shown in Fig. 7.5, the EH_{00} mode and a wavelength of $1.52 \, \mu m$. The model of Utaka et al., [118] and Eq. (7.1.1), and the absorption wavelength $\lambda_g = 1.32 \, \mu m$ give a refractive index $n = 3.173$ for InP and $n = 3.408$ for GaInAsP. Using the effective-dielectric constant method, we find $N_I = N_{III} = 3.177 \, (= N_2)$ and $N_{II} = 3.266 \, (= N_1)$ which is calculated for a four-layer geometry. Consequently, the normalized contrast is $\log(1 - N_2^2/N_1^2) \approx -1.27$. From Fig. 5.3, we estimate a normalized radius of curvature of $\log(k_0 R_1 N_1) \approx 3.33$ or $R_1 = 158 \, \mu m$ in order to obtain a radiation loss of 1×10^{-3} dB/90°. From Fig. 5.5, we find $k_0 w N_1 \geq 45$ or $w_{curved} \geq 3.3 \, \mu m$. The lateral offset is determined from Fig. 5.7 as $6 < k_0 \Delta r N_1 < 8$ with a best interpolation around $k_0 \Delta r N_1 \approx 8$ or $\Delta r \approx 0.6 \, \mu m$.

A more precise analysis by means of the staircase approximation and the matrix-transfer algorithm results in a radiation loss of 1×10^{-3} dB/90° for a radius of curvature of $R_1 = 166 \, \mu m$. A minimized transition loss of 0.05 dB is found for a lateral offset of $\Delta r = 0.85 \, \mu m$ and a width of the straight waveguide of $w_{straight} = 2.2 \, \mu m$.

In section § 7.2, a loss of 0.5 dB/90° has been reported for a fabricated S-bend where $w_{curved} = 3.4 \, \mu m$, $w_{straight} = 3.0 \, \mu m$, $R_1 = 150 \, \mu m$ and $\Delta r = 0.9 \, \mu m$.

Bibliography

[1]   Abramowitz, M. and Stegun, I.A. (Eds.): Handbook of mathematical func-
        tions. Dover publications, New York, 1965

[2]   Albrecht, P., Döldissen, W., Niggebrügge, U., Nolting, H.-P. and Schmid,
        H.: "Waveguide-mirror components in InGaAsP/InP". Proceedings of the
        14th European conference on optical communication, Brighton, 1988, pp.
        235-238

[3]   American Institute of Physics Handbook. B.H.Billings *et al.* (Eds.),
        McGraw-Hill book company, New York, third edition.

[4]   Amersfoort, M.R., Oei, S.Y. and Smit, M.K.: "Measurement technique of
        waveguide losses based upon photoluminescence", Conference on semi-
        conductor and integrated optoelectronics SIOE' 90, March 27-28, 1990,
        Cardiff, United Kindom, paper 23

[5]   Angenent, J.H., Erman, M., Auger, J.M., Gamonal, R. and Thijs, P.J.A.:
        "Extremely low loss InP/GaInAsP rib waveguides", *Electronics Letters*, **25**
        (10), 1989, pp. 628-629

[6]   Austin, M.W. and Flavin, P.G.: "Small-radii curved rib waveguides in
        GaAs/GaAlAs using electron-beam lithography", *IEEE Journal of light-
        wave technology*, **LT-1** (1), 1983, pp. 236-240

[7]   Baets, R. and Lagasse, P.E.: "Loss calculation and design of arbitrarily
        curved integrated-optic waveguides", *Journal of the optical society of
        America*, **73** (2), 1983, pp. 177-182

[8]   Benson, T.M., Kendall, P.C. and Stern, M.S.: "Microwave simulation of
        optoelectronic bending loss in presence of dielectric discontinuity", *IEE
        Proceedings part J*, **135** (4), 1988, pp. 325-331

[9]   Benson, T.M., Kendall, P.C., Stern, M.S. and Quinney, D.A.: "New results
        for rib waveguide propagation constants", *IEE proceedings part J*, **136** (2),
        1989, pp. 97-102

[10]   Biehlig, W., Hehl, K., Langbein, U. and Lederer, F.: "Light propagation in
       a planar dielectric slab waveguide with step discontinuities", *Optical and
       Quantum Electronics*, **18**, 1986, pp. 219-246

[11]   Blok, H. and de Hoop, A.T.: "Source-type representation for fields in
       optical waveguide sections and their consequences for the spectral field
       constituents", in H.-C. Huang and A.W. Snyder (Eds.): Optical waveguide
       sciences, Part one. M. Nijhoff, The Hague, 1983, pp. 27-34.

[12]   Blok, H., van Splunter, J.M. and Janssen H.G.: "Leaky-wave modes and
       their role in the numerical evaluation of the field excited by a line source
       in a non-symmetric, inhomogeneously layered slab waveguide", *Applied
       scientific research*, **41**, 1984, 223-236

[13]   Bourbin, Y., Enard, A., Blondeau, R., Rondi, D. and Papuchon, M.: "Very
       low loss waveguides and efficient modulators in InGaAsP/InP", Proceed-
       ings of the conference on integrated and guided wave optics IGWO,
       Houston, U.S.A., February 6-8, 1989, paper MEE7

[14]   Bremmer, H.: "The W.K.B. approximation as the first term of a geometri-
       cal-optical series", *Communications of pure and applied mathematics*, **4**,
       1951, pp. 105(S169)-115(S179)

[15]   Buchmann, P. and Kaufmann, H.: "GaAs single-mode rib waveguides with
       reactive ion-etched totally reflecting corner mirrors", *IEEE Journal of
       Lightwave Technology*, 1985, **LT-3**, pp. 785-788

[16]   Chang, D.C. and Barnes, F.S.: "Reduction of radiation loss in a curved
       dielectric slab waveguide", Department of electrical engineering, Univer-
       sity of Colorado, Boulder, Colorado 80302, Scientific report No. 2
       (AFOSR-72-2417), 1973

[17]   Chang, D.C. and Kuester, E.F.: "A hybrid method for paraxial beam
       propagation in multimode optical waveguides", *IEEE Transactions on
       microwave theory and techniques*, **MTT-29** (9), 1981, pp. 923-933

[18]   Chen, S.-P. and Unger H.-G.: "Low loss bends for planar optical wave-
       guides", *Archiv für Elektronik und Übertragungstechnik*, 1988, **42** (4), pp.
       256-259

[19]   Chilwell, J. and Hodgkinson, I.: "Thin-films field-transfer matrix theory of planar multilayer waveguides and reflection from prism-loaded waveguides", *Journal of the Optical Society of America A*, 1984, **1**, pp. 742-753

[20]   Chu, Y.T., Bates, J.B., White, C.W. and Farlow, G.C.: "Optical dielectric functions for amorphous Al_2O_3 and γ-Al_2O_3", *Journal of applied physics*, **64** (7), 1988, pp. 3727-3730

[21]   Chung, Y., Yi, J.C., Kim, S.H., and Choi, S.S.: "Analysis of a tunable multichannel two-mode-interference wavelength division multiplexer/demultiplexer", *Journal of lightwave technology*, **7** (5), 1989, pp. 766-777

[22]   Clarricoats, P.J.B. and Sharpe, A.B.: " Modal matching applied to a discontinuity in a planar surface waveguide", *Electronics Letters*, **8** (2), 1972, pp. 28-29

[23]   Collin, R.E.: Electromagnetic fields. Chapter 1 in Antenna Theory, Inter-university electronics series, 7, R.E. Collin and F.J. Zucker (Eds.), McGraw-Hill book company, New York, 1969

[24]   de Bernardi, C., Morasca, S., Rigo, C., Sordo, B., Stano, A., Croston, I.R. and Young, T.P.: "Wavelength demultiplexer integrated on AlGaInAs/InP for 1.5 μm operation", *Electronics Letters*, **25** (22), 1989, pp. 1488-1489

[25]   Deri, R.J., Hawkins, R.J., Kapon, E. and Schiavone, L.M.: "Scattering and coherent coupling in low-loss GaAs waveguides and bends", Proceedings of the conference on integrated and guided-wave optics, Technical digest series, **Vol. 5**, OSA, Washington, 1988, pp. 40-43

[26]   Deri, R.J., Hawkins, R.J. and Kapon, E.: "Rib profile effects on scattering in semiconductor optical waveguides", *Applied physics letters*, **53** (16), 1988, pp. 1483-1485

[27]   de Ruiter, H.M.: "Radiation from the junction of two open waveguide sections", *Radio science*, **19** (5), 1984, pp. 1295-1300

[28]   de Ruiter, H.M.: Transmission, reflection and radiation at junction planes of different open waveguides. PhD Thesis, Eindhoven, 1989

[29]   de Zutter, D., Lagasse, P., Buus, J., Young, T.P., Dillon, B.M., Nolting,
       H.P., Weinert, C., di Vita, P., Potenza, M., Besse, P.A., Gu, J.-S., Galtaros-
       sa, A., Someda, C.G., Amann, M.-C., Borchert, B., van der Tol, J.J.G.M.,
       Baken, N.H.G., Bourbin, Y., Cavaillès, J.A., Erman, M., Gamonal, R.,
       Vasallo, C., Krijnen, G.J.M., Hoekstra, H.J.W.M. and Popma, T.J.A.:
       "COST-216 comparison of different modelling techniques for longitudi-
       nally invariant integrated optical waveguides", *IEE proceedings part J*, **136**
       (5), 1989, pp. 273-280

[30]   Doeksen, D.K., Groen, F.H., Oei, Y.S., Pedersen, J.W., Pennings, E.C.M.,
       van Brug, H. and van der Tol, J.J.G.M.: "Low propagation losses in
       LPE-grown InGaAsP waveguides", Proceedings of the European con-
       ference on optical integrated systems at Amsterdam (ECOISA '89),
       September 25-28, 1989, Amsterdam, the Netherlands, paper T2

[31]   Döldissen, W., Heidrich, H., Hoffmann, D., Thylén, L. and Lagerström, B.:
       "Reduction of bend-losses in integrated optics devices", Proceedings of the
       3rd European conference on integrated optics (ECIO '85), May 6-8, 1985,
       Berlin, F.R.G., pp. 210-214

[32]   Erman, M.: "Integrated Guided-Wave Optics on III-V Semiconductors",
       Proceedings of the 14th international symposium on Gallium Arsenide and
       related compounds, Heraklion Crete, Sept. 1987, pp. 33-40

[33]   Felsen, L.B. and Marcuvitz, N.: Radiation and scattering of waves. Pren-
       tice-Hall Inc., Englewood Cliffs, New Jersey, 1973

[34]   Fiedler, F. and Schlachetzki, A.: "Optical parameters of InP-based wave-
       guides", *Solid state electronics*, **30** (1), 1987, pp. 73-83

[35]   Ghatak, A.J., Thyagarajan, K. and Shenoy, M.R.: "Numerical analysis of
       planar optical waveguides using matrix approach", *IEEE Journal of light-
       wave technology*, **LT-5** (5), 1987, pp. 660-667

[36]   Gu, J.S., Besse, P.A. and Melchior H.: " Novel method for analysis of
       curved optical rib-waveguides", *Electronics letters*, **25** (4), 1989, pp. 278-
       280

[37]   Gu, J.S. and Melchior, H.: "Design of low-loss curved integrated optical rib-waveguides", Proceedings of the European conference on optical integrated systems at Amsterdam (ECOISA '89), September 25-28, 1989, Amsterdam, the Netherlands, paper W3

[38]   Harris, J.H., Shubert, R. and Polky, J.N.: "Beam coupling to films", *Journal of the optical society of America*, **60** (8) , 1970, pp. 1007-1016

[39]   Harris, J.H. and Shubert, R.: "Variable tunneling excitation of optical surface waves", *IEEE Transactions on microwave theory and techniques*, **MTT-19** (3), 1971, pp. 269-276

[40]   Heiblum, M. and Harris, J.H.: "Analysis of curved optical waveguides by conformal transformation", *IEEE Journal of quantum electronics*, **QE-11** (2), 1975, pp. 75-83. Plus correction, *ibidem*, **QE-12**, 1976, p. 313

[41]   Heiblum, M.: "The prism coupler and the dielectric bend: similarities and anomalous behaviour", *IEEE Journal of quantum electronics*, **QE-12**, 1976, pp. 463-469

[42]   Henry, C.H., Johnson, L.F., Logan R.A. and Clarke D.P.: "Determination of the refractive index of InGaAsP epitaxial layers by mode line luminescence spectroscopy", *IEEE Journal of quantum electronics*, **QE-21** (12), 1985, pp. 1887-1892

[43]   Hessel, A.: General characteristics of travelling-wave antennas. Chapter 19 in Antenna Theory, Inter-university electronics series, **7**, R.E. Collin and F.J. Zucker (Eds.), McGraw-Hill book company, New York, 1969

[44]   Himeno, A., Kobayashi, M. and Terui, H.: "High-silica single-mode optical reflection bending and intersecting waveguides", *Electronics letters*, **21** (22), 1985, pp. 1020-1021

[45]   Himeno, A., Terui, H. and Kobayashi, M.: "Guided-wave optical gate matrix switch", *Journal of lightwave technology*, **6** (1), 1988, pp. 30-35

[46]   Himeno, A., Terui, H. and Kobayashi, M.: "Loss measurement and analysis of high-silica reflection bending optical waveguides", *Journal of lightwave technology*, **6** (1), 1988, pp. 41-46

[47]   Hinken, J.H.: "Film mode attenuation due to random surface irregularities".
       Proceedings of the 6th European microwave conference, Rome, 1976, pp.
       513-517

[48]   Hockham, G.A. and Sharpe, A.B.: "Dielectric-waveguide discontinuities",
       Electronics Letters, 1972, **8** (9), 230-231

[49]   Hsue, C.W. and Tamir, T.: "Evolution of transverse-electric surface and
       leaky waves guided by an asymmetric layer configuration", *Journal of the
       Optical Society of America A*, **1**, 1984, p. 923

[50]   Jackson, J.D.: Classical electrodynamics. John Wiley & sons, New York,
       1975 (2nd ed.)

[51]   Kendall, P.C., Robson, P.N., Sitch, J.E.: "Rib waveguide curvature loss:
       the scalar problem", *IEE Proceedings part J*, **132** (2), 1985, pp. 140-145

[52]   Kendall, P.C., Marsh, J.H., Robson, P.N., Hewson-Browne, R.C.: " Fraun-
       hofer interference of a dielectric interface with travelling wave radiation
       and the consequent reduction in dielectric waveguide bending loss", *IEE
       Proceedings part J*, **132** (6), 1985, pp. 354-358

[53]   Kendall, P.C., Stern, M.S. and Robson, P.N.: "Huygens-type formula for
       curvature loss from dielectric waveguides in optoelectronics", *Electronics
       letters*, **23** (16), 1987, pp. 850-851

[54]   Kendall, P.C., Adams, M.J., Ritchie, S. and Robertson, M.J.: "Theory for
       calculating approximate values for the propagation constants of an optical
       rib waveguide by weigting the refractive indices", *IEE Proceedings part J*,
       134 (8), 1987, pp. 699-702

[55]   Kendall, P.C., Stern, M.S. and Robson, P.N.: "A new curvature loss formula
       of Huygens-type for rib waveguides", *IEE Proceedings part J*, **135** (1),
       1988, pp. 11-16

[56]   Kendall, P.C., Adams, M.J., McIlroy, P., Ritchie, S. and Robertson M.J.:
       "A new technique for analysing planar optical waveguides", Proceedings
       of the conference on integrated and guided wave optics (IGWO'88), March
       28-30, 1988, Santa Fe, U.S.A., paper MF5

[57]   Knox, R.M. and Toulios P.P.: "Integrated circuits for the millimeter through optical frequency range", Proceedings of the symposium on submillimeter waves, March 31-April 2 1970, pp. 497-516. Microwave research institute symposia series, Volume XX, J.Fox (Ed.), Polytechnic press, New York, 1970

[58]   Koehler, B.G. and Bowers, J.E.: "In-line single-mode fiber polarization controllers at 1.55, 1.30 and 0.63 μm", *Applied optics*, **24** (3), 1985, pp. 349-353

[59]   Kolk, E.W., Baken, N.H.G. and Blok, H.: "Domain integral equation analysis of integrated optical channel and ridge waveguides in stratified media", *IEEE Transactions on microwave theory and techniques*, **38** (1), 1990, pp. 78-85

[60]   Kramers, H.A.: "Wellenmechanik und halbzahlige Quantisierung", *Zeitschrift für Physik*, **39**, 1926, pp. 828-840

[61]   Kou, F.Y. and Tamir, T.: "Evolution of transverse-magnetic surface and leaky waves guided by an asymmetric layer configuration", *Journal of the Optical Society of America A*, **3**, 1986, p. 417

[62]   Kuznetsov, M. and Haus, H.A.: "Radiation loss in dielectric waveguide structures by the volume current method", *IEEE Journal of quantum electronics*, **QE-19** (10), 1983, pp. 1505-1514

[63]   Landau, L.D. and Lifschitz, E.M.: Quantum mechanics, non-relativistic theory, Volume 3 of course of theoretical physics. Pergamon, 1965

[64]   Levinson, N. and Redheffer, R.M.: Complex variables. Holden-Day, San Fransisco, 1970

[65]   Lewin, L., Chang, D.C. and Kuester E.F.: Electromagnetic waves and curved structures. IEE Electromagnetic waves series 2, J.R.Wait et al. (Eds.), Peter Peregrinus Ltd., Stevenage, 1977

[66]   Marcatili, E.A.J.: "Dielectric rectangular waveguide and directional coupler for integrated optics", *the Bell system technical journal*, **48** (7), 1969, pp. 2071-2102

[67]   Marcatili, E.A.J.: "Bends in optical dielectric guides", *the Bell system technical journal*, **48** (7), 1969, pp. 2103-2132

[68]   Marcatili, E.A.J.: "Dielectric tapers with curved axes and no loss", *IEEE Journal of quantum electronics*, **QE-21** (4), 1985, pp. 307-314

[69]   Marcuse, D.: "Mode conversion caused by surface imperfections of a dielectric slab waveguide", *the Bell system technical Journal*, 1969, **48**, pp. 3187-3215

[70]   Marcuse, D.: "Bending losses of the asymmetric slab waveguide", *the Bell system technical Journal*, 1971, **50**, pp. 2551-2563

[71]   Marcuse, D.: Light transmission optics. Bell laboratories series. Van Nostrand Reinhold Company, New York, 1972

[72]   Marcuse, D.: Theory of dielectric optical waveguides. Academic press, New York and London, 1974

[73]   Mathews, J. and Walker, R.L.: "Mathematical methods of physics", the Benjamin/Cummings publishing company, Menlo Park, 1970

[74]   Merzbacher, E.: Quantum mechanics. John Wiley & Sons, Tokyo, 1961

[75]   Morita, N. and Yamada, R.: "Electromagnetic fields in circular bends of slab waveguides", *IEEE Journal of lightwave technology*, **8** (1), 1990, pp. 16-22

[76]   Neumann, E.-G. and Rudolph, H.-D.: " Radiation from bends in dielectric rod transmission lines", *IEEE Transactions on microwave theory and techniques*, **MTT-23** (1), 1975, pp. 142-149

[77]   Neumann, E.-G.: "Reducing radiation loss of tilts in dielectric optical waveguides", *Electronics letters*, **17** (11), 1981, pp. 369-371

[78]   Neumann, E.-G.: " Dielectric optical waveguide tilts with reduced losses", Proceedings of the 7th ECOC, Copenhagen, 1981, paper 9.3

[79]   Neumann, E.-G.: "Low loss dielectric optical waveguide bends", *Fiber and integrated optics*, **4** (2), 1982, pp. 203-211

[80]   Neumann, E.-G.: "Curved dielectric optical waveguides with reduced transition losses", *IEE Proceedings part H*, **129** (5), 1982, pp. 278-280

[81]   Neumann, E.-G. and Richter, W.: " Sharp bends with low losses in dielectric optical waveguides", *Applied optics*, **22** (7), 1983, pp. 1016-1022

[82]   Neumann, E.-G.: Patentschrift DE 31 07 112 C2, Deutsches Patentamt, Patentinhaber: Philips Kommunikations Industrie AG, 8500 Nürnberg, DE. September 5th, 1985

[83]   Niggebrügge, U., Albrecht, P. Döldissen, W., Nolting, H.-P. and Schmid, H.: "Self-aligned low-loss totally reflecting waveguide mirrors in In-GaAsP/InP", Proceedings of the European conference on integrated optics ECIO'87, 1987, pp. 90-93

[84]   Neyer, A. and Dang, D.: "Guided-wave polarization splitter based on two-mode-interference", Proceedings of the conference on integrated and guided-wave optics (IGWO'88), March 28-30, 1988, Santa Fe, U.S.A., paper ME3.

[85]   Olver, F.W.J.: "Some new asymptotic expansions for Bessel functions of large order", *Proc. Cambridge Philos. Soc.*, **48**, 1952, pp. 414-427

[86]   Olver, F.W.J.: "The asymptotic expansion of Bessel functions of large order", *Philos. Trans. Royal Soc. London*, **A247**, 1954, 328-368

[87]   Papuchon, M.R. and Ostrowsky, D.B.: "Electrically active optical bifurcation: BOA", *Applied physics letters*, **31**, 1977, pp. 266-267

[88]   Pasmooij, W.A., Mandersloot, P.A., and Smit, M.K.: "Prism-coupling of light into narrow planar optical waveguides", *IEEE Journal of lightwave technology*, **7**, 1989, pp. 175-180

[89]   Pedersen, P. and Nightingale, J.L.: "A simplified method of calculating power transfer between nonparallel dielectric waveguides", Proceedings of the conference on integrated and guided-wave optics (IGWO'88), March 28-30, 1988, Santa Fe, U.S.A., paper MF4.

[90]   Pennings, E.C.M., Manhoudt, G.H. and Smit, M.K.: "Low-loss bends in planar optical waveguides", *Electronics letters*, **24** (16), 1988, pp. 998-999

[91]   Pennings, E.C.M.: "Small-radii curved waveguides for integrated optoelectronics", Conference on semiconductor and integrated optoelectronics (SIOE '89), March 20-21, 1989, Cardiff, United Kingdom, presentation 10

[92]   Pennings, E.C.M., van Schoonhoven, J., van Uffelen J.W.M. and Smit, M.K.: "Reduced bending and scattering losses in new optical 'double-ridge' waveguide", *Electronics Letters*, **25** (11), 1989, pp. 746-747

[93] Pennings, E.C.M.: "Small-radii curved waveguides for integrated optics", Proceedings of the European conference on optical integrated systems at Amsterdam (ECOISA '89), September 25-28, 1989, Amsterdam, the Netherlands, paper W4

[94] Ramaswamy, V.: "Strip-loaded film waveguides", *the Bell system technical journal*, **53** (4), 1974, pp. 697-704

[95] Lord Rayleigh: "The problem of the whispering gallery", *the London Edinburgh, and Dublin philosophical magazine and journal of science*, 6th series, **20**, 1910, pp. 1001-1004

[96] Lord Rayleigh: "Further applications of Bessel's functions of higher order to the whispering gallery and allied problems", *the London Edinburgh, and Dublin philosophical magazine and journal of science*, 6th series, **27**, 1914, pp. 100-109

[97] Rottmann, F., Voges, E.: "Low-insertion-loss, tunable wavelength multiplexer on lithium niobate", *Electronics Letters*, **23** (19), 1987, pp. 1007-1008

[98] Rottmann, F., Neyer, A., Mevenkamp, W. and Voges, E.: "Integrated-optic wavelength multiplexers on lithium niobate based on two-mode interference", *Journal of lightwave technology*, **6** (6), 1988, pp. 946-952

[99] Rozzi, T.E.: "Rigorous analysis of the step discontinuity in a planar dielectric waveguide", *IEEE Transactions on microwave theory and techniques*, **MTT-26** (10), 1978, pp. 738-746

[100] Rozzi, T., Cerri, G., Chiaraluce, F., de Leo, R. and Ormondroyd, R.F.: "Finite curvature and corrugations in dielectric ridge waveguides", *IEEE Transactions on microwave theory and techniques*, **36** (1), 1988, pp. 68-79

[101] Seto, M., Deri, R.J., Yi-Yan, A., Colas, E., John Tomlinson, W., Bhat, R. and Shahar, A.: "Fabrication of submillimeter-radius optical waveguide bends with anisotropic and isotropic wet chemical etchants", *Journal of lightwave technology*, **8** (2), 1990, pp. 264-270

[102] Sheem, S. and Whinnery, J.R.: "Guiding by single curved boundaries in integrated optics", *Wave Electronics*, **1**, 1974/75, pp. 61-68

[103] Sheem, S. and Whinnery, J.R.: "Modes of a curved surface waveguide for integrated optics", *Wave Electronics*, **1**, 1974/75, pp. 105-106

[104] Singh, J., Henning, I., Harlow, M. and Cole, S.: "Single mode low-loss buried optical waveguide bends in GaInAsP/InP fabricated by dry etching", *Electronics letters*, **25** (14), 1989, pp. 899-900

[105] Smit, M.K., Acket, G.A., and van der Laan, C.J.: "Al$_2$O$_3$ films for integrated optics", *Thin Solid Films*, 1986, **138**, pp. 171-181

[106] Snyder, A.W. and Love, J.D.: Optical waveguide theory. Chapman and Hall, London, 1983

[107] Stern, M.S., Kendall, P.C. and Robson, P.N.: "Estimation of rib waveguide radiation losses", *Electronics letters*, **24** (1), 1988, pp. 17-19

[108] Syms, R.R.A. and Peall, R.G.: "The digital optical switch: analogous directional coupler devices", *Optics communications*, **69** (3,4), 1989, pp. 235-238

[109] Tamir, T.: "Leaky waves in planar optical waveguides", *Nouv. Rev. Optique*, **6** (5), 1975, pp. 273-284

[110] Tamir, T. (Ed.): Integrated optics. Topics in applied physics, **Vol. 7.** Springer Verlag, Berlin, 1979

[111] Taylor, R.I., Walker, R.G., Robbins, D.J. and Wale, M.J.: "BPM modelling of InP/InGaAsP curved couplers", Conference on semiconductor and integrated optoelectronics (SIOE '89), March 20-21, 1989, Cardiff, United Kingdom, presentation 9

[112] Thyagarajan, K., Shenoy, M.R. and Ghatak, A.K.: "Accurate numerical method for the calculation of bending loss in optical waveguides using a matrix approach", *Optics letters*, **12** (4), 1987, pp. 296-298

[113] Tien, P.K. and Ulrich R.: "Theory of prism-coupler and thin-film light guides", *Journal of the optical society of America*, **60** (10), 1970, pp. 1325-1337

[114] Tien. P.K.: "Light waves in thin films and integrated optics", *Applied optics*, **10** (11), 1971, pp. 2395-2413

[115] Tijhuis, A.G.: "Angularly propagating waves in a radially inhomogeneous, lossy dielectric cylinder and their connection with the natural modes", *IEEE Transactions on antennas and propagation*, **AP-34** (6), 1986, 813-824

[116] Ulrich, R. and Kamiya, T.: "Resolution of self-images in planar optical waveguides", *Journal of the optical society of America*, **68** (5), 1978, pp. 583-592

[117] Unger, H.-G.: Planar optical waveguides and fibres. Clarendon press, Oxford, 1977

[118] Utaka, K., Kobayashi, K.-I. and Suematsu, Y.: "Lasing characteristics of 1.5-1.6 μm GaInAsP/InP integrated twin-guide lasers with first order distributed bragg reflectors", *IEEE Journal of quantum electronics*, **QE-17** (5), 1981, pp. 651-658

[119] van Brug, H., Groen, F.H., Oei, Y.S., Pedersen, J.W., Pennings, E.C.M., Doeksen, D.K., van der Tol, J.J.G.M.: "Low-loss straight and curved ridge waveguides in LPE-grown GaInAsP", *Electronics letters*, **25** (20), 1989, pp. 1330-1331

[120] van der Drift, E., Rousseeuw, B.A.C., Romijn, J., Pennings, E.C.M. and Groen, F.H.: " High resolution patterning of aluminumoxide for integrated optical devices", Proceedings of the international conference on microlithography ME'88, September 20-22, 1988, Vienna, Austria, pp. 499-502

[121] van der Tol, J.J.G.M. and Baken, N.H.G.: "Correction to effective index method for rectangular dielectric waveguides", *Electronics letters*, **24** (4), 1988, pp. 207-208

[122] Verbeek, B.H., Pennings, E.C.M., van Uffelen, J.W.M. and Thijs, P.J.A.: "Fabrication and analysis of low-loss InGaAsP/InP optical waveguides with extremely small bends", Proceedings of the 15th European conference on optical communication ECOC '89, September 10-14, 1989, Gothenburg, Sweden, paper PDB-9

[123] Wasylkiwskyj, W.: "Diffraction by a concave perfectly conducting circular cylinder", *IEEE Transactions on antennas and propagation*, **AP-23** (4), 1975, pp. 480-492

[124] Xu, S.-J.: "Dielectric-waveguide branching directional coupler", *IEE Proceedings part H*, **135** (4), 1988, pp. 282-284

List of symbols and acronyms

ELECTROMAGNETIC AND RELATED QUANTITIES

Symbol	Name or description	Unit
E	Electric field strength in the time domain	$V\,m^{-1}$
H	Magnetic field strength in the time domain	$A\,m^{-1}$
S	Poynting's vector in the time domain (Eq. (2.1.18))	$W\,m^{-2}$
P	Electromagnetic power (Eq. (2.3.14))	W
E	Electric field strength in the frequency domain	$V\,m^{-1}$
H	Magnetic field strength in the frequency domain	$A\,m^{-1}$
D	Strength of the frequency-domain electric induction	$C\,m^{-2}$
B	Strength of the frequency-domain magnetic induction	T
$\tilde{E}$	Fourier transform of the frequency-domain electric field strength with respect to the coordinate of propagation	$V\,m^{-2}$
$\tilde{H}$	Fourier transform of the frequency-domain magnetic field strength with respect to the coordinate of propagation	$A\,m^{-2}$
$e_\mu^\pm$	The modal distribution of the frequency-domain electric field strength corresponding to the propagation constant β_μ or γ_μ for the straight and the curved waveguide, respectively. The $+$ and $-$ sign indicate waves that propagate in the forward or backward direction. (Pages 25 and 30)	$V\,m^{-1}$
$h_\mu^\pm$	The modal distribution of the frequency-domain magnetic field strength corresponding to the propagation constant β_μ or γ_μ for the straight and the curved waveguide, respectively. (Pages 25 and 30)	$A\,m^{-1}$
β_μ	Propagation constant of the guided mode with mode number μ in a straight waveguide	m^{-1}
β	Propagation constant of a continuous mode in a straight waveguide	m^{-1}
γ_μ	Propagation constant of the guided mode with mode number μ in a curved waveguide	1
γ	Propagation constant of a continuous mode in a curved waveguide	1
γ^0	Lowest-order approximation to γ	1

Symbol	Name or description	Unit
$c_\mu^\pm$	Excitation coefficient of the guided mode with mode number μ in straight and curved waveguides. (Eqs. 2.3.3 and 2.3.17)	1
$c^\pm(\beta)$	Excitation coefficient of the continuous mode with propagation constant β in a straight waveguide. (Eq. 2.3.3)	m
$c^\pm(\gamma)$	Excitation coefficient of the continuous mode with propagation constant γ in a curved waveguide. (Eq. 2.3.17)	1
ε	Dielectric permittivity (Eqs. 2.1.6, 2.1.8 and 2.1.9)	$F\,m^{-1}$
ε_0	Dielectric permittivity of the vacuum $\varepsilon_0\mu_0 c^2 = 1$ $$\varepsilon_0 = 8.854187817\ldots \times 10^{-12}$$	$F\,m^{-1}$
μ_0	Permeability of the vacuum $\mu_0 \stackrel{\text{def}}{=} 4\pi \times 10^{-7}$	$N\,A^{-2}$
n	Plane-wave index of refraction (Eq. 2.1.10)	1
N	Effective index of refraction (Eqs. 2.3.9 and 2.3.26)	1
$\aleph$	Parameter defined in Eq. (4.1.8)	1
α	Attenuation of light in a straight waveguide (Eq. 2.3.10)	dB/cm
α_0	Proportionality constant in Eq. (6.4.1)	dB/cm
α_1	Proportionality constant in Eq. (6.4.1)	dB
α	Attenuation of light in a curved waveguide (Eq. 2.3.27)	dB/90°
K_μ	Normalization constant of the guided mode with mode number μ. (Eqs. 2.3.11 and 2.3.39) (Eqs. 4.2.1 through 4.2.4)	W $W\,m^{-1}$
$K(\beta)$	Normalization constant of the continuous mode in a straight waveguide with propagation constant β. (Eq. 2.3.13)	$W\,m^{-1}$
$K(\gamma)$	Normalization constant of the continuous mode in a curved waveguide with propagation constant γ. (Eq. 2.3.41)	W
S	Scattering matrix of a junction (Eq. 4.2.16 and Table 4.1)	1
T	Transmission matrix of a junction (Eq. 4.2.16 and Table 4.1)	1
R	Reflection matrix of a junction (Eq. 4.2.16 and Table 4.1)	1
$C, \tilde{C}$	Overlap matrix C and its transpose $\tilde{C}$ (Eqs. 4.2.24 and 4.2.25 and Table 4.1)	
η	Coupling or transition loss (Eq. 4.2.57)	dB
E_0	Photon energy $hc/(e\lambda_0)$ (Eq.7.1.1)	eV

Symbol	Name or description	Unit
E_g	Photon energy which corresponds to the band-gap absorption wavelength $hc/(e\lambda_g)$ (Eq.7.1.1)	eV
N_e	Concentration of free electrons (Eq.7.1.5)	m^{-3}
$m_e, m_{e,eff}$	Mass and effective mass of the electron (Eq.7.1.5)	kg

MATHEMATICAL SYMBOLS

Symbol	Name or description	Unit
∇	Nabla operator	m^{-1}
$\tilde{\nabla}^2$	Laplacian operator in cylindrical coordinates (Eq. 2.3.24)	m^{-2}
$\times$	Vector cross product	
$\cdot$	Vector dot product	
j	Imaginary unit $\sqrt{-1}$	
∂_x	Partial derivative with respect to coordinate x ($\partial_x = \partial/\partial x$)	m^{-1}
$\delta_{\mu,\nu}$	Kronecker delta symbol ($= 0$ if $\mu \neq \nu$; $= 1$ if $\mu = \nu$)	1
$\delta(\beta - \beta')$	Delta function ($= 0$ if $\beta \neq \beta'$ and $\int \delta(\beta - \beta')d\beta = 1$)	m
$\delta(\gamma - \gamma')$	Delta function ($= 0$ if $\gamma \neq \gamma'$ and $\int \delta(\gamma - \gamma')d\gamma = 1$)	1
μ, ν	Mode numbers	
B	Branch cut	
z^*	Complex conjugate of the complex variable z	
$<>$	Time-average (used in Eq. 2.1.18)	
$\langle \mid \rangle$	Dirac's bracket notation	
$\propto$	Proportionality	
Δ	Difference operator	
$\overset{\text{def}}{=}$	Equality by definition	
$\Leftarrow$	Implied by, follows from	
$\Leftrightarrow$	Equivalence	
D_s	Eigenvalue equation of the straight slab waveguide	
D_c	Eigenvalue equation of the curved slab waveguide	
D_{WKB}	Eigenvalue equation for the single-boundary bend as found from the WKB approximation	
$J_\gamma(z)$	Bessel function of the first kind and order γ (§ 4.1.2)	
$Y_\gamma(z)$	Bessel function of the second kind and order γ (§ 4.1.2)	
$H_\gamma^{(1)}(z)$	Hankel function of the first kind and order γ (§ 4.1.2)	

Symbol	Name or description	Unit
$H_\gamma^{(2)}(z)$	Hankel function of the second kind and order γ (§ 4.1.2)	
a, b	Label that are used to denote both waveguides at a junction	
i	Index or label	
l	Index or label	
M	Total number of guided modes or total number of partitions	
m	Number of partitions in one domain	

QUANTITIES RELATED TO SPACE AND TIME

Symbol	Name or description	Unit
S	Description of a surface	
V	Description of a volume	
D_i	Description of a domain with index i	
$\hat{n}$	Outward pointing unit vector, normal to a surface	1
r	Position vector	m
x	Coordinate of a Cartesian or a cylindrical coordinate system	m
$\hat{x}$	Unit vector $\hat{x} = x/|x|$	1
y, z	Coordinates of a Cartesian coordinate system	m
$\hat{y}, \hat{z}$	Unit vectors	1
k_z	Fourier transform variable (Eq. (2.3.1))	m^{-1}
r	Radial coordinate of a cylindrical coordinate system	m
$\hat{r}$	Unit vector $\hat{r} = r/|r|$	1
Δr	'Lateral offset' (Eqs. 4.1.49 and 5.2.5)	m
R_i	Radius of curvature of interface i	m
R_{sc}	Radius of curvature of the perfect conductor that screens the origin	m
R_t	Parameter of the transformation Eq. (4.1.16) or a parameter that is used to introduce an effective index of refraction for the curved waveguide (Eq. 2.3.26)	m
φ	Angular coordinate of a cylindrical coordinate system	1
$\hat{\varphi}$	Unit vector	1
k_φ	Fourier transform variable (Eq. 2.3.15)	1
Φ	Section angle of a curved waveguide (Eq. 2.2.5)	m
θ	Angle (Eqs. 4.4.4 or 6.1.1)	
u	Transformed coordinate (Eqs. 4.1.16 and 4.4.3)	m

Symbol	Name or description	Unit
U_{sc}	Location of the screen expressed in coordinate u	m
v	Transformed coordinate (Eq. 4.4.3)	m
h	Height of waveguide or film	m
H	Ridge height	m
D	Distance between the sides of the first and the second ridge	m
w	Width of waveguide	m
L_{MMI}	Length of the straight section in the two-mode interference coupler (Fig. 5.8)	m
L_π	Beat length between the two lowest-order modes (Eq. 5.3.1)	m
λ_g	Band-gap absorption wavelength	m
λ_0	Wavelength in vacuum $\lambda_0 = 2\pi/k_0$	m
k_0	Wave number in vacuum (Eq. 2.1.11)	m^{-1}
c	Speed of light in vacuum $c \stackrel{\mathrm{def}}{=} 299792458$	$m\,s^{-1}$
t	Time coordinate (Eq. 2.1.1)	s
T	Period of an oscillation with angular frequency $\omega = 2\pi/T$	s
ω	Angular frequency (Eq. 2.1.1)	s^{-1}
$k_{x,i}$	Component $k \cdot x$ of the local wave number in a domain that has been labeled i. (Similarly for other components)	m^{-1}

ACRONYMS

Acronym	Name
BPM	Beam-propagation method
CEIM	Corrected effective-index method
COST	Coopération Européenne dans le domaine de la science et de la technologie (European cooperation in the field of scientific and technical research)
DRG	'Double-ridge' waveguide
ECOC	European conference on optical communication
EDC	Method of effective dielectric constant
EIM	Effective-index method
LPE	Liquid-phase epitaxy
LPMOCVD	Low-pressure metallo-organic chemical-vapor deposition
MMI	Multi-mode-interference coupler
MOCVD	Metallo-organic chemical-vapor deposition
MOVPE	Metallo-organic vapor-phase epitaxy
OEIC	Optoelectronic integrated circuit
RIE	Reactive-ion etching
SADE	Self-aligned doubly etched curved waveguides
SEM	Scanning electron microscope
SRG	'Single-ridge' waveguide
TE	Transverse-electric modes or polarization
TM	Transverse-magnetic modes or polarization
TMI	Two-mode-interference coupler
WGM	Whispering-gallery mode
WKB	Wentzel-Kramers-Brillouin approximation

Samenvatting

Dit proefschrift gaat over de modellering en de vervaardiging van gebogen optische golfgeleiders en de bepaling van hun verliezen.

De eigenschappen van gebogen golfgeleiders—de afstralingsverliezen en de velddistributiefuncties van de modi—zijn berekend met behulp van de effectieve index methode in combinatie met drie andere methoden die geschikt zijn voor de analyse van de resulterende gebogen planaire golfgeleider; (a) een methode, die gebruik maakt van de Bessel functies, (b) een transformatie, die een gebogen planaire golfgeleider in een rechte golfgeleider transformeert, gecombineerd met de WKB benadering en (c) dezelfde transformatie samen met een discretisatie en het formalisme van de overdrachtsmatrix. De numerieke resultaten van deze drie methoden bleken in goede onderlinge overeenstemming te zijn. Ook is aangetoond, dat de effectieve index methode op een vergelijkbare wijze op gebogen optische golfgeleiders toegepast mag worden, als waarop zij op rechte golfgeleiders toegepast wordt.

De koppeling van de gebogen en de rechte golfgeleider is mede bestudeerd en met het oog daarop zijn orthogonaliteitsrelaties afgeleid voor de gebogen golfgeleider. Exacte oplossingen zijn bepaald voor de koppeling van planaire golfgeleiders. Numerieke resultaten zijn daarentegen verkregen door deze exacte oplossingen te benaderen door overlapintegralen.

Een transformatie is geïntroduceerd voor de analyse van twee gekoppelde golfgeleiders met identieke kromtestralen en tegengestelde kromming. Deze transformatie biedt inzicht in de koppel- en verliesmechanismen van een dergelijke configuratie en kan gebruikt worden om numerieke resultaten te verkrijgen. Dergelijke numerieke berekeningen zijn niet gedaan.

De ontwikkelde modellen en de bijbehorende computerprogrammatuur zijn gebruikt om de verliezen van gebogen golfgeleiders te minimaliseren. Genormaliseerde grafieken zijn vervaardigd voor de afstralingverliezen, de minimale breedte die een gebogen optische golfgeleider dient te hebben en de laterale compensatie ter plaatse van de koppeling. Ontwerpregels zijn gegeven voor deze minimalisatie.

De ontwikkelde computerprogrammatuur is ook toegepast op de multimodale interferentiekoppelaar. De resultaten van de modellering tonen aan dat een multimodale koppelaar, die elf modi geleidt eigenschappen kan vertonen die een verbetering vormen ten opzichte van de gangbare bimodale koppelaar. De verklaring, die hiervoor is gevonden, berust op de zelfafbeeldende eigenschappen van multimodale planaire golfgeleiders.

Experimenten zijn uitgevoerd met begraven multimodale Al_2O_3/SiO_2 richelgolf-geleiders bij golflengten van 0.6328 μm en 1.3 μm en met multimodale GaInAsP/InP golfgeleiders bij golflengten van 1.3 μm en 1.52 μm.

De invloed, die de laterale compenserende verplaatsing van de gebogen golfge-leider ten opzichte van de rechte golfgeleider op de verliezen heeft, is experimen-teel onderzocht. Hieruit is gebleken, dat het minimale verlies optreedt bij een waarde van de laterale compenserende verplaatsing die zeer dicht in de buurt ligt van de voorspelde waarde.

Twee nieuwe oplossingen zijn bedacht en uitgevoerd om het grote laterale brekingsindexverschil, dat nodig is voor de realisatie van kleine gebogen golfge-leiders met lage verliezen, en het kleine laterale brekingsindexverschil, dat nood-zakelijk is voor de reductie van verstrooiingsverliezen en voor de monomode werking van golfgeleiders, te combineren op één substraat.

De 'dubbel-richel' golfgeleider vertoont sterk verminderde verstrooiings- en afstralingsverliezen ten opzichte van de conventionele 'enkel-richel' golfgeleider. Dit is aan de hand van experimenten geverifieerd.

De 'vanzelf uitgerichte dubbel geëtste' gebogen golfgeleider heeft een richel-hoogte, die groter is voor de gebogen golfgeleider dan voor de rechte golfgeleider. S-bochten van dit type zijn vervaardigd in de vorm van begraven richelgolfge-leiders met behulp van een vanzelf uitgerichte fotolithografische techniek. De kleinste gemeten waarde voor de additionele verliezen bedraagt 0.5 dB/90° en is gevonden voor de S-bocht met een kromtestraal van 200 μm en bij een golflengte van 632.8 nm. Deze waarde van 0.5 dB moet grotendeels toegeschreven worden aan de overgangsverliezen van één koppeling van een monomode golfgeleider met een klein lateraal brekingsindexverschil en een golfgeleider met een groot lateraal brekingsindexverschil.

De kleinste gemeten additionele verliezen voor verschillende S-bochten zijn; 0.23 dB/90° voor $R = 75$ μm in Al_2O_3/SiO_2 golfgeleiders bij $\lambda_0 = 1.3$ μm, 0.6 dB/90° voor $R = 50$ μm in de Al_2O_3/SiO_2 'dubbel-richel' golfgeleider bij $\lambda_0 = 632.8$ nm en 0.5 dB/90° voor $R = 150$ μm in MOVPE-gegroeide GaInAsP/InP richelgolfgeleiders bij $\lambda_0 = 1.52$ μm.

Deze experimentele resultaten bevestigen de doelmatigheid van de ontwikkelde modellen en de gekozen strategieën om de verliezen en de kromtestraal te verkleinen van gebogen optische golfgeleiders.

Acknowledgements

I am indebted to Mrs J.B. Zaat-Jones for her corrections to the manuscript in respect to the proper use of the English language.

In particular, I would like to thank my parents, who have encouraged me in my studies and thesis research and who have always provided both moral and financial support when needed.

Finally, I would like to thank all of my friends. They have not contributed to the thesis, but they provide the fun and the joy that makes life worth living.

Biography

Erik Pennings was born in Sassenheim, the Netherlands, on November 3, 1960. In 1979 he started studying applied physics at the University of Groningen, the Netherlands, from where he graduated cum laude in 1986. In that year, he started to work on his thesis on curved optical waveguides at the Department of Electrical Engineering, Delft University of Technology, the Netherlands.